

N 72:27737

**NASA CONTRACTOR
REPORT**



NASA CR-2252

**CASE FILE
COPY**

**SITE ALTERATION EFFECTS FROM
ROCKET EXHAUST IMPINGEMENT DURING
A SIMULATED VIKING MARS LANDING**

Part I - Nozzle Development and Physical Site Alteration

by G. L. Romine, T. D. Reisert, and J. Gliozzi

Prepared by
MARTIN MARIETTA CORPORATION
DENVER DIVISION
Denver, Colo.
for Langley Research Center

NATIONAL AERONAUTICS AND SPACE ADMINISTRATION • WASHINGTON, D. C. • JULY 1973

1. Report No. NASA CR-2252		2. Government Accession No.		3. Recipient's Catalog No.	
4. Title and Subtitle SITE ALTERATION EFFECTS FROM ROCKET EXHAUST IMPINGEMENT DURING A SIMULATED VIKING MARS LANDING - PART I. NOZZLE DEVELOPMENT AND PHYSICAL SITE ALTERATION				5. Report Date July 1973	
				6. Performing Organization Code N61-9000	
7. Author(s) G. L. Romine, T. D. Reisert, and J. Gliozzi				8. Performing Organization Report No.	
9. Performing Organization Name and Address Martin Marietta Aerospace Denver Division, P. O. Box 179 Denver, CO 80201				10. Work Unit No. 815-20-00-00-00	
				11. Contract or Grant No. NAS1-9000	
12. Sponsoring Agency Name and Address National Aeronautics and Space Administration Washington, DC 20546				13. Type of Report and Period Covered Contractor Report	
				14. Sponsoring Agency Code	
15. Supplementary Notes					
16. Abstract <p>A potential interference problem for the Viking '75 scientific investigation of the Martian surface resulting from retrorocket exhaust plume impingement of the surface was investigated experimentally and analytically. It was discovered that the conventional bell nozzle originally planned for the Viking Lander retrorockets would produce an unacceptably large amount of physical disturbance to the landing site. An experimental program was subsequently undertaken to find and/or develop a nozzle configuration which would significantly reduce the site alteration. A multiple nozzle configuration, consisting of 18 small bell nozzles, was shown to produce a level of disturbance that was considered by the Viking Lander Science Teams to be acceptable on the basis of results from full-scale tests on simulated Martian soils.</p>					
17. Key Words (Suggested by Author(s)) Mars landing Rocket exhaust impingement Landing site alteration Viking Lander retrorockets				18. Distribution Statement Unclassified - Unlimited	
19. Security Classif. (of this report) Unclassified		20. Security Classif. (of this page) Unclassified		22. Price* \$3.00	
				21. No. of Pages 161	

FOREWORD

The investigations described herein were performed under NASA contract NAS1-9000 for the Viking Project with Mr. A. F. Carter, Viking Project Office, NASA-Langley Research Center, as coordinator. The LRC 60-foot sphere experimental work included in this report was conducted by Mr. Leonard V. Clark of the Viking Project Office and has been included in this report for completeness of the critical events of this study.

Acknowledgements are also made to the Aerojet General Corporation who supplied the engine used in the WSTF Phase IA testing, the Rocket Research Corporation who supplied the engine for the initial WSTF Phase II tests, and the TRW Corporation who supplied the "boilerplate" engine which could accomodate nozzle changes in the WSTF Phase II testing. Also to the Rocket Research Corporation for supplying the multi-two dimensional nozzle for testing impingement pressure performance and to the TRW Corporation who supplied the annular nozzle for testing impingement pressure performance.

SITE ALTERATION EFFECTS FROM ROCKET EXHAUST IMPINGEMENT
DURING A SIMULATED VIKING MARS LANDING

Part I. Nozzle Development and Physical Site Alteration

by G. L. Romine, T. D. Reisert and J. Gliozzi

SUMMARY

A potential interference problem for the Viking '75 scientific investigation of the Martian surface resulting from retrorocket exhaust plume impingement of the surface was investigated experimentally and analytically. It was discovered that the conventional bell nozzle originally planned for the Viking Lander retrorockets would produce an unacceptably large amount of physical disturbance to the landing site. An experimental program was subsequently undertaken to find and/or develop a nozzle configuration which would significantly reduce the site alteration. A multiple nozzle configuration, consisting of 18 small bell nozzles, was shown to produce a level of disturbance that was considered to be acceptable on the basis of results from full-scale tests on simulated Martian soils.

The selected multiple nozzle configuration also permitted a thrust cutoff altitude corresponding to footpad contact, much lower than originally planned, which resulted in reduced lander weight and shock loads on lander components. The present paper describes the problem and the effort which led to redesign of the Viking Lander retrorocket nozzle. In addition the paper presents the physical disturbance results of full-scale tests to establish the level of site alteration which will occur during the Viking Mars landing.

TABLE OF CONTENTS

	Page
INTRODUCTION	1
SYMBOLS	3
SOIL EROSION MECHANISMS	5
Viscous Erosion	5
Diffused Gas Erosion	5
Bearing Capacity Failure	6
TEST APPARATUS AND PROCEDURES.	7
WSTF - Phase IA	7
LRC	7
MMC	8
WSTF - Phase II	8
RESULTS AND DISCUSSION	17
Baseline Nozzle Impingement Pressures	17
Cold Gas Baseline Nozzle Tests to Estimate Site	
Alteration Effects for the Viking Lander	18
Sub-scale soil tests	18
Full-scale soil tests	19
Alternate Nozzle Designs to Reduce Site Alteration	19
Establishment of Impingement Pressure Criteria for the	
Alternate Nozzles	22
Full and Sub-Scale Nozzle Tests to Evaluate Alternate	
Nozzle Configurations	23
LRC cold-gas alternate nozzle tests	23
MMC cold-gas exploratory tests	25
Full-scale tests	28
Characterization of Site Alteration with Selected Nozzles	33
Soil erosion in lunar nominal soil	33
Soil erosion in volcanic dune sand	34
Soil heating	36
Analytical comparison with experiment and extension	
to Mars	37
Comparison of Soil Test Results with Mission Criteria	39
CONCLUDING REMARKS	43
APPENDIX	45
REFERENCES	49
TABLES AND FIGURES	52

INTRODUCTION

A primary mission objective of Project Viking is the search for extra-terrestrial life through a scientific investigation of the Martian surface. The Viking Lander, shown in figure 1, incorporates propulsive terminal descent in order to soft-land the scientific payload. The general question of native surface modification by the engine plumes had to be examined closely in order to establish the relevance of the returned scientific data. It was found that the descent engines had to be modified to achieve this result.

A multiphase test program has been conducted to investigate the amounts of physical, chemical, and biological alteration of simulated Martian surfaces that would occur as a result of the terminal engine plumes and to investigate vehicle design changes that could be made to minimize the site alterations. The baseline design of the Viking landing sequence called for the use of three monopropellant engines with conventional bell nozzles having an area ratio of 20 to 1. An impingement pressure test, designated Phase IA, of a full-scale prototype terminal descent engine in a simulated Martian environment was conducted in the NASA Manned Spacecraft Center White Sands Test Facility (WSTF) to determine the radial variation of surface impingement pressure as a function of engine altitude above the surface. Soil erosion tests were then conducted in the Langley Research Center 60-foot vacuum sphere using sub-scale and full-scale cold gas jets, modeled to match hot jet pressures, to determine the severity of the physical alteration that could be expected. These tests indicated that physical erosion of simulated Martian soil by the exhaust plume of an engine with a conventional nozzle descending toward the surface would not be acceptable.

Success criteria for defining the allowable limits of physical, chemical and biological alteration were established. A comprehensive Phase II Site Alteration Test Plan was then formulated to evaluate candidate engine/nozzle performance against these criteria. Concurrently, several analytical studies of the behavior of soils under the influence of plume impingement were conducted by the Martin Marietta Corporation and by investigators at the University of Colorado. These studies attempted to describe analytically viscous erosion and the onset of bearing capacity failure.

When it became apparent that engines with conventional bell nozzles would not meet the established physical criteria, sub-scale cold-gas nozzle tests were conducted at the Langley Research Center (LRC) and at the Martin Marietta Corporation (MMC) to develop nozzle designs which would reduce surface impingement pressures. The LRC tests were conducted in the 60-foot sphere under simulated Martian pressure conditions. The MMC tests were conducted in the Denver Division Cold Flow Laboratory under earth ambient conditions. Based on the results obtained from these sub-scale cold-gas tests, full-scale engine nozzle configurations were designed and fabricated. These nozzles were tested on a "boilerplate" engine which could accommodate nozzle changes. These flat plate impingement pressure tests together with

the soil impingement tests were conducted under simulated Martian pressure and CO₂ environments in a test chamber at the NASA Manned Spacecraft Center White Sands Test Facility. Flat plate impingement pressures and temperatures of the engine exhaust were evaluated for 10 different nozzle configurations at a lander descent rate of 1.52 m/sec. For selected engine nozzle configurations, impingement effects of the engine exhaust on simulated Martian soils were evaluated to determine soil cratering, soil transport and deposition, temperature profiles, and soil chemical and biological effects. From an evaluation of these test data a multiple nozzle configuration, consisting of 18 small bell nozzles, was selected for use on the Viking Lander.

The present paper describes in some detail the nature of the Mars landing site alteration problem discovered for retrorockets having a conventional bell nozzle, and the subsequent effort leading to the redesign of the Viking Lander retrorocket nozzle. In addition the physical disturbance results of full-scale tests to establish the level of site alteration which will occur during the Viking Mars landing are presented. The chemical and biological effects of the rocket exhaust impingement are discussed in Part II of this report.

SYMBOLS

c	Soil cohesion
CWP	Cumulative weight percent (eq. 7 appendix A)
D_p	Particle diameter, microns
d_e	Nozzle exit diameter ($= 2 r_e$)
d_{eq}	Diameter of equivalent circular diameter ($= 2 r_{eq}$)
dA	Unit area on surface $= r dr d\theta$
dl	Erosion depth (eq. 6 appendix A)
dt	Exposure time (eq. 3 appendix A)
Δt	Computing time interval
dW	Weight of soil per unit surface area and depth D_p , $= g dm$
g	Acceleration due to gravity (assumed Earth $g = 9.8 \text{ m/sec}^2$, Mars $g = 3.7 \text{ m/sec}^2$)
h	Engine exit plane height above surface
L_t	Total eroded depth (eq. 9 appendix A)
$\frac{\dot{m}_x}{\dot{m}_e}$	Mass flux in jet at axial distance x compared to exit plane mass flux
N	Number of particles per unit volume
P_e	Nozzle exit static pressure
P_c	Engine chamber pressure
P_I	Flat plate impingement pressure above ambient pressure
P_∞	Ambient pressure
P_{t_2}	Total pressure behind normal shock

r	Radius
t	Time
T	Temperature
V	Engine descent velocity
V_{mass}	Velocity at which particles leave surface after impulse from shear forces
x	Axial distance from nozzle exit plane (eq. 5 appendix A)
α	Descent angle from vertical
β	Soil slope
γ_p	Particle density = $g \rho_p$
γ_s	Soil bulk density = $g \rho_s$
ϵ	Nozzle area ratio
τ_{wj}	Wall jet surface shear stress
τ_R	Soil resisting stress
ϕ	Internal angle of friction
Φ	Particle distribution function (appendix A)
η	Molecular weight

Subscripts

b	Body
co	Engine cutoff
i	Initial
p	Particle
t	Total

SOIL EROSION MECHANISMS

Unlike the lunar landings where a vacuum permits the retrorocket exhaust to spread over a wide area, an atmosphere collimates the flow of an optimum designed nozzle within an area as small as the nozzle exit. With a finite Martian atmosphere and the 3 Viking Lander engine nozzles designed for optimum thrust performance, there exists a potential for severe soil disturbances during a Mars landing. The physical disturbance of a soil caused by an exhaust plume impinging on its surface has been separated into three distinct mechanisms by Scott and Ko in reference 1. These include viscous erosion, diffused gas erosion, and bearing capacity failure.

Viscous Erosion

The term "viscous erosion" is applied to the movement of particles by surface shear stresses of an impinging jet. As the impinging gases are directed along the surface, viscous effects set up a boundary layer and transmit a shear force to the surface which disturbs the soil particle and initiates motion. The phenomena is no different than that in the familiar dust storms, drifting snow, and changing river beds. The Apollo lunar landings clearly show the presence of viscous erosion due to LM descent engine exhaust impingement. Prior to the Apollo and Surveyor lunar landings a number of experimental investigations were conducted for this visibility problem, references 2 through 4 among others. Analytically, Roberts first formulated the viscous erosion for the lunar landing studies in references 5 and 6. The extent of viscous erosion expected for the Viking Mars landing was computed in reference 7 to be between 1.5 cm and 7.6 cm. This was based on a 20:1 area ratio bell nozzle with 667 newtons (150 pounds) thrust and an engine 'cutoff' height ranging from 4.6 to 1.2 meters above the surface. The present study used a modification to Roberts' viscous erosion theory which differs in the interpretation of momentum transfer to particles and allows for an arbitrary soil model composed of a wide distribution of particle sizes. This formulation is included in Appendix A.

Diffused Gas Erosion

Diffused gas erosion, as shown analytically and experimentally in reference 1, involves the flow of exhaust gases into and through the pores of a granular soil and appears in two stages. The first stage, found during engine firing, is caused by the gas flowing into the soil beneath the high pressure impingement region and back out of the soil at a lower pressure region. Depending upon soil properties, the rate of gas outflow can be great enough to overcome the soil weight and remove soil. The second stage of diffused gas erosion occurs at engine shut-down. When the impingement pressure at the surface is suddenly removed, gases which have been forced into the soil are allowed to escape (usually at a high rate). An analysis of gas outflow erosion and the shut-down eruption was performed by Ko (reference 8a) using the techniques outlined in reference 1, the nominal engine and landing sequence for Viking, and a range of soil parameters. Results

indicated a toroidal depression 4 cm deep for gas outflow erosion, and a dish shaped region of unstable soil 10 cm deep beneath the engine for the shutdown eruption. The results are sensitive to the descent profile, engine shutdown sequence, and soil properties (density, porosity, and permeability of the medium to gas flow).

Bearing Capacity Failure

During the descent of an engine with an impinging turbulent jet, the load (thrust) on the surface is concentrated within a descreasingly small area. The third cratering mechanism occurs as the resulting stresses within the soil exceed the soil shear strength and thus the soil load bearing capacity. Upon failure, a general region beneath the gas load becomes fluidized and offers little resistance to excavation by the gases. The phenomenon is basically similar to the principal behind hydraulic mining. Bearing capacity failure, also referred to as pressure cratering, was observed by Alexander, Roberds, and Scott (see reference 9) for stationary and descending high pressure jets under earth ambient conditions. Initially, they observed viscous erosion, followed suddenly by a massive eruption and geyser of soil. As the soil failed, a deep vertical walled crater was formed which redirected the impingement gases upwards accompanied by eroded soil.

Investigations as to the severity of pressure cratering expected for the Viking mission with the baseline engine and descent profile were conducted both experimentally and analytically. The experimental results and consequent nozzle development are presented in the following sections. Analytically, Ko included the effects of pore pressures with a method developed in reference 9 to compute the onset of bearing capacity failure and crater depths for the Viking descent. For the range of atmospheric pressures and soil models as specified in the Mars Engineering Model, reference 10, results indicated bearing capacity failure could be expected at altitudes below 5 meters with crater depths as great as 60 cm for the baseline bell nozzle (reference 7 and 8).

In comparing the relative amounts of erosion computed for the three mechanisms during a Viking landing, bearing capacity failure appeared to represent by far the greatest amount of soil disturbance. It has the most impact on the mission's scientific results, and also presents a hazard to the Lander. The experimental program described in the present report was formulated to investigate the severity of pressure cratering, to guide in the development of engine nozzle designs to lessen the exhaust gas/soil interaction, and to characterize in detail the experimental site alteration results of a redesigned system.

TEST APPARATUS AND PROCEDURES

White Sands Test Facility - Phase IA Tests

The Phase IA testing was conducted in the NASA White Sands Test Facility (WSTF), Test Stand 302. The 302 facility is a cylindrical vacuum chamber 9.75 meters in diameter and, for the Phase IA testing, 10.9 meters high. In order to measure plume impingement pressures during a simulated descent of the Viking Lander with a prototype monopropellant engine having a 20:1 bell nozzle, a moveable flat plate was used with the engine installed in a fixed position to existing structural members of the test chamber. During engine operation, the flat plate impingement surface was cycled beneath the engine to vary the axial distance between 10 and 26 nozzle diameters (1.58 to 4.02 meters) as shown in figure 2. The .95 cm thick stainless steel plate was .91 meter in diameter, and was instrumented as shown in figure 2 with fifteen pressure transducers located beneath the plate. The plate traveled at a rate of approximately .2 m/sec along a guide rail and was chain driven by a hydraulic actuator connected to an eccentric lever/sprocket system. A potentiometer, driven by the top sprocket through reduction gearing, was used to indicate axial distance from the nozzle exit to the flat plate.

The plate motion was initiated after the vacuum chamber had been evacuated and backfilled with N₂. Engine start command was given when the flat plate was approximately 3 seconds from reaching the nearest position to the engine. The engine operated for 38.8 seconds during which time the plate traveled slightly more than two cycles. With two axial surveys for each cycle, four and one-half axial impingement pressure surveys were obtained. During this time, the ambient pressure increased from 3.2 mb to 30.8 mb. The thrust was nearly constant at 667 newtons (150 lbs) with an engine chamber pressure which was 427 kN/m² at the start and steadily decreased to 407 kN/m² by the completion of the test period. Further details of operational procedures, calibration, accuracy, and data reduction techniques of the Phase IA testing are provided in reference 11.

NASA/Langley Research Center Tests

Experimental tests conducted by L. V. Clark at NASA/LRC were performed in the 60-foot diameter sphere. Several different lander retrorocket nozzle and surface target configurations were tested during the course of the study; the basic experimental test setup is shown in the schematic of figure 3. The model Viking Lander or single full-scale "cold-gas" nozzle was cantilevered from a carriage mounted on a rail. The rail extended from the top of the vacuum chamber to the floor of the chamber and could be tilted from the vertical. The model Viking Lander or single full-scale nozzle was moved along the rail by an electric-motor-driven chain-and-brake system, and was oriented so that the exhaust gases would impinge upon the target surface (either a pressure-gage instrumented flat plate or a particulate "soil" surface).

The tests were conducted in the sphere using either high-pressure helium or air at ambient temperatures to model the "hot" exhaust gases from the Viking Lander terminal descent engines. The sphere atmosphere was residual air at the desired level of ambient pressure representative of that anticipated on Mars (4 to 20 mb).

The test procedure started with the evacuation of the 60-foot sphere to the desired level of ambient pressure. The impingement pressure tests were performed very rapidly by setting nozzle pressure and lowering the test nozzle over the desired range of altitude above the flat plate. The effect of ambient pressure was evaluated by partially repressurizing the sphere. The soil impingement tests, however, could only be conducted one at a time because of the disturbance to the soil. After each soil test, the resulting disturbance was measured, after which the surface was smoothed and otherwise prepared for the next test. Microswitches located along the rail and tripped by the passage of the carriage terminated nozzle thrust at selected altitudes above the surface, and actuated a large magnetic brake to stop the carriage. The data from the study were recorded on an oscillograph, including the signals from the microswitches.

Martin Marietta Corporation Cold Flow Laboratory Tests

The exploratory tests of alternate nozzle concepts conducted at the MMC Cold Flow Laboratory (CFL) were designed to run at atmospheric pressure, 81.4 kN/m² (11.8 psi), using a high pressure nitrogen gas supply. In order to achieve a jet structure near that for a full-scale engine in a Mars environment, the pressure ratio at the nozzle exit was duplicated for the 20:1 expansion ratio using a chamber pressure of 23,400 kN/m² (3400 psi). A conical nozzle with an exit half-angle of 15 degrees, and a 5.08 cm exit diameter (1/3-scale) was used. An instrumented flat plate, .91 meters in diameter was used as a target surface, and a hydraulic actuator was used to drive the plate over a 2.44 m distance for the axial survey. The plate and drive mechanism was the same as used for the WSTF Phase IA test, but was inverted for this test. The nozzle assembly was mounted at the ground plane for easy access and exhausted vertically upward. Sixteen pressure ports were relocated for the 1/3-scale test for the radial distributions as shown in figure 4.

White Sands Test Facility - Phase II Tests

For the WSTF Phase II site alteration tests a 6.1 meter section was added to the cylindrical part of the test stand 302 vacuum chamber to extend the useable height to 14.3 meters as shown in figure 5. This additional height was required in order to simulate the significant part of the exhaust/soil interaction which would occur during the terminal descent phase of the Viking landing. For these tests, the use of 3 full-scale rocket engines as on the Viking Lander was not practical; therefore, a 1/3-segment of the Viking Lander

was simulated with one full-scale engine attached and, as shown in figure 6, reflection planes 4.9 meters high were used to simulate the jet interaction effects of the other two engines. The 1/3-lander segment was attached to a carriage designed to ride smoothly on a vertical track. Travel of the carriage, including starting, the constant velocity descent, and stopping, was controlled by a hydraulic motor and an electro-mechanical brake through a chain and sprocket drive mechanism. The shock absorber shown in figure 6 was located at the bottom of the track as a back-up arrest system. A potentiometer attached to the upper sprocket of the chain drive assembly was used to record lander position on the track as a function of time. From these data the lander descent velocity was computed for each test. Surfaces used in the Phase II testing included an instrumented flat plate, a pressure and temperature rake, and an instrumented soil bed with two soil models.

Propulsion system - Two hydrazine fueled catalytic rocket engines were used for the Phase II tests. Initial exhaust gas sampling tests were conducted using a flight weight engine with a 20:1 area ratio conventional bell nozzle having a 15.24 centimeter exit diameter. The remainder of the sampling tests and the pressure and soil tests (see table I) were conducted using a "boilerplate" engine. This engine, which can be seen in figure 6, had a heavy wide-flange joint between the nozzle and the catalyst bed that made it possible to change engine nozzle configurations. Both engines were capable of producing 2669 newtons (600 lbs) of thrust, but were throttled to 667 newtons (150 lbs) during the Phase II testing to simulate the Viking Lander near surface thrust. Engine performance was monitored by recording engine run tank pressure, engine injector manifold pressure, engine chamber pressure, and gas temperature in the engine below the catalyst bed.

Nozzles - Ten different nozzle configurations were tested on the boilerplate engine during the Phase II tests. All of these configurations were tested on a descending lander to measure the impingement pressure distribution on a flat steel plate.

The initial configuration tested (see figures 6 and 7) was a 20:1 conventional bell nozzle having a 15.24 centimeter exit diameter. The other 9 configurations tested were designed to reduce the maximum impingement pressures from the rocket exhaust. Seven of the configurations were designed by MMC and the other two tested were provided by other contractors.

One nozzle provided had an annular exit and is shown in figure 7. Another nozzle also shown in figure 7, was a multiple two-dimensional nozzle configuration. MMC designs are shown in figures 7 and 8. They include 1) a seven-nozzle configuration, 2) a 24-nozzle configuration, 3) the 24-nozzle configuration modified to an 18-nozzle configuration by plugging every other nozzle in the outside ring, 4) the 24-nozzle configuration modified to an 18-nozzle configuration by plugging the 6 nozzles in the inner ring, 5) a fluted nozzle, 6) the fluted nozzle modified, and 7) a full-scale 18-nozzle configuration. Sketches of MMC designed nozzles showing the geometry and pertinent dimensions are presented in figure 9.

Flat plate impingement pressure measurements - A stainless steel flat plate simulating the landing surface was located on top of the soil bed under the engine as shown in figure 10. Plume impingement pressures and heating rates were measured with 14 pressure transducers and 11 calorimeters located as shown in figure 11. Absolute pressure transducers were packaged under the flat plate and connected to the orifices in the plate by approximately 1.2 meters of .216 centimeter ID stainless steel tubing. Each of the pressure transducers was calibrated in the WSTF calibration laboratory prior to installation. All were found to be accurate within $\pm 1\%$ of full-scale and in most cases were an order of magnitude better. Pressures and heating data were reduced at the WSTF Data Center and recorded on magnetic tape. Further details of instrumentation, calibration, and data reduction of the Phase II tests are given in reference 12.

Engine plume rake - A rake to measure the temperature and pressure distribution in the engine plume as a function of distance from the engine nozzle centerline was used on the final test. A photograph of the rake installed in the test chamber is shown in figure 12. Installation was made so that the openings of the pressure tubes and the thermocouples were located .61 meters above the flat plate.

Soil container -

Soil bed: The soil bed container consisted of a steel tank 7.0 meters long and 2.3 meters wide. Along a center strip .76 meters wide, the bed was .91 meters deep. The top .15 meter of the container side walls were vertical, then sloped at a 45° angle to a horizontal .76 meter wide bottom. At one end of the bed which formed the base of the engine reflection planes, the walls were vertical, forming an included angle of 120° with a full depth of .91 meter. The opposite end of the bed was formed by a 45° sloping surface.

The soil bed container was filled with lunar nominal soil .91 meter deep for only soil test 12A. For the other three tests with lunar nominal soil (tests 12C, 12D, 12E) a false bottom was added to the initial soil bed container and fabricated such that the soil bed could degas during pump-down of the chamber from the top and bottom surfaces. A steel support grating was installed upon which aluminum screen wire was placed. Unbleached muslin was stretched across this screen and held in place by aluminum perforated plates of 40% porosity. The soil bed was then constructed utilizing the test procedure outlined in reference 12.

A plan view of the soil bed container and adjoining soil trays is shown in figure 13. Figure 14 is a schematic drawing of the false bottom incorporated in the soil bed and figure 15 shows the installation of this permeable false bottom.

Because of the high permeability of the volcanic dune sand soil model, the full depth (.91 meter) of the soil bed under the engine was used on all dune sand soil tests. Two meters from the end of the container, a bulkhead

made of the same materials as the false bottom was constructed with the remainder of the soil container as it was for the lunar nominal model soil tests, i.e., .305 meter deep. (See figure 14).

Soil trays: Along one side of the bed were two soil trays which extended along radial lines from the engine centerline. One tray which adjoins the reflection plane extended 4.57 meters beyond the soil bed container for a total distance from the engine center point of 5.94 meters. The second tray extended 4.42 meters beyond the soil bed for a total distance of 6.84 meters from the engine center point. These trays contained the sealable soil cups for measuring chemical contamination of the soil, open soil cups for measuring soil erosion and transport, and unobstructed areas for assessing the effect of engine plume gases on prepared surface morphological features.

A third soil tray adjoining the engine reflection planes on the opposite side from the two soil trays was used to assess biological degradation as a result of engine plume impingement. All three side trays were 7.6 centimeters deep.

The distribution of three adjoining soil trays together with the main soil bed cover most of the sampling area available to the Viking Surface Sampler. This geometry was used so that the symmetry of plume/soil interaction could be assessed throughout the sampling area to determine if certain areas were more favorable for sampling. Figure 13, a plan view of the main soil container and soil trays, shows the area available to the Surface Sampler.

Open soil cups: Open soil cups were placed in the soil trays to make measurements of soil transport and deposition during severe soil disturbances. After the first engine firing in soil, test 12A, the open soil cups were discontinued because the soil erosion and transport was primarily viscous shear and the collected material (very small amount) was assessed to be insignificant, particularly in view of the preparation of the soil cups, which was very time consuming.

Sealable soil cups: Two types of remotely controlled sealable soil cups were used in the Phase II tests. One type was filled with soil prior to testing and sealed during the test either just before or just after engine firing. The other type was an auger which dug a soil sample from the main soil bed after engine firing and was then sealed in a fitted cap. The sealable soil cup designs, operations, and results are presented in Part II of this report.

Louvered collecting baffle - At the end of the soil bed, which was 6.22 meters from the engine centerline, a louvered baffle .62 meters wide extending 1.75 meters above the soil bed surface was installed to collect soil being ejected from the soil bed crater by the engine plume. The louvers were made from 16 Vee-shaped trays located to collect the soil from 23 centimeters above the soil bed in 10 centimeter increments. A photograph of the baffle assembly is presented in figure 16.

Recirculation baffles - In order to minimize soil particle circulation within the 302 test chamber during an engine firing on a soil test, panels of untreated fiberglas filter material were installed around the inside walls on a wire frame. These panels were approximately 2.7 meters high and were installed approximately .6 meters from the inside wall of the test chamber with the bottom at the floor level. These panels collected a large part of the soil eroded from the bed as shown in figure 17; however, the fine particles that were not collected by the baffles were suspended in the test chamber atmosphere and interfered with motion picture photography during the later part of the engine firing.

Additional apparatus - During selected tests of the Phase II Site Alteration Test Program, additional apparatus was used for further defining the environment during the simulated Viking landing. Engine nozzle base pressures were measured between nozzles of the multiple-nozzle configurations. The engine exhaust soil interaction effects on the lander bottom were measured with pressure transducers, calorimeters, and a small pressure rake. A simulated footpad was added and instrumented to measure pressures, heating rates, and total temperatures as it entered the wall jet flow during the vehicle descent. Lander acoustic environments were measured near the terminal descent engine. Three orthogonal accelerometers were used to obtain vibration measurements on the engine carriage mounting brackets. A radar system was mounted on the lander base to evaluate its performance as affected by the engine induced dust motion for both the lunar nominal and dune sand soil models. Dust collecting cups were placed on top of the lander in an attempt to differentiate accumulation effects with and without a residual charge. Finally, samples of Viking Lander imagery camera window material were exposed to the dust environment. Further information and detailed results of these experiments may be found in reference 12.

Soil models - The two soil types employed in the Phase II site alteration tests are based on the specifications presented in the Mars Engineering Model (reference 10). Although five surface models are presented in this document, only two were selected for testing. These were a lunar nominal model based on Apollo samples and a natural occurring volcanic sand dune model.

The rationale for selecting these two soil models was based on a number of considerations. The Apollo analyses represents the only real data from another planetary body and one in which the dominant surface morphology is characterized by impact craters. This lunar nominal model is well-graded and contains a particle size distribution from sub-micron size particles to a very coarse fraction. Because of this feature the model can be prepared in various ways to give a wide range of surface mechanical properties. The volcanic sand dune model has a narrower particle size distribution band due to wind sorting action and was selected because analytical studies of the engine plume/surface interaction indicated that this highly porous/permeable material would represent a worst case condition in terms of site erosion by the lander. This was substantiated by the test results.

Lunar nominal model: The lunar nominal model specifications are based on screen analysis provided by the Apollo 11 mission results. A cumulative distribution of particles by weight percent is presented in figure 18. The technique employed in the fabrication of the lunar nominal model was to take volcanic rock aggregate in the size range of 5 centimeters to pan size from Table Mountain, Golden, Colorado, and grind it in an allochthonous mill charged with a few steel-alloy balls. The fine fraction of the model was separated in discrete size fraction by an air classifier. The coarse-size particles were separated by screening. The crushed rock product was then blended in individual 55-gallon covered steel drums to achieve the desired particle size distribution for each drum. Although continental basalt and latite were used in the preparation of the model, it is believed that adequate compositional simulation was achieved for these tests.

Dune sand model: The second soil model used in the Phase II site alteration tests was a natural occurring dune sand of volcanic origin. The material was collected near Sunset Crater, Arizona, in the Elden Ranger District of the Cononico National Forest. The origin of the sand dune material is pyroclastic debris ejected from Sunset Crater around 600 A.D. This mafic, scoracious debris has been sorted by wind action on the high plateau of Arizona and piled into active dunes of moderate height. The material was relatively well-sorted and coarse with a mean particle size of about 0.6 mm. A cumulative distribution of soil particles by weight percent is given in figure 18. The mechanical properties of the simulated Martian soils are discussed in reference 12, and a complete laboratory analysis of their mechanical properties together with three additional models is treated in reference 8b.

Soil bed instrumentation - Instrumentation of the soil bed was selected to determine the form of the crater made by the engine plume, temperature distribution of the soil, pore pressure in the soil during evacuation of the test chamber and during a test, soil transportation and the distribution of ammonia and other chemical compounds in the soil bed. Two 16-mm motion picture cameras were used to photograph the soil bed during the soil tests. One was located on the first level platform 1.89 meters above the soil bed and was used to obtain a close-up view of the soil bed directly under the engine. The second camera was located on a higher level platform 5 meters above the soil bed to obtain a view of the soil sampler area as well as the area under the engine. The shape of the craters formed by the engine plume was recorded by photographs taken before and after an engine firing. Physical measurements were made of erosion where significant.

Soil heating was measured by two techniques. The first method was by thermocouples placed in the soil to measure sub-surface heating from conduction and diffused gases. The second technique employed to measure surface heating utilized the natural infrared thermal emission of the soil. A scanning mirror directed the thermal emission from the soil to a detector which produced a thermal image of the target area on a vidicon screen. The detector response and scanning rate of the mirror allowed 16 frames/second to be produced on the vidicon screen which was recorded by a 16-mm movie camera. The surface temperature/time history of the plume impingement area was then recorded.

Temperature distribution within the soil bed was measured with 59 buried thermocouples. Pore pressure in the soil bed was measured by burying pressure transducers in the soil bed on the line of symmetry. The pressure diaphragm was protected from measuring the static load of the soil by inserting a porous foam plastic plug in the transducer opening. This plug allowed pore pressure changes to be measured without influence of the static soil load. These transducers were also used to monitor the differential pressure between pore pressure in the soil bed and the test chamber pressure during test chamber evacuation.

Test preparation and procedures - Test conditions for the 31 tests conducted for Phase II at the WSTF 302 vacuum chamber are presented in table I. Test numbers refer to the type of test described in reference 13 and not to the order in which they were conducted. Other than equipment checkout tests, the program can be divided into 4 types of tests conducted under simulated Martian conditions:

1. Static firing of engine to collect exhaust gas samples for chemical analyses (covered in Part II of the report).
2. Engine descending with plume impinging on a flat plate instrumented with pressure orifices and calorimeters.
3. Engine descending with plume impinging on simulated Martian soil.
4. Engine descending toward a temperature and pressure rake.

Pressure plate tests: Ten tests to measure the axial and radial distribution of impingement pressures on a flat plate for 10 engine nozzle configurations were conducted during Phase II testing. For all of these tests the following procedure was used. The propellant tank on the lander was filled with hydrazine well in advance of the test, usually the day before. When all systems were checked out the test chamber doors were closed and the test chamber evacuated to 21 newtons/meter². The test chamber was then backfilled with carbon dioxide gas to approximately 1000 newtons/meter² of pressure. The lander propellant system was pressurized to the level consistent with the thrust desired. The lander segment was raised with the hydraulic system to the top position of the rail assembly which was 12.2 meters above the flat plate. The engine was started with about 667 newtons of thrust and approximately 2.4 seconds later the lander descended at a constant rate of 1.52 meters per second toward the instrumented flat plate described in the previous section of this report. For most of the tests the engine firing switch was cut-off just before the lander assembly was stopped by the electro-mechanical brake or shock absorber. A time history of the pressure and temperature within the vacuum chamber was recorded before, during and after each run.

Soil tests: Two simulated Martian surface models were used in the Phase II site alteration tests; a lunar nominal and a volcanic dune sand model. Because of the unique physical properties of these two models, each required a different preparation technique. As outlined in more detail in reference 12 the lunar nominal soil model was added to the soil bed in layers, smoothed, compacted, and was measured for soil density. In certain tests, the lowest densities were achieved by sifting in the material and allowing only the

compaction resulting from the overlying material. A reasonably homogeneous model of the dune sand material was achieved by simply pouring in the material from a fixed height and raking smooth between applications. The mechanical properties of the two soil models employed in the Phase II site alteration tests were experimentally determined by a triaxial shear test and were related to soil density in reference 8b. Two graphs from this report showing cohesion and internal angle of friction versus bulk density are shown in figures 19 and 20. Density measurements during soil bed preparation, prior to testing, and after each test were made with a density-moisture gauge operating on a gamma-ray back scatter technique. Cohesion was also measured with a shear vane and torque watch.

After extensive preparation of the soil bed, the chamber was closed and the pump down was initiated but at approximately 1/3 the system pumping rate. Soil pore pressures were continuously monitored to avoid soil bed eruptions due to excessive pressure differentials between the test chamber and the gases within the soil bed. The CO₂ backfill before the test and the N₂ backfill after engine firing were regulated so as not to disturb the surface features on the soil bed.

Several techniques were attempted to measure directly the amount of soil eroded as a result of the engine firings. Two general types were implemented; one which measured the net loss during the test and one which measures absolute removal of soil. A stake network was placed in the soil bed before each firing. The density of the stake network varied from test to test as more experience was gained. These stakes consisted of rods .32 centimeter in diameter which were marked with one-millimeter blue and red colored stripes and a second set which were made of aluminum weld-rod .24 centimeter in diameter with a single scribe mark. Both were placed in the soil to a known depth before the tests. After the test, the distance from the pre-test mark to the new soil surface was measured as a positive number if the soil was above the mark and a negative number if below the mark. This measurement represented the net erosion value for that point in the bed. The distribution of the stake farm for each soil test is discussed further in reference 12.

In order to assess the actual erosion during the test, a quantity of lunar nominal soil model was dyed with two different colors using machinist lay-out dye. The material was screened so that the largest remaining particles were less than one-millimeter in diameter. In most tests a strip .3 meter wide and 2.44 meters long was prepared by scraping the surface with a blade positioned by two level channels. The prepared surface was dusted with red-colored soil and rescraped after repositioning the blade one-millimeter higher than the initial surface. The result was a one-millimeter layer of colored soil over the test bed. This technique was repeated for a second color which resulted in a strip two-millimeters thick from the engine center point along an engine radial to the baseline limit of the Viking soil sampler area. After the engine firing the actual amount of erosion could be assessed by defining the post-test extent of the colored soil layers. This technique proved to be a very sensitive measure of erosion and values of less than one-millimeter could be determined.

After each soil test, the engine center point in the soil was defined. For most cases in lunar nominal soil, this area was a shallow, scrubbed depression with poor crater definition. In tests utilizing the volcanic sand dune model, distinct crater shapes were formed reflecting the engine nozzle geometry. Stake measurements and level rails placed across the soil bed were used to define the extent of erosion.

Several indirect techniques for measuring soil erosion were incorporated in the tests to verify the direct measurement results. During the final preparation of the soil bed, the surface was varied by forming several surface features. These included ridges and troughs positioned transverse and radially to the engine centerline, preformed craters, cones and triangles of fluffed soil, and surface markings formed by pressing a grid into the surface. These features were measured and photographed before and after the tests to assess the degree of erosion they had experienced.

A network of rocks of various sizes was placed on the soil bed prior to each test. The displacement of these selected equi-dimensional rock samples was a fairly sensitive measure of the deflected plume gases, since the force required to initiate their movement is approximately equal the rock weight.

The actual movement of the soil was documented by high-speed photography and on video tapes. Confinement of the plume gas to near-surface environment was demonstrated. Still photography documented the net erosional effects and recorded the degradation of surface morphological features and markings.

Engine plume rake test: The procedure for the engine plume rake test (test 29) was the same as that used for the pressure impingement tests described previously. The lander was allowed to descend with engine operating at a velocity of approximately 1.52 meters per second in a simulated Martian atmosphere toward the plume rake described in the instrumentation section which was located .61 meter above the flat plate. Total temperatures and pressures were measured.

RESULTS AND DISCUSSION

Baseline Nozzle Impingement Pressures

Phase IA results of a full-scale monopropellant engine exhaust plume (early prototype for the Viking baseline engine with a 20:1 area ratio bell type nozzle) impinging on a moving flat plate are shown in figure 21 for four and one-half passes of the plate motion. During the engine firing, the plate motion was programmed to cycle between 20 ± 10 nozzle diameters (nominal Viking engine cutoff height). The pressure results are presented as impingement pressures above ambient normalized with engine chamber pressure (P_I/P_C), versus axial distance in nozzle diameters (x/d_e). Test conditions are summarized in table II, with full details of results in the Phase IA test report, reference 11. There was no pumping of the test chamber during engine firing; therefore, the test chamber ambient pressure increased with each plate pass and covered the range of ambient pressures expected on Mars (reference 10). The corresponding pressure ratio, exit-to-ambient, is also included as a function of axial distance. The exit pressure was computed as 3.46×10^{-3} times the engine chamber pressure assuming a constant ratio of specific heats of 1.315.

As indicated by the results, a maximum impingement pressure related to engine chamber pressure of 0.12 was found for a pressure ratio near 0.5 ($P_I = 7$ psi). In general, it was determined that a high impingement pressure will be found for pressure ratios between 0.4 and 1.5. Above a pressure ratio of approximately 2, the impingement pressure will decrease. Similar pressure ratio effects were shown by Clark (reference 14) for a 2:1 area ratio helium jet. Also shown by the results in figure 21, a through e, the core length decreases for pressure ratios below one and increases with nozzle under-expansion up to the maximum tested pressure ratio of 3. Downstream of the core structure, the observed mixing decay characteristics of the jets are essentially the same for the test pressure ratios between 0.4 and 1.4.

The effects of pressure ratio on the jet structure are further shown by the results replotted at fixed axial locations. Figure 22 shows the radial variation of impingement pressures for each pass when the plate was 12 and 14 exit diameters away from the exit. The 12 exit diameter distance represents the location of the highest pressures found, and the 14 exit diameter location represents the minimum pressure region of the same shock cell for the fourth pass.

A second full-scale engine was run during the Phase II testing (see reference 12) with impingement pressures measured during the last 80 nozzle diameters of the simulated descent. Results of the axial survey are presented in figure 23 for the centerline location while the radial variation for 5 altitudes is shown in figure 24. The results compare favorably in magnitude to the Phase IA pressures, with some differences in the shock structures and locations of high pressure regions. These fluid dynamic effects are caused by differences in ambient pressure and gas species, operating conditions, and nozzle and engine differences of the two tests.

The impingement pressure results as shown in figures 21 through 24 establishes the basis for simulation of the cold-gas erosion tests, and establishes the pressure levels of the baseline engine and nominal descent conditions to be used in further erosion calculations. They also establish a basis for the comparison of the alternate nozzle impingement results.

Cold-Gas Baseline Nozzle Soil Tests to Estimate Site Alteration Effects for the Viking Lander

Sub-scale soil tests - Several sub-scale tests were conducted in the NASA/Langley 60-foot sphere to obtain a qualitative measure of the extent of jet exhaust-soil interaction problems for the Viking Lander. These tests were conducted with a 1/6-scale model of the Lander, which utilized three "cold-gas" jets to simulate the terminal descent engines. The scaling philosophy of the tests was to duplicate the impingement pressure time-history variation with altitude as measured during the full-scale engine tests at the NASA/White Sands Test Facility. A comparison of the jet exhaust centerline impingement pressure variation with altitude as measured under one of the 1/6-scale nozzles (using helium) with the full-scale impingement pressure variation with altitude is shown in figure 25. For the soil tests, the descent velocity of the model was chosen to be approximately 1/6 of the planned full-scale velocity in order to duplicate (as nearly as practical) the full-scale exposure time. For these tests the model descent velocity was approximately 0.58 m/sec which scales to 3.5 m/sec full-scale velocity (current plans call for this velocity to be within the range 2.4 ± 1.0 m/sec for the actual Viking Lander at touchdown).

Figure 26 presents a sequence of test photographs which illustrate to scale the approximate surface cratering which would be experienced by the Viking Lander during touchdown on a lunar nominal soil model, using the originally planned nozzles. The surface disturbance begins when the Lander is at a considerable altitude above the surface, as previously reported in reference 14. The erosion pattern shown in the photographs for high lander altitudes has been termed viscous erosion by previous investigators of jet-erosion problems. The effect of having three retrorockets becomes quite evident as the model lander descends to lower altitudes. The exhaust gases stagnate on the surface beneath each engine and subsequently expand in all directions along the surface to the lower ambient pressure. The exhaust gases from each engine collide beneath the lander creating a strong updraft which carries eroded materials upwards toward the approaching spacecraft. As the lander gets relatively close to the surface, the character of the surface interaction phenomena changes from viscous erosion to bearing capacity failure and/or diffused gas erosion as discussed in a previous section of this report. Tests such as those portrayed pictorially in figure 26 led to the initial concern that perhaps the Viking Lander would require some redesign in an effort to reduce the alteration of the Mars landing site to an acceptable level from both an engineering and science standpoint. The lower value of Martian gravity would make the erosion problem more severe than that shown by the experimental tests.

Figure 27 presents additional test photographs which illustrate the effect of retrorocket cutoff altitude on the magnitude of site alteration. As expected site alteration increases with decreasing cutoff altitude. This is more clearly evident by the measured crater profiles shown in figure 28 for the two tests shown in the previous figure.

Full-scale soil tests - Several full-scale cold-gas nozzle tests were conducted in the LRC 60-foot sphere to confirm the previous results obtained with sub-scale nozzles. For these tests a single 20:1 area ratio conical nozzle was used with air. It would have been extremely difficult to use three full-scale nozzles considering the mass flow requirements and how quickly ambient pressure simulation would be lost. The cold-gas nozzle was operated at a chamber pressure approximately the same as the prototype retrorocket, although at a lower value of thrust because of the difference in gas properties. The degree of impingement pressure simulation achieved is shown in figure 29. The simulation was not as good as with the sub-scale nozzles using helium, particularly at the higher nozzle heights. Nevertheless, the results of soil impingement tests with this degree of full-scale simulation confirm the earlier sub-scale tests as shown in the test photographs of figure 30. The test photographs illustrate the effect of descent velocity on the magnitude of surface cratering for a 3 meter thrust cutoff altitude (equivalent to an altitude of 20 nozzle-exit diameters). The test at a descent velocity of 2.8 m/sec (18.4 d_e /sec) can be compared with one of the sub-scale tests for approximately the same test conditions as shown in figure 31. As shown in the figure the crater profiles do not compare too favorably which may be directly attributable to the poorer simulation of the impingement pressure history with the full-scale cold-gas nozzle considering the thrust cutoff altitude. At a thrust cutoff altitude of 1.5 m (10 d_e) the cratering is extremely severe as shown in the test photographs presented in figure 32. At this low value of cutoff altitude the proper magnitude of impingement pressure is simulated as shown in figure 29.

Alternate Nozzle Designs to Reduce Site Alteration

As indicated by the previous tests and analytical studies, the Viking vehicle with baseline engines descending towards the Martian surface would induce an unacceptable level of site alteration and environment around the lander at touchdown. Various techniques were considered for reducing site alteration to a level acceptable for the Viking mission. However, all methods imply a weight and/or reliability penalty or a new landing technique. One technique is to alter the thrust-altitude program by, for example, increasing the altitude at which retrorocket thrust is terminated. However, this would mean higher impact loads on the lander components and a stronger, heavier landing leg design. A second technique would be to translate the vehicle laterally either after impact to avoid all disturbances (which means a completely new landing technique) or during descent with a high horizontal velocity in order that the touchdown site would experience a minimum time of exposure to the impinging gases. However, this later technique would not only increase impact loads but also increase the landing stability

problems. A third technique would involve canting the retrorockets inward or outward to lessen the amount of direct exhaust impingement. There is some loss of effective thrust associated with canting the retrorockets. The fourth technique available is to minimize the load concentration on the soil by spreading out the momentum flux of the exhaust gases, i.e., reducing impingement pressures. From a lander systems viewpoint, the most desirable method of reducing impingement pressures is to redesign the engine nozzle keeping the descent sequence, the engine location, and the engine catalyst bed and injection design unchanged. Four basic nozzle design concepts were investigated to determine their impingement pressure reduction and their weight, reliability, cost, and schedule to the program. These concepts include reducing the scale of flow by using multiple nozzles, increasing the mixing rate with the Martian atmosphere, decreasing nozzle area ratio, and modifying the exit plane momentum distribution.

Multiple nozzles - The first and most obvious technique of reducing jet impingement pressures is to decrease the scale of the jet flow by dividing the thrust among a number of smaller nozzles. If the jets are allowed to mix with the atmosphere unimpeded by adjacent jets, the flow will scale by the exit diameter. Thus, the larger the number of nozzles, the smaller the scale of the flow and the lower the impingement pressures for a constant cut-off height. Nozzle spacing and divergent cant angles are design variables which will permit the entrainment demands of each jet to be met in order to achieve individual free jet mixing.

Increase mixing rate - The relationship between jet centerline impingement pressure decay and the jet entrainment was computed for the nominal Viking descent conditions by the method in reference 15 and is presented in figure 33. In order for mixing to reduce the maximum jet impingement pressure from the baseline engine by a factor of 10, for instance, the jet must entrain and mix in the ambient atmosphere such that the mass flux in the jet is approximately 7 times that at the exit. The distance required to entrain and mix this amount thus determined the mixing rate, or equivalently, the entrainment mass flux per unit axial distance. As the jet entrainment may be related to the momentum flux in the mixing layer, an increase in the shear surface area will increase the shear force and thus the entrainment. Increasing the peripheral surface of the exhaust plume may be achieved by elongating the nozzle exit into two or more slots while maintaining the same exit area.

Exhaust flow characteristics of slotted nozzles, fluted nozzles and other non-circular nozzles were experimentally investigated for application to VTOL downwash suppression in references 16 and 17. Results indicated significant reductions in dynamic pressure for all nozzles with the most improvement from those nozzles with the greatest perimeter ratio, non-circular exit perimeter to circular nozzle circumference. The decay characteristics of three dimensional nozzles (slotted, elliptic, square and triangular) were investigated by Trentacoste and Sforza, reference 18, who observed three distinct regions in the axial velocity decay. The first region is the core with properties unchanged from the exit values, followed by a mixing region where the velocity decay rate falls between $1/x$ for axisymmetric jets and $1/\sqrt{x}$ for two

dimensional jets. The third region is in the far field of the jet where the flow becomes axisymmetric and decays as if it originated from an equivalent circular nozzle. The effect of perimeter ratio may be seen in figure 34 where the results of reference 18 are replotted as perimeter ratio versus scale factor of the flow. The scale factor is defined as the ratio of core lengths of the circular nozzle to the non-circular nozzle. As seen by the figure, increasing the perimeter ratio with non-circular nozzles is more effective in the near field than multiple axisymmetric circular nozzles.

Another method of increasing the mixing rate is to add disturbances and turbulence to the nozzle flow and to design in flow nonuniformities. As found in reference 16, wall roughness, vortex generators, and turbulence rings placed in the low velocity flow upstream of the throat do not significantly alter the free jet mixing characteristics. Obstructions placed at or near the exit in the high velocity flow, however, could produce large scale turbulence and flow disturbances which would affect the mixing rate. A number of other techniques to enhance mixing were examined by Hetrick, reference 19, including boundary layer and inviscid flow perturbations, plug and expansion/deflection nozzles, acoustic disturbances, fluidic disturbances, swirl flow, inducing shocks and other perturbations, and manipulating eddy viscosity dependencies. In general, these techniques were found not sensitive enough or too little information was available.

Decreasing area ratio - The third alternate nozzle concept considered was to reduce the nozzle area ratio. An optimally designed nozzle has the exit pressure matched with the ambient pressure; however, if the area ratio were less than optimum, the gases would continue expanding outside the nozzle and spread the momentum over an area larger than the optimum exit area. An additional factor which might contribute to the lowering of impingement pressures is the increased mixing from vorticity introduced into the flowfield from the shock structure of underexpanded jets. Pressure ratios up to 800 are expected for a Mars lander with sonic nozzles descending into a 4 mb atmosphere. One disadvantage of using this concept is the performance loss, nearly 30% for a sonic nozzle. Separating the expanding part of the nozzle at lower altitudes during the descent was suggested, but this would add weight and another critical sequence to the landing.

Modifying exit plane momentum flux - The fourth concept has been termed a thrust plate and consists of a few hundred sub-scale nozzles mounted on a plate. The momentum from these jets should redistribute itself between nozzles to give a core impingement pressure roughly equal to the thrust divided by plate area. The primary mechanism, then, involves small jets expanding and mixing with each other. The particular arrangements of the small nozzles could allow mixing with the atmosphere for further pressure reduction. In order to achieve a factor of 16 reduction in core pressure, the plate diameter must be 4 times that of the axisymmetric nozzle diameter. Such increases in size exceed space limitations in the aeroshell and complicate attachment of the nozzle to the engine catalyst bed.

Establishment of Impingement Pressure Criteria for the Alternate Nozzles

Alternate nozzles based on the preceeding concepts and combinations of concepts were evaluated in terms of their effectiveness in reducing jet impingement pressures to a level associated with acceptable site alteration. Chemical, biological and physical disturbance levels in line with the scientific mission objectives were established and outlined in reference 20. The physical disturbance levels were defined as:

- Not more than 60% of the soil sample area will experience more than 2 mm erosion,
- 5 cm maximum allowable crater depth,
- No more than 8 mm of eroded material redeposited within the sampler area,
- For at least 60% of the area accessible to the surface sampler, no more than 20% of the sample taken from the top 4 cm of the surface shall have been heated in excess of 40°C.

Further, these criteria must be met for the range of ambient pressures that are specified in the Mars Engineering Model (reference 10). In order to meet the criteria, it is obvious bearing capacity failure must be avoided. Diffused gas outflow erosion and viscous erosion are ever present, but their effects can be minimized by a reduction in impingement pressure.

Information as to the impingement pressure levels necessary to meet the criteria was obtained from movies and still photographs of the LRC soil tests and the LRC pressure tests. Reviewing motion pictures of the tests, the altitude was noted for which the erosion mechanisms first deviated from viscous erosion. The impingement pressure at this altitude was then obtained from the flat plate pressure tests. For all the descents with and without horizontal velocity, the pressure levels thus obtained range between 1.38 and 2.75 kN/m² (0.2 to 0.4 psi). Also, acceptable erosion results were measured with the sonic nozzle in which the impingement pressure never exceeded 1.38 kN/m² (0.2 psi). Considering the unknowns associated with the extension of results from the cold-jet laboratory tests to the full-scale Mars environments, an impingement pressure criteria was established at 2 kN/m² (0.3 psi) within the nominal engine cutoff height of 3 ± 1.5 m (10 ± 5 ft). A further objective was to obtain this pressure level at an even lower engine cutoff height. This pressure criteria represents a factor of 23 reduction in impingement pressures from that measured with the baseline bell nozzle.

Full and Sub-Scale Nozzle Tests to Evaluate Alternate Nozzle Configuration

Very little data existed concerning the exhaust flowfield characteristics of unconventional nozzles which necessitated an experimental program to guide in the nozzle redesign. Sub-scale and full-scale cold-gas tests were setup at both LRC and MMC to investigate the effectiveness and influential parameters for each of these concepts. The more promising of these concepts were then used to design full-scale nozzles for the prototype engine impingement pressure tests and ultimately, using the best candidate, to characterize the interaction with simulated Martian surfaces.

LRC cold-gas alternate nozzle tests

Low area ratio nozzles with and without canting: A variety of alternate nozzle configurations were examined in an effort to find a nozzle configuration which would satisfy the previously established impingement pressure criterion. The initial approach taken at NASA/LRC was to evaluate the possible advantages of using less than optimally expanded nozzles (less than 20:1 area ratio for the required thrust and the Mars ambient pressure conditions). The lowest value of impingement pressure should be obtained from a sonic nozzle. Figure 35 presents a sequence of test photographs illustrating the surface disturbance of lunar nominal soil which occurred with the 1/6-scale model lander employing sonic nozzles using helium. As shown in the photographs considerably less erosion occurs than with optimally expanded nozzles. The sonic nozzles operate in a greatly underexpanded condition which causes the exhaust gases to expand outside of the nozzle to the lower Mars ambient pressure thereby lessening the resulting impingement pressure (see reference 14 for further discussion). The amount of viscous erosion appears similar to that obtained with the optimally expanded 20:1 area ratio nozzle; however, the magnitude of impingement pressure is obviously below that value which causes severe bearing capacity failure and/or diffused gas eruption.

Figure 36 presents full-scale impingement pressure data which illustrates the effect of area ratio. In order to yield the necessary thrust from a low area ratio nozzle, the nozzle must be operated at a higher pressure which is an obvious disadvantage of using such nozzles, e.g. for a given value of thrust more propellant would be required. Figure 37 presents test photographs which illustrate very clearly the effect of nozzle area ratio on the magnitude of surface disturbance in lunar nominal soil. These tests utilized a single full-scale air nozzle and were conducted within the expected range of conditions. The cratering becomes severe for an area ratio nozzle of 3:1 and above.

The next approach investigated was to evaluate the combined effect of low area ratio nozzles and canting of the nozzles away from the spacecraft vertical. Figure 38 presents test photographs which show the surface disturbances which occurs with a 7:1 area ratio nozzle canted 15°, and with

the baseline 20:1 area ratio nozzle canted 20° . Each of these nozzle configurations appeared to be an acceptable compromise provided the surface sampler could sample between adjacent craters rather than near one of the craters. The effect of a thrust loss resulting from nozzle canting and the use of less than optimally expanded nozzles was evaluated for typical Viking Lander descent profiles with a maximum of 35 kg penalty with sonic nozzles canted 30° . Using the baseline 20:1 area ratio nozzle canted 20° results in a fuel weight penalty of approximately 3.6 kg and the 7:1 area ratio nozzle canted 15° results in a weight penalty of approximately 7.7 kg.

Two-dimensional nozzles: Also studied for its effectiveness was a long two-dimensional nozzle. Figure 39 presents the full-scale impingement pressure data as measured with the 20:1 area ratio, 2-D nozzle using air. The axial impingement pressures measured with this nozzle are considerably less than those measured with the baseline conventional nozzle above an altitude of about 2 meters. This particular nozzle was further modified as shown in the sketch accompanying figure 40 by sectioning and alternately canting the resulting 14 individual 2-D nozzles to an angle of 15° . A remarkable reduction of impingement pressure resulted from this nozzle modification as shown by the data of figure 40. The pressures shown were the maximum measured on the surface and did not occur directly beneath the nozzle configuration because of the nozzle cant angles.

This particular nozzle was used for the soil tests shown in the test photographs of figure 41. This figure illustrates the surface erosion which results on two soil models, dune sand and lunar nominal, with thrust cutoff at 0.67 meters (near footpad touchdown). The weight penalty associated with this nozzle configuration was not determined, although tests with this nozzle indicated that small multiple nozzles with canting was an acceptable approach for alleviating site alteration as a major problem during touchdown of the Viking Lander on Mars.

Horizontal velocity: Another alternate approach which was investigated experimentally involved adding a high horizontal velocity to the lander during its descent. The rationale being that the surface sampler area would experience a minimum of exposure time to the high impingement pressures and perhaps avoid the onset of bearing capacity failure. Three cold-gas jets on a 1/6-scale lander were used to evaluate the soil disturbance for a descending lander with horizontal velocity. Test conditions were comparable to those of the vertical descent test of figure 27. As revealed in the test photographs of figure 42, the magnitude of surface disturbance when the lander has some horizontal velocity is greater than that which occurs for a vertical descent. Once the impingement pressure on the surface reaches a level sufficient to cause a severe disturbance, then the effect of lander horizontal velocity is to aggravate the problem by exposing more surface to high impingement pressure (e.g. like plowing the ground with the impinging exhaust gases). The conclusion is that reducing impingement pressures to avoid serious disturbances is more effective than reducing the exposure time.

MMC cold-gas exploratory tests - As previously stated, page 8, another approach to modeling was to use high pressure jets exhausting to atmospheric pressure.

Low area ratio nozzles: The axial variation of centerline impingement pressures is given in figure 43 for the 20:1 conical nozzle tested in the MMC Cold Flow Laboratory (CFL). The nozzle operated at a pressure ratio of .75 which gave an exhaust flow structure very similar to those found with a real engine in the Phase IA and Phase II tests. The nitrogen gas supplied for these tests entered the nozzle chamber at ambient temperature ($7^{\circ} - 10^{\circ}\text{C}$) and therefore N_2 condensation formed in the jet. The amount of mass involved was computed to be a maximum of 8%. The condensate was very useful in that it provided flow visualization allowing photographs to be taken of the flow. Recognizing differences from full-scale ratio of specific heats, exit Mach number, density ratios at the exit, and the presence of condensate, the cold-gas jet is not an exact simulation of the full-scale exhaust. However, in view of the goal of a factor of 23 reduction in pressure, information as to trends of pressure reductions and feasibility of the alternate nozzle concepts can be gained if they are run under the same conditions and compared to 20:1 results of figure 43. For these reasons, all the following CFL pressure results are normalized by the maximum 20:1 impingement pressure of 2178 kN/m^2 (316 psi). The axial distances are normalized by the reference 20:1 exit diameter, 5.08 cm. Test results of the 1/3-scale 20:1 nozzle and the following alternate nozzles tested in the CFL are detailed further in reference 21.

CFL impingement pressure results of decreased area ratios are presented in figure 44 where all nozzles were operated at the same chamber pressure. Considering that lower area ratio nozzles lose efficiency and a corresponding increase in chamber pressure would be necessary to maintain the thrust-altitude landing program, the test should have maintained thrust rather than chamber pressure. Higher chamber pressures, however, were beyond the gas supply capability. Photographs of the flow, figure 44, indicate the greater than optimum scale of expansion within the first shock cell. Mixing and shock profiles past the Mach disc were not visible. A sketch of the 20:1 nozzle is shown in figure 45 in which several notches on the nozzle cone may be seen. These were added to assure a known exit diameter as the nozzle was cutoff to area ratios of 10, 5, 3, 2, 1.5 and 1. It should be noted that the axial surveys shown are from the nozzle centerline locations. Out of 16 radial pressure port locations, the highest peaks were recorded at the center. The normalizing reference diameter for each case is the 20:1 value. As seen by the results summarized in figure 46 for axial distances 10 diameters or greater, the sonic nozzle is the most effective in reducing impingement pressures. Also, the pressure reduction is sensitive to area ratios near one and rather insensitive for larger area ratios.

Conventional nozzles with vortex/shock generators: The effectiveness of adding disturbances to the jet flow was investigated for several body shapes placed over the exit of the 20:1 nozzle. The CFL test results are summarized in figure 47 where a drag coefficient of 2 was used to compute thrust reduction. The body shapes most effective in reducing pressures at a minimum thrust loss are the single wire and the wire ring. The heavy mesh screen was closest to meeting the pressure reduction goal, but it has the most blockage or thrust penalty. For the Viking mission, these mixing aids would have to be used in conjunction with other alternate nozzles to achieve the desired pressure reduction. Also, as the thrust penalty would be too great for any of these devices attached for the complete descent burn, they would have to be implemented at a lower altitude to be practical.

Axial variations in centerline pressures (maximum found) are shown in figures 48 through 52 for several of the mixing aids. As seen in the photographs, several interesting patterns and severe disturbances to the flow were produced. An axisymmetric shock pattern was set up in the flow with the wire ring which propagated downstream in a similar manner as the free jet shock structure. The flow structure set up by the heavy mesh screen was like a highly underexpanded jet. In this case, the screen held a normal shock which covered the exit. The gas then expanded through the wire screen as an under-expanded sonic jet with its Mach disc barely visible.

Fluted nozzle: A nozzle with 6 flutes was designed and built which had a perimeter ratio of four, the same exit area as the 20:1 and a single axisymmetric throat. (Shown in figure 53). The expansion to each of the flutes began at the throat section. As indicated by the centerline pressure survey shown on figure 54, the results show very good mixing characteristics compared to the conical 20:1. Between 8 and 10 diameters the pressure rises very rapidly. This may be due to an inefficient nozzle design, or the flow at the center of the flute was not able to entrain sufficient air to mix. A wire was placed across the central core to investigate its effect. Results of this disturbance are also presented in figure 54 and as shown an improvement was made at the lower altitudes. Concluding from these tests, it was determined that fluted nozzles do appreciably increase the mixing rate and thus reduce impingement pressures. Further, the nozzle contour should be as efficient as possible and the nozzle exit shape should distribute the exhaust for the most entrainment with no flow at the center. Triangular segments like those in reference 16 appear to be the most efficient as long as the number is low so as not to interfere with neighboring entrainment demands.

Multiple nozzles: Based on meeting the pressure criteria at the nominal 3.0 m engine cutoff height, the number of nozzles for the multiple nozzle configuration was established at seven. Three configurations were built with 0, 10 and 20° outward cant on the peripheral nozzles so that the blockage effects on entrainment could be assessed. Shown in figure 55, the individual nozzles were spaced 2 exit-diameters apart for all configurations. The cold-flow impingement results showing the maximum pressures, found beneath the center nozzle, are presented in figure 56. The accompanying photographs show the core structure of the individual jets impinging on the target plate. For plate locations near the nozzle, the peripheral jets were observed to bend out slightly before impinging. No photographs of the 0° cant flow were

available, but there was no observed difference in core structure compared to the 10 and 20° cases. As the results indicate, the jets mix and decay as single free jets for the 10 and 20° cant angles. With no canting of the outboard nozzles, the space between jets is reduced and the central jet is blocked from free entrainment thus affecting the pressure decay. In establishing guidelines for full-scale nozzle designs, it was concluded that nozzle spacing and cant angles affect the mixing decay region of the individual jets, while the primary design variable is the number of nozzles themselves as the nozzle scale determines the length of the high pressure core.

Thrust plate: The objective in designing an alternate nozzle based on the thrust plate concept is to increase the plate diameter according to the desired level of pressure reduction. The size required to meet the Viking pressure criteria, however, is too large to fit in the aeroshell and the 1/3-scale thrust plate design, shown in figure 57, is the largest size feasible. A number of other techniques were consequently incorporated into the design. To induce mixing, the nozzles were staggered in a ray pattern with more flow concentrated at the edge than the center. The outer nozzles were doubled in diameter and canted outward 15°. All nozzles were made with area ratios of 10 to increase the underexpansion and decrease the plate thickness. The nozzles had cylindrical throats and conical contours of 15° half-angle.

Results of the axial and radial surveys showed the maximum impingement pressure peaks of the exhaust structure were located on the engine centerline. As shown in figure 58 for version 1, the peak pressures of the core were reduced by a factor of approximately 2 compared to the conceptual factor of 4. In addition the factor of four reduction in maximum pressure was not achieved until 17.6 equivalent circular nozzle diameters downstream. The 20:1 reference nozzle requires only 32 diameters to get to the same pressure level. During the test, it was observed that the flow from the outer canted nozzles turned vertically or slightly inward. Unfortunately, the photographs of this test showed no flow structure. It was concluded that the low pressure region responsible for the change in flow direction occurred as the entrainment demands of the inside jets was blocked by the peripheral jets. Further, it was concluded that as the internal jets were operating on the principal of a thrust plate, the distance required to redistribute the momentum flux over the thrust plate area is too long and the thrust plate concept was considered not practical for obtaining the Viking objectives.

Reconsidering the thrust plate only as a multiple nozzle arrangement, an investigation was undertaken to determine the amount and pattern of holes which had to be plugged so as to improve the impingement performance. Results of one particular run are included in figure 58, termed version 2, with those nozzles blocked as indicated by the shaded exits in figure 57. The results indicated that by plugging up the nozzles in the center, the entrainment demands are lessened, and by plugging up nozzles around the periphery, there is less blockage for entrained air to enter between rays. Also important is that while the multiple jet flow pattern is not a free jet flow scaled by the individual nozzles, it does have significantly reduced pressures. The conclusion drawn is the same as with the seven-nozzle configuration. The

nozzle numbers determine the extent of the high pressure region and nozzle spacing and cant angles influence entrainment and the lower pressure mixing decay regions.

Full-scale tests - Based on the preceeding exploratory cold-gas tests a number of full-scale alternate nozzle configurations were designed and built. The nozzles were bolted on the catalyst bed of a prototype engine for the pressure plate and soil tests at the WSTF. In addition, some of these nozzles were used for cold-gas tests at the LRC 60-foot sphere to investigate the impingement pressure as affected by ambient pressure.

7-nozzle configuration: The first alternate nozzle designed for full-scale testing was a 7-nozzle configuration based on meeting the impingement pressure criteria at the nominal 3.0 meter engine cut-off height. The nozzle spacing was approximately .2 exit diameters with a 10° outward cant angle for the 6 outer nozzles (see figure 9). Test 11C, table I, was conducted with the seven-nozzle configuration but fuel handling difficulties were experienced and applicable data was obtained only from 12.2 m to 5.5 m. The data trend indicated that the flow pattern was close to that of seven individual free jets. No rerun of test 11C was made, however, because a 7-nozzle configuration would not allow lower engine cutoff heights which studies showed to be desirable for vehicle weight savings and reduction of g-loadings at touchdown.

24-nozzle configuration: The second full-scale alternate nozzle was designed for reduced pressures at engine cutoff heights below the nominal 20 ± 10 nozzle diameters. It consisted of 24 nozzles arranged in three concentric rings with 12 in the outer and 6 in the inner two rings. As shown in figure 9, the inner nozzles were located in line with the spaces between nozzles of the outer ring. The cant angles, from the inside ring, to the outside ring, were 7° , 12° and 20° . The nozzle spacing was minimized to conserve engine weight with the intent that the resulting merged jet flow would still realize a significant pressure reduction. The effectiveness of this design is seen in the impingement pressure results in figures 59 and 60. As shown in the centerline axial survey of figure 59, the pressure normalized by engine chamber pressure was approximately .0055 within 20 equivalent circular nozzle-exit-diameters which is a factor of 22 reduction in pressure compared to the baseline nozzle. The pressure rises rapidly, however, so that at 13 equivalent exit-diameters there is only a factor of 11 reduction. The radial distribution at four nozzle altitudes is given in figure 60 with the pressure ratio of the nozzle exit shown for each altitude. As shown, the flow from the 24-nozzle configuration has merged in the far field to an axisymmetric pattern in a manner similar to that found in reference 8 for slot nozzles.

24-nozzle configuration modifications: Noting that the exhaust flow is a merged jet flow and not 24 free jets, it was concluded that the nozzles, spaced to conserve weight, were too close to allow for the entrainment demands of adjacent jets. Based on the CFL scale tests and the improvements made by selectively reducing the number of nozzle flows, two tests with

nozzle modifications were then conducted. The first modification to the 24-nozzle configuration involved blocking every other nozzle on the outer ring at the throat (see figure 9). Impingement pressure results of test 11D with 6 periphery nozzles removed indicated that the pressures were not reduced from the 24-nozzle configuration. Either the additional area opened up for entrainment flow was not sufficient to meet the demands of the inner ring of nozzles, or the inside nozzles were spaced too closely.

The second modification to the 24-nozzle configuration, therefore, was to remove the 6 nozzles at the center of the cluster. This had two effects, it reduced the amount of ambient entrainment flow which had to pass between the outer jets and also provided more mixing area for the jets of the second nozzle ring. Test results of the 24-nozzle with the 6 center nozzles blocked in the WSTF test 11E are shown in figures 61 and 62. Tests 11D and 11E were considered as $\sqrt{.75}$ scale runs as 25% of the throat area was blocked and the fuel flowrate was adjusted to give the nominal engine chamber pressure. The normalizing equivalent circular diameter and radius in figures 61 and 62 are reduced accordingly. As indicated by the results a significant reduction in impingement pressures was found for the 18 nozzles compared to the 24-nozzle configuration indicating the inner 6 nozzles were in fact spaced too closely. Further, the results meet the design goal pressure criteria established for acceptable site alteration levels. The maximum impingement pressure found was 2.27 kN/m^2 (.33 psi) or .0046 when normalized by engine chamber pressure. This represents a factor of 26 reduction in pressure within a 7.5 equivalent nozzle diameter altitude.

The radial pressure survey of test 11E is given in figure 62 in which it is seen that the flow is merged at altitudes greater than 30 nozzle diameters, but deviates at closer altitudes. Inspection of the pressure records at 7.5 diameters height indicated definite high pressure peaks traceable to the individual nozzles. It should be noted that radial pressure distributions were available only along one ray in the WSTF testing. Angular pressure variations about the engine centerline were not surveyed. The nozzles were aligned so as to place the maximum impingement pressures over the single pressure port line. All multiple nozzle configurations were aligned with a nozzle of the innermost operative ring centered over this line.

Annular and multi-two-dimensional nozzles: Two additional alternate nozzle configurations were designed, built, and provided for testing by other contractors. One configuration consisted of 16 two-dimensional nozzles located about the engine centerline with alternate 5° and 20° cant angles (figure 7). Test 11G was conducted with the multiple two-dimensional nozzle configuration with one of the 5° cant nozzles aligned over the pressure port line. The maximum impingement pressures were found on the centerline, and these results are given in figure 63 as a function of altitude. The results indicate this configuration met the pressure criteria at the 20 equivalent diameter altitude, and had a maximum pressure of 5.1 kN/m^2 (.74 psi) at the .68 m test cutoff altitude (.0095 related to chamber pressure).

The next pressure test, 11H, utilized the annular nozzle which is shown in figure 7. The major diameter of the annular nozzle was maximized to fit within the aeroshell size constraints. The maximum pressures found were located at 2 equivalent radii from the engine centerline. These results are also shown in figure 63, where it can be seen that normalized pressures as high as .0165 were found at the lowest altitude of 4.6 equivalent diameters. As tested, both configurations produced acceptable impingement pressure performance at the nominal 20 diameter cutoff altitude, but they do not allow lower engine cutoff altitudes. Further development of these configurations was not pursued in view of the improved pressure performance obtained with the 18-nozzle configuration.

Fluted nozzle: The full-scale fluted nozzle configuration used in test 11I and shown in figures 7 and 9 was designed with eight flutes, a perimeter ratio of 4.9, and an exit profile which concentrates flow near the outer edge with none at the center. Arranged over the combustion chamber are eight slotted throats separating the flow before entering the individual nozzles. The flow in the nozzles is nearly two-dimensional. The effectiveness of the fluted nozzle configuration is indicated by the axial variation in impingement pressures at the centerline in figure 64. The results show a significant reduction in pressure compared to the baseline and meet the pressure criteria at an altitude of 13 equivalent diameters with a maximum of .013 related to chamber pressure at the test cutoff altitude of 4.7 nozzle diameters (5.56 kN/m^2 or .809 psi maximum). The radial pressure survey shown in figure 65 indicates that the flow has merged to some degree but has still retained the effect of the outward cant angle of each nozzle. The results were taken with one of the nozzles aligned over the radial pressure port line. A particularly desirable characteristic of the fluted nozzle is that the impingement pressure remains low for most of the descent before the rapid pressure increase during the last few nozzle diameters of the descent. The time that the soil is exposed to a high pressure region and high surface shear is thereby much less with this configuration than with any previously tested. The rapid rise in pressure from 7.5 diameters on down is characteristic of that observed in the MMC cold-flow tests in which the flow in the center of a scaled fluted nozzle was seen to coalesce to a high pressure core. These results and the effects found by blocking the inner 6 of the 24-nozzle configurations led to the decision to block the central portion of each flute with a wedge tapering to zero at the throat (see figure 9g).

Fluted nozzle modified: The modified fluted nozzle retained the same throat area, but the exit area was reduced to give a 16.7:1 area ratio nozzle compared to the previous 20:1. The flow angle at the inner lip at the wedge is 15° and the outer lip 20° with an effective cant angle of approximately 18° . The modified fluted nozzle was tested in test 11J with the impingement pressure results shown in figures 66 and 67. The high pressure central core was eliminated and the pressures were significantly reduced during the entire descent. The maximum pressure found in fact, was only 1.17 kN/m^2 . Subsequent full-scale cold-gas tests indicate that a high pressure region exists beyond the 8 radii location of the outermost pressure port as the result of the effective cant angle of each flute.

The radial pressure profile shown in figure 66 shows the high pressure region of the canted nozzle coming onto the outermost pressure pickup at 5 equivalent nozzle diameters altitude. Little change was noted between 15 and 80 equivalent diameters altitude.

18-nozzle configuration: Based on the favorable results achieved with 18 of 24 nozzles in test 11E, a full-scale 18-nozzle version (figures 7 and 9) was built and attached to the engine with an inner nozzle aligned over the pressure port line. The results as shown in figures 68 and 69 for test 11K indicate very good agreement with the scale corrected result of test 11E. Overall, the pressure criteria level of 2.07 kN/m^2 (.3 psi) was found at an altitude of 12.4 diameters and a maximum of 2.21 kN/m^2 (.321 psi) within the minimum 5 diameter cutoff altitude. The radial distribution shown in figure 69 supports the conclusion of the earlier results in test 11E. The flow has merged above 15 diameters. (The pressure transducer located at 3 equivalent radii appears to have been consistently high for the test).

Flat plate heat flux measurements for the 18-nozzle configuration indicated a maximum of 64.7 kw/m^2 (5.7 BTU/ft²-sec) at the stagnation point. As the heating from the configuration does not represent a problem, full results will not be given here, but will be found in reference 12.

To aid in better defining the 18-nozzle configuration exhaust flow structure, a test was implemented to probe the free jet before impingement. Results for the pitot pressure rake placed 4 equivalent diameters above the test bed are shown in the centerline axial survey of figure 70 and the radial distribution in figure 71. Compared to the flat plate impingement pressures, the pitot pressures are slightly lower at altitudes above 25 equivalent diameters. The highest pitot pressure found was 11.78 kN/m^2 (1.71 psi) at the minimum 1.1 diameter altitude and was located 1.5 radii off centerline. The radial distribution for several altitudes shown in figure 71 illustrates the presence of the single jet that was aligned over the rake. The entrainment pressure field about the edge of the jet structure was picked up between 5.3 and 10 radii during the last few diameters of the descent as evidenced by the pitot pressures reading below ambient.

Ambient pressure effects: The preceeding investigation resulted in two candidates, the 18-nozzle cluster and the modified fluted nozzle, which met site alteration pressure criteria at the specific ambient pressure levels tested. The Martian surface pressures based on Mariner VI and VII data, range between 4 and 20 mb. The effect of ambient pressures on the impingement pressure was established using the full-scale nozzles and cold-gas (air) in the LRC 60-foot sphere. As the cold-gas pressure results are not directly comparable to the hot-engine results, only the comparative differences of the nozzles can be assessed. Results in figure 72 show the maximum impingement pressure (related to nozzle pressure) as a function of pressure ratio at the nozzle exit. The maximum pressures are taken from the radial and axial surveys down to and including the axial distance noted. As seen by the results for nozzle height of 3.6 equivalent diameters and greater above the flat plate, the fluted nozzle is quite sensitive to ambient pressure and has greater pressures

than for the other configurations for all pressure ratios of interest. The modified fluted nozzle had pressures significantly lower than the 18-nozzles for pressure ratios slightly below one, in agreement with the hot-jet results. Above pressure ratios greater than 1.5, however, the 18-nozzle configuration is better and shows less sensitivity. It should be also noted that with a radial line of pressure ports extended from the Phase II - test 11J, the highest pressures of the modified fluted nozzle could be measured and the effects of the high cant angle could be followed during the descent. This configuration had free jet flow from each flute, while the 18-nozzle flow readily merges. The axial pressure distribution for the 18-nozzle configuration is shown in figure 73 where the development of merged flow above 10 diameters can be seen for the cold-gas test. The effect of ambient pressures on this development can be seen in the radial distribution for 5 pressure ratios shown in figure 74 for axial distances of 4, 6 and 12 equivalent exit diameters.

Concluding from the impingement pressure investigations, the modified fluted nozzle and the 18-nozzle configuration are both acceptable alternates with the 18-nozzles showing slightly lower pressures over the design range of ambient pressure levels. Both will allow lowering the engine cutoff height, possibly down to footpad contact. The final acceptability test is, of course, their performance with soil in the Phase II - 12 test series. Other significant considerations concerning a nozzle configuration acceptable for the Viking mission include its weight and thrust performance. A flight weight fluted nozzle was estimated to be heavier, and has a larger thrust loss due to cant than the 18-nozzle configuration. The 18-nozzle configuration was therefore considered as the prime nozzle candidate for the Viking mission, with the modified fluted nozzle retained as a backup throughout the following soil tests.

Characterization of Site Alteration with Selected Nozzles

A total of seven soil tests utilizing three candidate engine nozzles and two simulated Martian soil models were conducted. A detailed description of the test results for the selected 18-nozzle configuration impinging on lunar nominal soil and dune sand models is given in the following paragraphs. A summary of test results for all soil tests follows that discussion.

Soil erosion in lunar nominal soil

Pretest soil bed preparation: The main soil bed was prepared with lunar nominal soil as described in reference 12 in which successive 5 cm layers are laid and soil properties controlled by compaction. The only variations were the incorporation of two low density soil wedges which extended into the main soil bed from the adjacent soil trays, (figure 75). The soil wedges were truncated in the main soil bed to provide soil auger sampling sites which had to be of baseline compacted soil in order to relate these test results to previously conducted soil chemistry tests. Density measurements of the soil bed are shown in figure 76.

The side soil tray which is parallel to the engine reflection plane was prepared with an average bulk density of 1490 kg/m^3 . Shear vane torque values ranged from .021 to .025 meter newtons with an average value of .023. This would translate into cohesion values of 690 to 826 with an average value of 760 N/m^2 . A strip of red-dyed soil one millimeter thick and about .1 meter wide was placed over the soil of this tray and was terminated at the edge of the main soil bed so as not to influence soil auger sampler sites.

The second soil tray was prepared with an average bulk density of 1380 Kg/m^3 . Shear vane torque values for this tray ranged from .013 to .023 meter newtons with an average value of .020. Soil cohesion values of 428 to 760 with an average value of 660 N/m^2 were determined. Like the other soil tray, a colored strip .1 meter wide and one millimeter thick was placed over the soil tray and extended about .6 meter into the main soil bed. The low density soil wedge of this tray extended from the side tray into the main soil bed forming an apex directly under the engine center point. The low density wedge was truncated by an area about .3 meter square provided as a collecting site for the soil auger. Figure 77 shows the distribution of these surface test elements in the plume impingement area. Figure 78 is a view of the side soil trays and one mm colored soil strips.

Two triangular mounds of fluffy soil were placed on the surface of the main soil bed at 0.5 and 1.0 meters from the engine center point. The mound at 0.5 m position was oriented with its apex toward the engine, while the mound at the one meter position was oriented with its blunt side toward the engine. A third triangular fluffy soil mound was positioned on the second soil tray at 5.0 meters from the engine.

Post-test soil bed surface description: The area directly below the engine center point was severely scrubbed, but exhibited no discrete crater. The soil model was uniformly removed until a layer of coarse particles was exposed at the surface which appeared very much like a fine-grained lag gravel. Very little fluffy overburden was detected in this test.

The soil wedges of low density, one of which extended to the engine center point, likewise showed no significantly different response to the engine plume gases than the baseline compacted soil with the possible exception that their resulting surfaces were slightly rougher in texture. No change in surface relief between the low density soil wedges and the baseline soil was observed. Figure 79 is a view of the general area below the engine showing the scrubbed nature of this surface. This figure should be compared with figure 77 of the pre-test condition of this surface.

The general results of the surface morphology experiments were very much the same as those for other tests which utilized lunar nominal soil as the test bed. Facets of fluffy soil wedges facing the engine were extensively scrubbed; preformed craters near the engine were somewhat obliterated by erosion and deposition.

Surface gas pressure estimates based on the movement of rock samples indicate that the plume gas pressure normal to the surface at a distance of .6 meter from the engine centerline was very close to 552 N/m^2 .

An excellent tool for the post-test analysis of physical site alteration on all soil tests was the use of stereo-photography. This type of photography was implemented by building a test fixture composed of a support rod and two camera brackets. A Speed-Graphic camera used to document the test results was equipped with a support bracket which mated with the rod brackets. The positions of the camera optic axis to simulate as closely as possible those of the Viking Lander imaging system were located with these brackets.

Figure 80 shows an example of a pretest 12E stereo-pair. Figure 81 is the same scene after engine firing. Stereoscopic reconstruction can be accomplished by cutting out these photographs and properly positioning them with the aid of a pocket stereoscope.

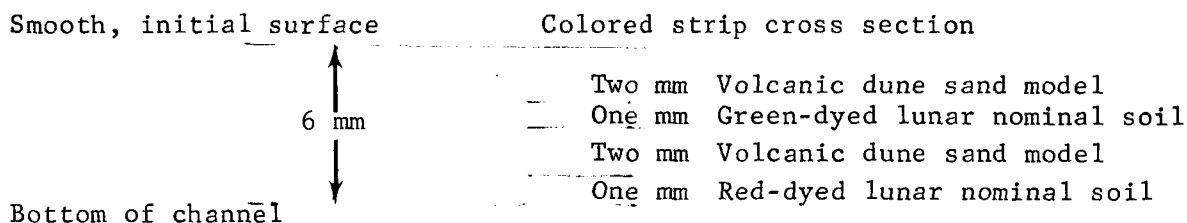
Soil erosion in volcanic dune sand

Pretest soil bed preparation: For test 12F of the Phase II site alteration program the volcanic dune sand soil model was used as the simulated Martian surface model. Because of the high porosity/permeability of this model, it was felt that the soil container should be modified in the plume impingement area so that induced plume gases in the soil pore spaces would not be restricted by wall-effects of the container.

After the lunar nominal soil model employed in previous soil tests was drained from the soil container, the first two meter sections of the soil

bed's false floor was removed to provide a full .91 meter depth of the soil container. A retaining wall utilizing the same fabrication technique as that employed on the false floor was built between the true floor of the container and the .3 meter level false floor. Figure 82 shows the bare soil container prior to filling.

After an initial smooth surface of the volcanic dune sand model had been prepared, the same types of surface features and markings that had been employed with the lunar nominal model were constructed. The dual layer color strip which had been so successful on previous tests had to be modified for the volcanic dune sand model. The reason for this modification was that one millimeter thick layers of this model could not be constructed since the mean particle size was very close to this dimension. Consequently, two aluminum channels were placed on the soil bed to be used as guides for a scraping device which excavated a channel in the bed 6 mm deep over an area 2.44 x .3 meters. This channel was then filled in the following manner:



When the channel fill was completed, it was randomly sectioned to verify continuity of the described layers.

Anticipating more erosion in this model than with the lunar nominal model, a more extensive stake farm was deployed. Additionally, a more dense array of surface morphological features than was used on previous tests was constructed. These surface features can be seen in figure 83 and their distribution identified on the pretest map, figure 84(a). The density of the soil was measured and results are shown in figure 85.

Post-test soil bed surface description: Site erosion effects of the volcanic dune sand model in the plume impingement area were quite spectacular when compared with those developed in the lunar nominal soil. A central crater area measuring 1.15 meters in diameter was formed by the coalescence of eighteen discrete depressions. The deepest depressions in the middle of the central crater were 3.8 cm deep as measured from the initial soil bed surface. Common ridges between adjacent craters were built up between high pressure plume stagnation regions to a height of 3.8 cm above the initial surface for a total crater topographic relief of 7.6 cm. Much of the near surface thermocouple instrumentation was exposed and dislodged during the test. Figure 86 is a view of the near field of the central crater showing the eighteen depressions and exposed instrumentation.

The first .6 meter length of the multilayered colored soil strip was totally missing after the test. At .76 meter from the engine centerline, the first appearance of a continuous red soil layer was found indicating

5 mm of erosion up to this point. These results were substantiated by stake measurements. At 1.22 meters the first appearance of a continuous green layer was found indicating 2 mm of erosion. Figure 87 shows the post-test sectioning of the test strip.

A continuous line of pre-formed craters constructed in the test bed extending from 0.25 to 4.25 meters was nearly completely obliterated. Only a faint expression of the two craters at 4.25 m was identifiable after the test.

Those surface features which had topographic relief prior to the test suffered the most erosion. Unlike those tests which utilized lunar nominal model where gas scrubbing predominated, these features appeared to be sand-blasted by entrained particles of the volcanic dune sand model. Surface features with relief were cleanly cut away near the engine and those at some distances were neatly faceted. Some rock samples actually tumbled forward because their bases were undercut by this action.

Only two rock samples were displaced indicating a gas dynamic pressure of 372 N/m^2 . However, two other rock samples in the same grouping which should have been moved at this dynamic pressure did not. This indicates a very non-homogeneous distribution of gas pressures as substantiated by the stake farms. It appears that radial lines from the small discrete craters are regions of high pressure. Radial lines extended from the adjacent ridges between craters were plume stagnation regions of low pressure. These areas can be extended to the center of the test bed on the basis of stake erosion data. Figure 88 shows this erosion and disposition pattern quite clearly as crater formation uncovers the prepared colored soil strip.

Soil heating

Thermocouple data: Results of the 18-nozzle configuration on both soil models from tests 12E and F are summarized in table III with the maximum temperature change of each thermocouple shown. Thermocouples located on the surface were covered by a thin soil layer and in most cases indicated surface gas temperatures. In general, the results are consistent with the pore pressure build up indicating the majority of the sub-surface heating comes from an energy flux associated with gas diffusion into the porous medium rather than conduction through the grains. Conduction effects were seen on the lowest thermocouples at a much later time (3 to 4 minutes) and indicated very small temperature rises. The thermocouples located on the surface and 305 and 456 cm from engine centerline on test 12F indicated a drop in temperature which is probably due to a cooling effect of the wall jet over an area heated by the camera lights.

Thermovision data: Test 12E was conducted with the lunar nominal soil model and because of soil fines which became suspended during the run and for approximately 3 minutes after engine cut-off, the thermovision was not able to read soil bed temperatures but rather the maximum temperature of the suspended particles. This temperature never exceeded $+13^{\circ}\text{C}$ over an ambient bed reference. During the test checkout it became apparent that two heating mechanisms would dominate in the soil heating. The first, of course, is the energy added by the engine exhaust gases impinging on the soil. The second mechanism, as revealed by the thermovision, is heating by radiation from the camera lights. Prior to the test, the thermovision indicated surface temperature peaks as much as $+19^{\circ}\text{C}$ under the lights compared to the non-lighted areas. In as much as the temperature results of the suspended particles are within the limits of the movie lights the only conclusion about exhaust impingement heating is that it is equal or less than that contributed by the lights.

Test 12F used a full-scale 18-nozzle configuration on a dune sand soil model. The time histories of the change in soil surface temperature at various locations with respect to the engine centerline were reduced from the 16 mm motion pictures. Depending upon location, the soil surface temperatures rose between 6 and 12°C within 1.5 seconds after engine ignition. The maximum 12°C was located .84 meters from engine centerline. Between 1.5 seconds and 18 seconds, the soil bed was obscured due to the blowing soil fines used on the colored soil strip. The peak temperatures occurred before 18 seconds thus only the temperature decay characteristics after 18 seconds were obtained. Two observations can be made for this test, (1) from 18 seconds on, the higher soil surface temperatures were found between 2.4 and 2.7 meters from engine centerline, and (2) the return to pretest soil temperatures occurred in about 60 seconds.

The most complete soil temperature data was obtained during test 12G which was all dune sand but with a fluted nozzle configuration. It was noted that beneath the engine on the centerline, the temperature at 60 seconds was still greater than ambient by more than 1.5°C . The highest ΔT observed was less than 15°C and occurred a fraction of a second before engine cut-off. Negative ΔT 's were found which are both cool areas that have been uncovered and also cooler particles deposited on the flood light heated regions.

Analytical Comparison with Experiment and Extension to Mars Conditions

The following section is a brief summarization of the analysis of site alteration erosion and comparison with the experiment that was performed in reference 22. The previous soil erosion results indicated that the primary erosion mechanism using the 18-nozzle configuration is viscous shear, consequently, it is the only mechanism considered in the analytical comparison. The formulation for these calculations is included in Appendix A. As indicated, in order to compute viscous erosion the distribution of surface shear stress is necessary which implies that details of the impingement flow must be

known. No analytical tools are available to compute the free jet and impingement flow structures of the unconventional nozzle exhaust, so that the jet flow field was approximated by using the baseline 15.2 cm diameter bell nozzle and chamber conditions with an axial shift in the jet flow properties to match centerline impingement pressures with the maximum of the test 11K 18-nozzle pressure data. Referring to the radial distribution of impingement pressures for the 18-nozzle configuration in figure 69, it is seen that the flow has merged and is radially symmetric for altitudes 15 equivalent nozzle diameters and greater justifying the assumption of one parent nozzle. Below 15 diameters the actual flow is unsymmetric with high pressure regions traceable to the individual nozzles thus the possible analytical and experimental agreement will be somewhat limited. The single jet flow was computed by the method of Donaldson and Gray for mixing of dissimilar gases, reference 15. Upon impinging on the Mars surface, the exhaust gases are turned and follow the soil contour in what is usually termed the wall jet. The wall jet flow used for the analysis is based on the results of an analytical and experimental study of wall jet flow and heat transfer, presented in reference 23. The surface shear stress, τ_{wj} , was computed by the classical Reynolds analogy relating surface heat flux to shear stress. The surface heating, as outlined by Donaldson, et al, reference 22 consists of the stagnation region heating and the wall jet heating. The laminar stagnation region formulation of Lees was used with the velocity gradient related to free jet centerline properties. The experimental correlation to turbulent jet flow found in reference 23 was then applied. The wall jet heating formulation is also taken from reference 22 with a curve fit to the experimental correlation of radial distribution of Nusselt number, based on free jet properties, divided by Reynolds numbers to the .8 power. Further details of the procedures used to arrive at a shear stress distribution are given in reference 23. The radial variation of surface shear stress computed for the 18-nozzle jet impingement under the test 12E conditions is presented in figure 89 for a number of vehicle altitudes.

The computational results of viscous erosion of the lunar nominal and dune sand soil models with the number distributions of table IV, the shear stress distribution of figure 89, and the formulation of Appendix A is given in figures 90 and 91, respectively. The experimental results shown are from the previously discussed tests 12E and 12F stake farm data. The high scatter of data at any radial station is due to the fact there are 18 high pressure swaths over the soil during the last meter of the descent which gives a 3-dimensional erosion pattern. Comparison of the theory based on an axisymmetric pattern of merged flow indicated reasonable agreement considering the assumptions involved. Qualitatively, the trend with soil models is predicted with the dune sand crater 4.9 times deeper than the lunar nominal soil model. Better agreement of theory and test would be dependent upon: 1) a more accurate description of the jet and impingement flow, 2) a technique to account for particles redeposited downstream, and 3) a technique to account for particles possibly removed beneath the high pressure impingement region due to diffused gas causing a local surface failure. The third region of impingement differs from the general bearing capacity failure analyzed in reference 8a in that it is a local bearing capacity failure that propagates beneath the impingement region. It is expected that when refinements allowing smaller time increments in the coupled gas diffusion and finite element load

analysis program of reference 8c are made, it will provide the necessary time dependent local soil failure information.

An extension of the viscous soil erosion calculations was made to the Viking Mars landing conditions. The variation of crater depth with altitude is shown in figure 92 for the nominal 2.44 m/sec descent velocity and the lunar nominal and dune sand soil models. The lunar nominal soil model begins eroding sooner but at a lower rate than the larger sized particles in the dune sand soil model. Figure 93 presents the crater shapes for the nominal and design tolerance limits in the descent velocity for both soil models. The effects of soil density, and ambient pressure were computed to be much less than of descent velocity. These are covered in more detail in reference 22.

It should be noted that all the viscous erosion calculations presented here were made with the cohesion set to zero. K_o , in reference 8b, experimentally determined the lunar nominal soil model cohesion to range from 82.6 N/m² to 585 N/m², depending upon soil density, and the dune sand was found to be cohesionless. These values were determined from a triaxial shear test on a bulk soil sample, however, it is believed that for the top layer of particles with a turbulent gas stream flowing along the surface, there are no particle bonds and the surface layer is cohesionless.

Comparison of Soil Test Results with Mission Criteria

The discussion here summarizes how the Phase II tests met the success criteria for physical disturbance of the soil models with the engine nozzles tested. In order to assess how well the criteria were met, the following methods were applied for verification:

- A contour map of the soil transportation and deposition was obtained through direct measurement and analysis.
- Direct measurement of the disturbance of the soil, and the crater depth during the WSTF Phase II test program in lunar nominal soil.
- Analysis of crater depth and soil transportation considering soil models other than lunar nominal.

1. Figure 94 represents a compilation of the -2 mm erosion contour for each test conducted in lunar nominal soil. Figure 95 is a map of the same -2 mm erosion contour for tests conducted in volcanic dune sand. The percent

area of the region available to the surface sampler encompassed by these contours is summarized in table V. As can readily be seen from this table, all soil tests met the erosion criteria and additionally, no test deposited 8 mm of transported soil in the Surface Sampler area.

The results of the first three tests in lunar nominal soil (12A, C and D) utilizing an engine with a 24-nozzle modified to 18-nozzle configuration are very similar. One must remember that the techniques for measuring erosion are not precise, valid perhaps to only ± 0.5 mm and we are attempting to define a -2 mm erosion region. In view of this fact the data may be considered consistent when one also considers the variations in test parameters cited in table I and the difficulty in uniformly preparing a baseline soil test bed. The last test in lunar nominal soil utilized a full-scale 18-nozzle configuration in which an area equivalent to 18.0% of the Surface Sampler area was eroded more than 2 mm.

As expected, test 12F conducted in volcanic dune sand model with the same full-scale 18-nozzle configuration resulted in a larger -2 mm erosion area (43.3%) than that which developed in lunar nominal soil (test 12E, 18.0%). This was the largest area of erosion experienced during the test program. The fluted nozzle, test 12G, showed significantly less erosion (14.2%), however, estimated weight, schedules and costs did not allow it to be selected for the flight hardware.

2. The response of the lunar nominal soil model to engine plume gas impingement was rather insensitive in respect to its mechanical properties for an initially flat, smooth surface. Because of the low permeability of this soil model, very little plume gas was induced into the pore spaces and consequently the chief erosion mechanism was viscous shear. Other erosion mechanisms which involve the bulk physical properties of the soil (i.e., bearing capacity failure and shut-down eruption) were not encountered over the range of soil densities (1360 - 1810 Kg/m³) and engine nozzle configurations employed in the Phase II, site alteration tests.

3. For initially irregular surfaces composed of lunar nominal soil, e.g. triangular mounds, cones, ridges, etc.; low soil density features are eroded preferentially. As material was selectively removed from the engine facing slopes, an armor of coarse particles developed which retarded further erosion at least for the duration of engine firings employed in Phase II testing.

4. For the lunar nominal soil model, particle transport essentially followed plume gas flow across the soil test bed. A clear demonstration of this phenomena is shown in those soil tests, e.g., 12D, in which an incipient crater is formed and plume gases are deflected upward. On these tests, transported material is collected high above the soil bed (above 1.75 meters) in louvered soil baffle collection trays (see table VI) in a higher proportion than on those tests in which little or no crater formation was evident.

5. The response of the volcanic dune sand model to plume gas impingement was significantly different than that of the lunar nominal soil model.

Experimentally derived data during the Phase II, site alteration tests indicate that the larger size particles (mass average particle size of 580μ) of the volcanic dune sand model erode at a greater rate than do the fine particles of the lunar nominal model (mass average particle size of 59μ). This general trend has been shown analytically in reference 22 in which an upper cutoff limit based on particle weight is established at about 650μ particle diameter.

Additionally, in dune sand the plume gas is transporting more large particles of higher mass than with the lunar nominal soil model and since the morphological features constructed of volcanic dune sand are more easily eroded, all pre-formed features exhibited more severe alteration.

Concluding from this discussion, all criteria were met for the selected 18-nozzle configuration. Further, these criteria were met for nozzle exit plane altitudes corresponding to footpad contact (.58 meters) on the Viking Lander compared to the original 3 meter engine cutoff altitude. Thus, the nozzle which was redesigned for reducing site alteration also allowed a vehicle redesign with significant program impact. Sensors on the footpad now terminate thrust, the landing leg is designed for less severe loads, and the components within the lander may be designed to much lower impact shock loads. Each of these represent substantial savings in weight, development time, and cost. A comparison plot of the pressure reduction achieved is presented in figure 96 which shows the original baseline bell nozzle pressures and the new 18-nozzle configuration impingement pressure as a function of distance from the nozzle exit. The flight-weight Viking terminal descent engine with the 18-nozzles is shown in figure 97.

CONCLUDING REMARKS

The Viking '75 mission flight profile utilizes a propulsive terminal descent system in order to soft-land the scientific payload on Mars. The landing site alteration caused by this system had to be closely examined to establish the relevance of the returned scientific data and to minimize site modification effects by influencing vehicle design. The flat plate impingement pressures of a typical terminal descent engine were determined experimentally at the WSTF facility during the Phase IA site alteration tests. The extent of landing site physical disturbance was then established by conducting soil impingement tests in the LRC 60-foot sphere using sub-scale and full-scale cold-gas jets modeled to match the pressure time history on a simulated Martian soil (lunar nominal model). Results of these tests indicated there would be massive soil disturbances and alteration of the landing site. Studies to determine means of lessening this interaction with a minimum of modification to the lander and engines indicated that the flat plate impingement pressures had to be lowered by a factor of 23 through a nozzle redesign. Exploratory experimental tests were then conducted with cold-gas to determine the most promising nozzle concepts.

Success criteria were established and test objectives of the Phase II site alteration program were defined to show experimentally how the scientific criteria could be satisfied. These included measurements of the amounts of physical, chemical and biological alteration and a study of the possible nozzle configurations and engine cutoff heights which could reduce the alteration effects. Tests of a full-scale terminal descent engine with a number of alternate nozzles attached were conducted in the NASA Manned Spacecraft Center White Sands Test Facility under simulated Martian atmospheres, pressures, and soils.

A full-scale 18-nozzle configuration and a full-scale fluted nozzle configuration produced the greatest reduction in impingement pressures. Tests conducted in two simulated Martian soil models met the pre-determined physical erosion criteria in which not more than 60% of the soil sampler area would suffer more than 2 mm of erosion. Additionally, no test in the lunar nominal soil model resulted in a crater depth greater than 5 cm nor deposited 8 mm or more of material in the soil sampling site. With the selected 18-nozzle configuration, all criteria were met for engine cutoff altitudes as low as footpad contact, thus saving substantially in vehicle weight, impact shock loads and cutoff sensor complexity associated with the higher altitudes of engine cutoff.

The chief erosion mechanism for the nozzles and soil models tested was viscous shear. Consequently, the physical disturbance results were rather insensitive to the bulk mechanical properties of the soil. This was especially true for the lunar nominal soil model tested over a range of soil densities. Phase II test results indicate that rate of soil erosion was particle size dependent with the larger particles of the volcanic dune sand model eroding at a greater rate than those of the lunar nominal model. Irregular soil surfaces represented by surface morphological features suffered the most erosion, especially on slopes facing the engine.

APPENDIX A

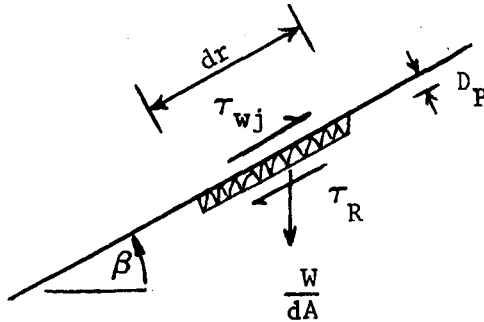
Viscous Erosion Formulation

The formulation for viscous erosion was first developed for the lunar landing by Roberts (references 5 and 6) and used by Hutton for Apollo and Mars landing studies (references 24,25). The approach taken here is similar to Roberts' approach, but differs slightly in the interpretation of momentum transfer to loosened particles.

The viscous erosion is formulated on a bulk mass basis rather than a single particle approach. In order to avoid following individual particle trajectories and making assumptions about particle blockage and collisions, the assumption is made that when the forces are sufficient to dislodge a layer of particles equal to the mass average particle diameter, the layer lifts off the surface as a whole. Once the particles are dislodged from the surface and enter the boundary layer, aerodynamic forces discriminate according to particle size and carry them away.

For a first approximation to the problem, the surface shear and soil slope are uncoupled. Effects of changing soil slope are included in the soil force balance, but the surface shear used is the flat plate value. This assumption breaks down with significant soil slope, $\beta \geq 30^\circ$, but by this time pressure cratering will have occurred to further change the flow properties into and out of the crater.

The force balance is applied to an elemental volume with unit surface area $dA = r \cdot d\theta \cdot dr$, a thickness equal to the average particle size diameter, D_p , and a mass computed from the bulk soil density γ_s . The viscous shear stress from the wall jet τ_{wj} acts on the top layer of soil with slope β , while the force per unit surface area τ_R acts to resist soil movement.



The resistance stress (τ_R) includes the soil cohesion (c), static friction, $(C_f F_{\text{normal}}/dA)$, and the weight of the soil. The weight of the soil per unit area is written with the local gravity as $g\rho_s D_p$. Therefore τ_R may be written:

$$\tau_R = c + \tan\phi (g\rho_s D_p) \cos\beta + (g\rho_s D_p) \sin\beta \quad (1)$$

The static friction coefficient, C_f , is expressed as the tangent of the soil internal angle of friction ϕ .

The force balance on the bulk soil sample is then:

$$\sum \frac{F}{dA} = \tau_{wj} - \tau_R$$

If $\tau_{wj} \leq \tau_R$ no soil movement occurs for the soil acts like a solid and resists deformation. When the shear stress exceeds the capability of the soil layer to resist, $\tau_{wj} > \tau_R$, the soil fails and is eroded away. Since τ_{wj} stress is applied to the ground by the viscous momentum flux and the soil is able to resist only τ_R at the same depth dl , the difference is the amount of force per unit area acting on the eroded particles. The impulse applied to the soil mass is:

$$\frac{dm}{dA} V_{mass} = (\tau_{wj} - \tau_R) dt \quad (2)$$

where V_{mass} is the velocity that the soil mass achieves from viscous shear forces initiating motion. The exposure time required is then, from (2):

$$dt = \frac{\rho_s D_p V_{mass}}{(\tau_{wj} - \tau_R)} \quad (3)$$

During a computing interval Δt the depth of soil removed is equal to the number of layers times the average particle diameter, D_p , or

$$dl = \frac{\Delta t}{dt} D_p$$

or further, from equation (3)

$$dl = \frac{\Delta t (\tau_{wj} - \tau_R)}{\rho_s V_{mass}} \quad (4)$$

The remaining unknown is V_{mass} which is defined as the velocity that particles leave the surface after being acted upon by the shear force only. Aerodynamic forces act once the soil leaves the surface, but it is assumed the initial movement is due only to shear. Thus, V_{mass} must be of such value that the total momentum of the soil bulk, gas system is conserved. The viscous momentum flux is the force per unit area which has its normal aligned with the gas velocity gradient, and the particle momentum is defined as force per unit area which has its normal aligned with the soil-gas velocity vector, therefore equating forces gives:

$$(\tau_{wj} - \tau_R) r d\theta dr = \rho_s v_{mass}^2 D_p r d\theta$$

or

$$v_{mass} = \sqrt{\frac{(\tau_{wj} - \tau_R)}{\rho_s} \frac{dr}{D_p}} \quad (5)$$

where dr is a unit length in the radial direction. The eroded depth dl over the computing time interval Δt is therefore:

$$dl = \Delta t \sqrt{\frac{(\tau_{wj} - \tau_R)}{\rho_s} \frac{D_p}{dr}} \quad (6)$$

The viscous erosion thus formulated contains the proper trend with particle size as found by early soil erosion tests at LRC, reference 2 among others, and by the Viking site alteration tests at White Sands, reference 12; namely larger particles erode at a greater rate than smaller ones, but the smaller ones require less shear stress to initiate motion. This trend is illustrated in figure 98 by the maximum erosion depth for a range of uniform diameter soil models and computed for the Viking landing case.

Incorporation of Specific Soil Models

The previous formulation describes erosion of a soil model made up of a single particle size. For soil models consisting of many particle sizes, the computation of erosion may be approximated if the particle size distribution is known. In a manner familiar in two phase nozzle and exhaust flow studies, the technique adopted assumed that for each soil model a function $\phi(r_p)$ can be found which represents the fractional number of particles, per unit size, of radius r_p which are found to exist between $r_p - \frac{dr_p}{2}$ and $r_p + \frac{dr_p}{2}$. The number of r_p sized particles per unit volume is then,

$$N(r_p) = N_t \phi dr_p$$

where N_t is the total number of all sized particles per unit volume, thus:

$$N_t = \int_0^{\infty} N_t \phi dr_p$$

or the function ϕ is of form such that:

$$\int_0^{\infty} \phi dr_p = 1$$

The weight of r_p sized particles per unit volume is then:

$$g\rho_p \frac{4}{3} \pi r_p^3 N_t \phi dr_p$$

The weight of all sized particles per unit volume is the soil density and is expressed as:

$$\gamma_s = g\rho_s = g\rho_p \pi \frac{4}{3} N_t \int_0^{\infty} \phi r_p^3 dr_p$$

The cumulative weight per unit volume of particles r_p and smaller compared to the weight of all sized particles per unit volume is:

$$\frac{\int_0^{r_p} \phi r_p^3 dr_p}{\int_0^{\infty} \phi r_p^3 dr_p}$$

The cumulative weight percent, CWP, of particles r_p and larger is then

$$CWP = 1 - \frac{\int_0^{r_p} \phi r_p^3 dr_p}{\int_0^{\infty} \phi r_p^3 dr_p} \quad (7)$$

The CWP is obtained by a sieve analysis, and for the lunar nominal and dune sand soil models, the results are shown in figure 18. These soil models follow the specifications of the Mars Engineering Model, reference 10.

The fractional number $\frac{N(r_p)}{N_t}$ for each particle size can then be found by segmenting the CWP curve and dividing by the particle diameter cubed, or:

$$\frac{N(r_p)}{N_t} = \phi dr_p = \frac{\left[\frac{\Delta CWP}{D_p^3} \right]}{\sum_{D_p = \min}^{\max} \left[\frac{\Delta CWP}{D_p^3} \right]} \quad (8)$$

Fractional number results for the two soil models are given in table IV where it is seen that by number, both soil models are composed chiefly of the smallest size particles. The technique for computing erosion for soil models is therefore to compute the erosion depth for each particle size and using the appropriate number weighing function, equation 8, to sum the results over the particle size range:

$$L_t = \sum_{D_p = \min}^{\max} L(D_p) \left(\frac{N(D_p)}{N_t} \right) \quad (9)$$

REFERENCES

1. Scott, Ronald F.; and Ko, Hon-Yim: Transient Rocket-Engine Gas Flow in Soil. AIAA J., Vol. 6, No. 2, February 1968, pp 258-264.
2. Land, Norman S.; and Clark, Leonard V.: Experimental Investigation of Jet Impingement on Surfaces of Fine Particles in a Vacuum Environment. NASA TN D-2633, 1965.
3. Land, Norman S.; and Scholl, Harland F.: Scaled Lunar Module Jet Erosion Experiments. NASA TN D-5051, 1969.
4. Clark, Leonard V.: Experimental Investigation of Close-Range Rocket Exhaust Impingement on Surfaces in a Vacuum. NASA TN D-5895, 1970.
5. Roberts, Leonard: The Action of a Hypersonic Jet on a Dust Layer. IAS Paper No. 63-50, January 1963.
6. Roberts, Leonard: The Interaction of a Rocket Exhaust with the Lunar Surface. The Fluid Dynamic Aspects of Space Flight, Vol. 2, Gordan and Breach, 1966, pp 269-290. Proceedings of the AGARD-NATO Specialists' Meeting, Marseille, France, April 1964.
7. Romine, G. L.: Site Alteration - Erosion and Heating Study. Martin Marietta Corporation, Viking Project, VER-88, October 16, 1970.
8. Ko, Hon-Yim: Soil Properties Study. Martin Marietta Corporation, Viking Project, VER-181, October 15, 1971. (Compilation of work completed under subcontract):
 - a. Effects of Pore Pressure on Cratering Due to Rocket Exhaust-Gas Impingement, October 1970.
 - b. Determination of the Mechanical Properties of Simulated Mars Soil Models, January 1971.
 - c. Development of a Computer Program for the Prediction of Soil Erosion by Rocket Engine Plumes, August 1971.
9. Alexander, J. P.; Roberds, W. M.; and Scott, R.F.: Soil Erosion by Landing Rockets. Hayes International Corporation, Engineering Report No. 1301, July 15, 1966 (NASA/MSO Contract NAS9-4825).
10. Viking Mars Engineering Model by NASA Langley Research Center, Viking Project Office Report, M75-125-0, March 1971.
11. Click, B. F.: Experimental Plume Impingement Pressures on a Flat Plate Generated by a Prototype Viking Terminal Descent Engine. TR-3720054, Martin Marietta Corporation, April 1971 (NASA/LRC Contract NAS1-9000).

12. Reisert, T. D.; Gliozzi, J.; Romine, G.L.; and Fennessey, P.: Test Report for Viking Site Alteration Test, Phase II, in White Sands Test Facility 302. Martin Marietta Corporation, Viking Project, TR-3720209, November 1971 (NASA/LRC Contract NAS1-9000).
13. Reisert, T. D.: Pretest Report for Site Alteration Test Phase II, in White Sands Test Facility 302. Martin Marietta Corporation, Viking Project, TR-3720043, January 1971 (NASA/LRC Contract NAS1-9000).
14. Clark, Leonard V.: Retrorocket Plume Interaction with Extraterrestrial Surfaces. Presented at the JANNAF 6th Plume Technology Meeting, Monterey, California, March 9-11, 1971.
15. Donaldson, Coleman duP.; and Gray, K. Evan: Theoretical and Experimental Investigation of the Compressible Free Mixing of Two Dissimilar Gases. AIAA Journal, Vol. 4, No. 11, November 1966, pp 2017-2025.
16. Higgins, C.C.; and Wainwright, T.W.: Dynamic Pressure and Thrust Characteristics of Cold Jets Discharging from Several Exhaust Nozzles Designed for VTOL Downward Suppression. NASA TN D-2263, April 1964.
17. Higgins, C.C.; Kelley, D.P.; and Wainwright, T.W.: Exhaust Jet Wake and Thrust Characteristics of Several Nozzles Designed for VTOL Downwash Suppression. NASA CR-373, January 1966.
18. Trentacoste, Nicholas; and Sforza, Pasquale, M.: An Experimental Investigation of Three- Dimensional Free Mixing in Incompressible, Turbulent, Free Jets. Polytechnic Institute of Brooklyn, PIBAL Report No. 871, AFOSR 66-0657, March 1966.
19. Hetrick, M. A., Jr.: Study of Methods to Reduce Site Alteration. Martin Marietta Corporation, Viking Project, VER-140, March 1971.
20. Fennessey, P.V.; Schwartz, D.B.; Sterhardt, J.A.: Chemical, Biological and Physical Site Contamination and Alteration Criteria. Martin Marietta Corporation, Viking Project, VER-130-2B, April 30, 1971. (also included as appendix B in reference 12).
21. Romine, G. L.: Nozzle Configuration Changes Related to Site Alteration. Martin Marietta Corporation, Viking Project, VER-134, March 5, 1971.
22. Romine, G. L.: Analysis of Site Alteration Erosion and Comparison with Experimental Results. Martin Marietta Corporation, Viking Project, VER-180, October 15, 1971.
23. Donaldson, Coleman duP.; Snedeker, Richard S.; and Margolis, David P.: A Study of Free Jet Impingement, Part 2 - Free Jet Turbulent Structure and Impingement Heat Transfer. J. Fluid Mech. (1971) Vol. 45, part 3, pp 477-512.
24. Hutton, Robert E.: Mars Surface Soil Erosion Study. 09349-6001, R000 (JPL Contract No. 422060), TRW Systems, February 28, 1968.

25. Hutton, Robert E.: Lunar Surface Erosion During Apollo 11 Landing. 11176-6068-R0-00 (NASA/MCS Contract) TRW Systems, November 20, 1969.

TABLE I.-
SUMMARY OF WSTF PHASE II TEST CONDITIONS

Test no.	Test objectives	Test date	Target surface	Test Chamber Pressure		Test Chamber Temperature		Nozzle Configuration		Burn time, sec	Chamber pressure, N/m^2	Max. Chamber temperature, °K	Descent velocity, m/sec	Distance above soil surface		Hydrazine
				Initial, mb	Outoff, mb	Initial, K	Outoff, K	Baseline	Fltgn					Initial, m	Final, m	
1	Engine Checkout - Flight Weight	3/1/71	--	Amb.	Amb.	283.81	284.57	Baseline	Baseline	10.25	379 x 10 ³	--	0	3.048	3.048	Pure
2	Pure Hydrazine - Exhaust Gas	3/5/71	Quartz Plate	3.30	13.80	290.11	290.61	"	"	15.55	456	--	0	3.048	3.048	Pure
3	Pure Hydrazine - Exhaust Gas	3/9/71	Quartz Plate	9.93	21.20	287.60	288.10	"	"	15.40	452	--	0	3.048	3.048	Pure
10A	Test Chamber Chemical Background	3/10/71	--	4.74	4.74	--	--	--	--	--	--	--	--	--	--	--
9	M11 Spec Hydrazine - Exhaust Gas	3/16/71	Quartz Plate	4.47	14.90	289.61	290.86	Baseline	Baseline	15.35	451	--	0	3.048	3.048	M11 Spec
10	M11 Spec Hydrazine - Exhaust Gas	3/17/71	Quartz Plate	10.00	22.10	288.61	289.86	"	"	15.65	461	--	0	3.048	3.048	M11 Spec
1A	Engine Checkout - Boilerplate	3/26/71	--	Amb.	Amb.	291.61	292.11	"	"	10.44	345	1103.60	0	3.048	3.048	M11 Spec
4	Checkout of Rail Assembly	3/31/71	--	Amb.	Amb.	--	--	--	--	--	--	--	1.453	11.131	4.639	--
5	Checkout of Rail Assembly	3/31/71	--	Amb.	Amb.	--	--	--	--	--	--	--	1.435	11.131	1.359	--
11	Pressure Test	4/2/71	Flat Plate	11.30	19.90	292.35	293.10	Baseline	Baseline	10.93	361	1114.71	1.435	12.161	1.662	M11 Spec
11A	Pressure Test	4/6/71	Flat Plate	9.25	20.10	284.58	285.34	24	24	10.20	421	--	1.444	12.344	1.981	M11 Spec
11C	Pressure Test	4/7/71	Flat Plate	11.30	19.00	291.11	291.61	7	7	7.50	432	--	1.456	12.293	5.486	M11 Spec
3C	Pure Hydrazine - Exhaust Gas	4/16/71	Stainless Steel Plate	4.94	15.90	289.61	--	Baseline	Baseline	16.50	325	1074.15	0	3.048	3.048	Pure
3B	Pure Hydrazine - Exhaust Gas	4/19/71	Stainless Steel Plate	8.94	21.62	282.80	--	24	24	16.21	472	1078.60	0	1.524	1.524	Pure
3A	Pure Hydrazine - Exhaust Gas	4/20/71	Stainless Steel Plate	2.77	14.30	289.11	--	7	7	16.34	475	1081.38	0	1.524	1.524	Pure
1B	Engine Checkout - Boilerplate	4/26/71	--	Amb.	Amb.	293.07	--	24 (mod 1)	24 (mod 1)	10.16	537	1059.71	0	3.048	3.048	Pure
11D	Pressure Test	4/27/71	Flat Plate	11.12	18.70	299.76	--	24 (mod 1)	24 (mod 1)	10.38	481	1051.93	1.475	12.374	.640	Pure
11E	Pressure Test	4/28/71	Flat Plate	11.10	18.80	296.32	--	24 (mod 2)	24 (mod 2)	10.39	480	1044.16	1.639	12.387	.804	Pure
12A	Soil Cratering, Chemistry Effects	5/6/71	Lunar	11.68	19.90	299.51	307.77	24 (mod 2)	24 (mod 2)	9.33	630	1068.60	1.560	12.274	.691	Pure
11G	Pressure Test	5/21/71	Flat Plate	9.73	18.70	292.11	300.00	Multi-2-D	Multi-2-D	10.43	528	1120.82	1.427	12.292	.688	Pure
11H	Pressure Test	5/24/71	Flat Plate	10.10	18.90	291.61	299.51	Annular	Annular	10.05	447	950.28	1.600	12.301	.707	Pure
11I	Pressure Test	5/25/71	Flat Plate	10.40	19.80	293.60	301.47	Fluted	Fluted	10.38	541	1136.37	1.530	12.286	.722	Pure
12C	Soil Cratering, Chemistry Effects	6/8/71	Lunar	10.66	19.70	310.41	317.28	24 (mod 2)	24 (mod 2)	9.58	698	1117.48	1.578	12.274	.691	Pure
12D	Soil Cratering, Chemistry Effects	6/15/71	Lunar	10.80	19.00	312.79	--	24 (mod 2)	24 (mod 2)	10.05	644	1114.71	1.600	12.274	.691	M11 Spec
12E	Soil Cratering, Chemistry Effects	6/22/71	Lunar	10.80	18.70	311.62	315.67	18	18	9.99	463	1106.37	1.609	12.252	.658	M11 Spec
12F	Soil Cratering	6/28/71	Dune Sand	11.90	19.60	312.06	316.12	18	18	9.87	465	1108.04	1.639	12.252	.658	M11 Spec
12G	Soil Cratering	7/8/71	Dune Sand	11.55	19.80	304.88	308.01	Fluted (mod 1)	Fluted (mod 1)	9.77	503	1154.15	1.658	11.205	.633	M11 Spec
12H	Soil Cratering, Ammonia	7/13/71	Dune Sand	11.32	18.80	306.57	308.97	Fluted (mod 1)	Fluted (mod 1)	8.40	487	1139.70	1.609	11.205	1.942	M11 Spec
11J	Pressure Test	7/20/71	Flat Plate	9.40	17.90	296.56	301.73	Fluted (mod 1)	Fluted (mod 1)	14.24	497	1148.59	1.600	12.226	.722	M11 Spec
11K	Pressure Test	7/22/71	Flat Plate	10.32	19.30	295.56	301.23	18	18	10.16	451	1075.82	1.557	12.283	.762	Pure
29	Characteristics of Engine Plume	7/28/71	Flat Plate	9.47	19.10	297.06	302.67	18	18	14.26	469	1098.04	1.557	12.283	.762	Pure

TABLE II.- SUMMARY WSTF PHASE IA TEST CONDITIONS

Plate pass	Time, sec		Plate position, h/d _e		Engine chamber pressure, kN/m ²		Ambient pressure, mb	
	Initial	Final	Initial	Final	Initial	Final	Initial	Final
1	3.35	10.75	10.46	26.5	420.	420.	4.84	10.5
2	11.85	18.75	26.5	10.5	420.	411.	11.32	16.3
3	20.25	26.95	10.5	26.4	411.	408.	17.4	22.1
4	28.55	35.55	26.4	10.46	408.	406.	23.2	28.0
5	36.95	38.85	10.46	15.2	406.	406.	28.8	30.2

Plate velocity (unsteady) $\approx 3.6 d_e/\text{sec}$

Thrust $\approx 667\text{N}$

$\epsilon = 20$

$d_e = 15.24 \text{ cm}$

$T_e = 285^\circ\text{K}$

$\eta_e = 28 (\text{N}_2)$

TABLE III.-

SOIL BED THERMOCOUPLE RESULTS

Thermocouple location		Maximum temperature Change, °K	
Gage distance from engine centerline, cm	Gage depth, cm	Test 12E	Test 12F
0	0	19.2	> 80.4 *
5	0	13.8	> 80.2
10	0	8.1	> 79.5
15	0	6.1	> 80.9
20	0	88.3	10.8
30	0	5.4	66.3
40	0	3.8	> 80.9
50	0	1.2	18.9
61	0	.8	8.7
76	0	1.1	7.8
91	0	.8	6.9
122	0	.5	7.3
183	0	.7	1.4
244	0	.2	--
305	0	.3	-24.6
456	0	.2	-1.2
610	0	.7	.2
-61	0	.7	.5
-30	0	10.7	22.5
15	5	.5	.9
30	5	19.7	15.9
45	5	.5	.1
61	5	.8	2.2

Thermocouple location		Maximum temperature Change, °K	
Gage distance from engine centerline, cm	Gage depth, cm	Test 12E	Test 12F
76	5	.7	1.1
91	5	.7	1.6
0	10	.7	.3
76	10	.4	.3
91	10	.4	.7
122	10	.5	3.6
183	10	.7	.7
244	10	-.2	.2
305	10	.2	.2
15	15	.3	.1
30	15	.4	.3
45	15	.4	.4
61	15	.3	.4
76	15	.4	.3
0	20	.1	.7
0	30	.1	.3
15	30	.1	.1
30	30	.1	.3
30	30	.2	.5
45	30	.1	.2
61	30	.7	.3
61	30	.1	.4
0	35	1.3	.4

*Post-test inspection indicated a number of the top surface thermocouples were exposed to the gas flow.

TABLE IV.-

NUMBER DISTRIBUTION OF PARTICLE SIZES IN SELECTED SOIL MODELS

LUNAR NOMINAL		DUNE SAND	
D_p μ	$\frac{N(D_p)}{\sum N}$	D_p μ	$\frac{N(D_p)}{\sum N}$
3	.55769	75	.4263
4.6	.15460	102	.1695
7.1	.08414	145	.1180
9.2	.03867	179	.06272
11.2	.02143	206	.04115
13	.01370	230	.02956
14.6	.009636	255	.02169
16.1	.007216	280	.01638
17.5	.005619	300	.01332
19	.00439	318	.01118
20.3	.003599	330	.01001
22	.002828	348	.008536
23.8	.002233	364	.007459
.	.	.	.
.	.	.	.
59.5	9.494 - 6	580	.001843
.	.	.	.
.	.	.	.
236	2.291 - 6	830	.000629
.	.	.	.
.	.	.	.
12,700	2.940 - 11	2000	.000045

TABLE V.-

SUMMARY OF SOIL EROSION MEASUREMENTS FOR WSTP PHASE II TESTS

Test							
	12A	12C	12D	12E	12F	12G	12H
Engine Nozzle Configuration	24, Mod 2	24, Mod 2	24, Mod 2	18	18	Fluted, Mod 1	Fluted, Mod 1
Soil Type	Lunar Nominal	Lunar Nominal	Lunar Nominal	Lunar Nominal	Volcanic Dune Sand	Volcanic Dune Sand	Volcanic Dune Sand
Fuel	Purified	Purified	Mil-Spec	Mil-Spec	Mil-Spec	Mil-Spec	Mil-Spec
Radar		Landing Radar			Landing Radar		
Soil Erosion Depth at* Radius from engine centerline $r = 0$ m	-4 mm	-12 mm (6 mm fluff)	-5 mm	-7 mm	-37 mm (one of 18 depressions)	0 to -15 mm (one of 8 depressions)	-1 mm
$r = .914$ m	-3 mm	-1 mm	-2 mm	-2 to -4 mm	0 to -7 mm	0 to 2 mm	-1/2 mm
$r = 1.829$ m	-2 mm	-1/2 mm	-1/2 to -1 mm	-2 mm	-3 mm	0 to -3 mm	-1/2 mm
$r = 3.05$ m	0	0	0	-1 mm	0 to -4 mm	0 to +1 mm	0
Remarks		Torroidal shaped crater with 3 distinct depressions	like 12C	fine scrubbed under engine centerline	18 distinct depressions		
Percent of Surface Sampler Area Eroded More than 2 mm	9.5	2.6	9.4	18.0	43.3	14.2	0

NOTE: Ranges shown like 0 to -3 are for variations along the radius.

* Average Depth

TABLE VI.-
GRAMS OF SOIL COLLECTED IN LOUVERED BAFFLE TRAYS DURING WSIF PHASE II TESTS

Tray No.	Collecting area, cm above bed	12A lunar nominal	12C lunar nominal	12D lunar nominal	12E lunar nominal	12F dune sand	12G dune sand	12H dune sand
1	22.9-33.0	10.18	6.81	15.48	13.67	84.87	57.5	39.05
2	33.0-46.2	--	4.16	6.57	6.50	67.75	45.41	27.07
3	46.2-53.3	4.85	4.40	5.24	4.90	50.87	26.64	16.68
4	53.3-63.5	4.28	3.42	4.66	3.95	29.78	18.11	9.61
5	63.5-73.7	3.05	2.76	3.22	2.91	20.03	12.42	6.22
6	73.7-83.8	2.23	2.13	2.15	2.04	17.61	9.57	4.97
7	83.8-94.0	1.61	1.46	1.90	1.85	11.97	6.38	3.42
8	94.0-104.1	1.50	1.33	1.45	1.59	10.54	4.69	2.40
9	104.1-114.3	1.16	1.01	1.38	1.31	7.93	3.27	1.67
10	114.3-124.5	1.03	0.95	1.27	1.28	6.17	2.79	1.40
11	124.5-134.6	0.90	0.85	0.93	1.02	4.87	2.07	1.13
12	134.6-144.8	0.93	0.82	1.00	1.03	4.04	1.68	0.96
13	144.8-154.9	0.89	0.76	0.97	1.00	3.15	1.15	0.53
14	154.9-165.1	0.90	0.93	0.97	0.97	2.55	0.98	0.50
15	165.1-175.3	0.95	0.82	0.98	1.02	1.44	0.98	0.32
16	Above 175.3	--	--	4.53	2.80	1.50	0.98	0.32

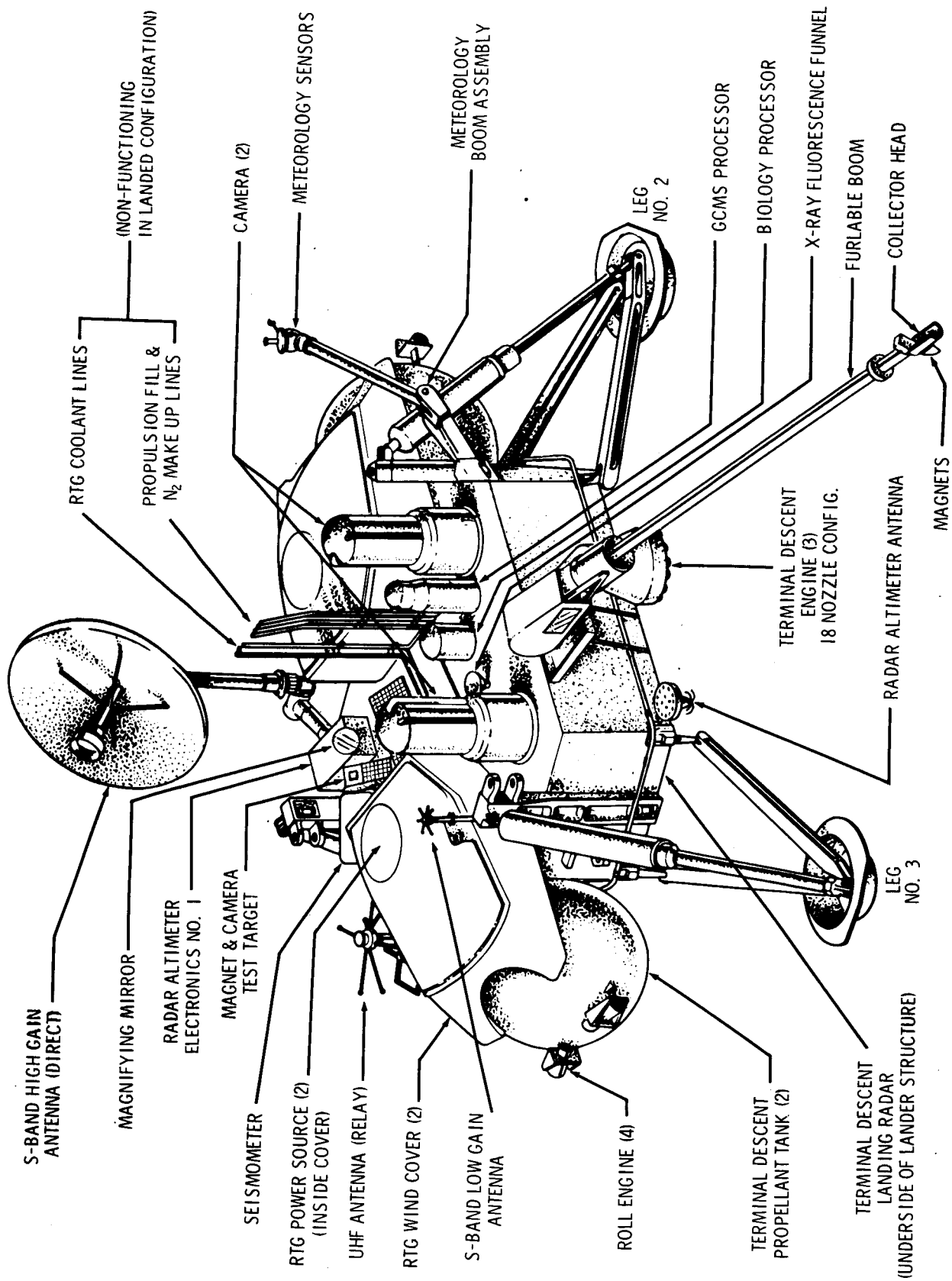
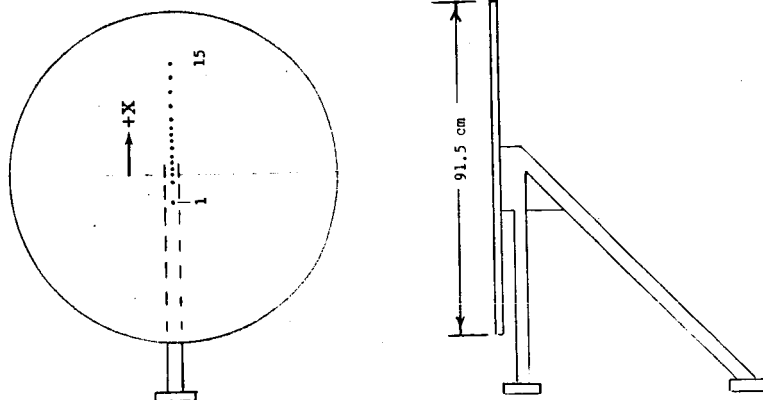


Figure 1.- Viking Lander Configuration.



Pressure port no.	X, cm
1	-7.6
2	-1.9
3	0
4	1.9
5	3.8
6	5.7
7	7.6
8	9.5
9	11.4
10	13.3
11	15.2
12	19.1
13	22.8
14	25.4
15	30.5

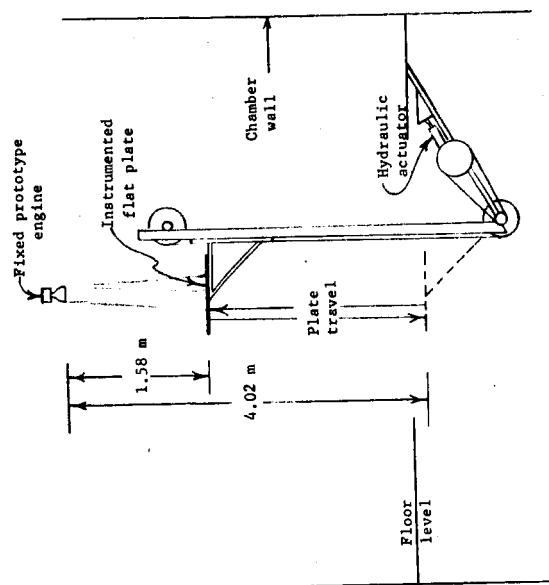


Figure 2.- Phase 1A test apparatus in WSTF 302 vacuum chamber.

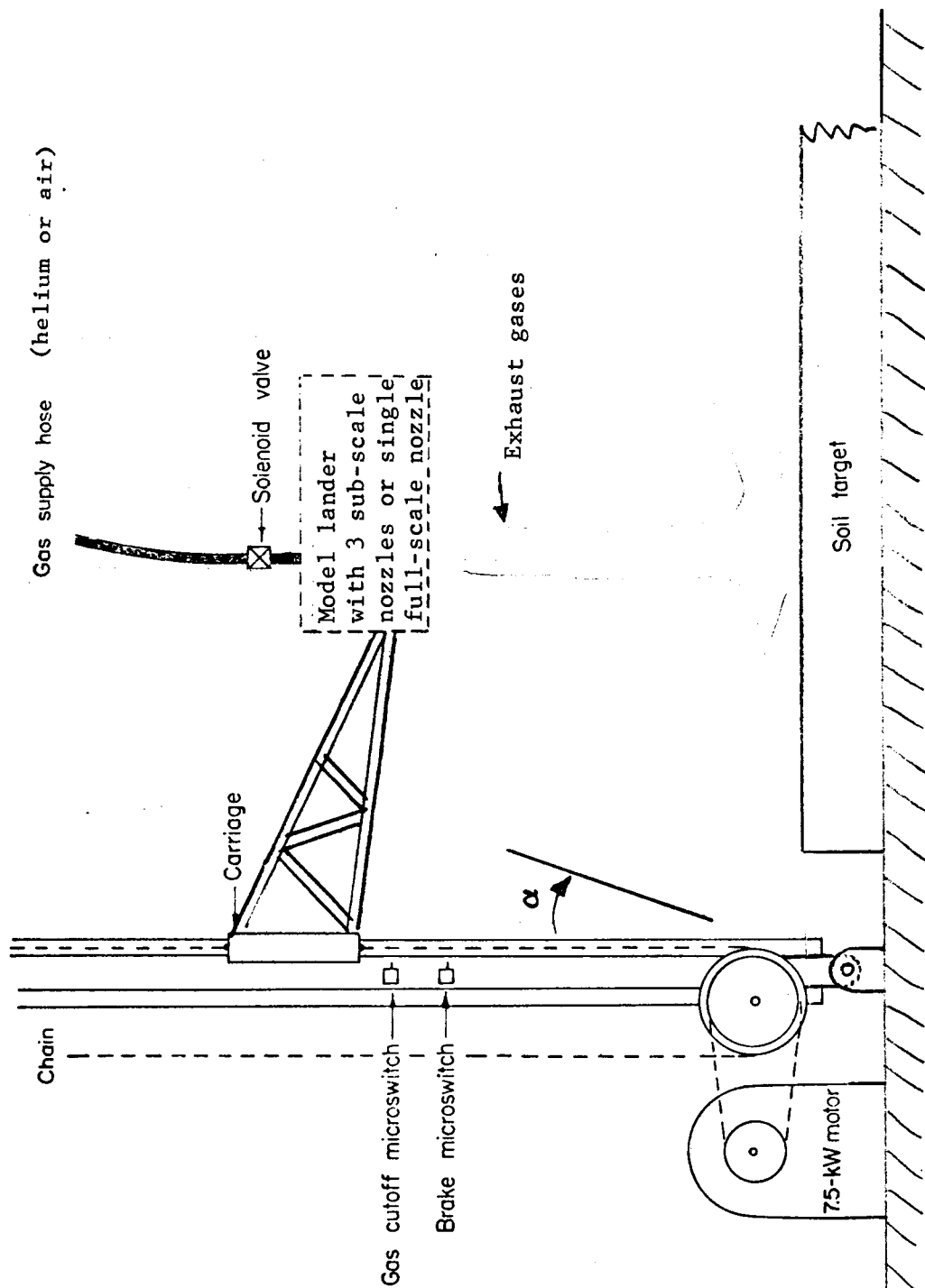


Figure 3.— Schematic of test apparatus used in NASA/Langley 60-foot sphere.

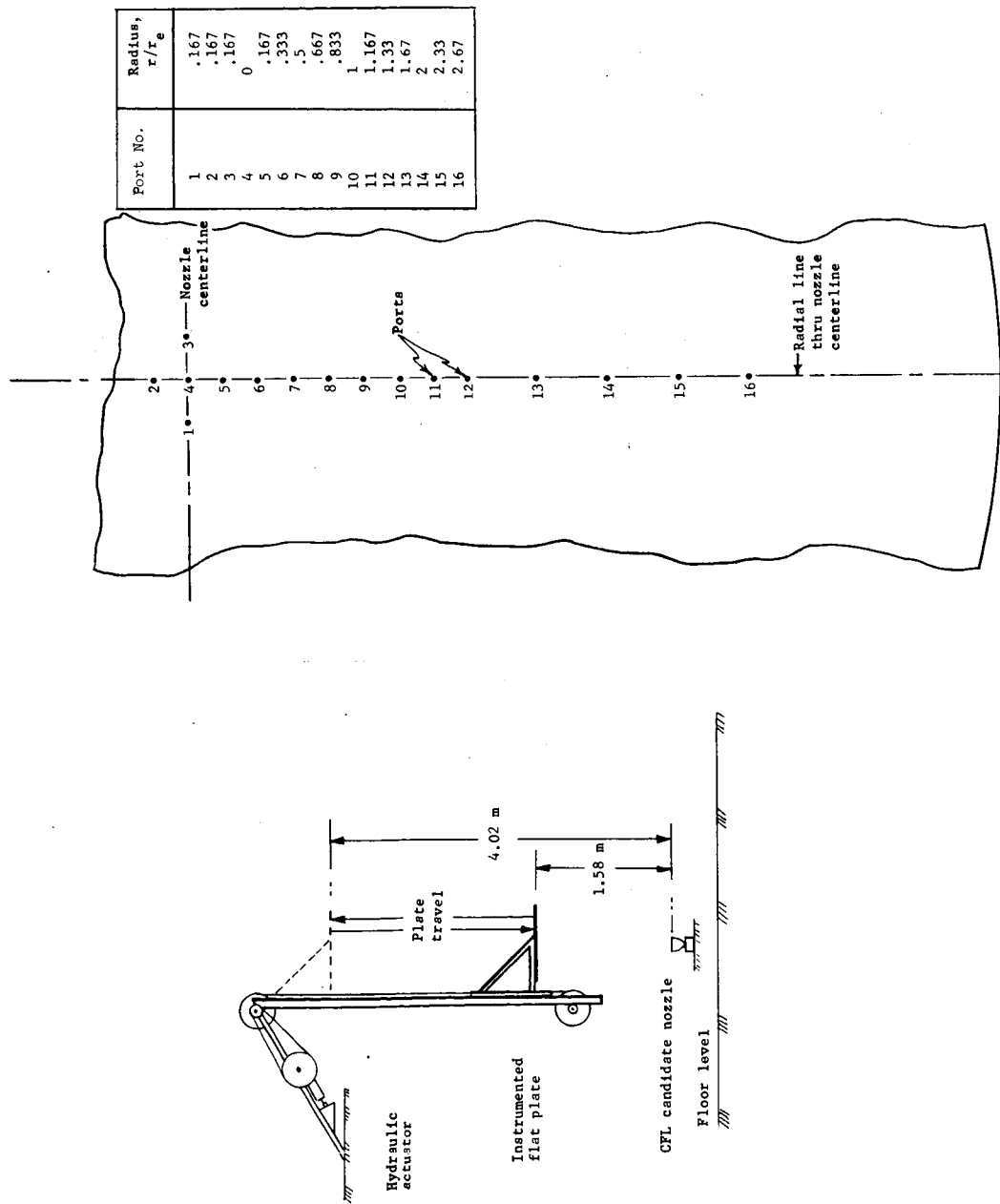


Figure 4.- Apparatus and pressure port locations for WMC CFL tests.

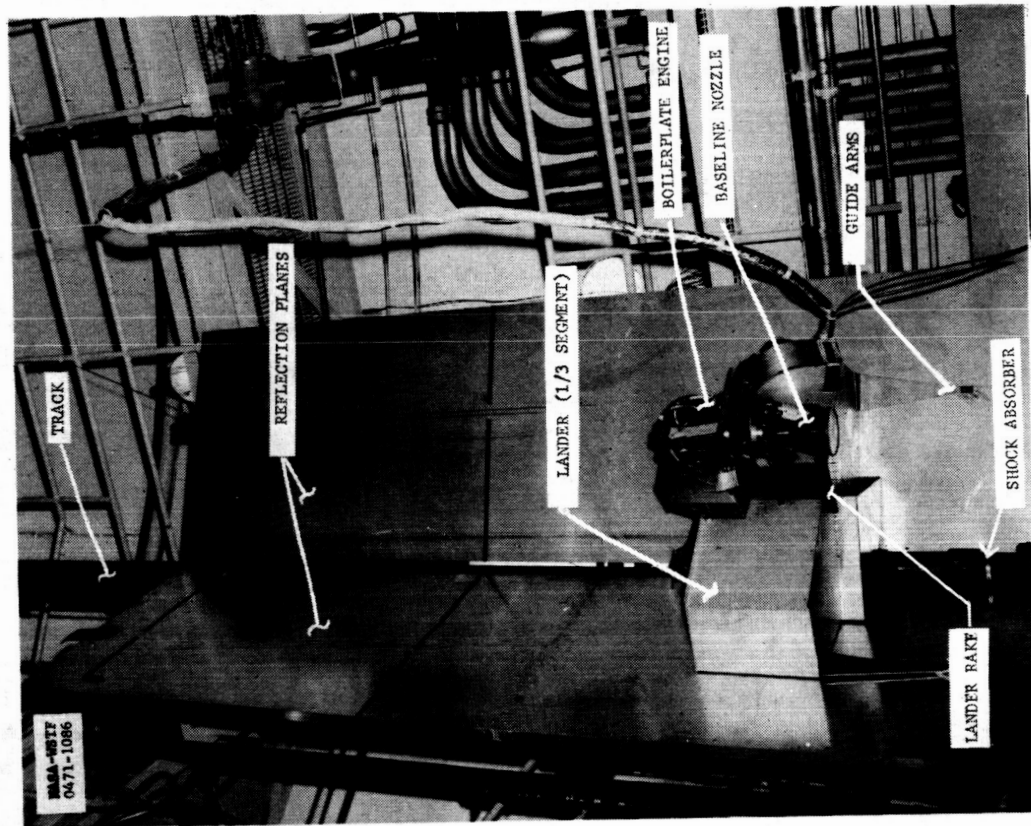


Figure 6.- Photograph of Phase II test apparatus installed in WSTF chamber.

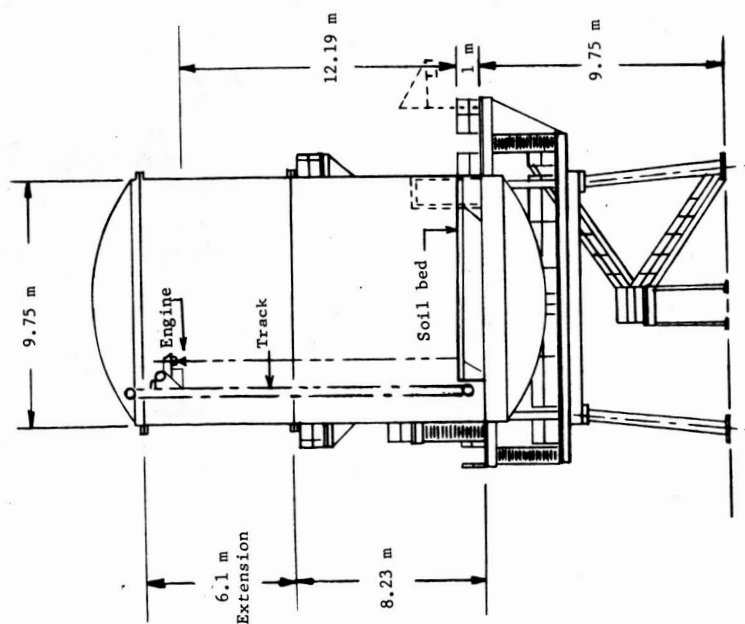
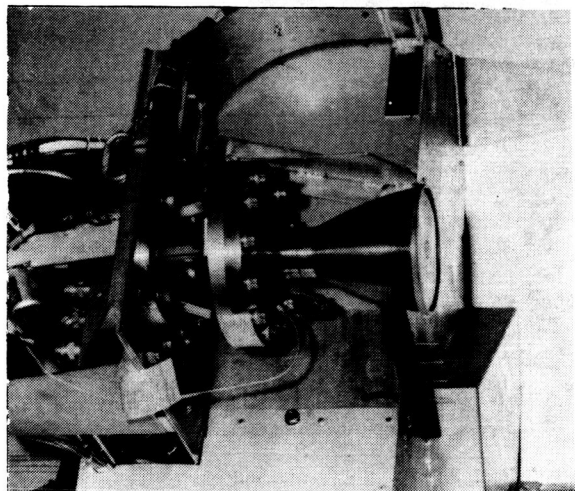
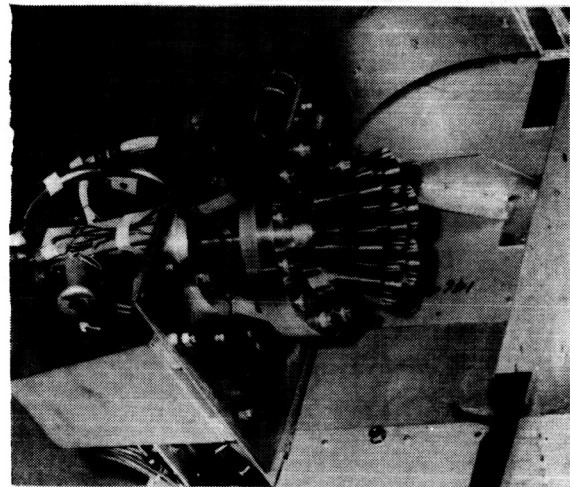


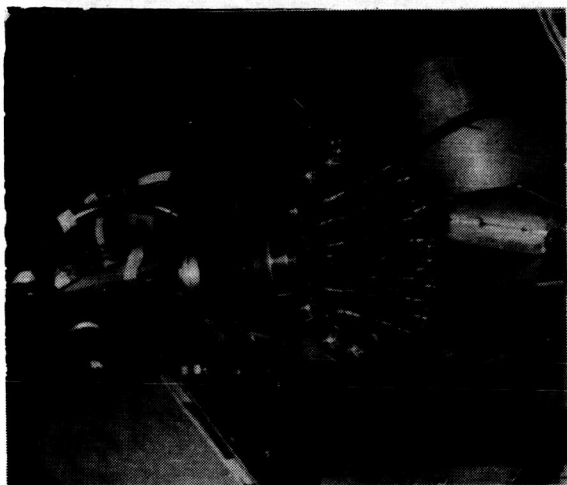
Figure 5.- White Sands Test Facility chamber 302.



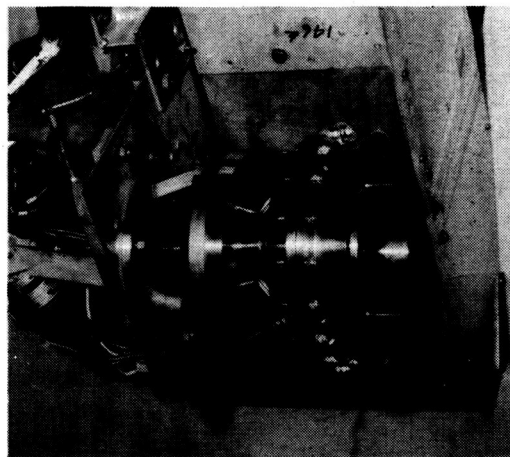
Baseline bell nozzle



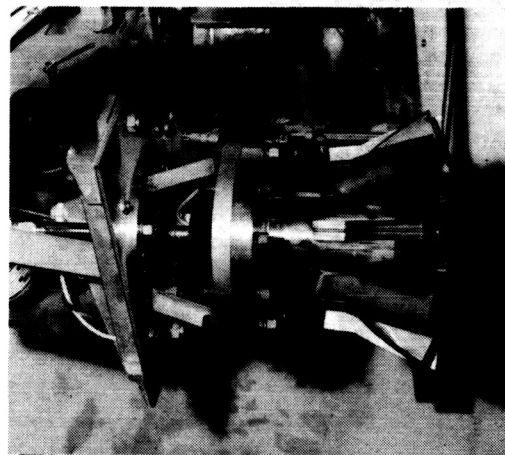
MMC 7-nozzle configuration



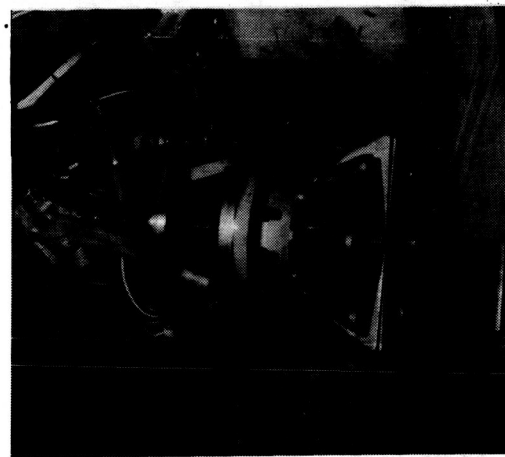
MMC 24-nozzle configuration
mod #1, 18-nozzles
mod #2, 18-nozzles



Annular nozzle



Multiple 2-dimensional configuration



MMC fluted nozzle
mod #1 fluted nozzle

Figure 7.- Nozzle configurations tested at WSTF using a "boilerplate" engine.



Figure 8.- Full-scale 18-nozzle configuration with "boilerplate" engine.

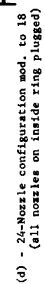
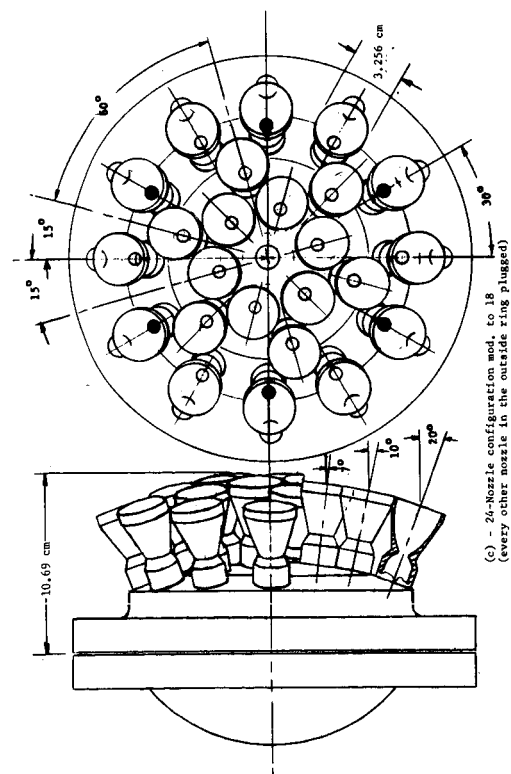
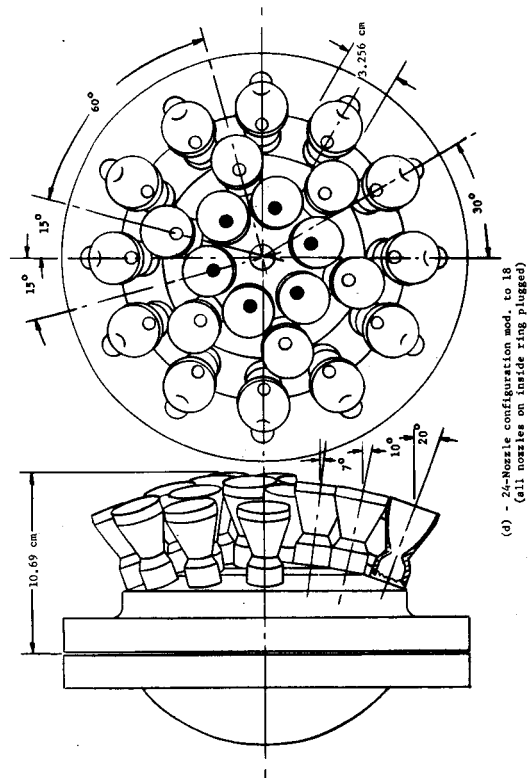
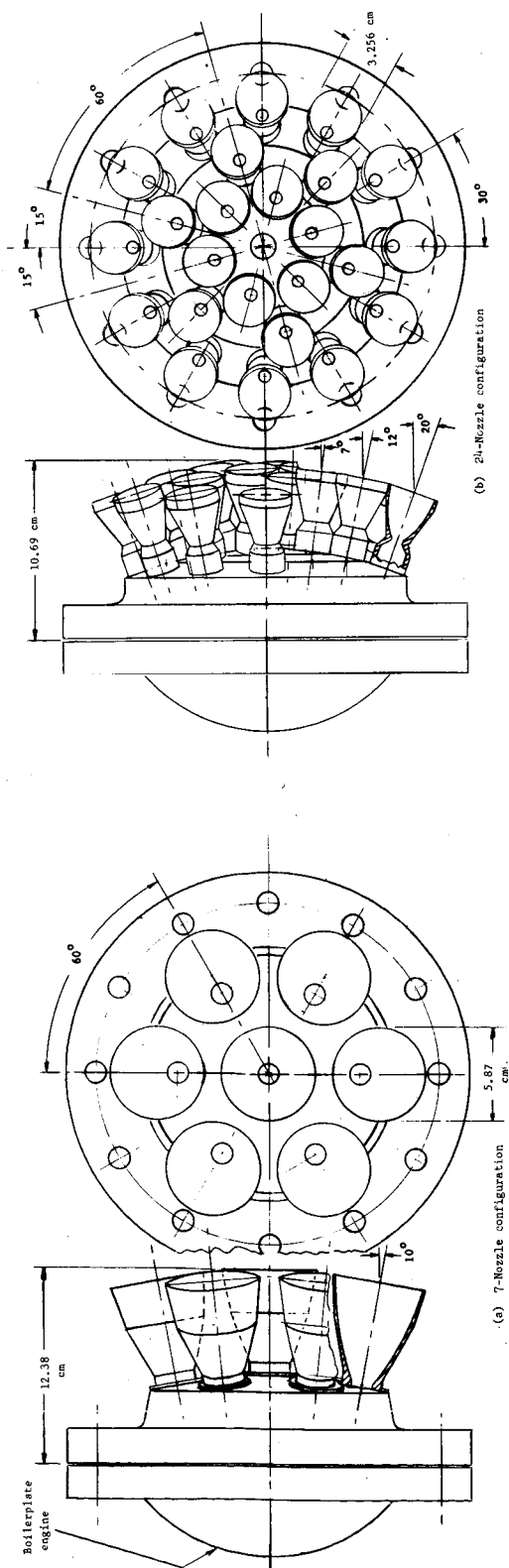


Figure 9.- Sketches of nozzle configurations tested in WST Phase II tests.

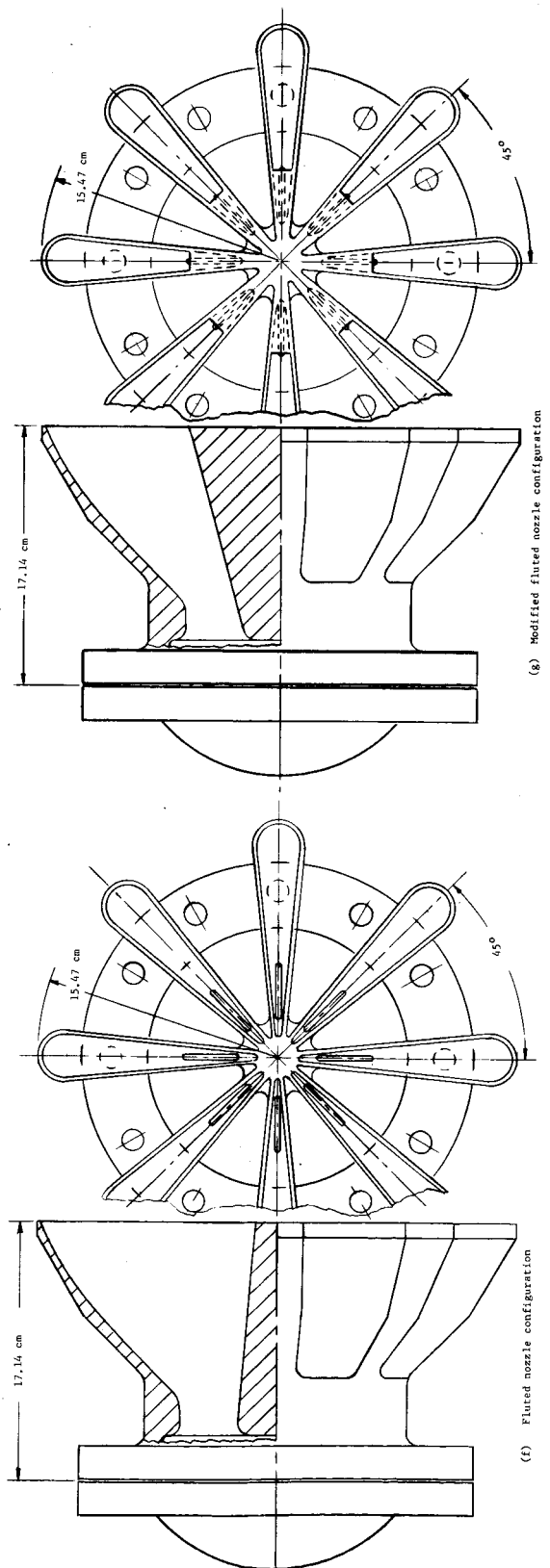
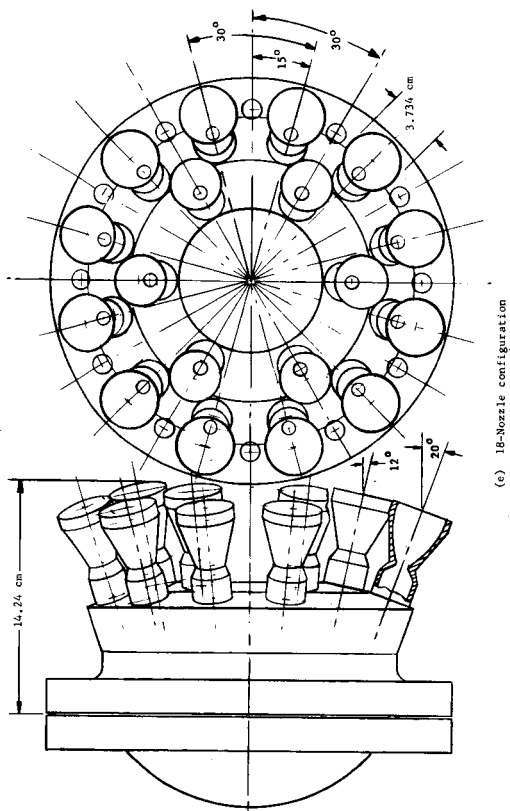


Figure 9.- Concluded.

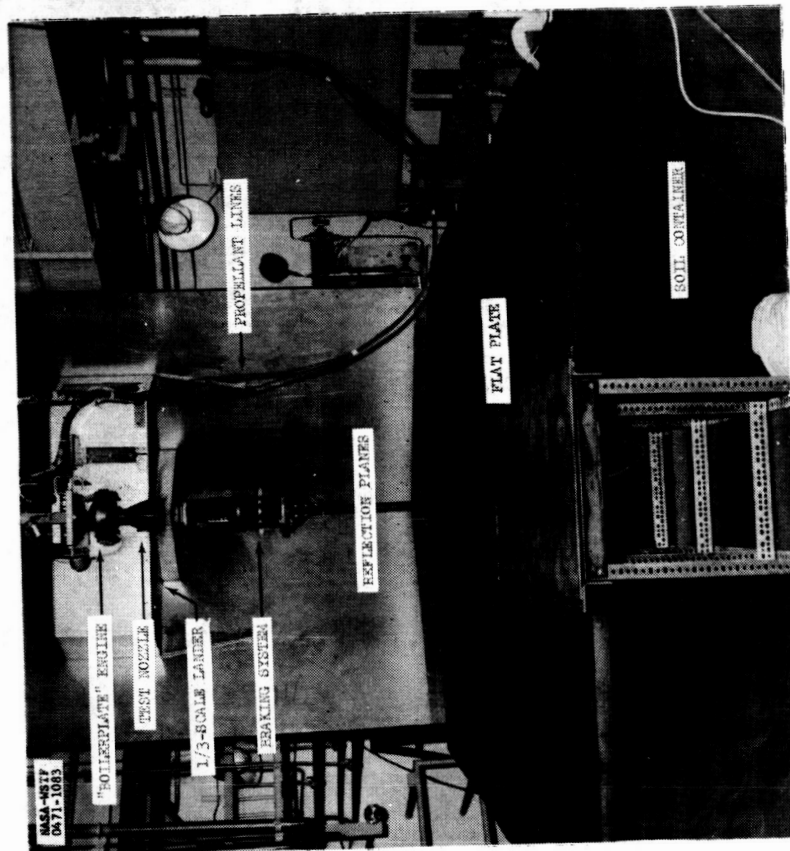


Figure 10.- Flat plate simulated landing surface instrumented with pressure gages and calorimeters.

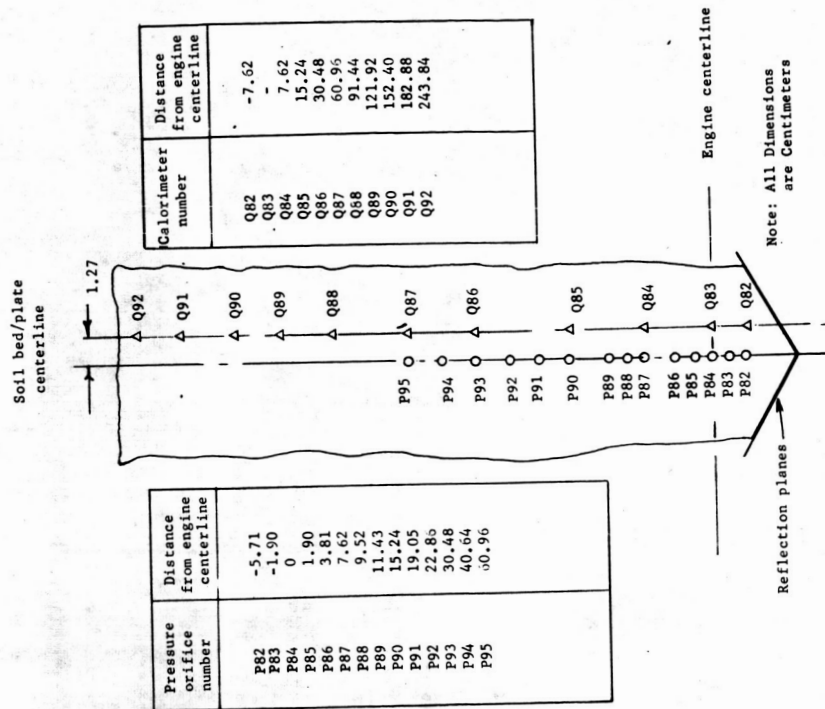


Figure 11.- Location of pressure orifices and calorimeters on flat plate impingement surface.

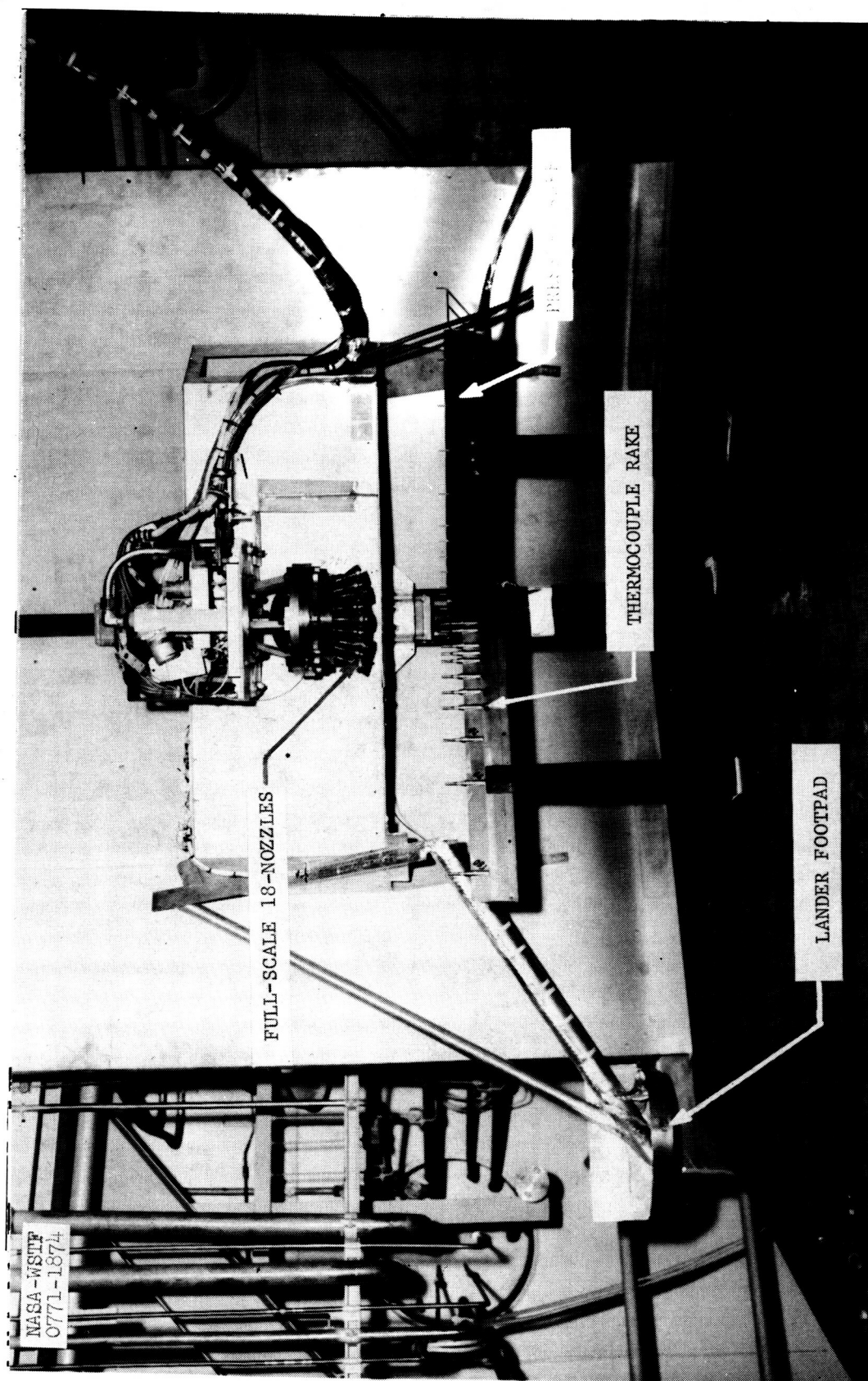


Figure 12.- WSTF Phase II pressure and temperature rake used to characterize flow.

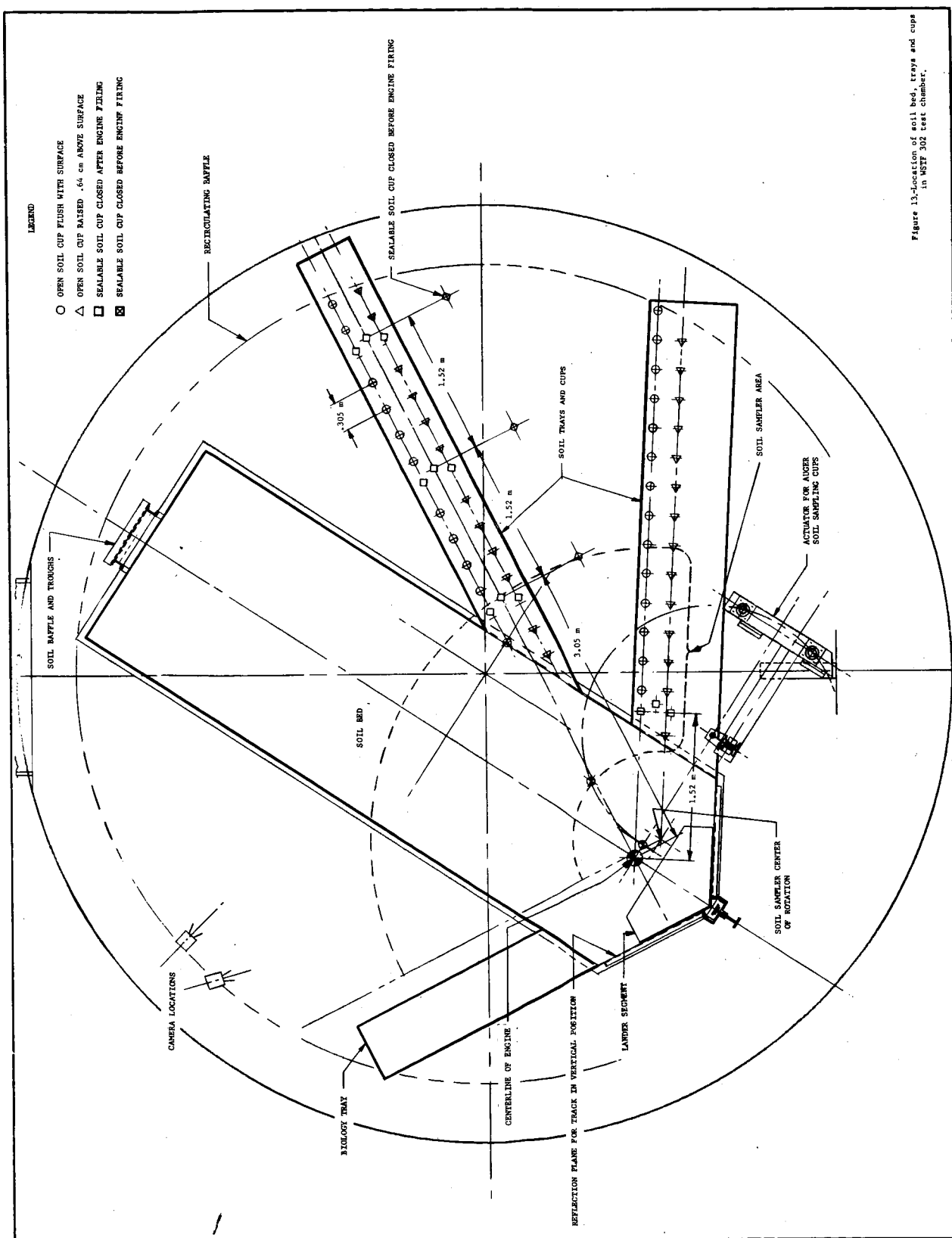


Figure 13-Location of soil bed, trays and cups in WSTF 302 test chamber.

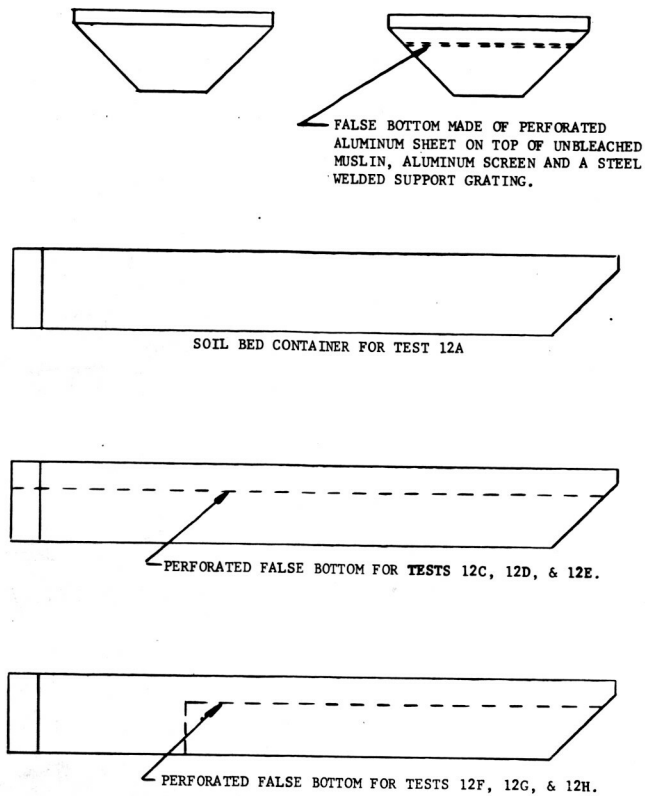


Figure 14.- Soil bed container configurations.

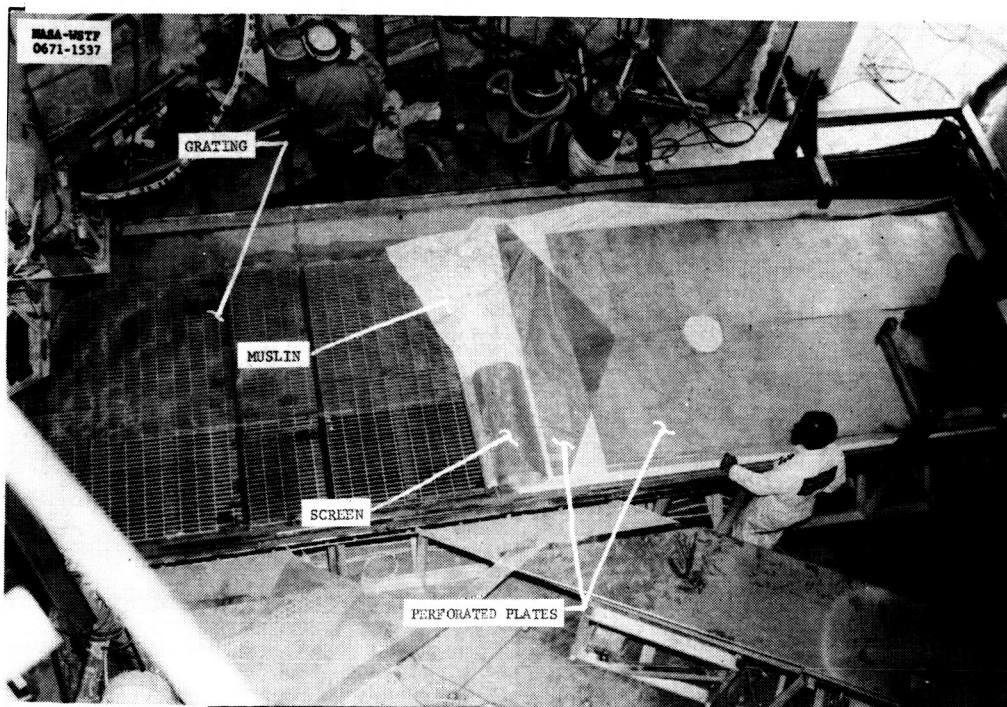
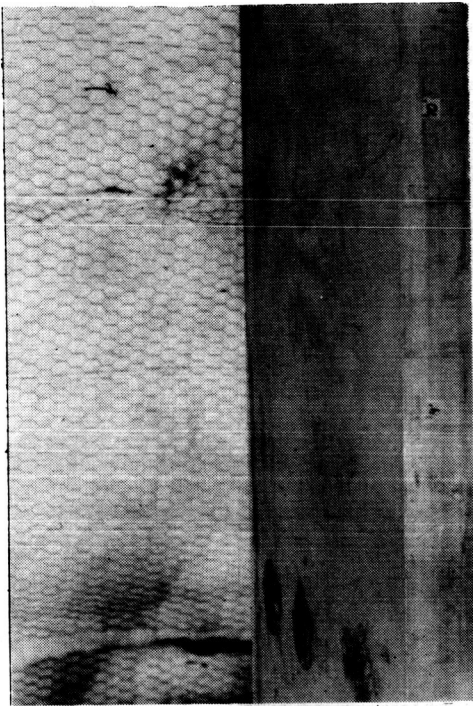


Figure 15.- Installation of permeable false bottom in soil bed.

Before engine firing



After engine firing

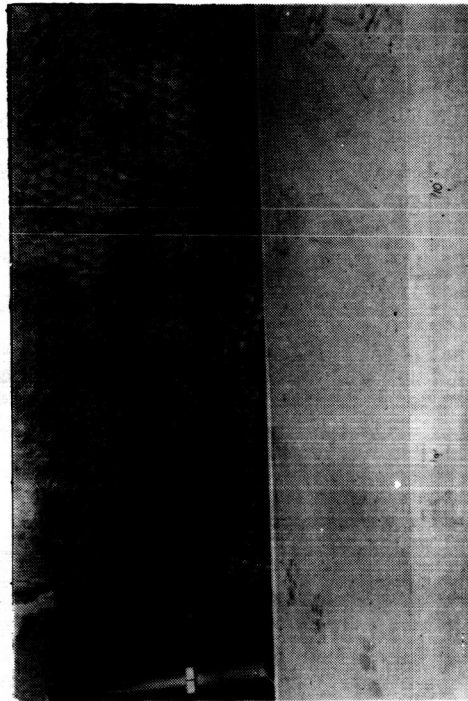


Figure 17.- View of recirculation baffles in WSTF test chamber.



Figure 16.- View of louvered baffle at end of soil bed.

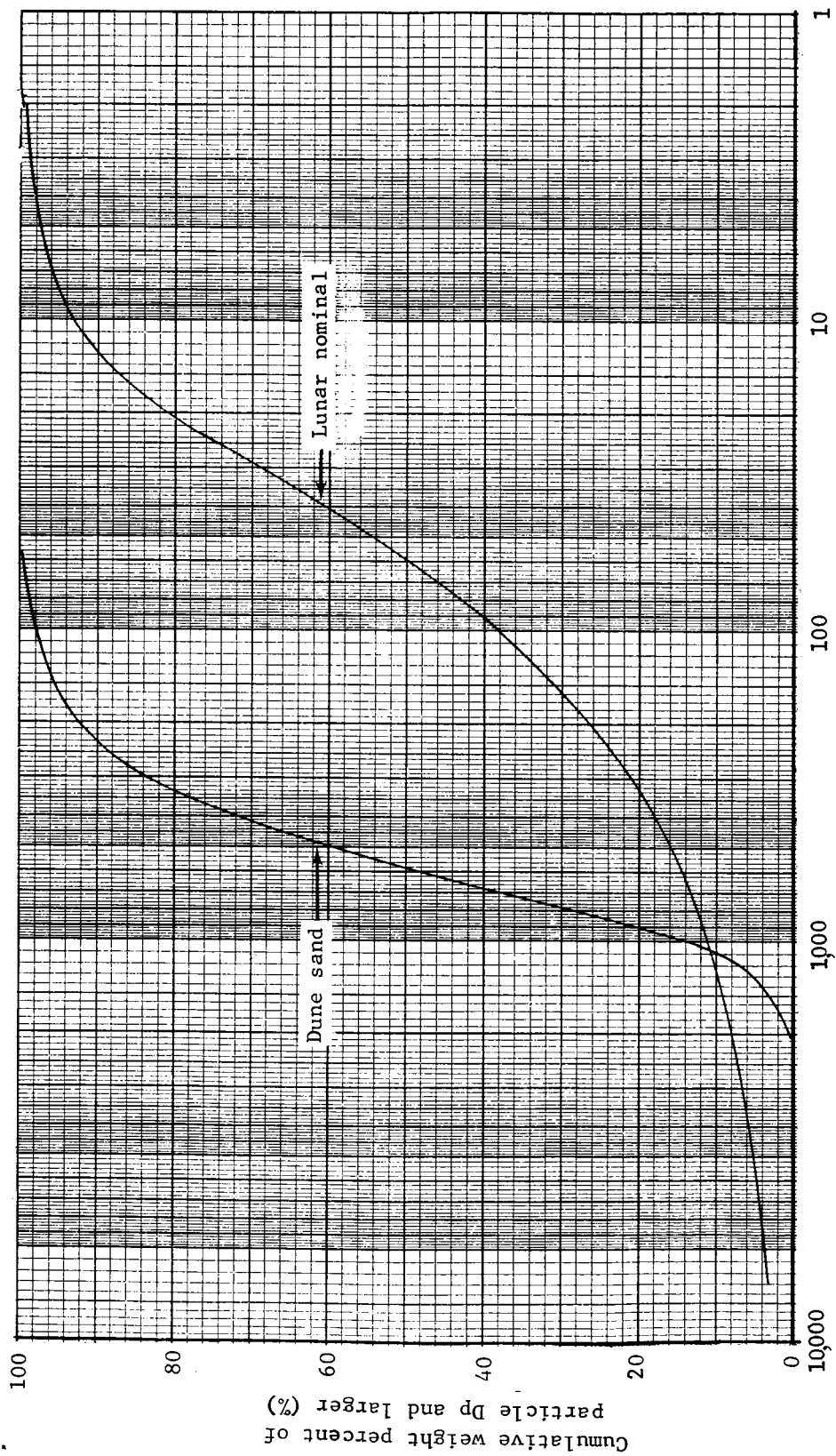


Figure 18.- Particle size distribution of soil models used in Phase II tests

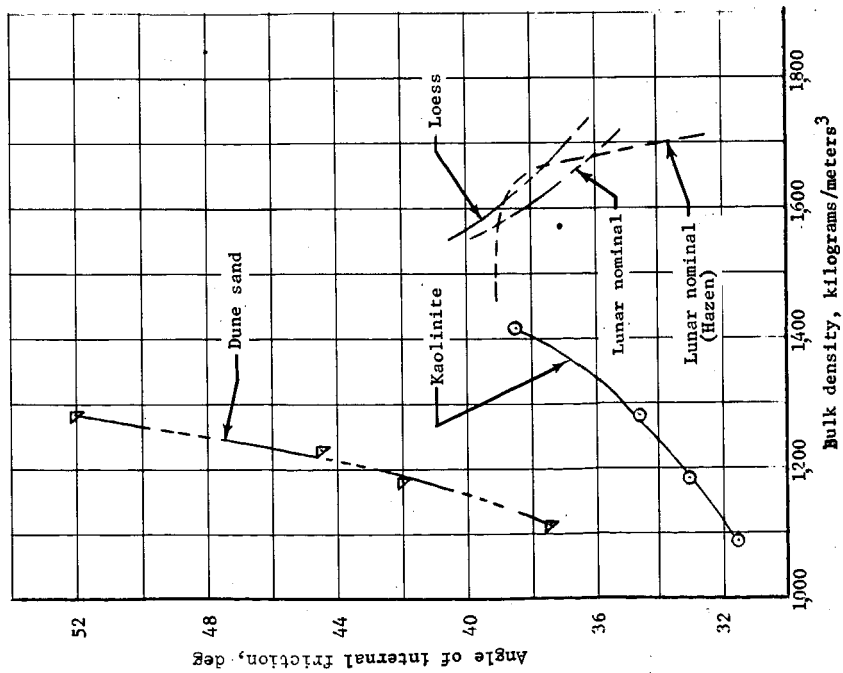


Figure 19.- Angle of internal friction of simulated Martian soils.

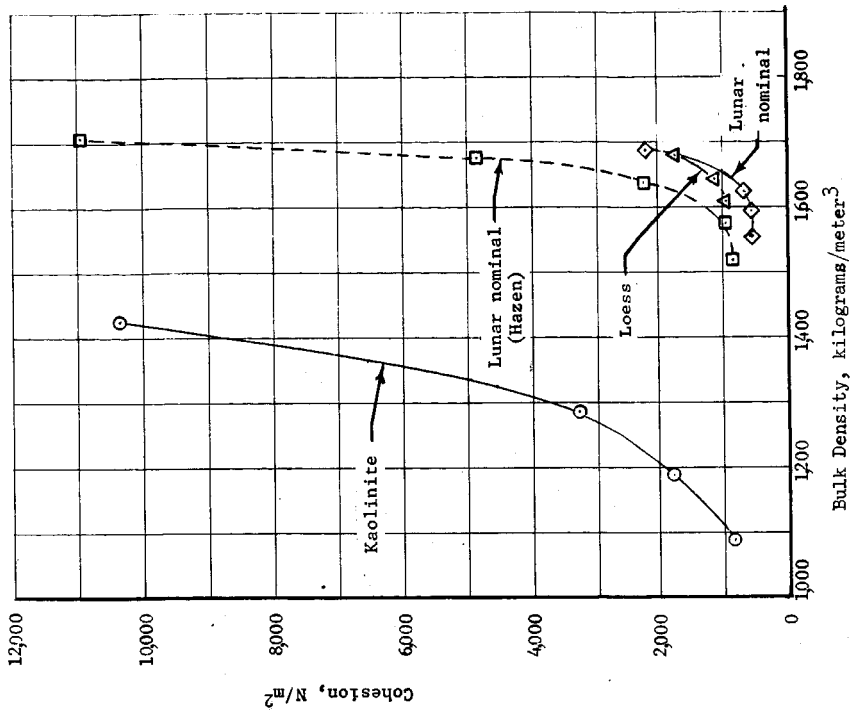
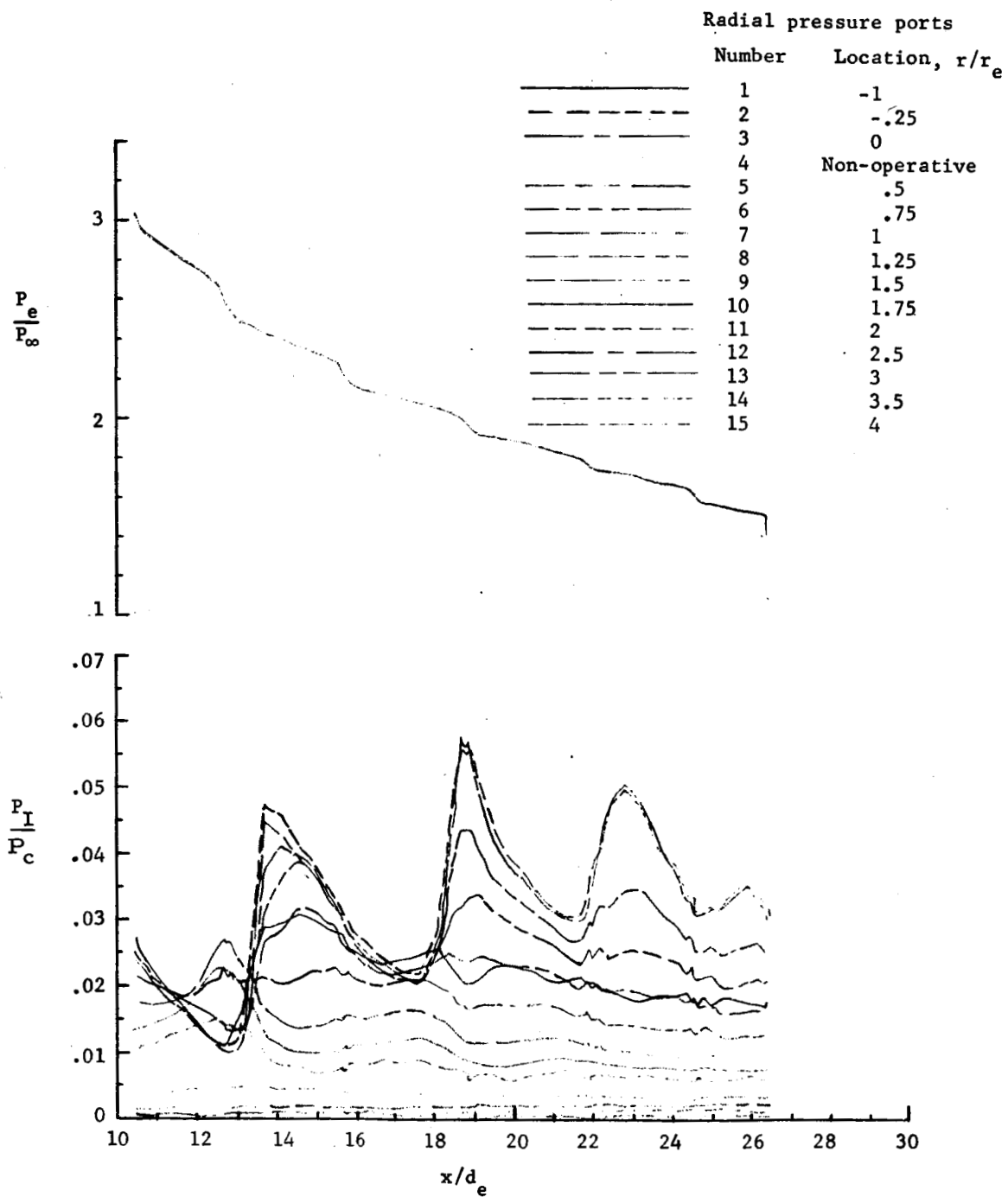
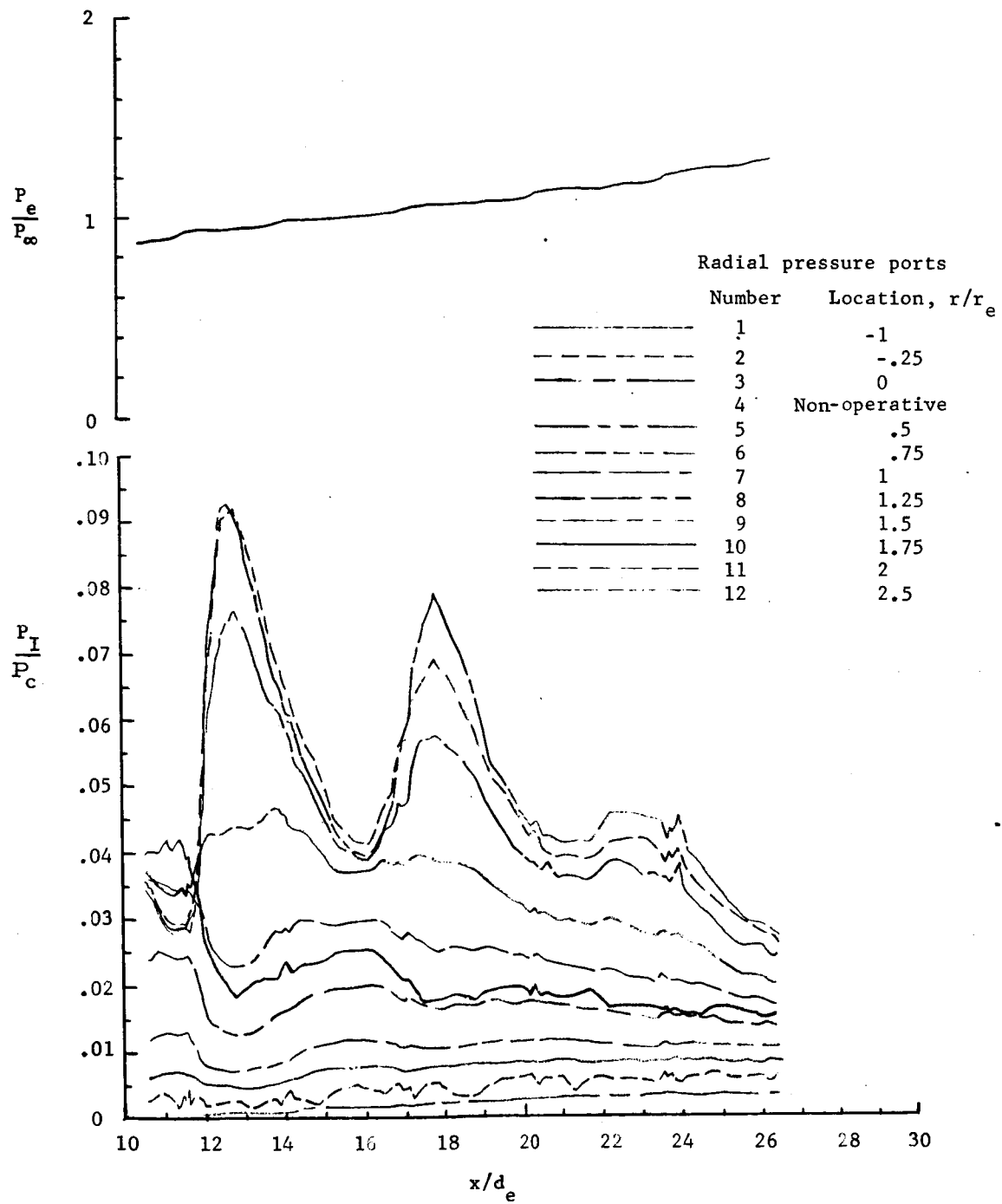


Figure 20.- Cohesion of simulated Martian soils.

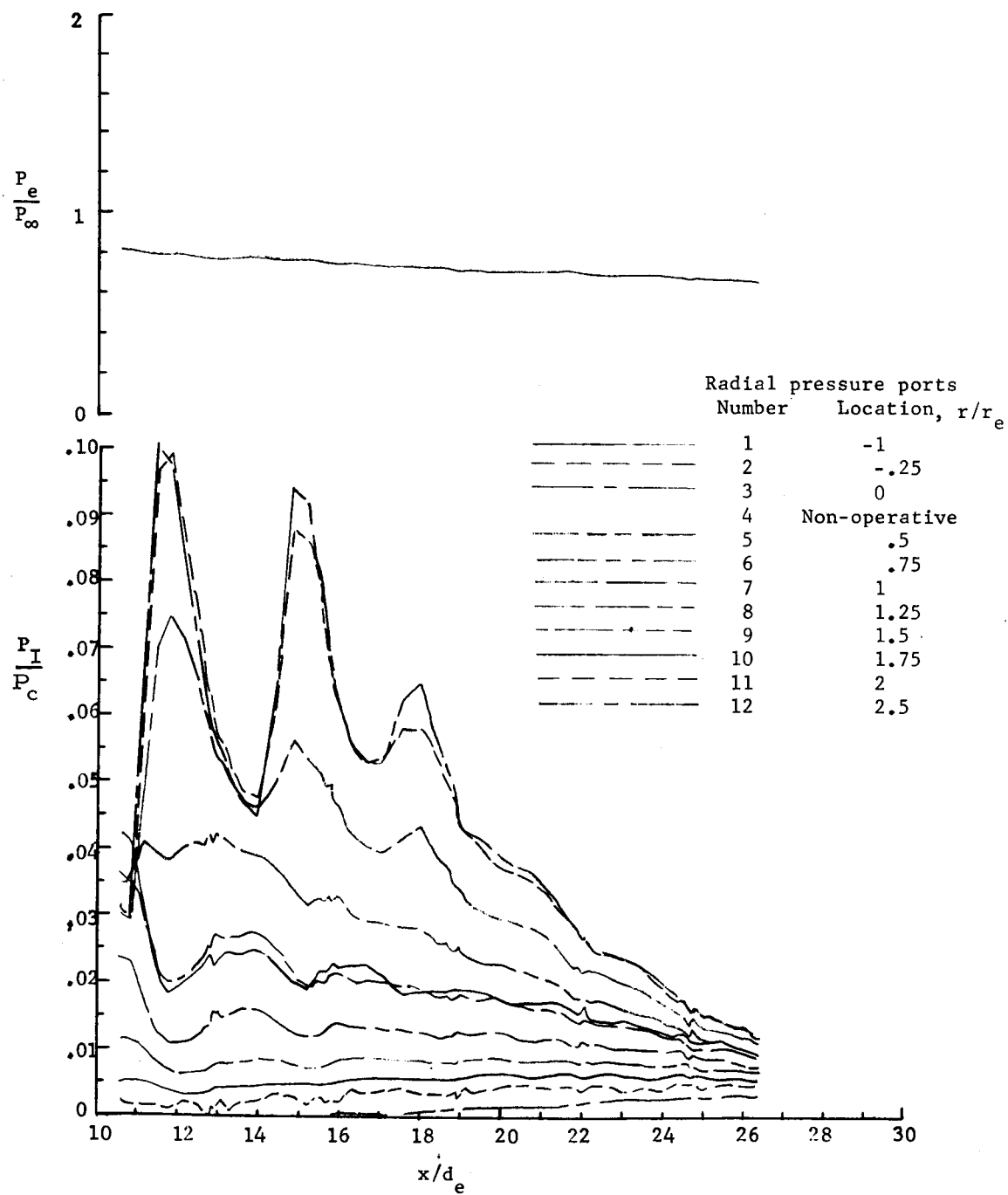


(a) Pass 1

Figure 21.- Axial variation of baseline nozzle impingement pressures, WSTF Phase IA.



(b) Pass 2



(c) Pass 3

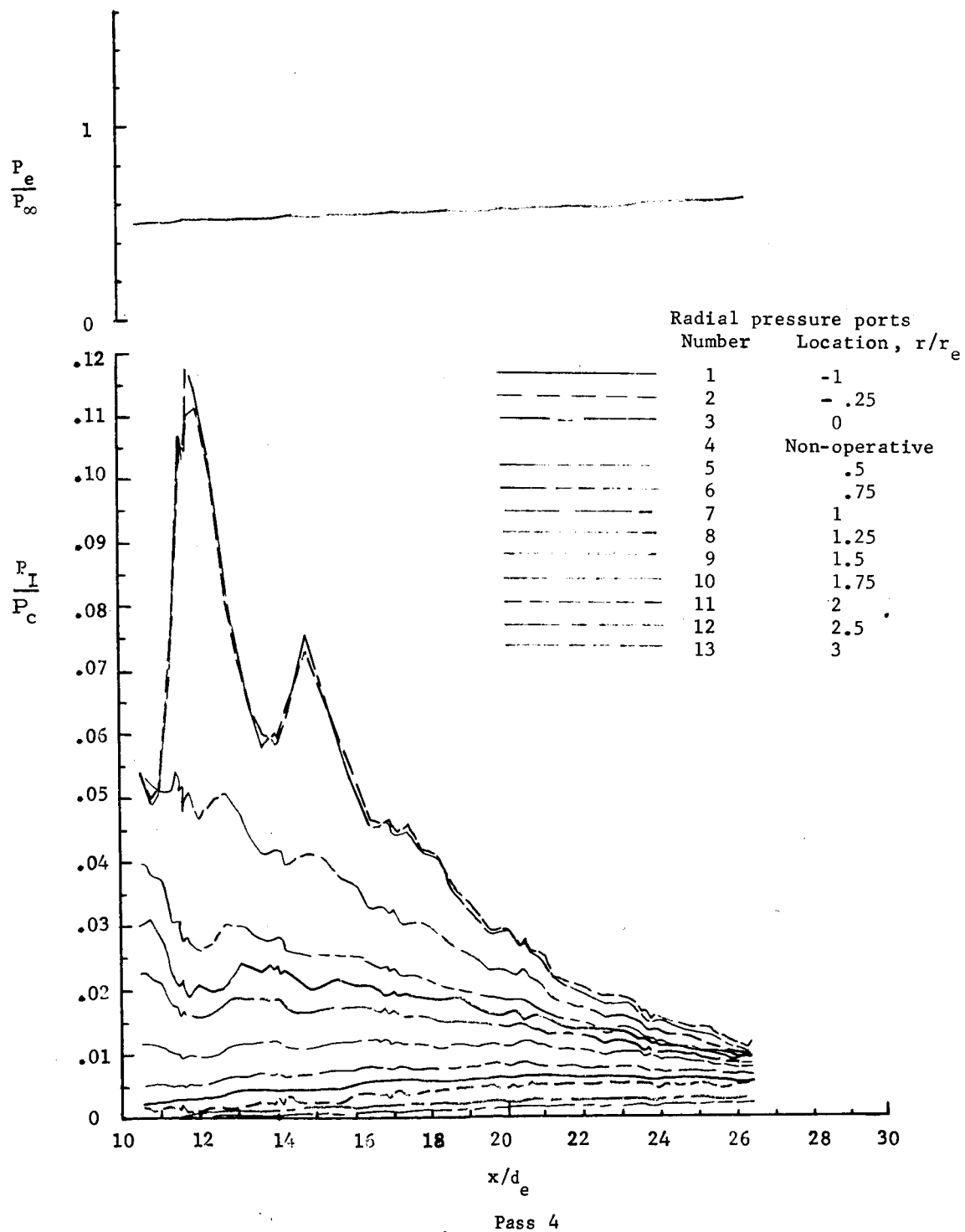
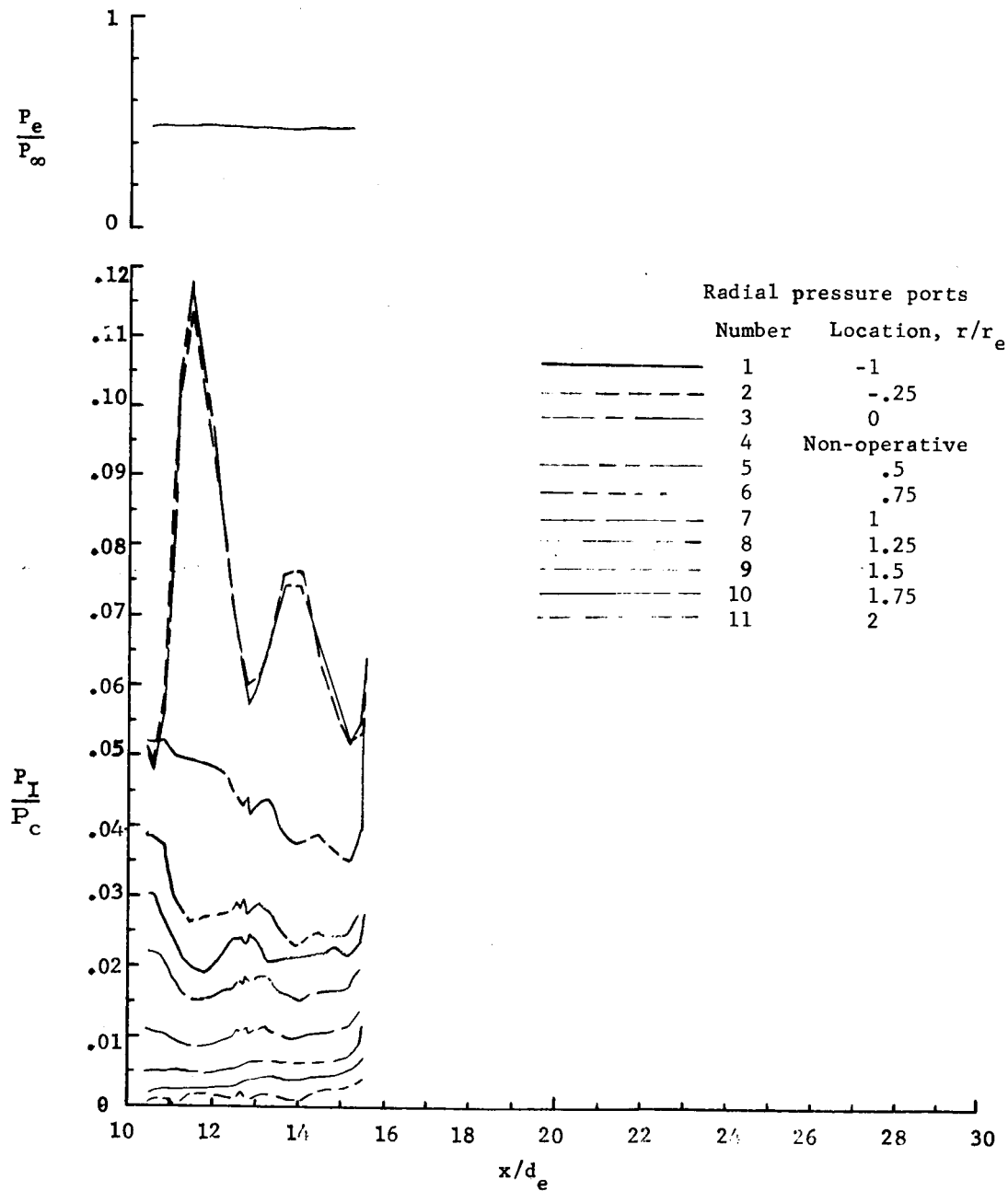


Figure 21.- Continued.



(e) Pass 5

Figure 21.- Concluded.

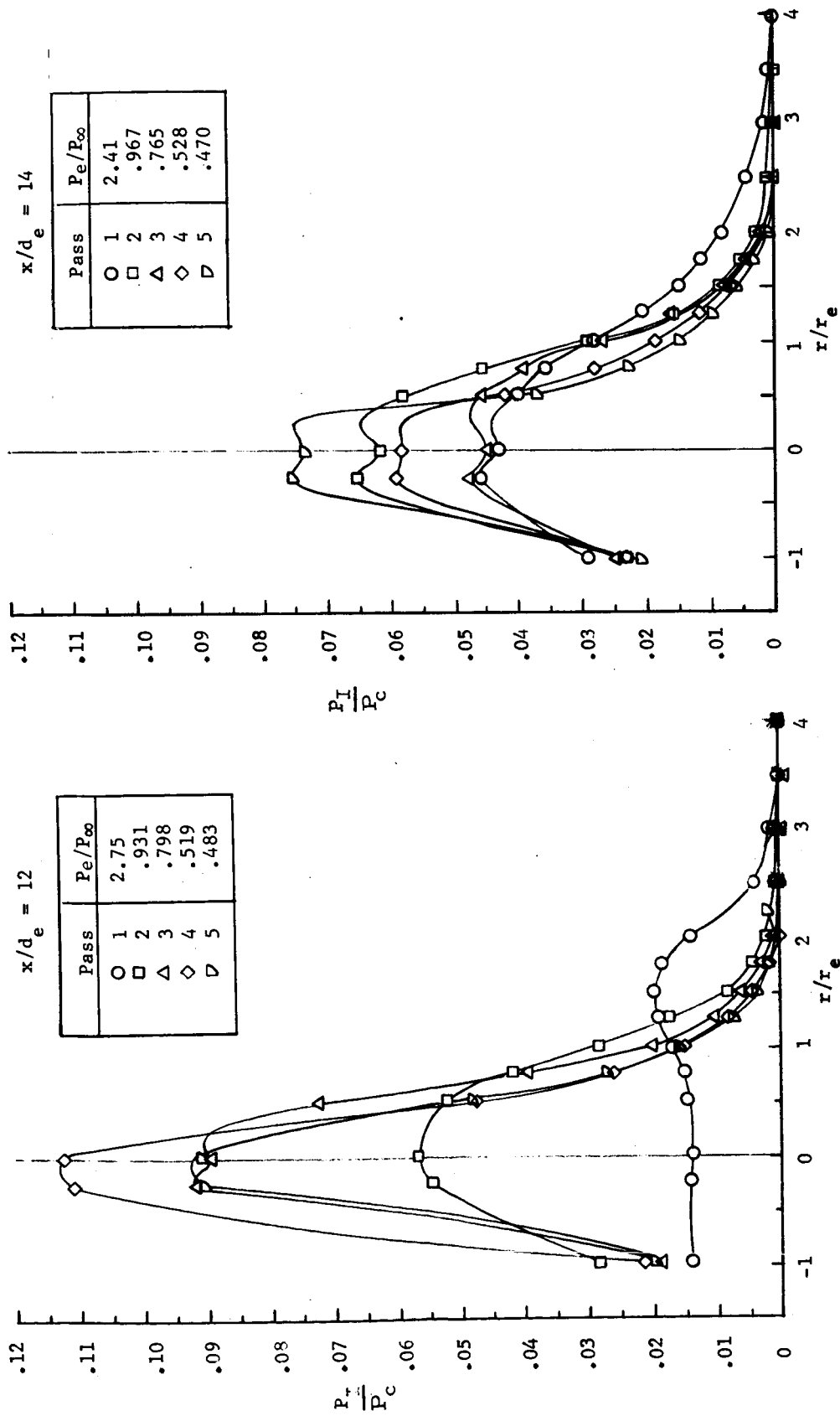


Figure 22.- Effect of pressure ratio on radial variation of baseline nozzle impingement pressures, WSTF Phase IA.

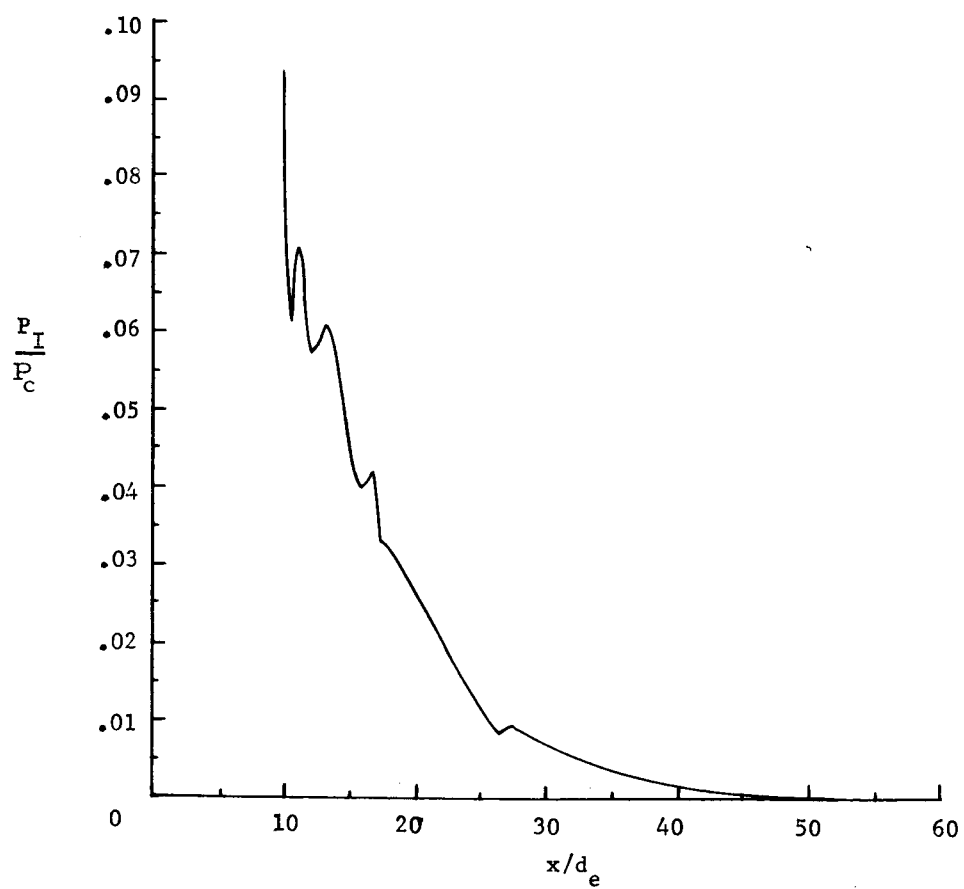


Figure 23.- Axial variation of baseline nozzle impingement pressures measured on engine centerline; WSTF Phase II, test 11.

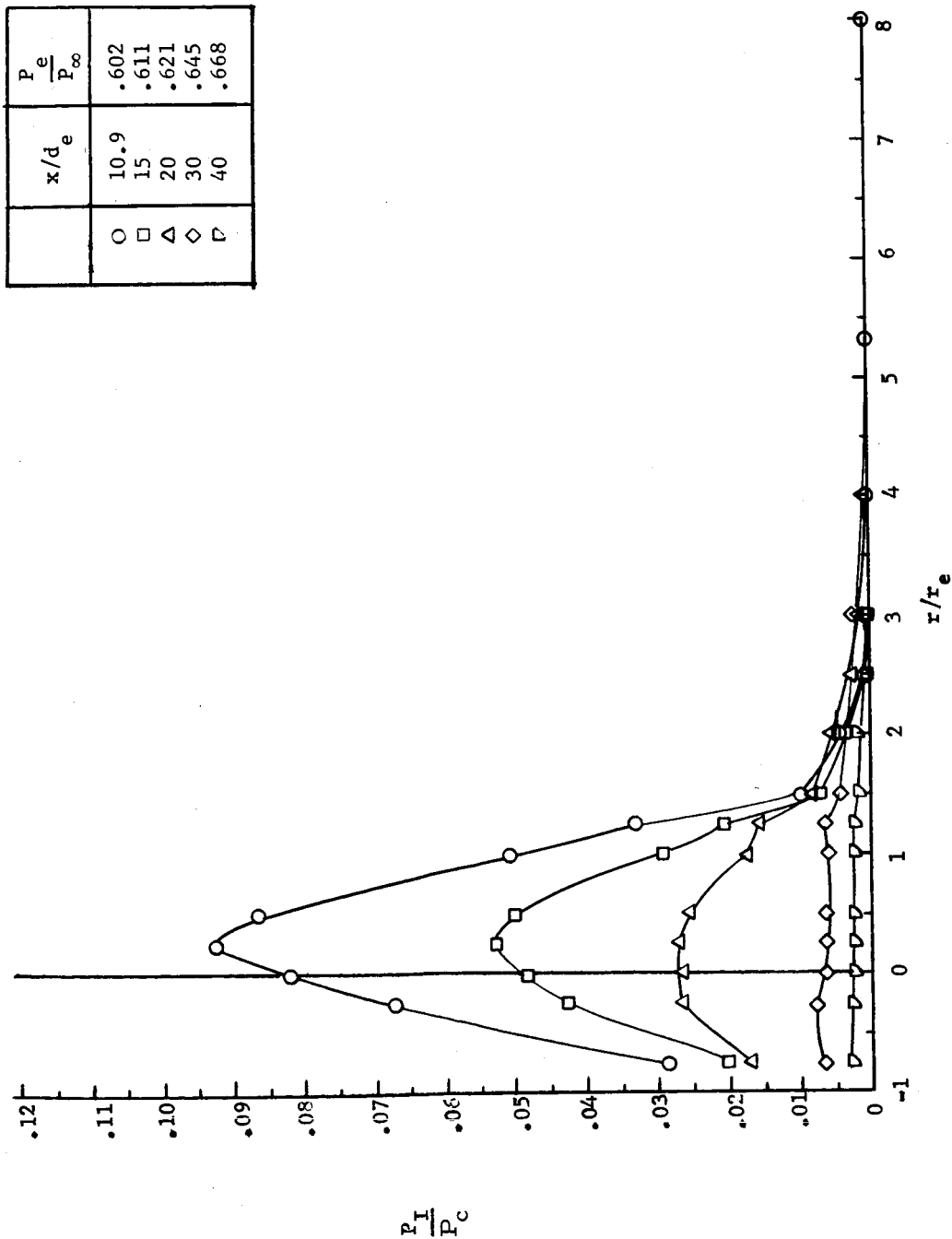


Figure 24.- Radial variation of baseline nozzle impingement pressures; WSTF Phase II, test 11.

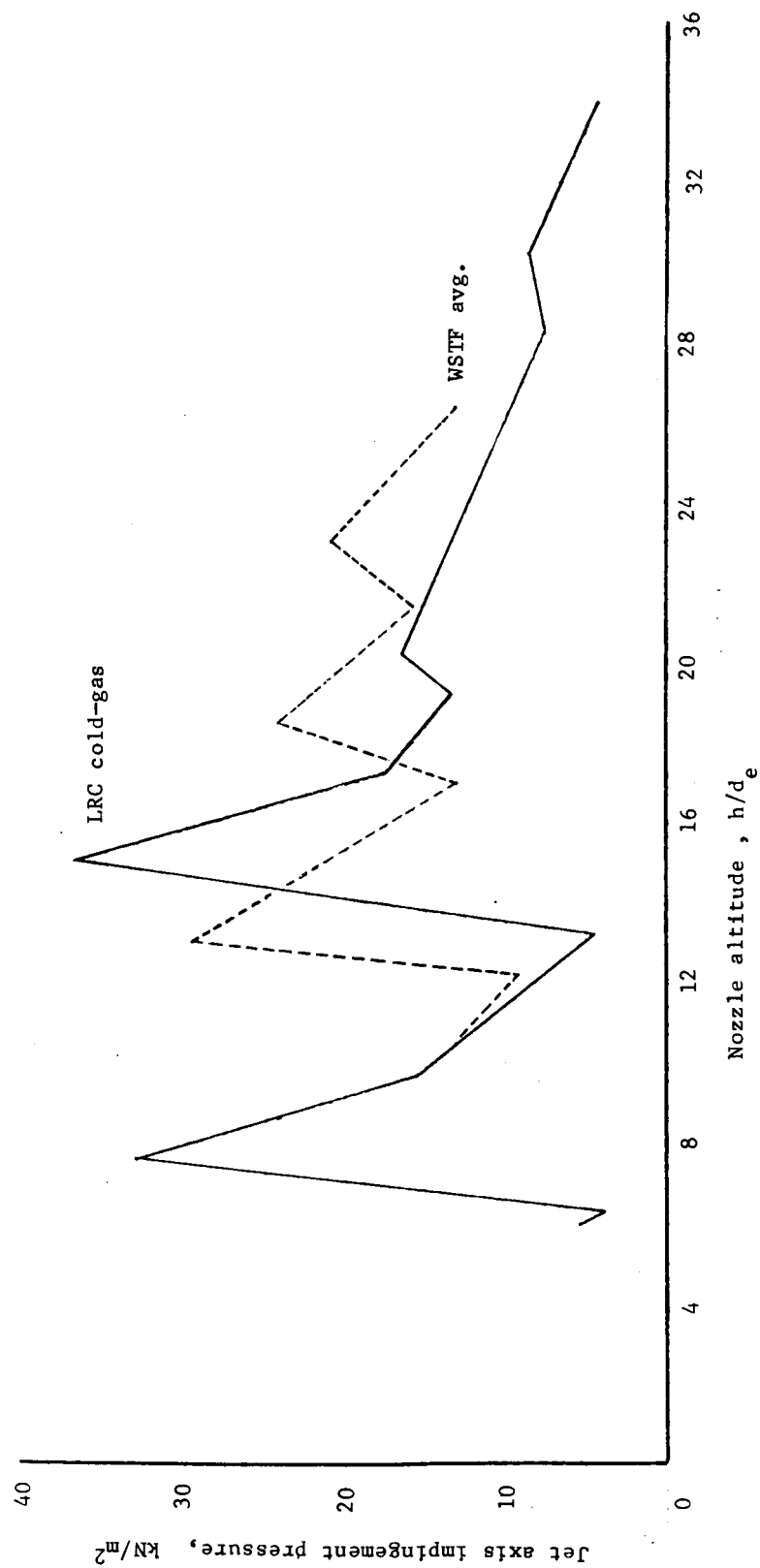


Figure 25.- Exhaust plume centerline impingement pressure versus altitude simulation using a one-sixth scale "cold-gas" nozzle.

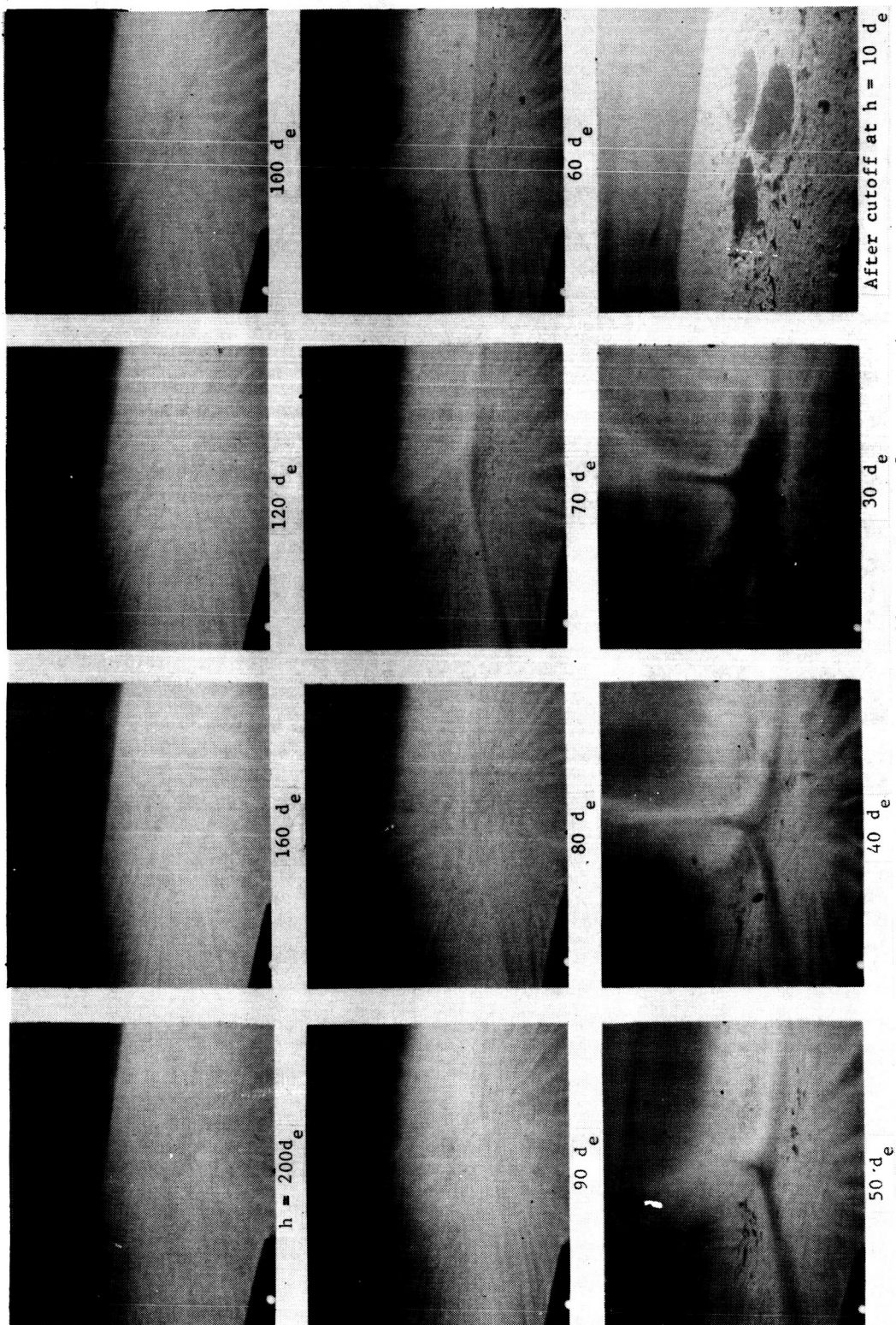


Figure 26.- Sequence of test photographs illustrating surface cratering on

lunar nominal soil with a one-sixth scale model lander having optimally expanded "cold-gas" nozzles: $\epsilon = 20$, $\gamma = 1.67$, $P_c = 800 \text{ kN/m}^2$, $P_{\infty} = 6.7 \rightarrow 9.3 \text{ mb}$, $V = 19.8 \text{ d}_e/\text{sec}$, $h = 240 \rightarrow 10 \text{ d}_e$.

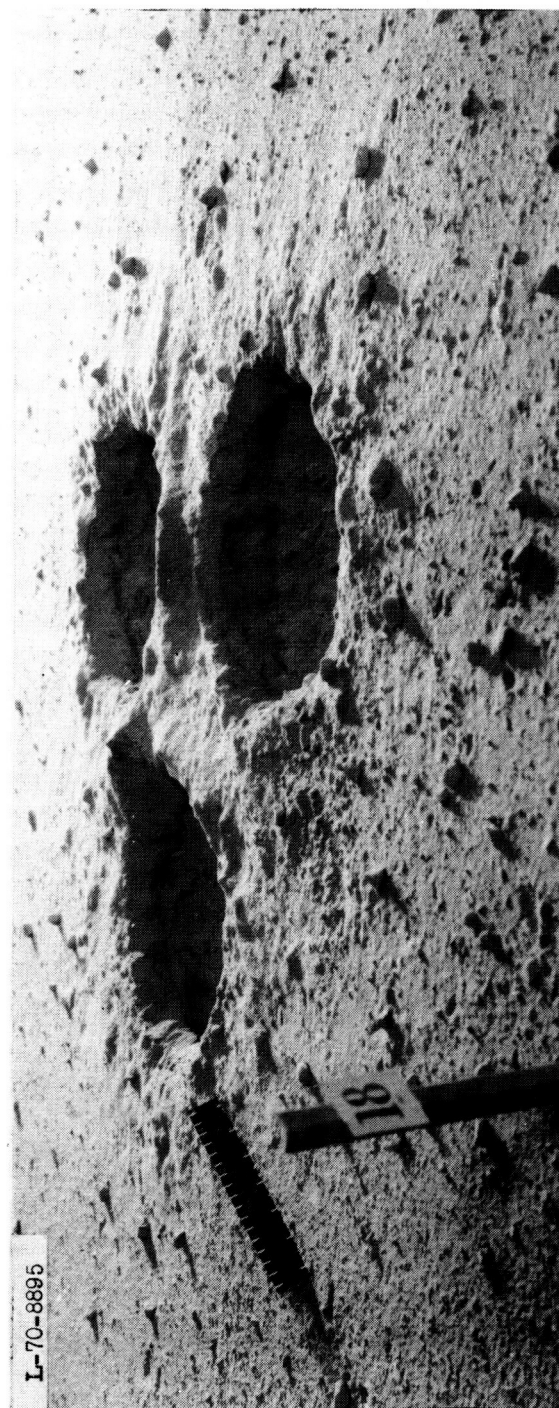
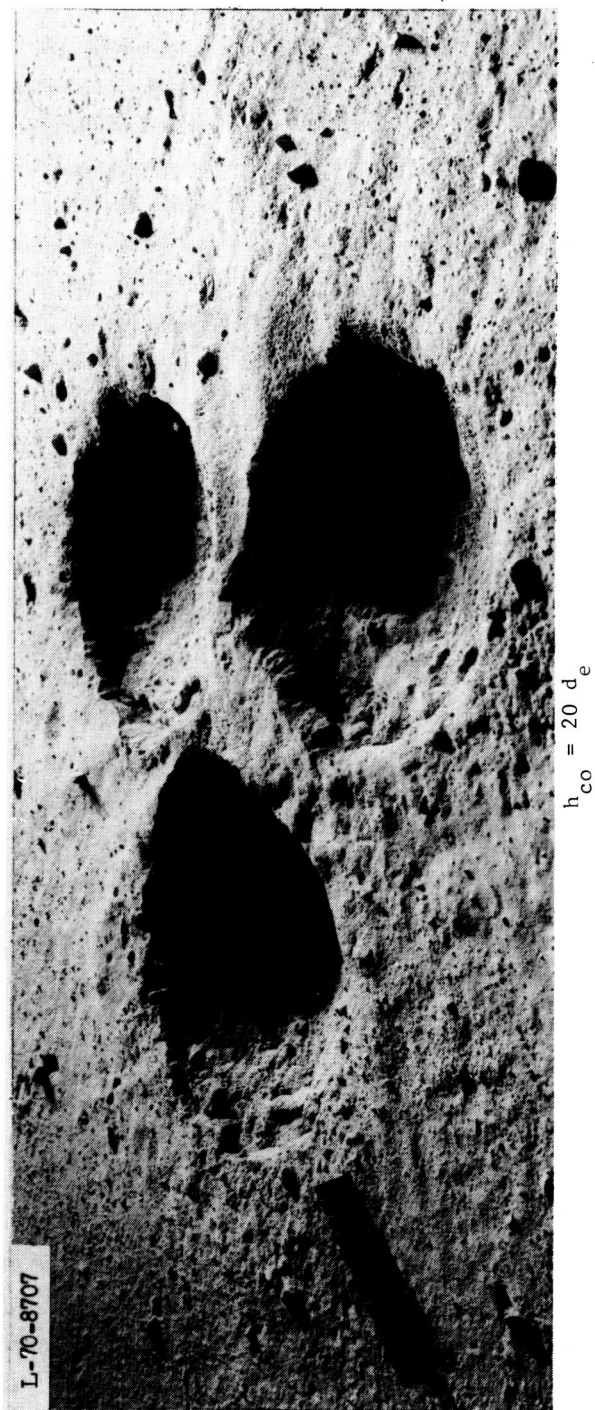


Figure 27.- Test photographs illustrating effect of cut-off altitude on surface cratering in lunar nominal soil with a one-sixth scale model lander having "cold-gas" nozzles; $\epsilon = 20$, $\gamma = 1.67$, $V = 22.8 d_e / \text{sec}$, $P_c \approx 730 \text{ kN/m}^2$, $P_\infty = 6.6 \rightarrow 9.2 \text{ mb}$, $h_i = 240 d_e$.

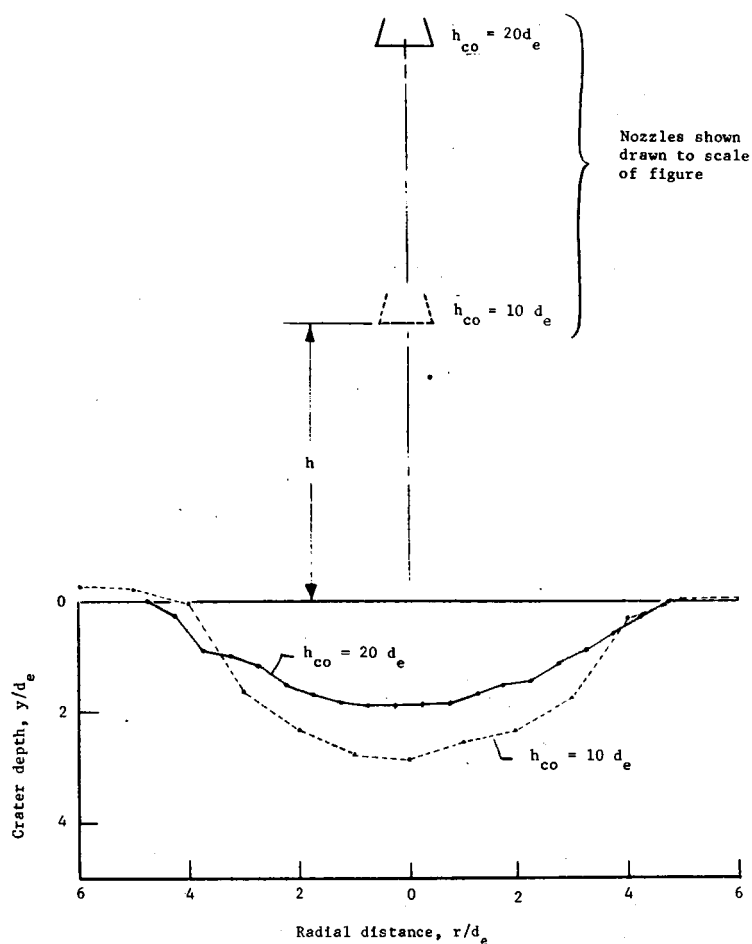


Figure 28.- Crater profiles in lunar nominal soil showing effect of thrust cutoff altitude using one-sixth scale "cold-gas" nozzles;
 $\epsilon = 20$, $\gamma = 1.67$, $P_c \approx 730 \text{ kN/m}^2$, $P_\infty = 6.6 \rightarrow 7.9 \text{ mb}$,
 $V = 22.8 d_e/\text{sec}$, $h_i = 240 d_e$.

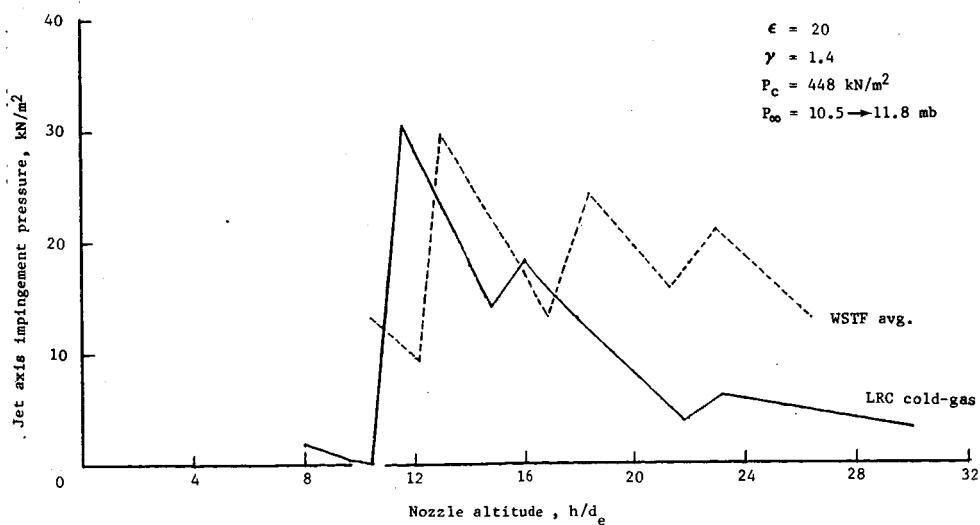
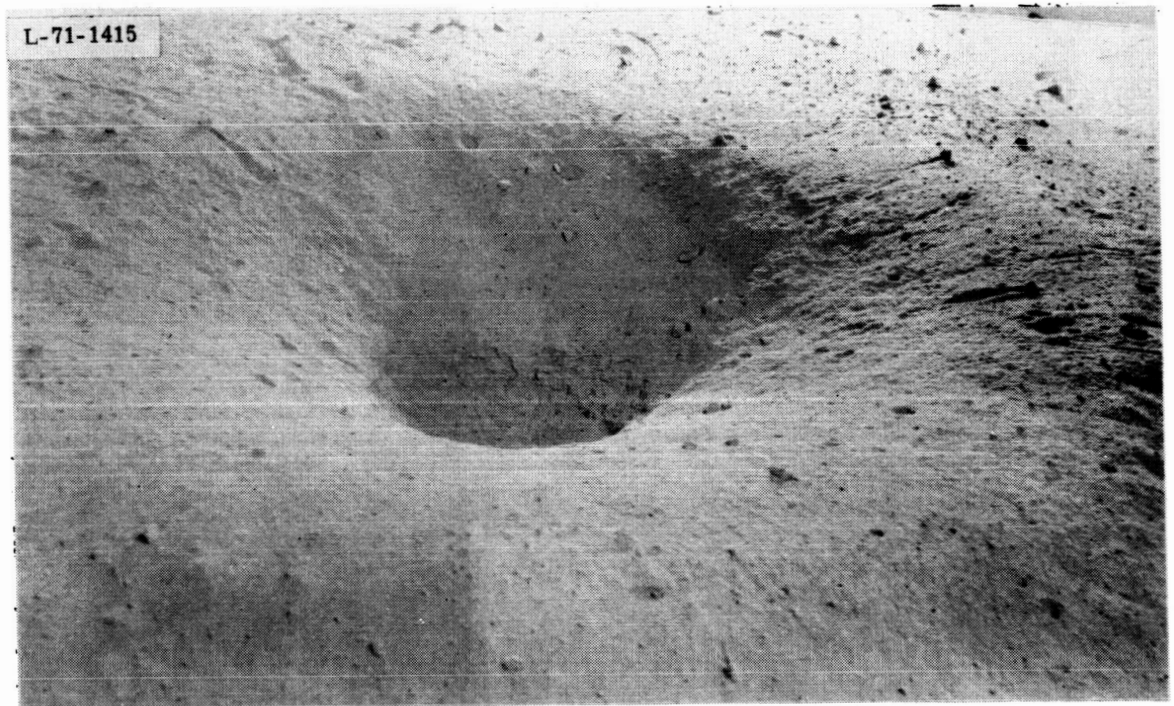
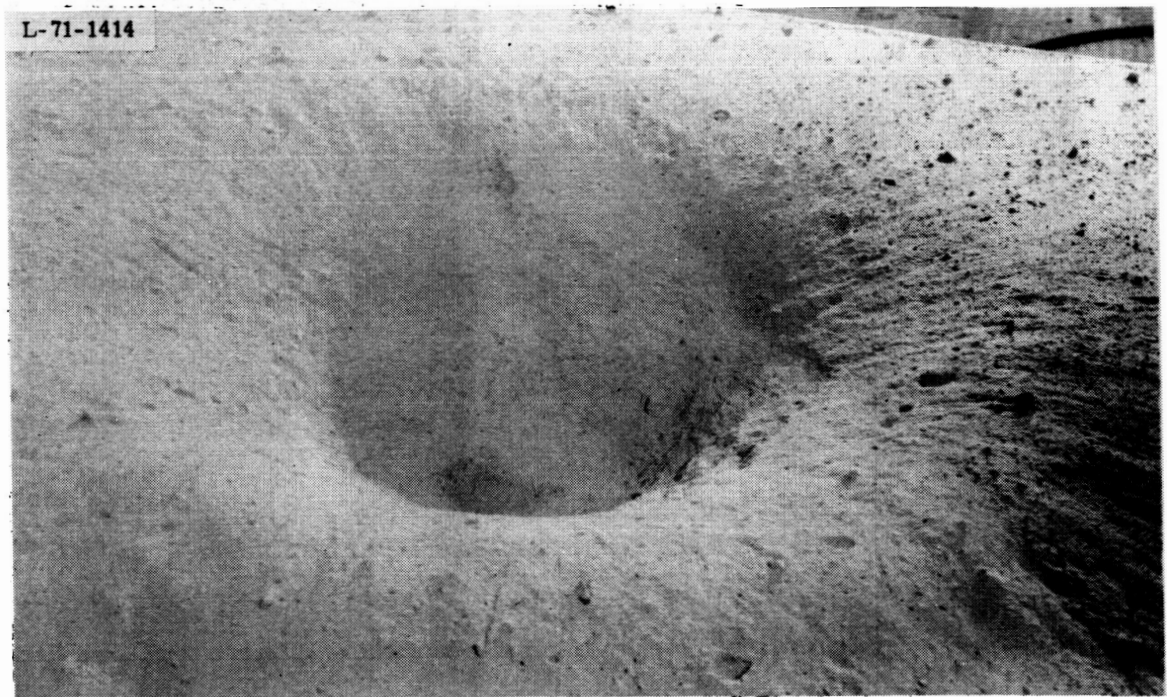


Figure 29.- Exhaust plume centerline impingement pressure versus altitude simulation using a full-scale "cold-gas" nozzle.



$V = 2.8 \text{ m/sec}$



$V = 1.2 \text{ m/sec}$

Figure 30.- Test photographs illustrating effect of descent velocity on surface cratering in lunar nominal soil with a full-scale "cold-gas" nozzle; $\epsilon = 20$, $\gamma = 1.4$, $P_c \approx 450 \text{ kN/m}^2$, $P_\infty \approx 12 \text{ mb}$, $h = 11.8 \rightarrow 3.05 \text{ m}$.

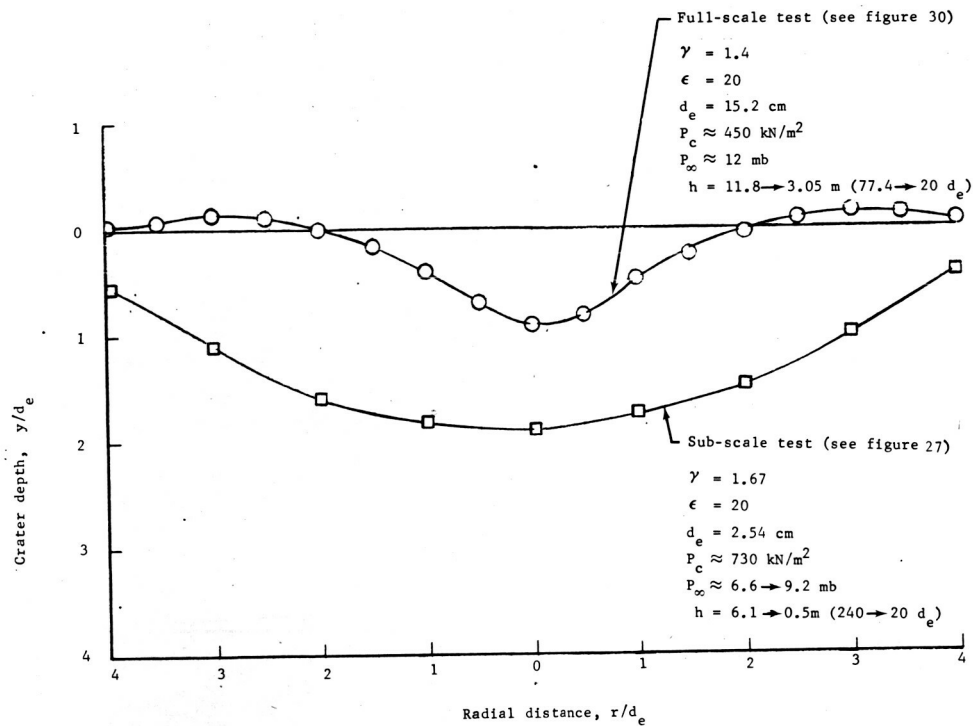


Figure 31.- Comparison of the crater profiles from full-scale and sub-scale "cold-gas" nozzle tests on lunar nominal soil for similar test conditions.



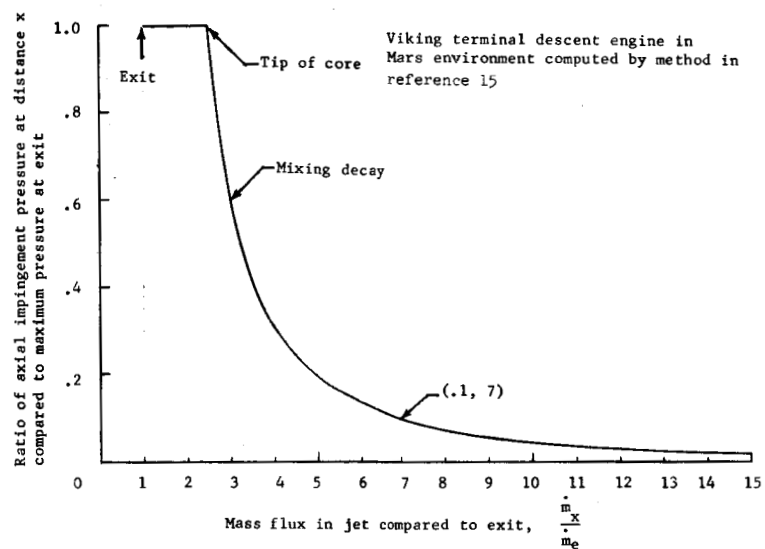


Figure 33.-Relation between jet entrainment and impingement pressure reduction.

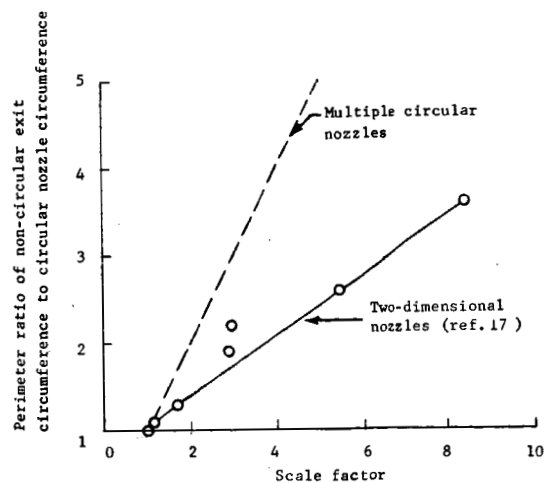


Figure 34.- Jet flow scale factor as a function of perimeter ratio.

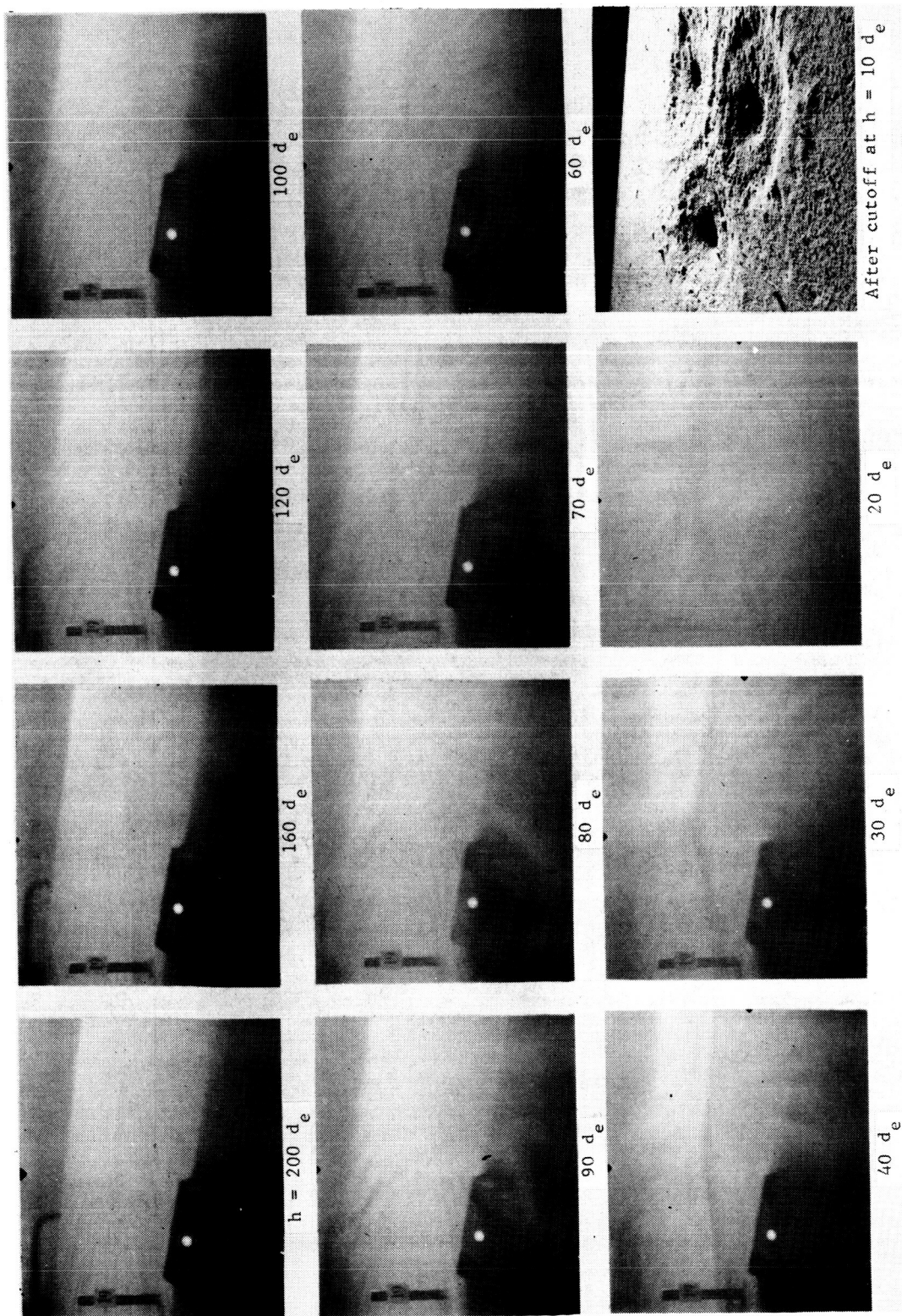


Figure 35.- Sequence of test photographs illustrating surface cratering on lunar nominal soil with a one-sixth scale model lander having sonic "cold-gas" nozzles; $\epsilon = 1$, $\gamma = 1.67$, $P_c = 765 \text{ kN/m}^2$, $P_\infty = 6.6 \rightarrow 9.3 \text{ mb}$, $V = 23.1 \text{ d}_e/\text{sec}$, $h = 240 \rightarrow 10 \text{ d}_e$.

ϵ	P_c , kN/m ²	Thrust, N
1	573	662
3	504	699

* Note: The nozzle altitude is measured with the $\epsilon = 20$ nozzle in place, in terms of the $\epsilon = 20$ nozzle - exit diameter.

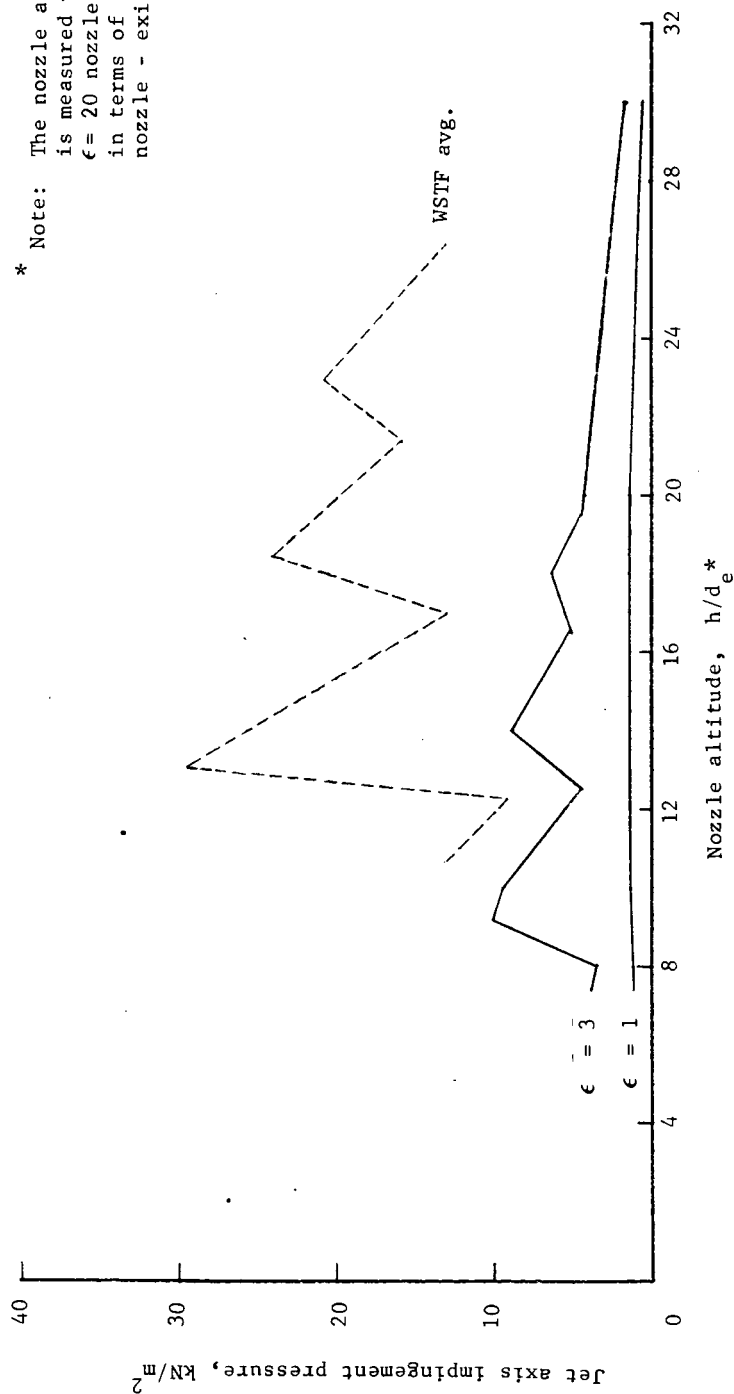
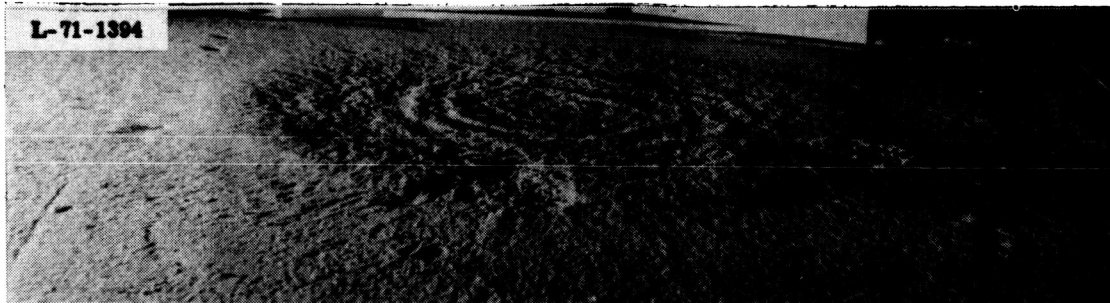
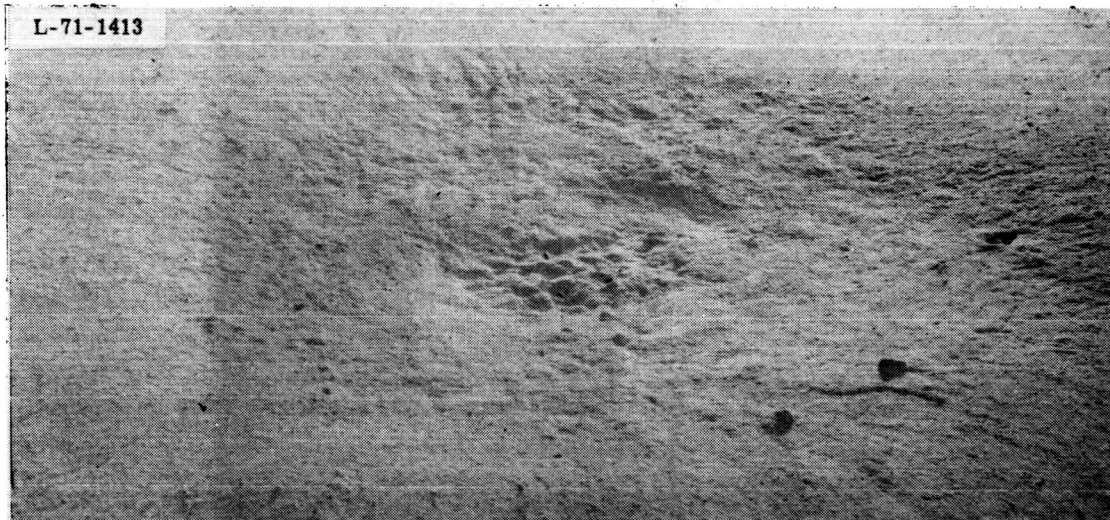


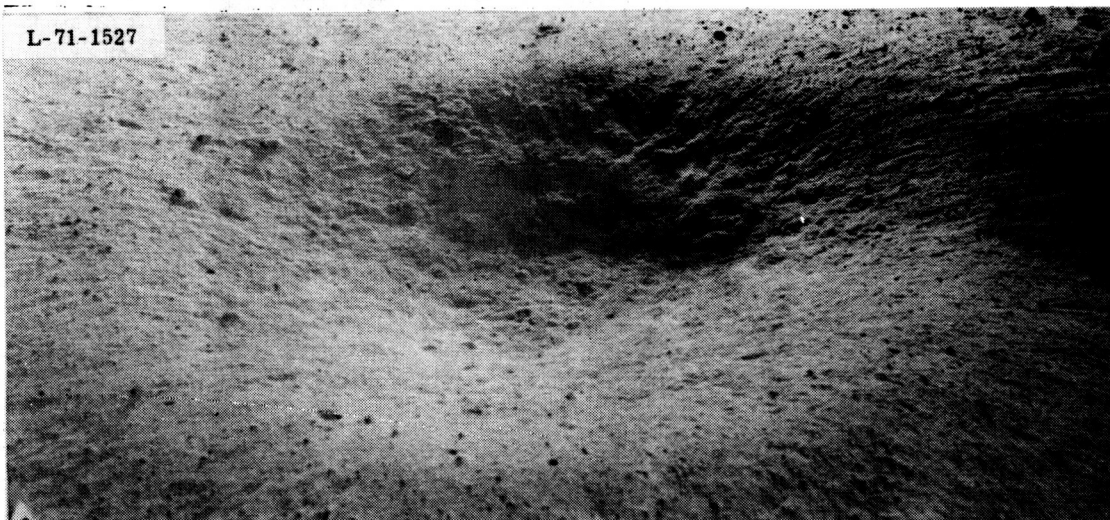
Figure 36.- Effect of nozzle area ratio on jet axis impingement pressure for full-scale "cold-gas" nozzles; $\gamma = 1.4$, $p_\infty = 10.5 \rightarrow 13.2$ mb.



Area ratio = 1 nozzle ($P_c = 555 \text{ kN/m}^2$)

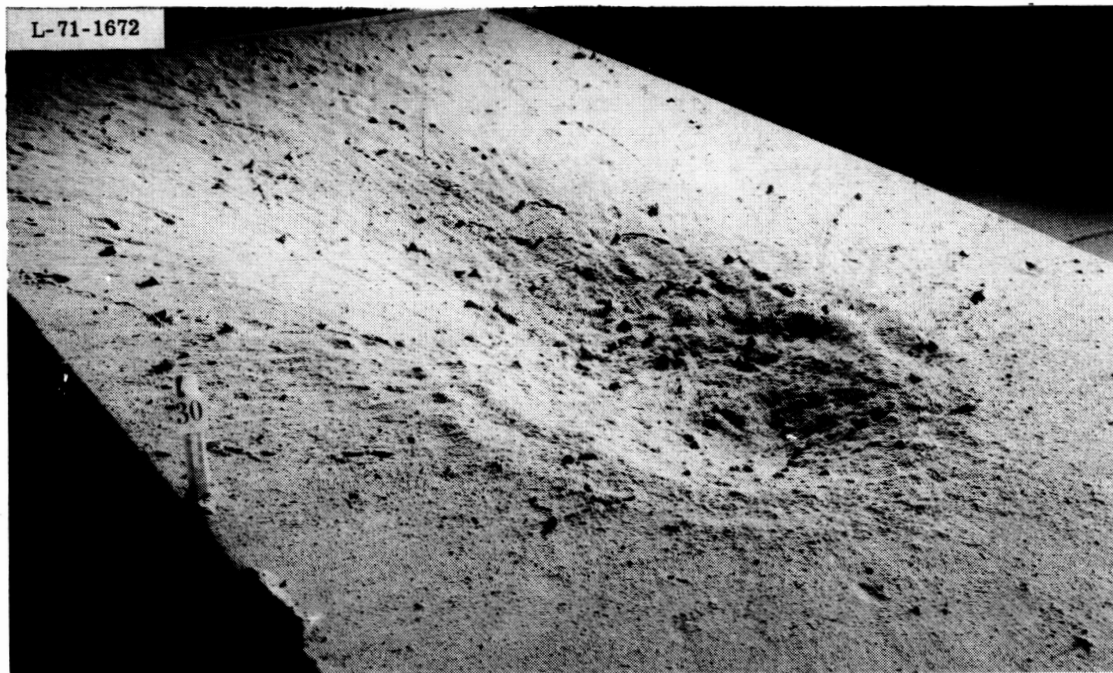


Area ratio = 2 nozzle ($P_c = 483 \text{ kN/m}^2$)

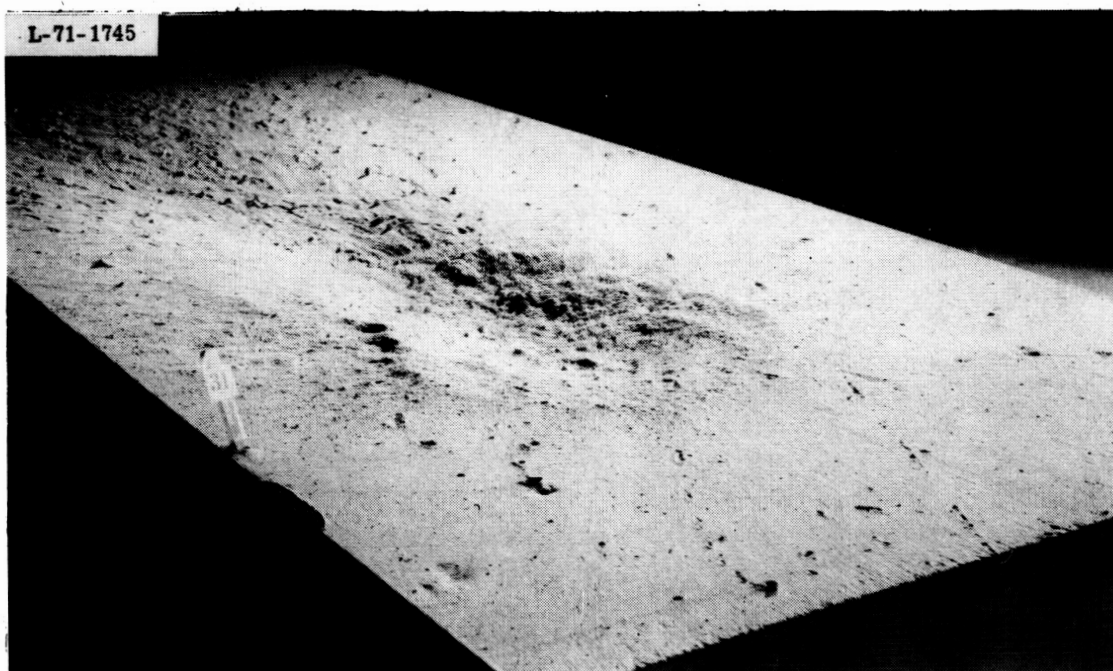


Area ratio = 3 nozzle ($P_c = 483 \text{ kN/m}^2$)

Figure 37.- Test photographs illustrating effect of nozzle area ratio on surface cratering on lunar nominal soil for full-scale "cold-gas" nozzles; $\gamma = 1.4$, $P_\infty \approx 12 \text{ mb}$, $h = 11.8 \rightarrow 1.5 \text{ m}$, $V \approx 2.7 \text{ m/sec}$.



Area ratio = 7 nozzle canted 15°



Area ratio = 20 nozzle canted 20°

Figure 38.- Test photographs illustrating effect of nozzle canting for a vertical descent on surface cratering in lunar nominal soil with a full-scale "cold-gas" nozzle; $\gamma = 1.4$, $P_c \approx 445 \text{ kN/m}^2$, $P_\infty \approx 11.5 \text{ mb}$, $V \approx 2.9 \text{ m/sec}$, $h = 11.8 \rightarrow 1.5 \text{ m}$.

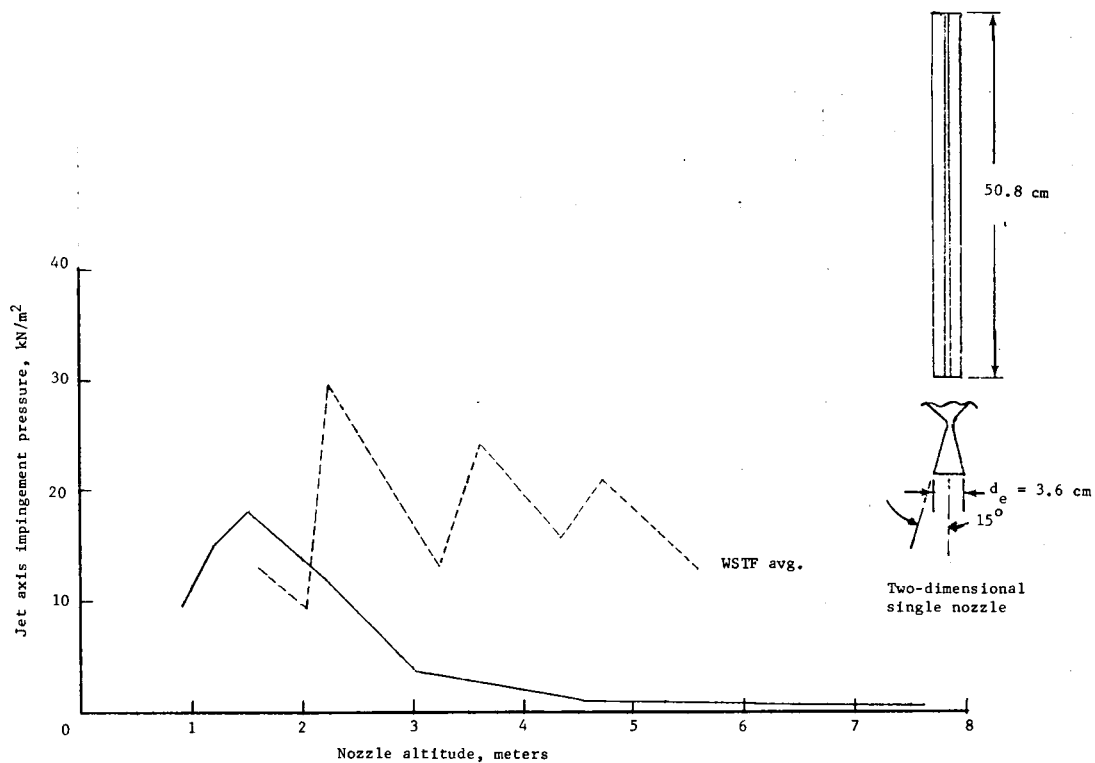


Figure 39.- Variation of jet axis impingement pressure with altitude for a full-scale 2-D "cold-gas" nozzle; $\epsilon = 20$, $\gamma = 1.4$, $P_c = 460$ kN/m², $P_\infty = 6.8 \rightarrow 7.9$ mb.

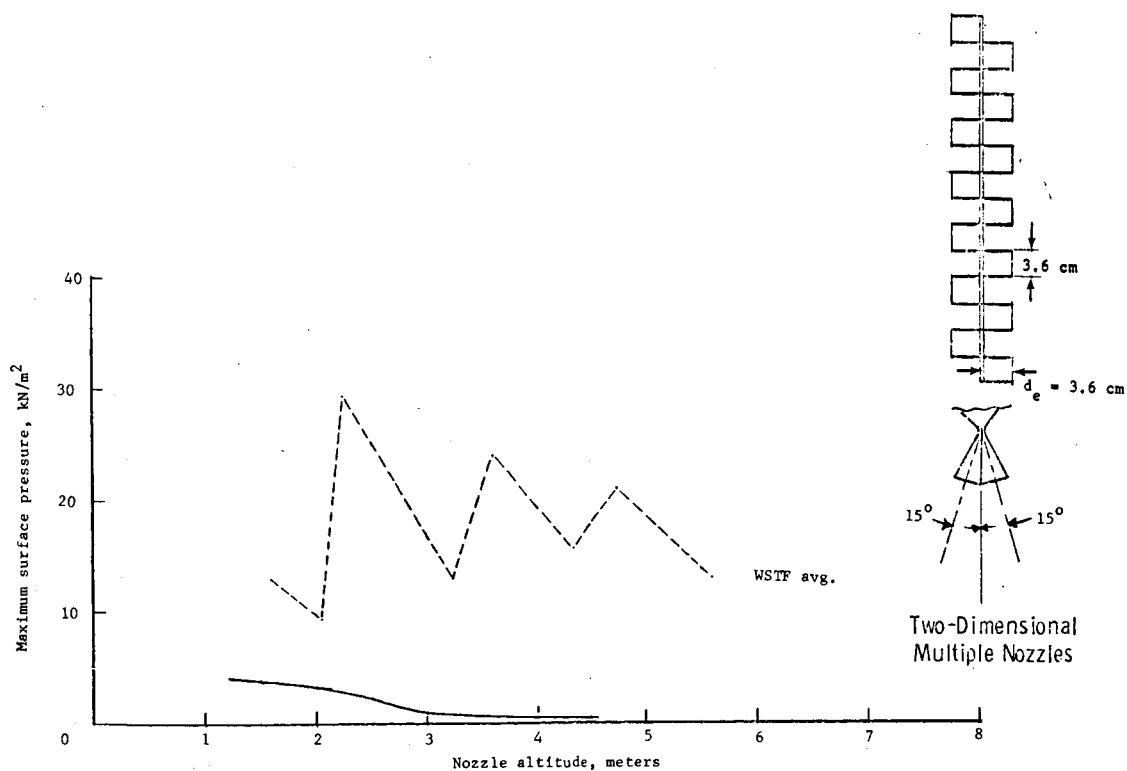
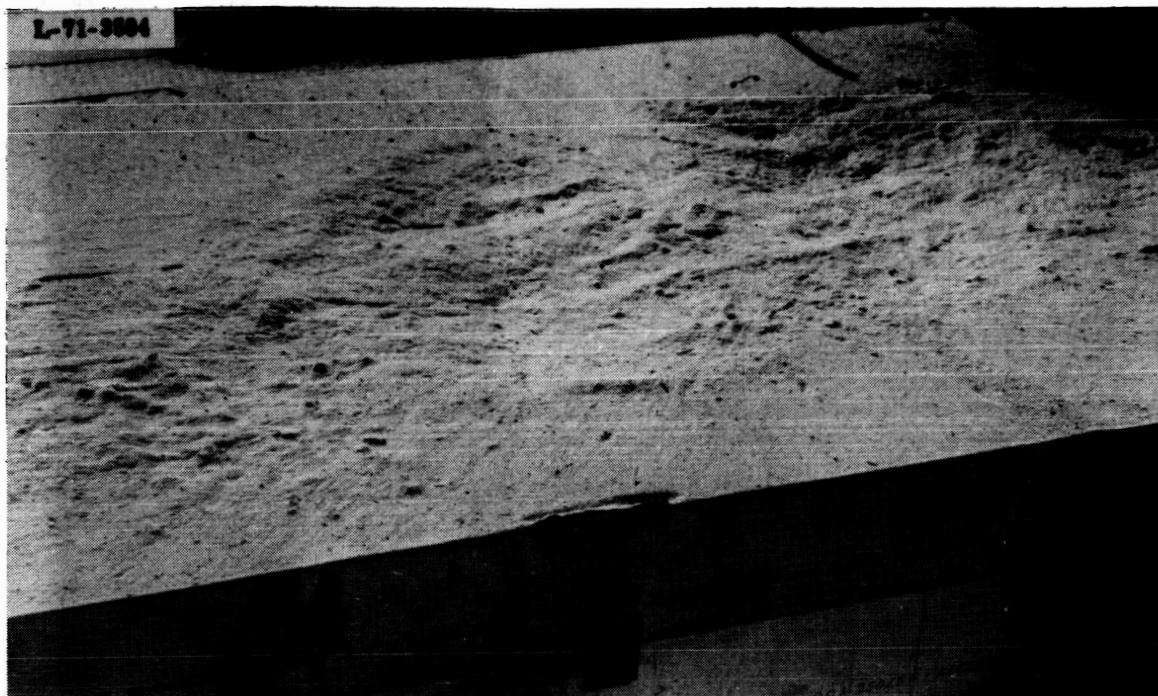
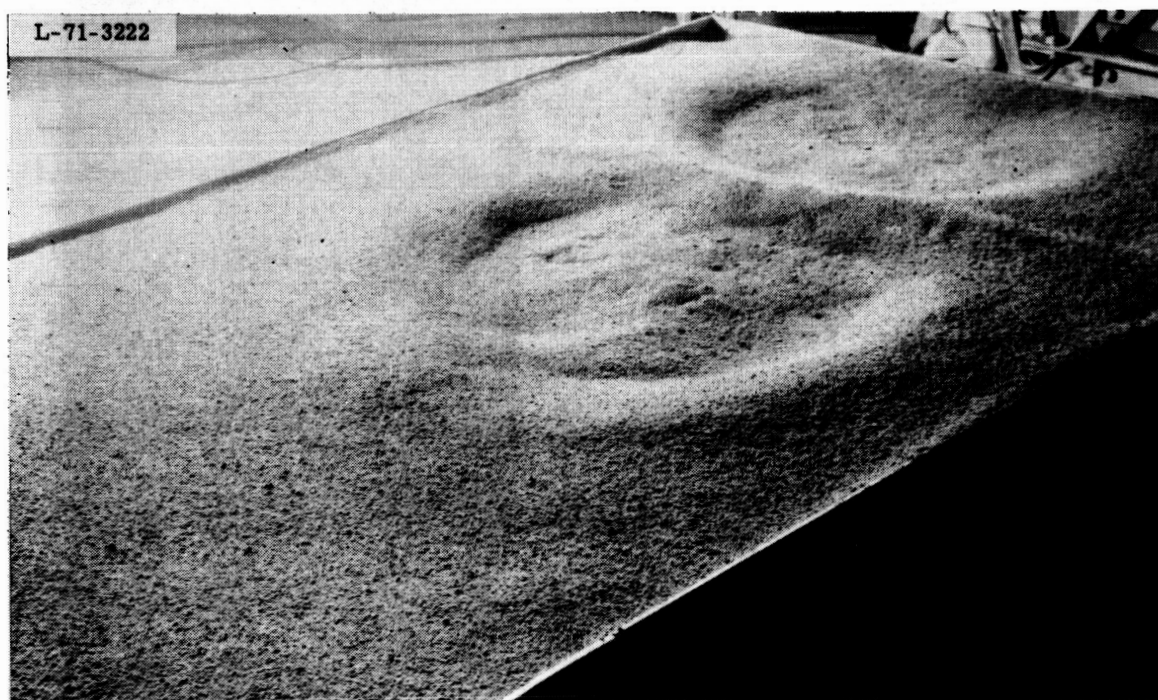


Figure 40.- Variation of maximum surface pressure with altitude of a full-scale linear array of 14 2-D "cold-gas" nozzles alternately canted 15°; $\epsilon = 20$, $\gamma = 1.4$.



Lunar nominal



Dune sand

Figure 41.- Test photographs illustrating surface cratering in lunar nominal and dune sand soil models with a full-scale linear array of 14 2-D "cold-gas" nozzles alternate canted 15° ; $\epsilon = 20$, $\gamma = 1.4$, $P_c \approx 475$ kN/m^2 , $P_\infty \approx 12$ mb, $V \approx 2.7$ m/sec, $h = 90 \rightarrow 0.6$.

L-70-8708

$V = 40 \text{ d}_e / \text{sec}$

L-70-8709

$V = 21.4 \text{ d}_e / \text{sec}$

Figure 42.- Test photographs illustrating effect of descent velocity for non-vertical landings on surface cratering in lunar nominal soil with a one-sixth scale model lander having "cold-gas" nozzles; $\epsilon = 20$, $\gamma = 1.67$, $P_c \approx 730 \text{ kN/m}^2$, $P_\infty = 6.6 \rightarrow 9.2 \text{ mb}$, $h_{co} = 20 \text{ d}_e$, $\alpha = 31^\circ$.

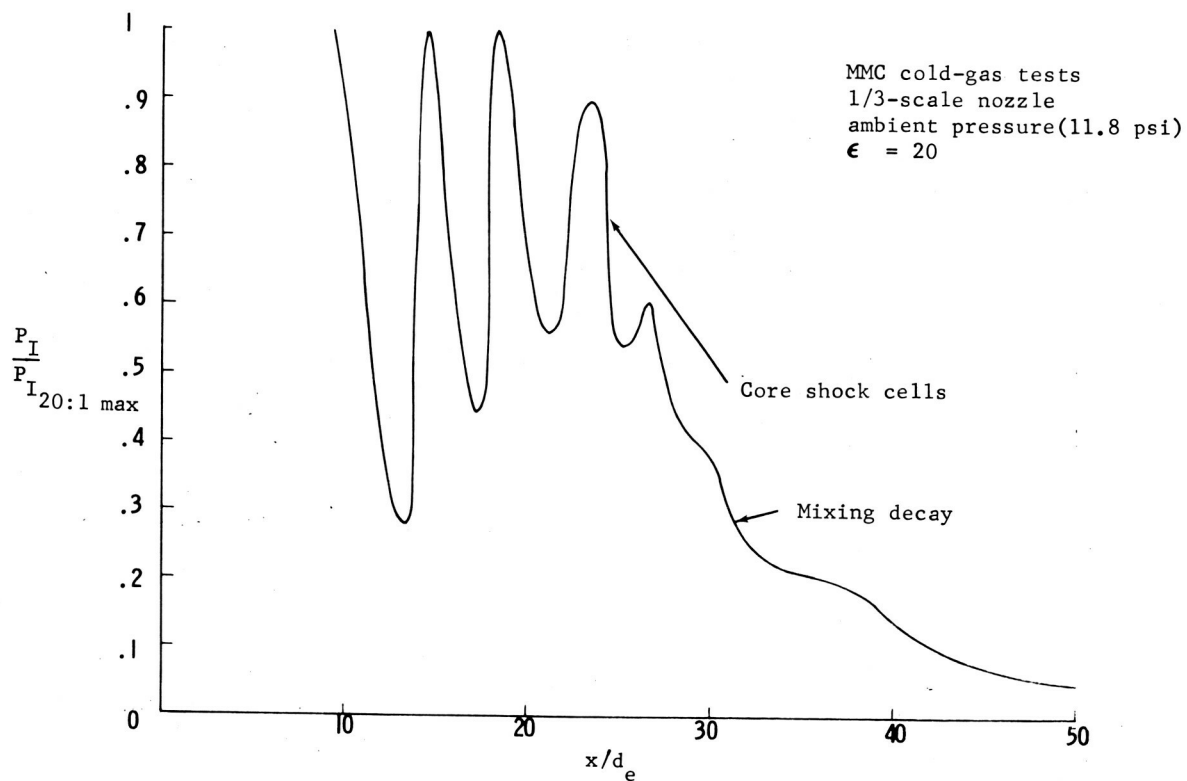


Figure 43a.- Axial variation of 20:1 conical nozzle impingement pressures ; CFL cold-gas.

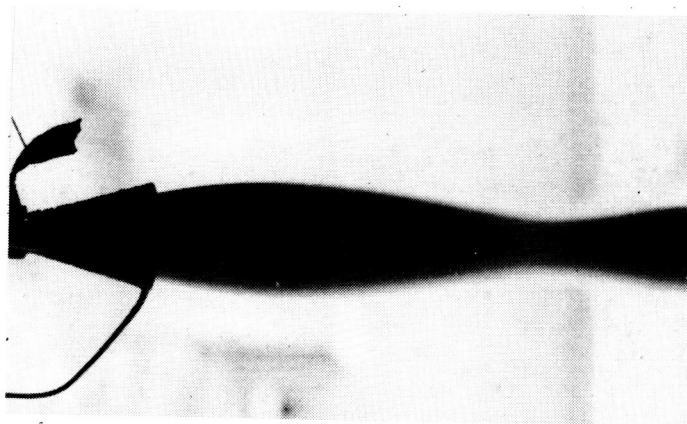


Figure 43b.- Photograph of nozzle flow.

$$\epsilon = 20, \quad \frac{P_e}{P_\infty} = .755$$

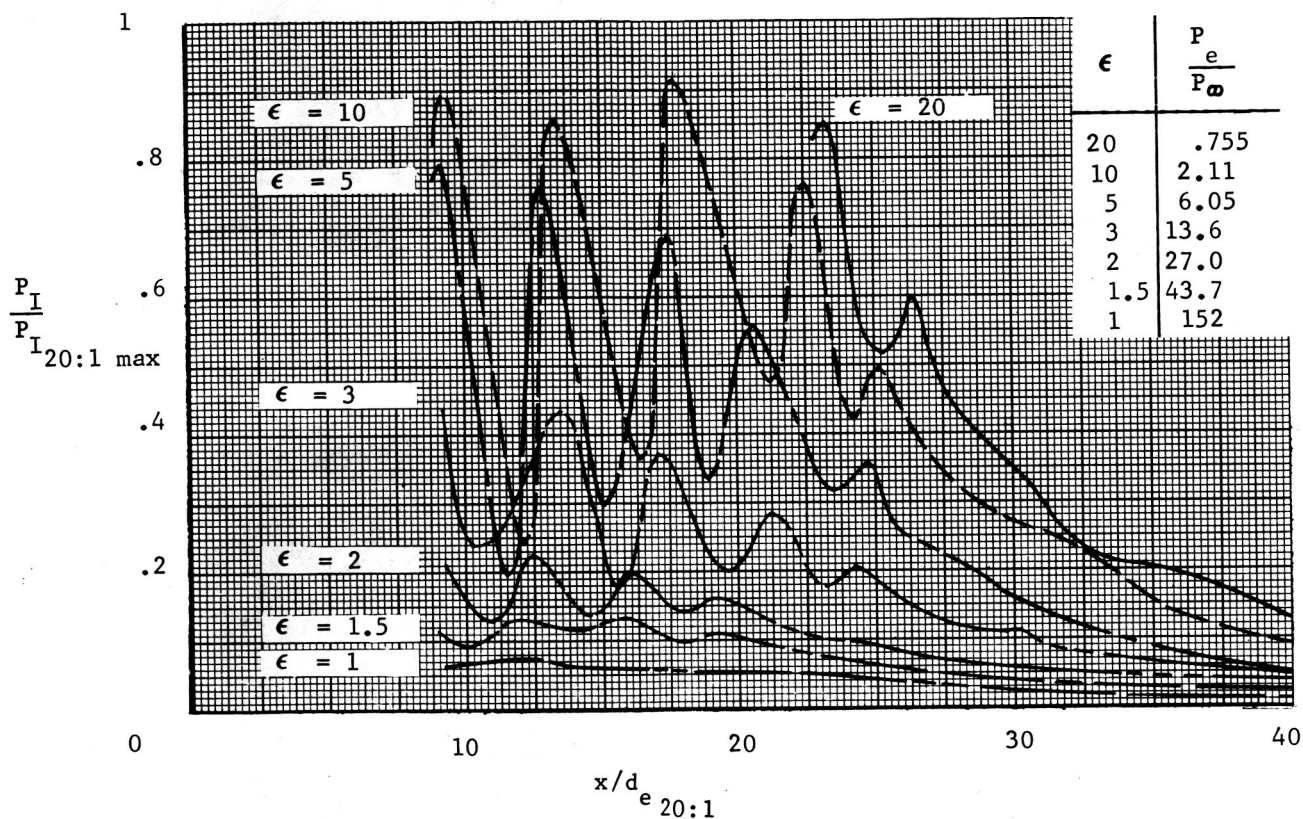


Figure 44 a.-Axial variation of impingement pressures with decreased area ratio nozzles; MMC cold-gas test.

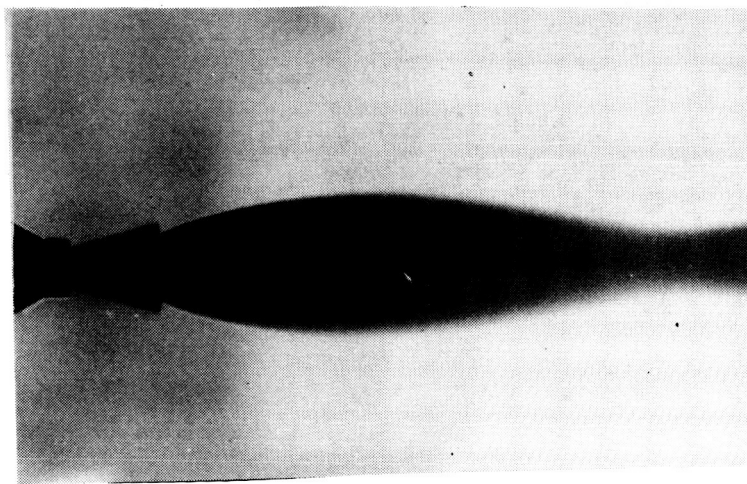
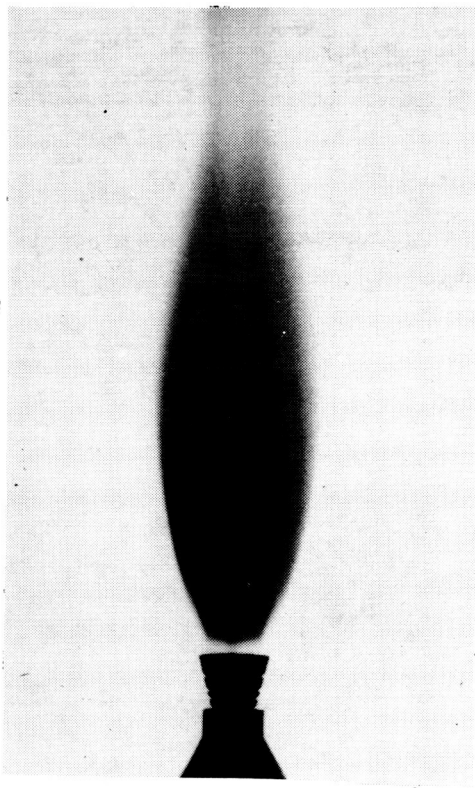
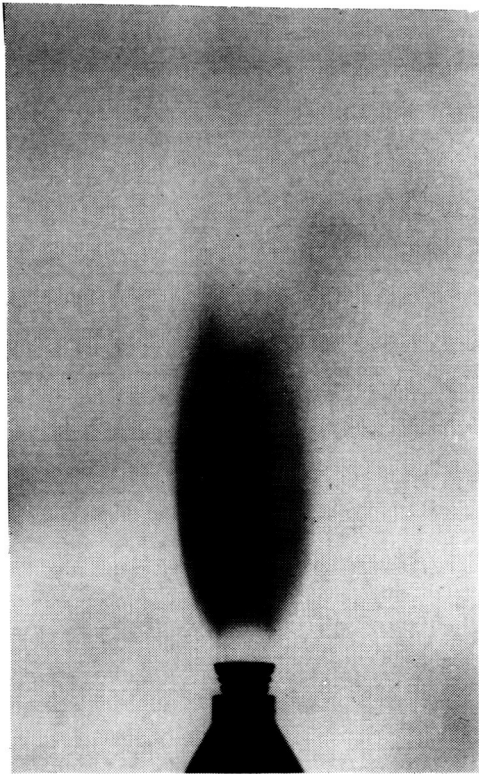


Figure 44b.- Photograph of nozzle flow.

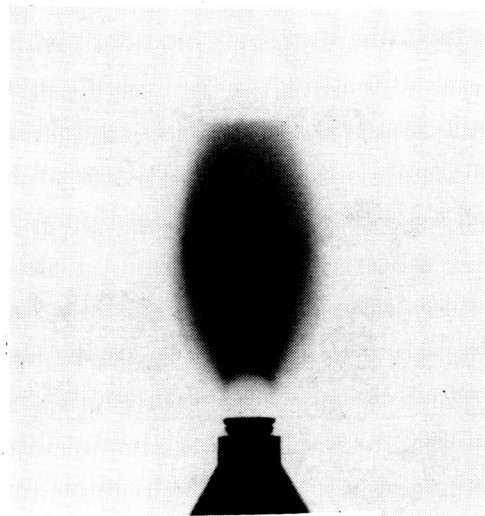
$$\epsilon = 10, \quad \frac{P_e}{P_\infty} = 2.11$$



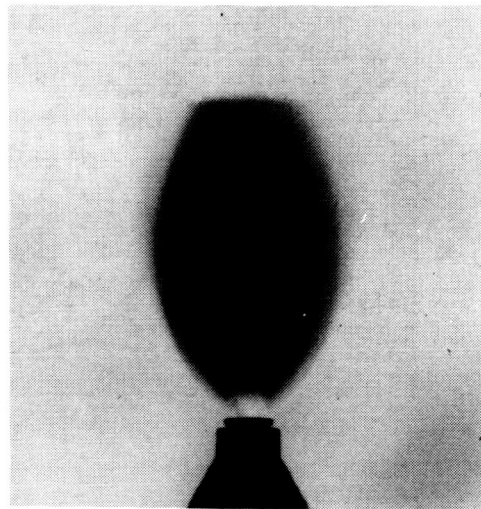
$$\epsilon = 5, \quad \frac{P_e}{P_\infty} = 6.05$$



$$\epsilon = 3, \quad \frac{P_e}{P_\infty} = 13.6$$



$$\epsilon = 2, \quad \frac{P_e}{P_\infty} = 21.1$$



$$\epsilon = 1.5, \quad \frac{P_e}{P_\infty} = 43.7$$



$$\epsilon = 1, \quad \frac{P_e}{P_\infty} = 152$$

Figure 44 c.- Photographs of nozzle flow for nozzle area ratios from $\epsilon = 1$ to $\epsilon = 5$; cold-gas tests at MMC.

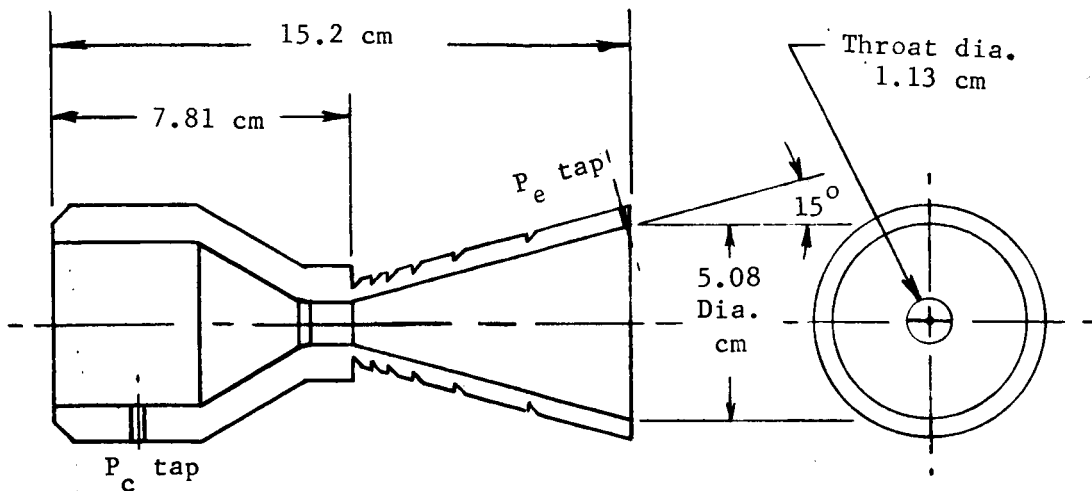


Figure 45.- Nozzle tested with cold-gas at the MMC CFL, $\epsilon = 20$.

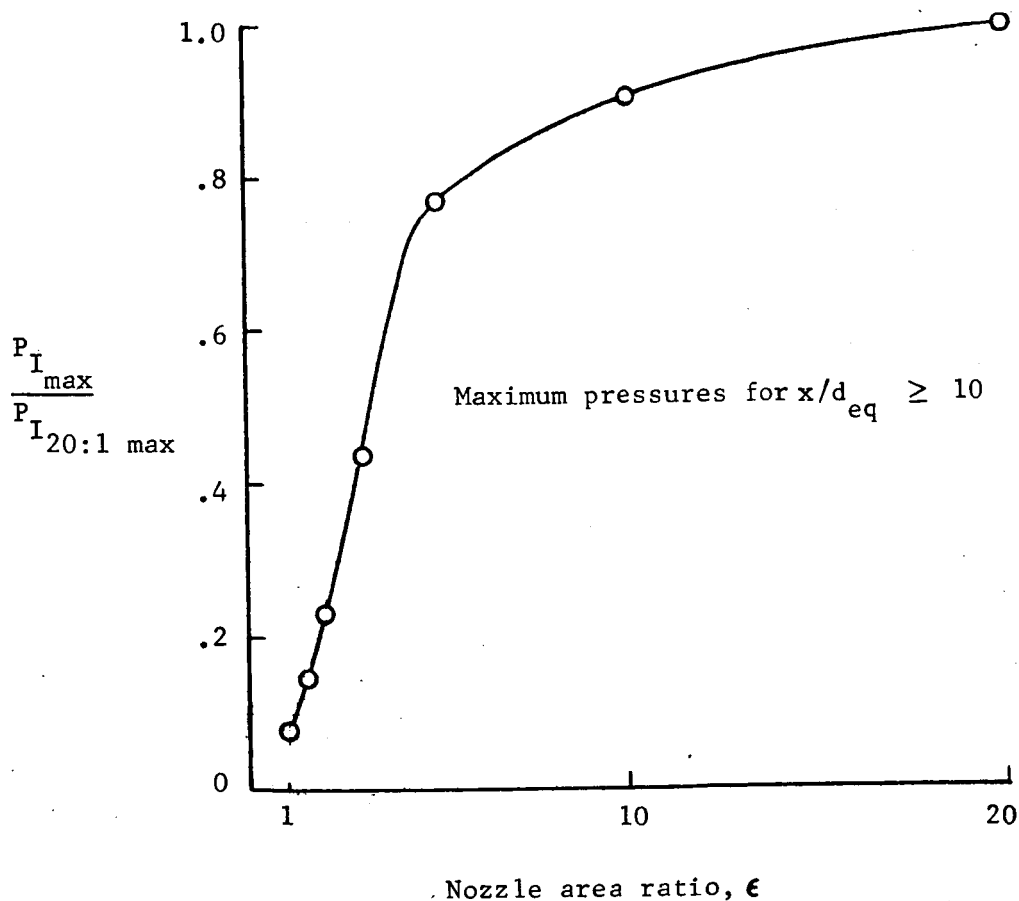


Figure 46.- Maximum impingement pressures as influenced by area ratio.


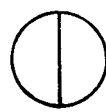
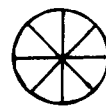
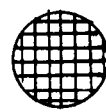
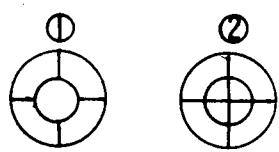
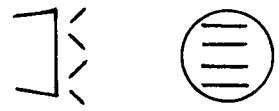
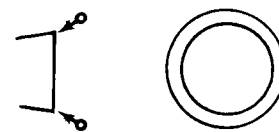
Configuration	A_b/A_{exit}	Thrust Reduction Ratio (Estimated)	Pressure Reduction Ratio (Measured)
 • = 20:1 Nozzle	0.0	1.0	1.0
 Single Wire	.0223	.977	.374
 Spoke	.0127 .0509	.987 .949	.666 .406
 Screen	.0400 .1280 .4200	.960 .872 .580	.740 .280 .100
 Wire Rings	.0589 ① .1415 ② .2004 ① + ②	.941 .858 .800	.286 .437 .200
 Vanes	.1710	.829	.2130
 Mass Injector	--	.979	.563

Figure 47.- Nozzle mixing aids and vortex/shock generators tested in the MMC CFL. ,

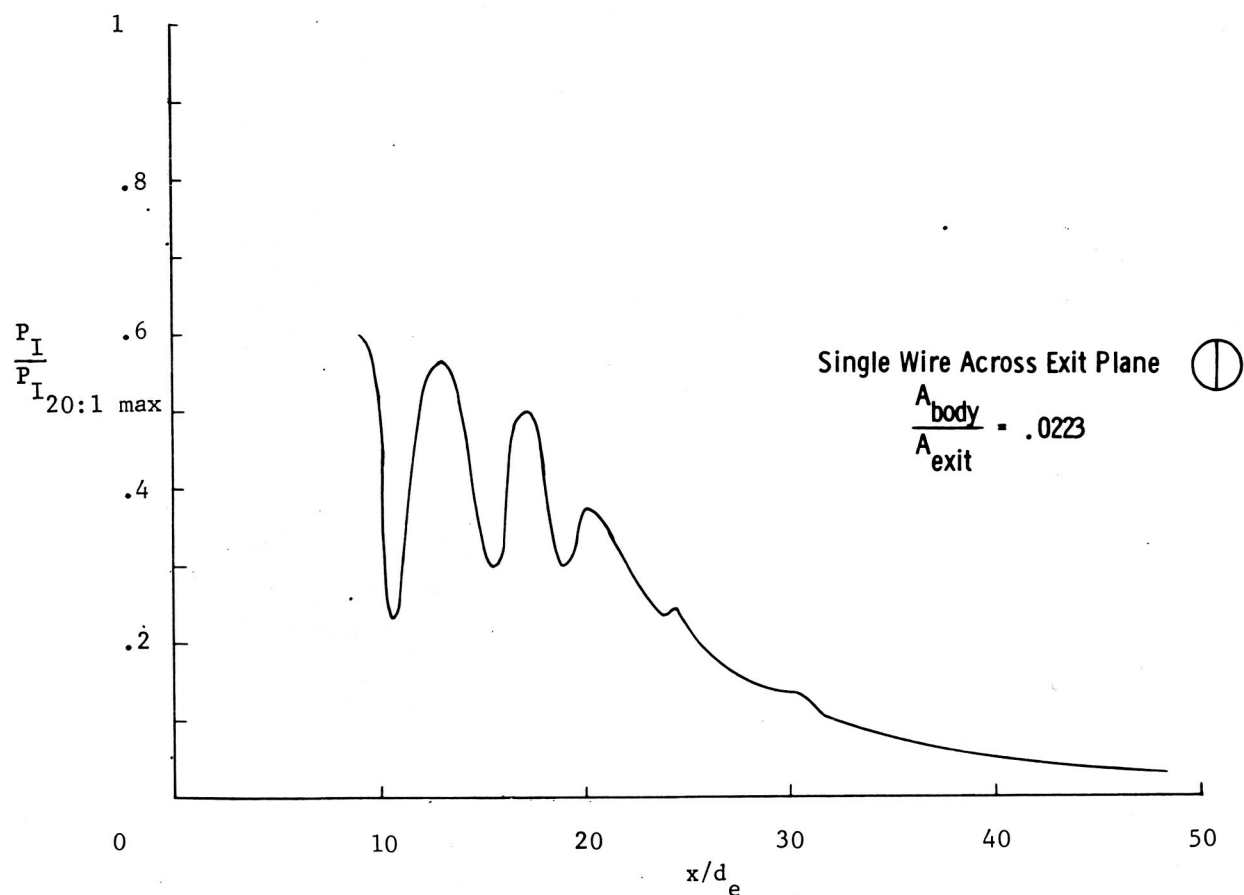


Figure 48a.-Axial variation of impingement pressures with single wire over 20:1 exit;
CFL cold-gas.

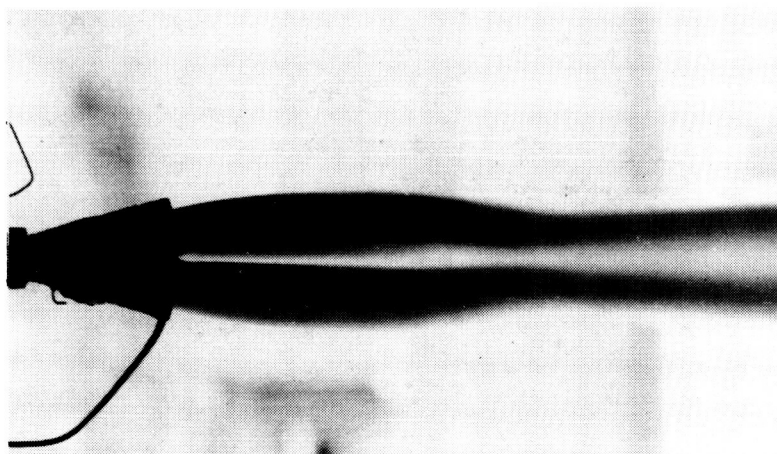


Figure 48b.- Photograph of nozzle flow
for single wire across 20:1 exit.

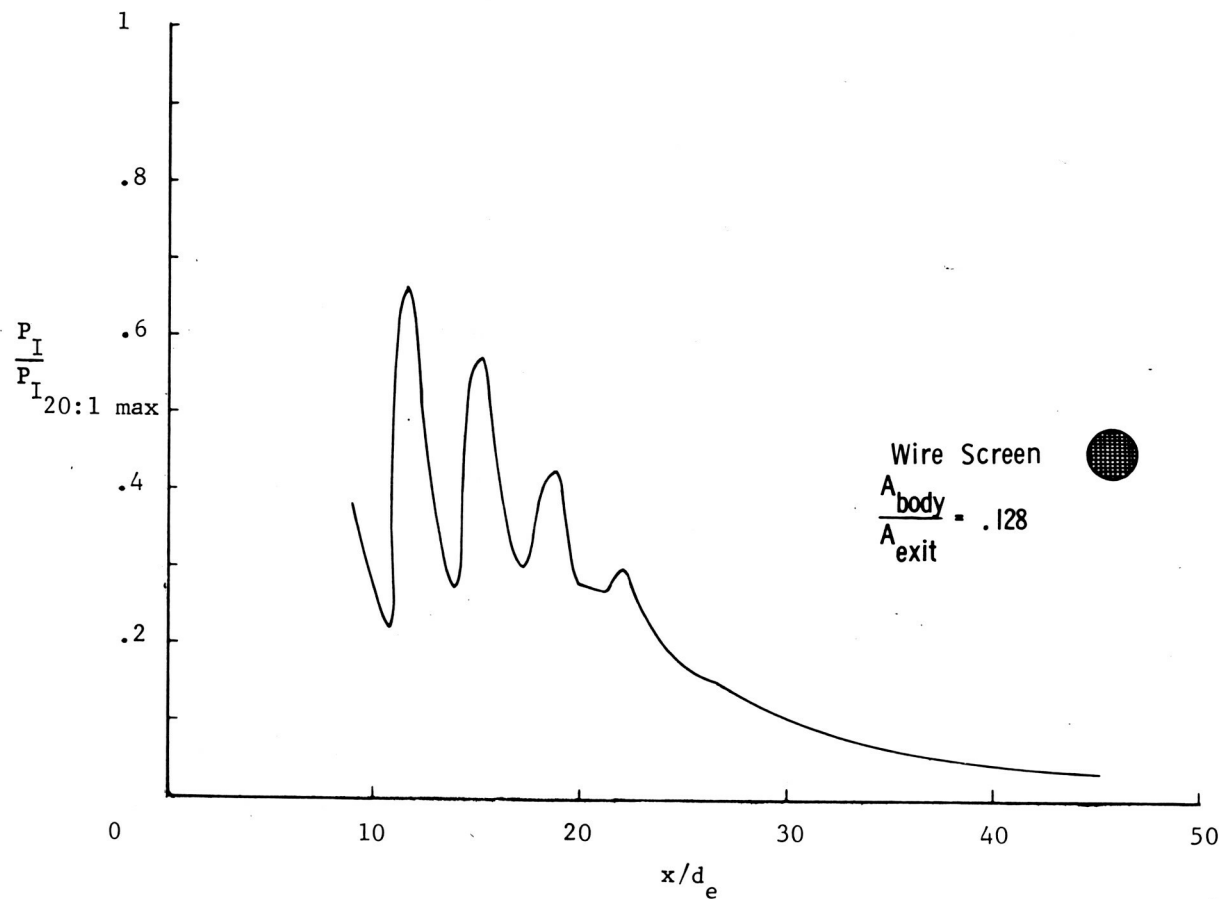


Figure 49a.-Axial variation of impingement pressures with wire screen over 20:1 exit; CFL cold-gas.



Figure 49b.- Photograph of nozzle flow for wire screen across 20:1 nozzle exit.

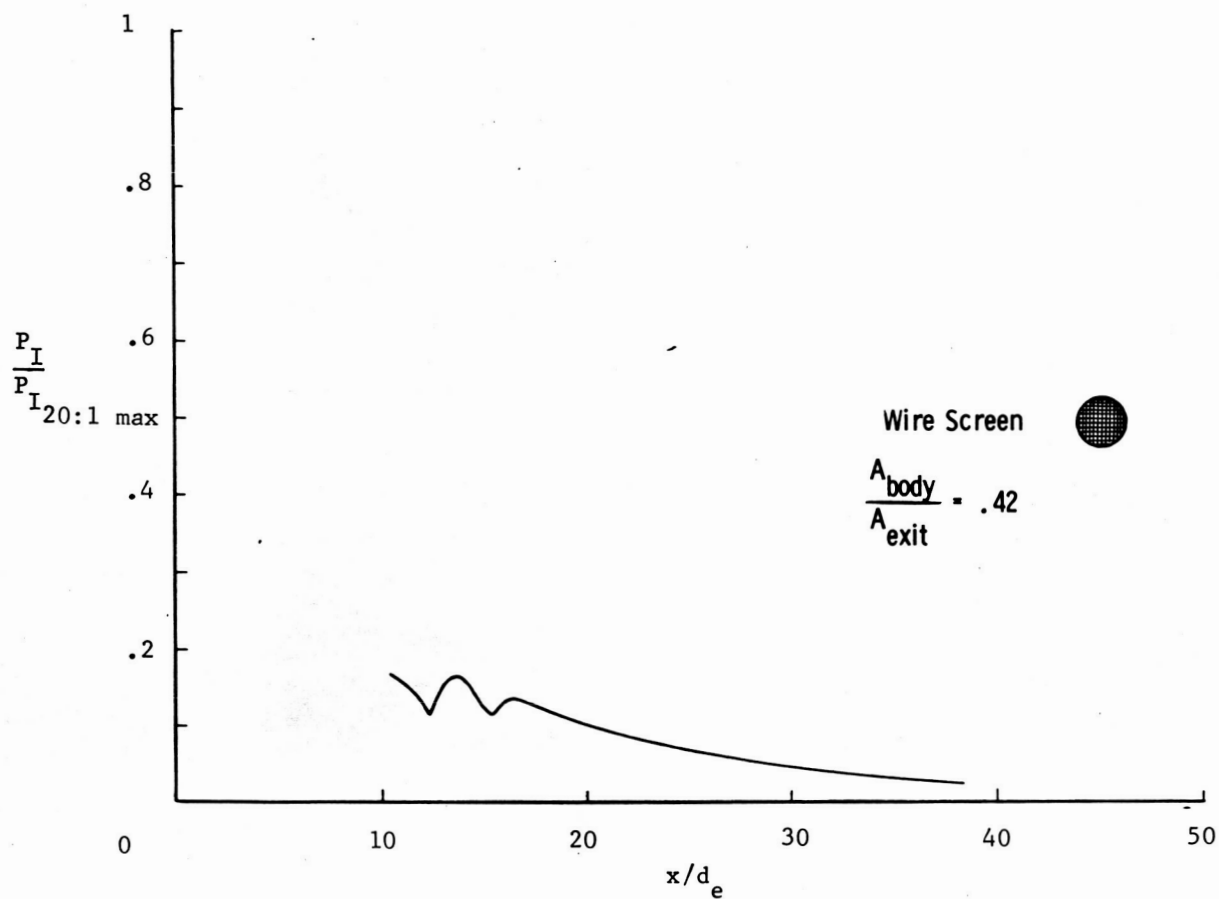


Figure 50a.-Axial variation of impingement pressures with wire screen over 20:1 exit; CFL cold-gas.

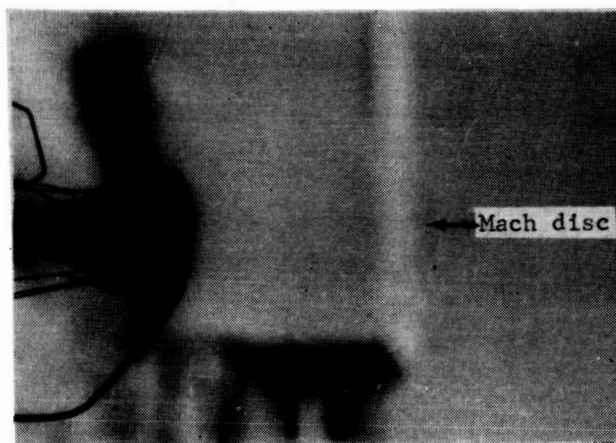


Figure 50b.-Photograph of nozzle flow for wire screen across 20:1 nozzle exit.

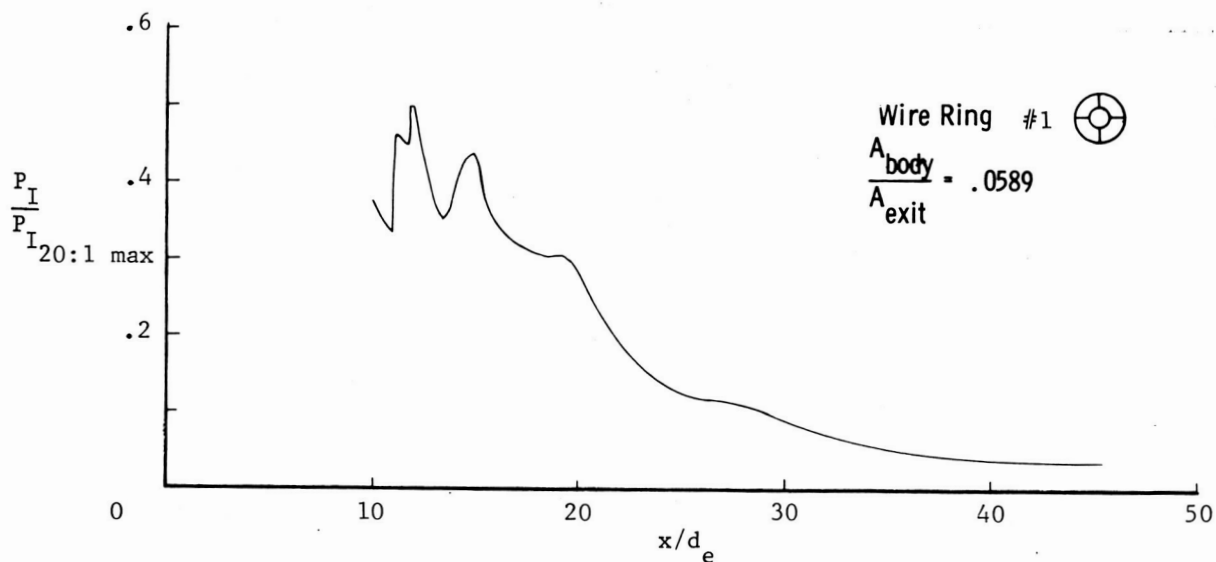


Figure 51a.-Axial variation of impingement pressures with wire ring over 20:1 exit; CFL cold-gas.

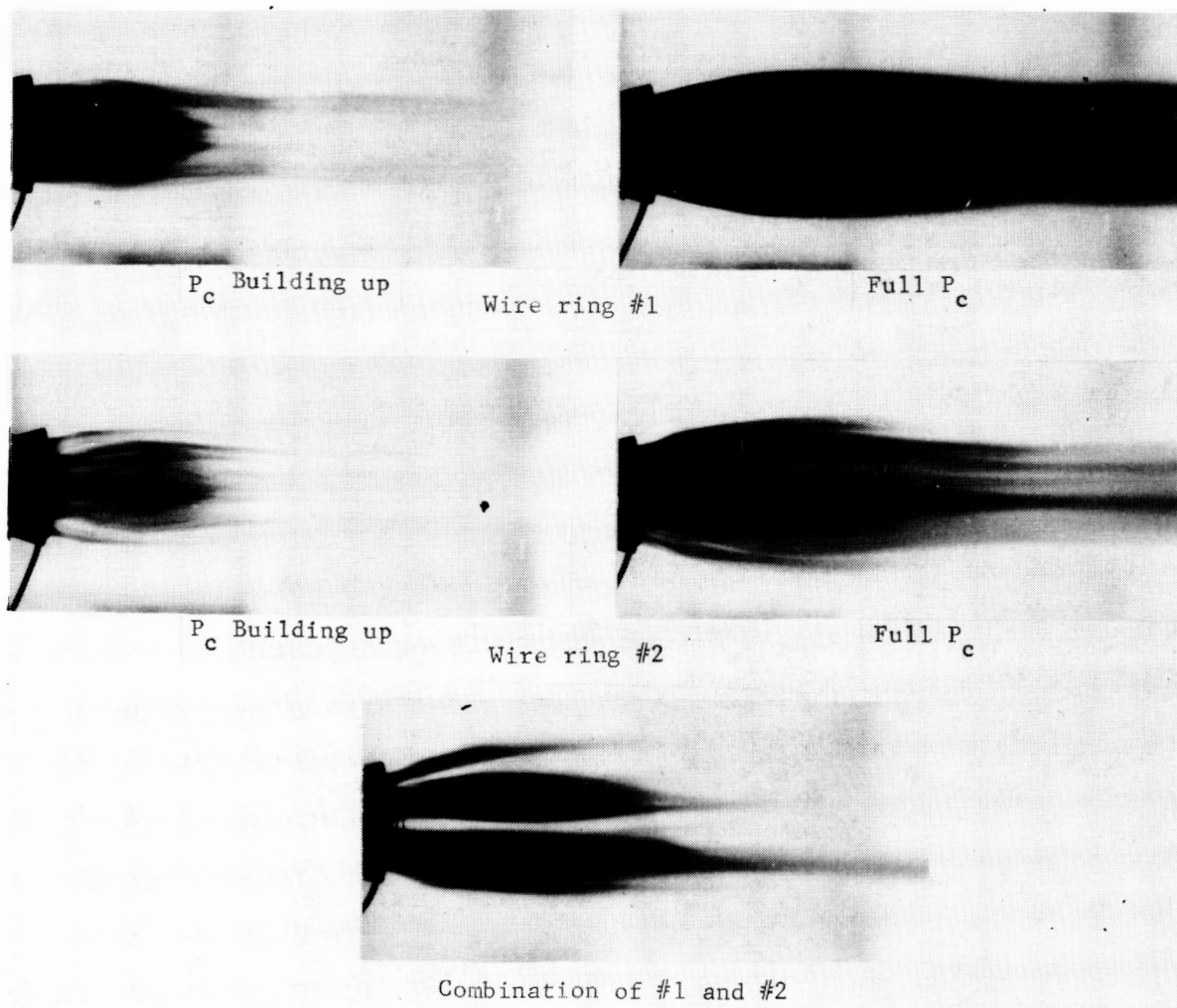


Figure 51b.-Photograph of nozzle flow for wire rings over 20:1 nozzle exit.

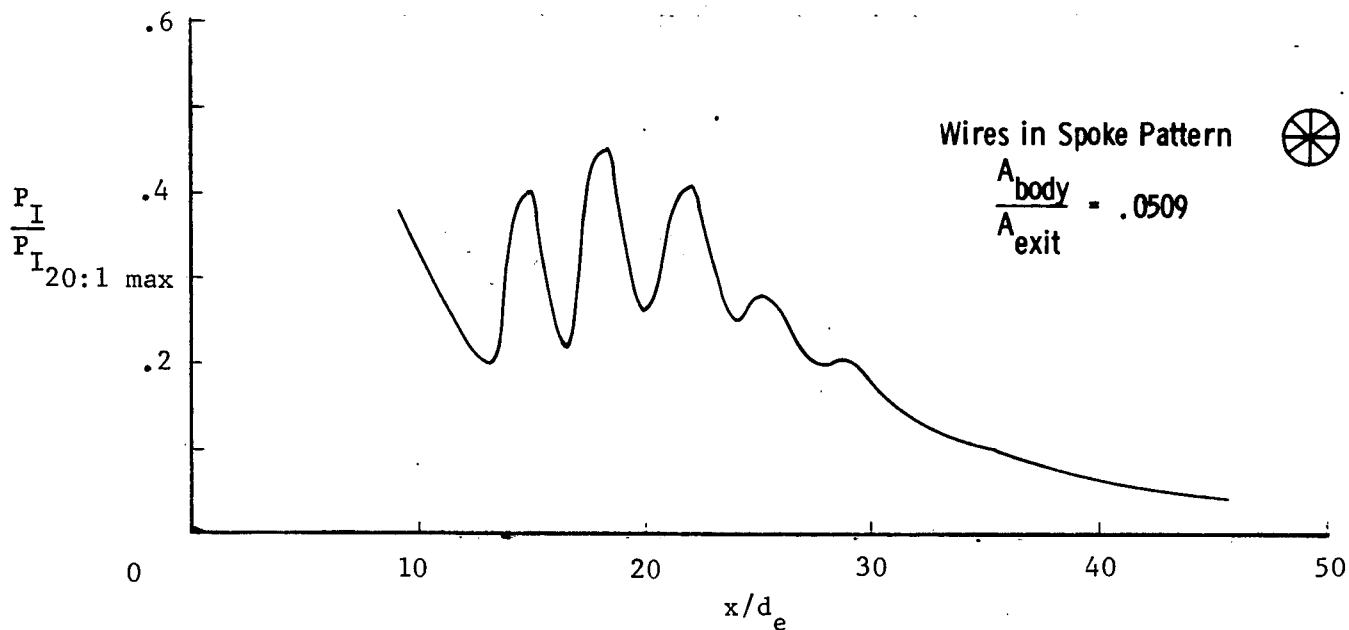


Figure 52a.-Axial variation of impingement pressures with wire spoke over 20:1 exit;
CFL cold-gas.

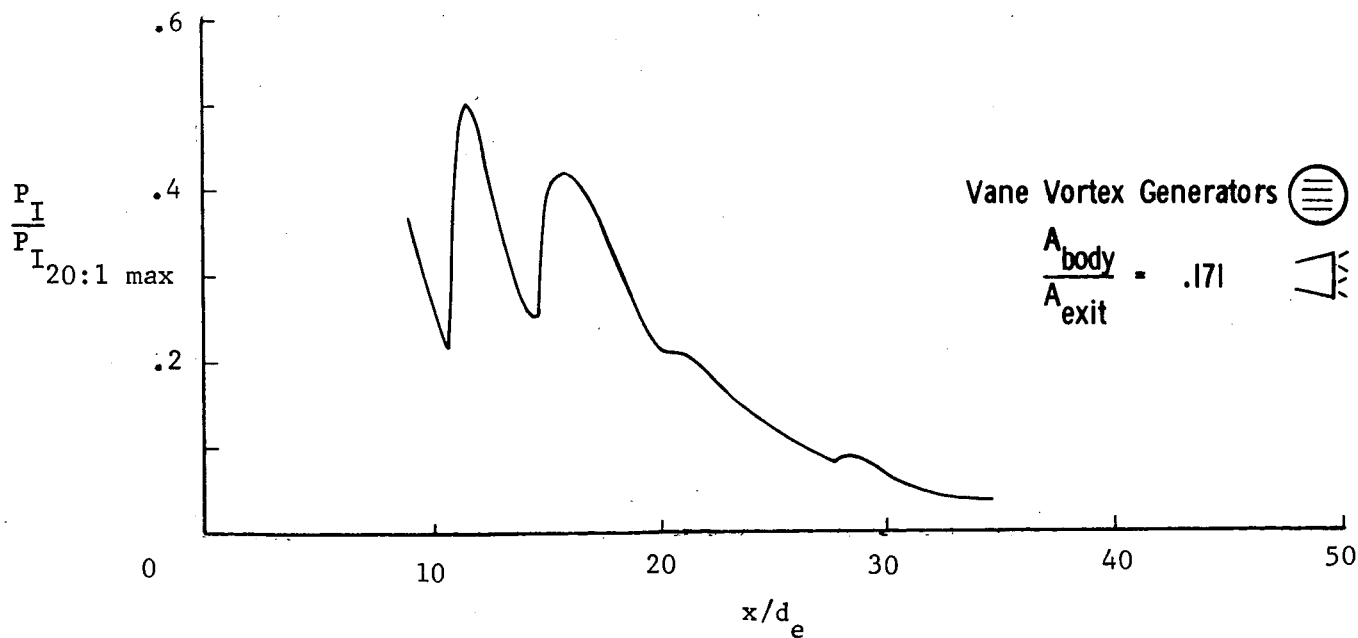


Figure 52b.-Axial variation of impingement pressures with vanes over 20:1 exit;
CFL cold-gas.

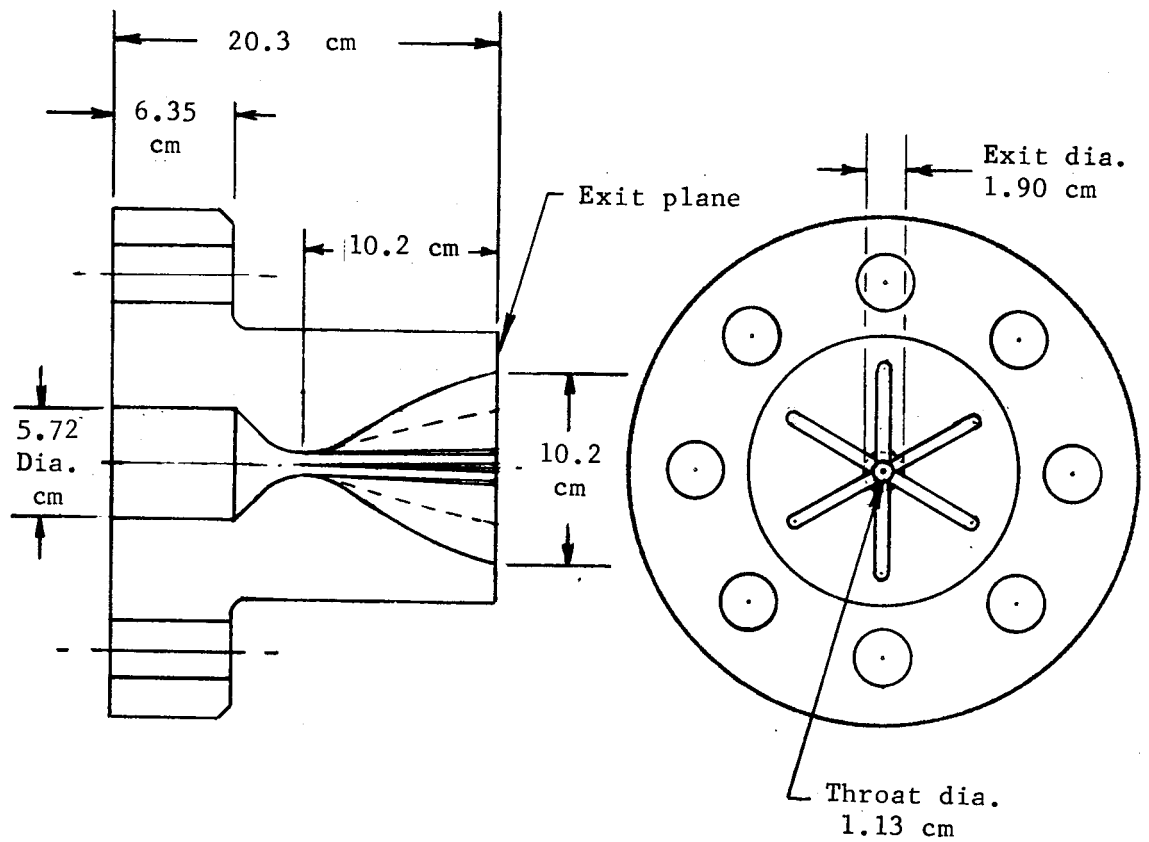


Figure 53.- Six-flute nozzle configuration tested at the MMC CFL.

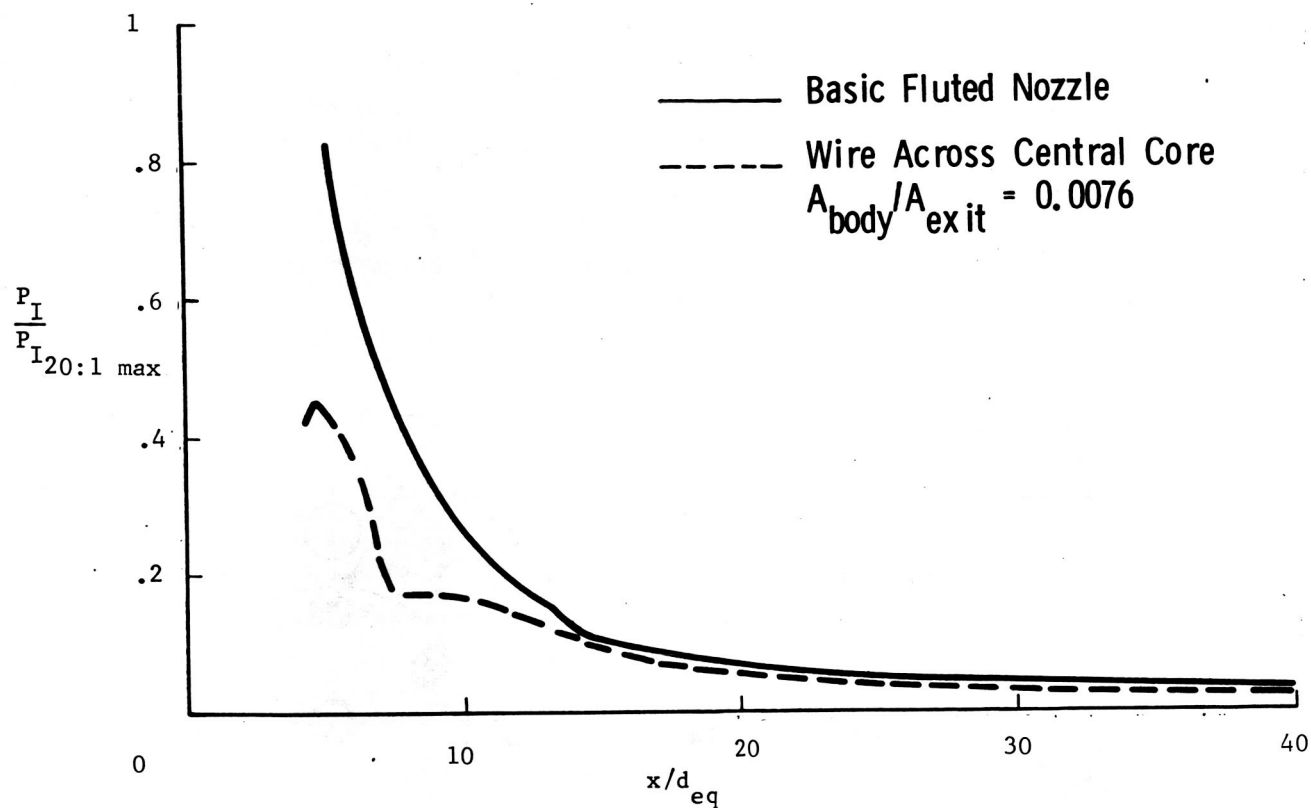


Figure 54a.- Axial variation of fluted nozzle impingement pressures; MMC cold-gas tests.

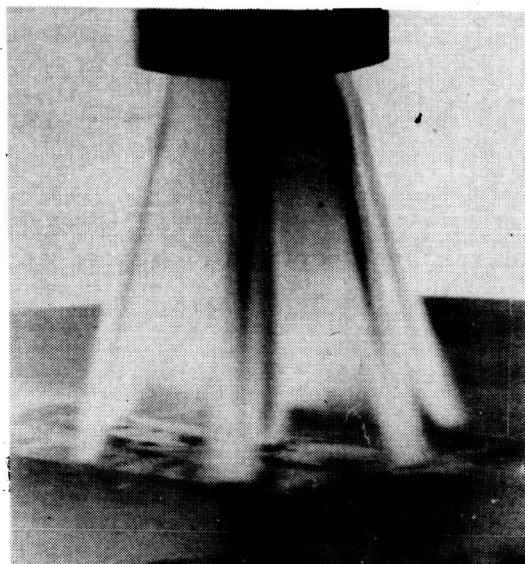


Figure 54b.-Photograph of six-flute nozzle flow impinging on plate.

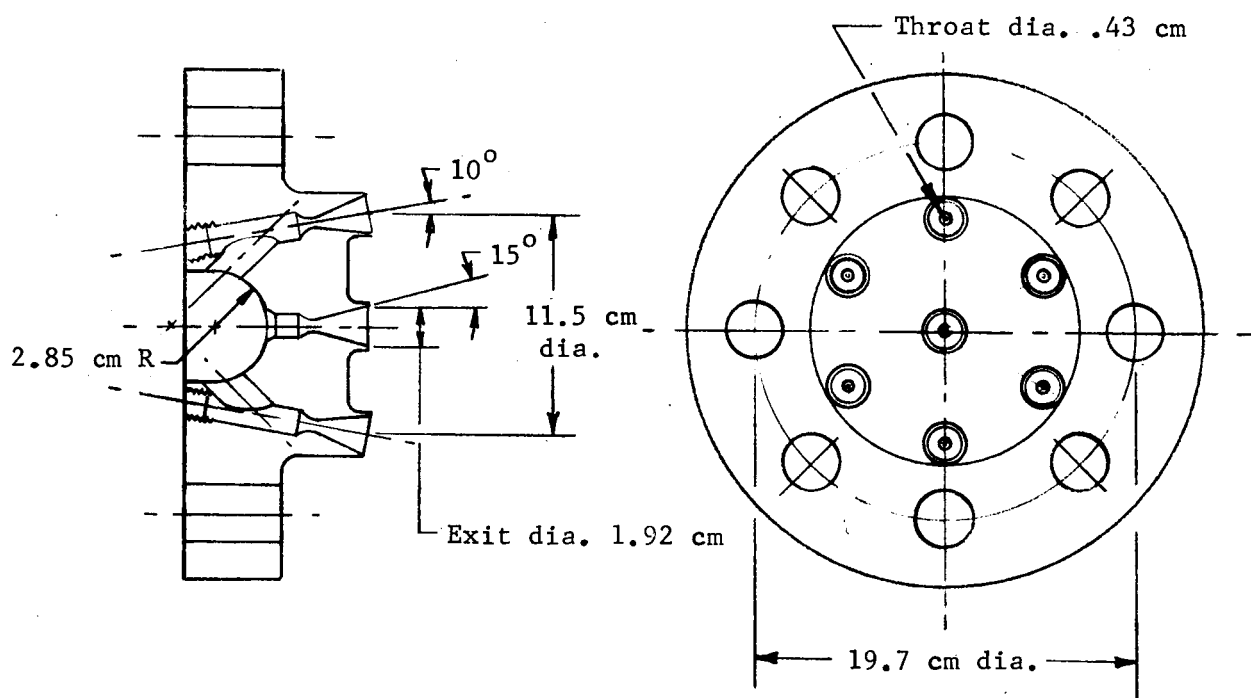


Figure 55.- 7-Nozzle cluster, area ratio 20:1 tested at MMC with cold-gas.

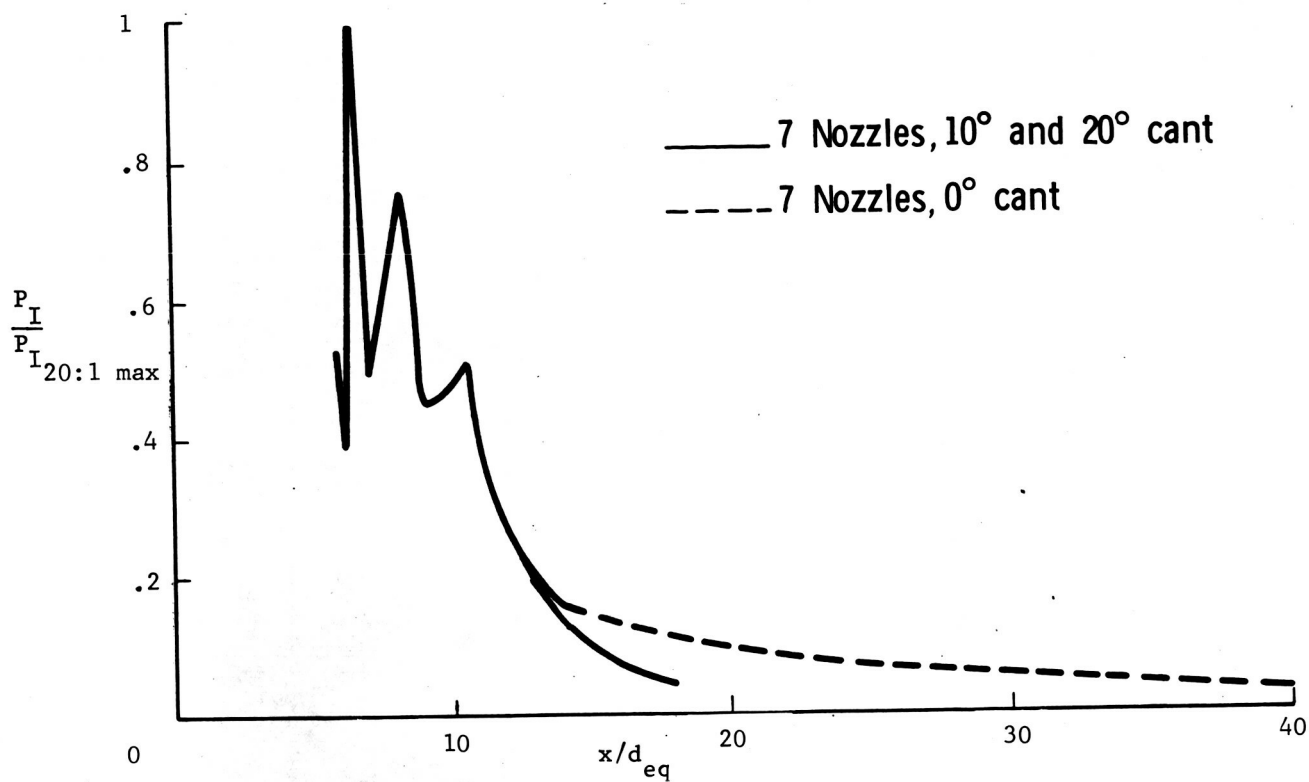
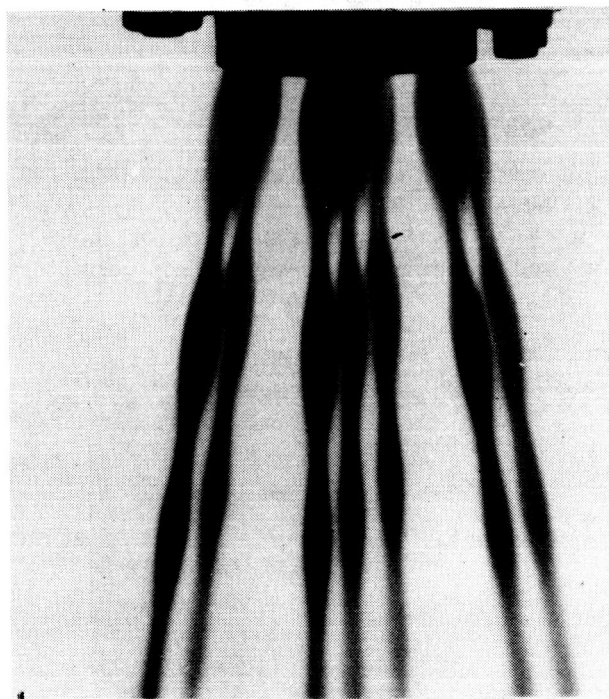
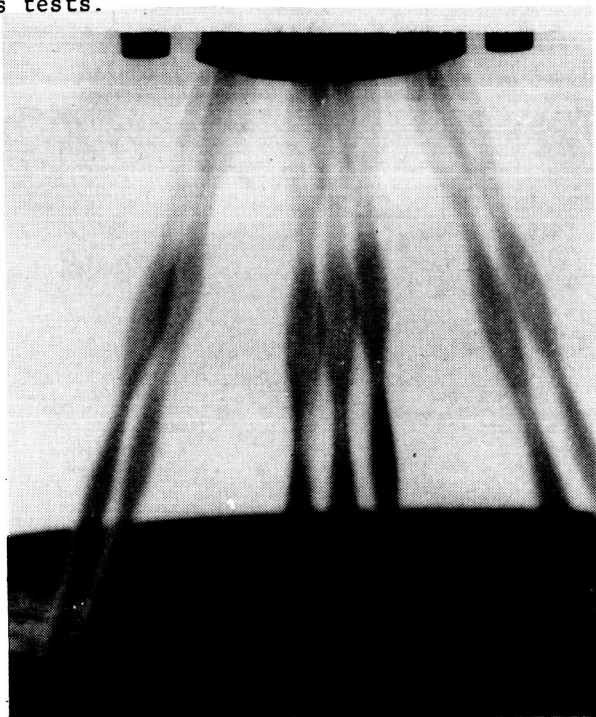


Figure 56a.-Axial variation of 7 nozzle configuration impingement pressures;
MMC cold-gas tests.

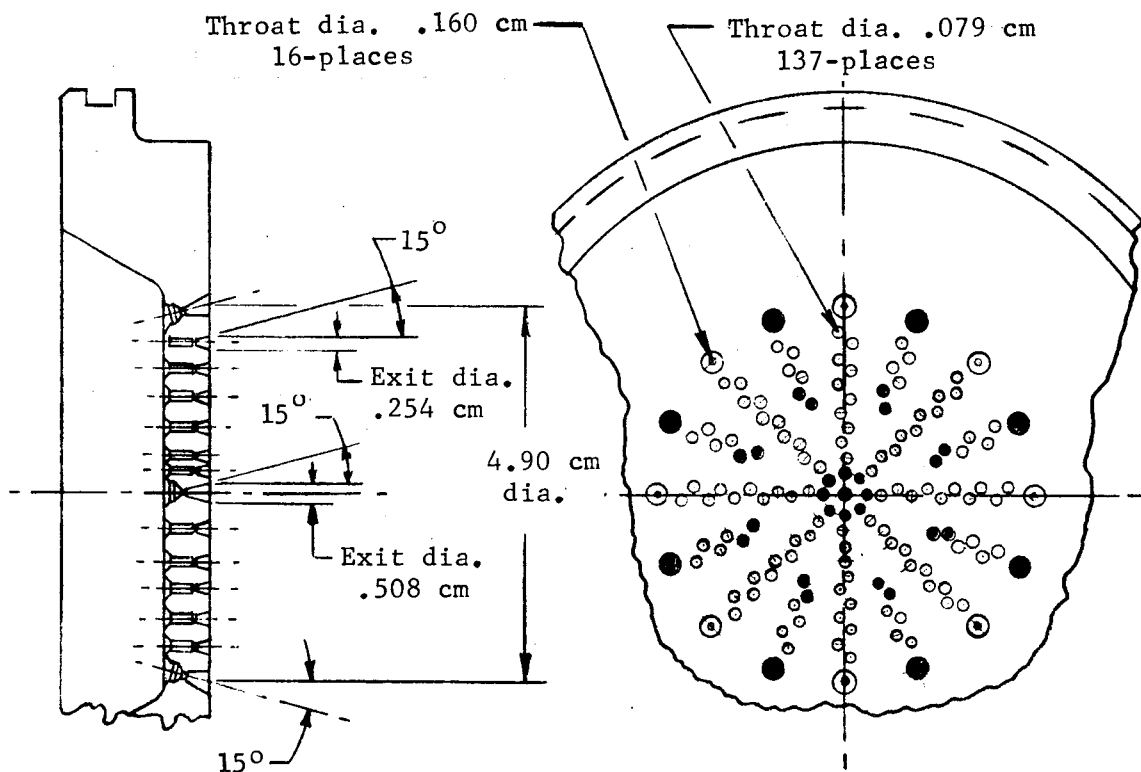


10° cant



20° cant

Figure 56b.- Photograph of seven nozzle flow for 10° and 20° cant angles;
MMC cold-gas tests.



All nozzles open for version 1.
Shaded nozzles plugged for version 2.

Figure 57.- Thrust plate nozzle tested at the MMC CFL.

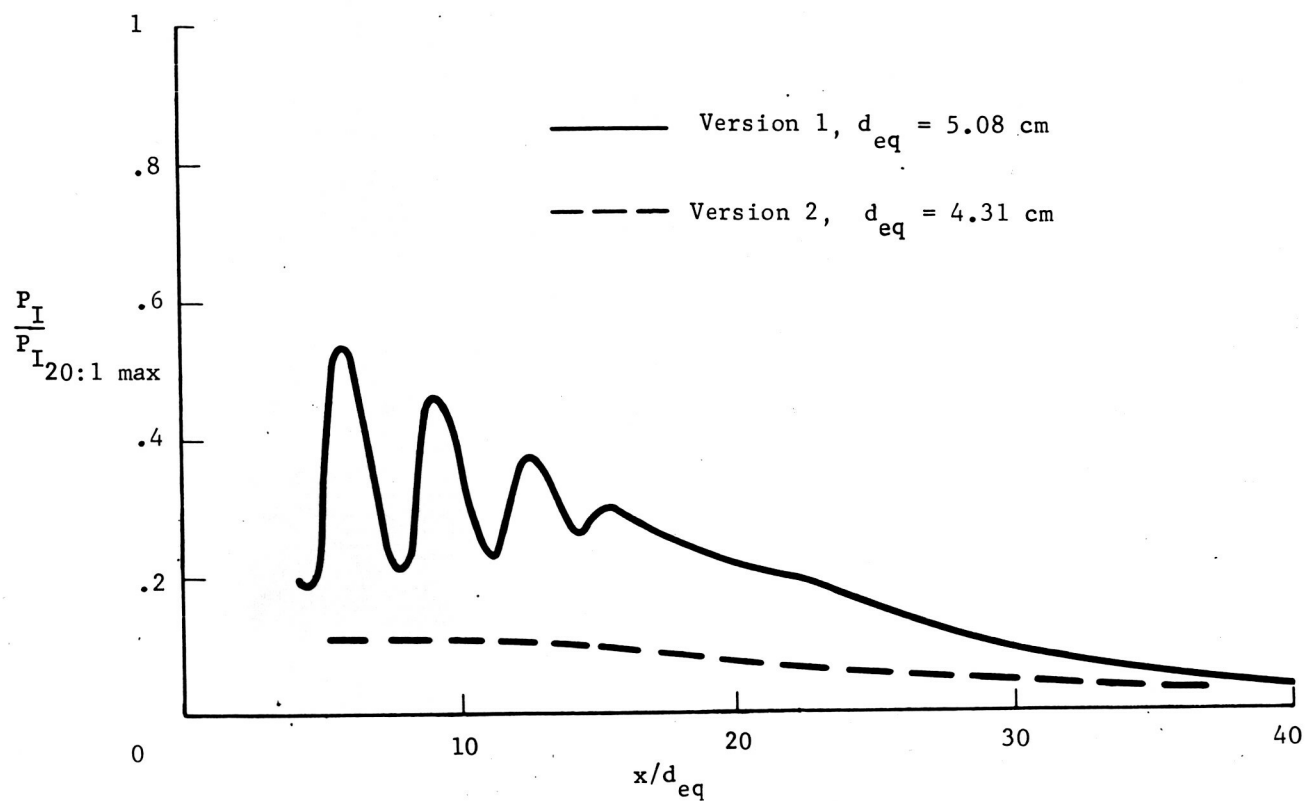


Figure 58a.-Axial variation of thrust plate impingement pressures; MMC cold gas tests.

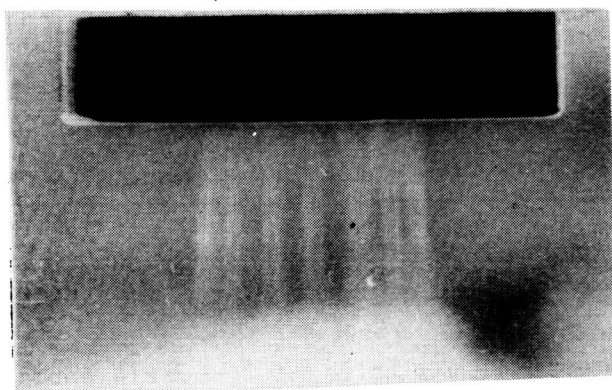


Figure 58b.- Photograph of version 2 thrust plate nozzle flow; MMC cold-gas tests.

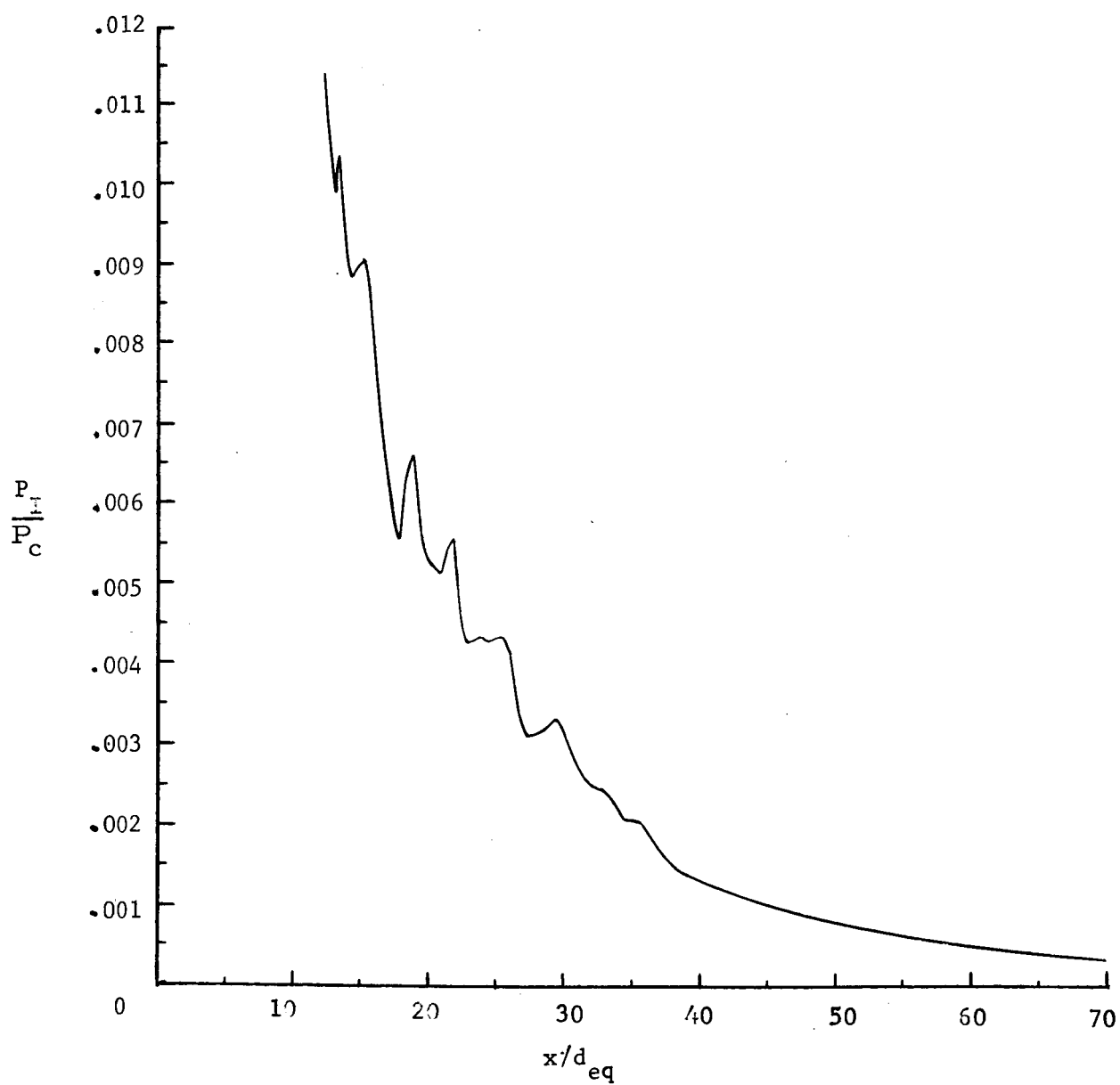


Figure 59.- Axial variation of 24-nozzle configuration impingement pressures; WSTF Phase II, test 11A.

	x/d_{eq}	$\frac{P_e}{P_\infty}$
○	13	1.17
□	20	1.19
△	30	1.26
◇	50	1.35

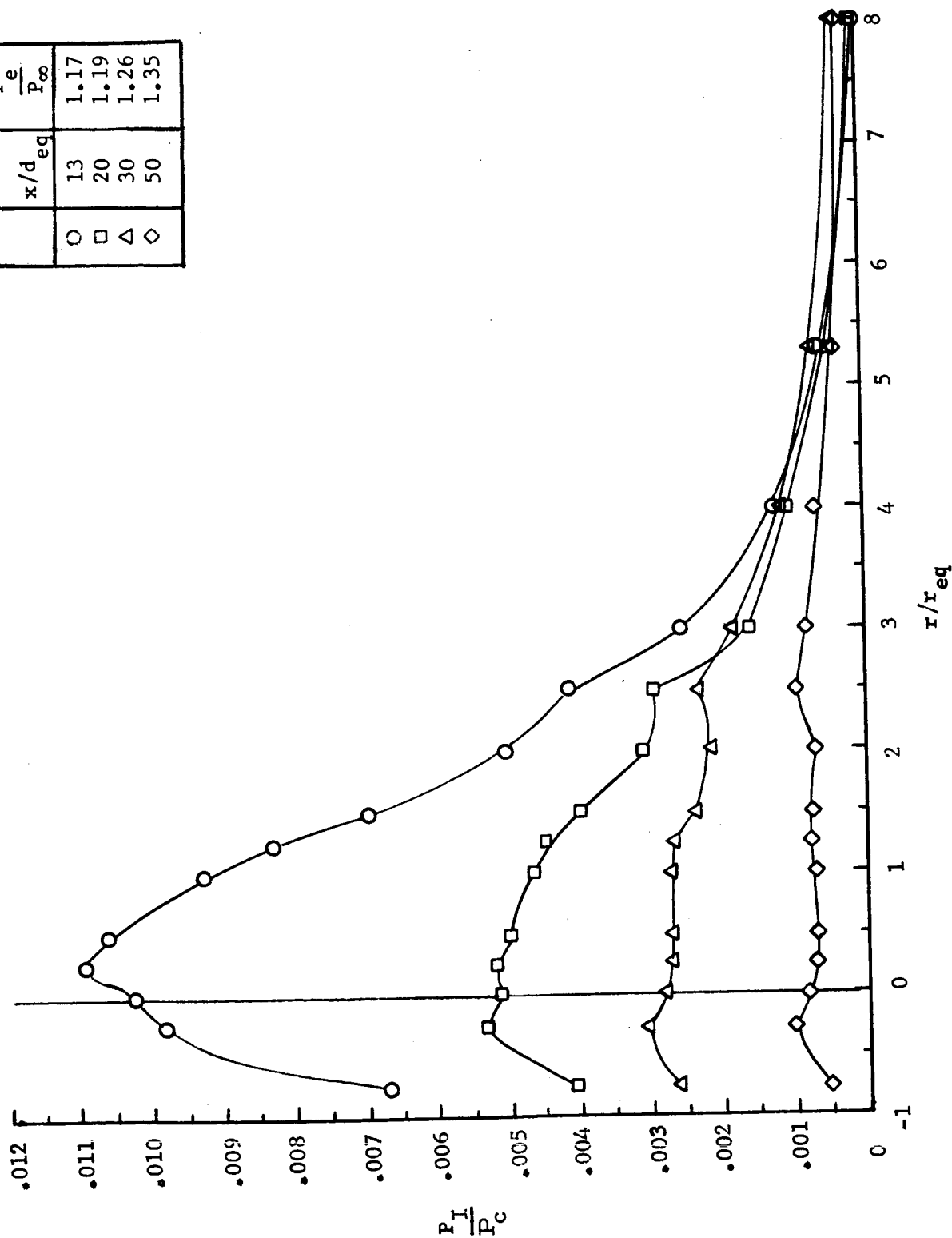


Figure 60.-Radial variation of 24-nozzle configuration impingement pressures;
WSTF Phase II, test 11A.

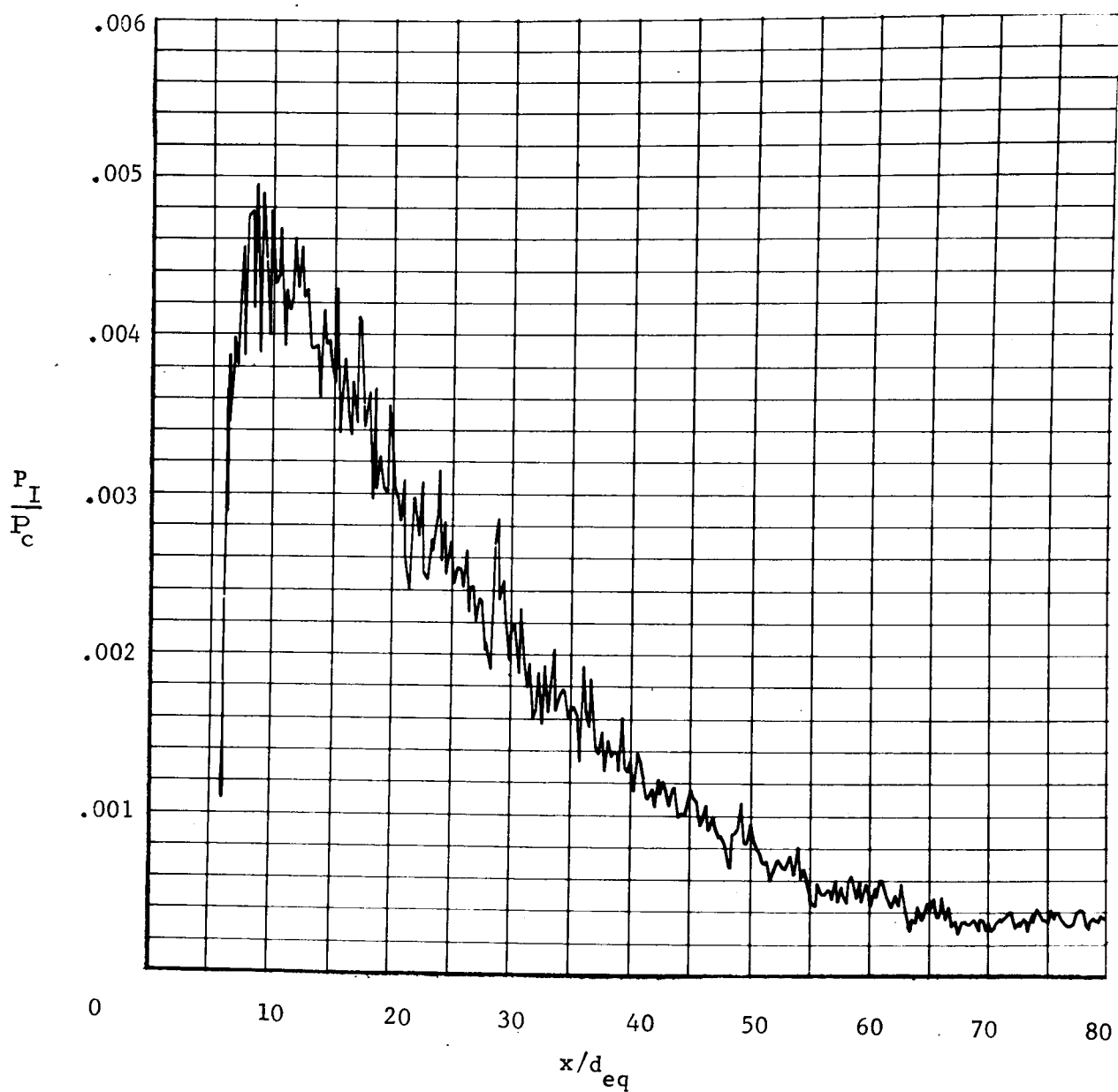


Figure 61.-Axial variation of 18 (24 - mod 2)-nozzle configuration impingement pressures; WSTF Phase II, test 11E.

	x/d_{eq}	P_e/P_∞
○	7.5	.88
□	10	.89
△	15	.90
◇	20	.91
▷	25	.925
○	30	.95
◐	40	.98
▽	50	1.0
☆	60	1.04
◊	75	1.12

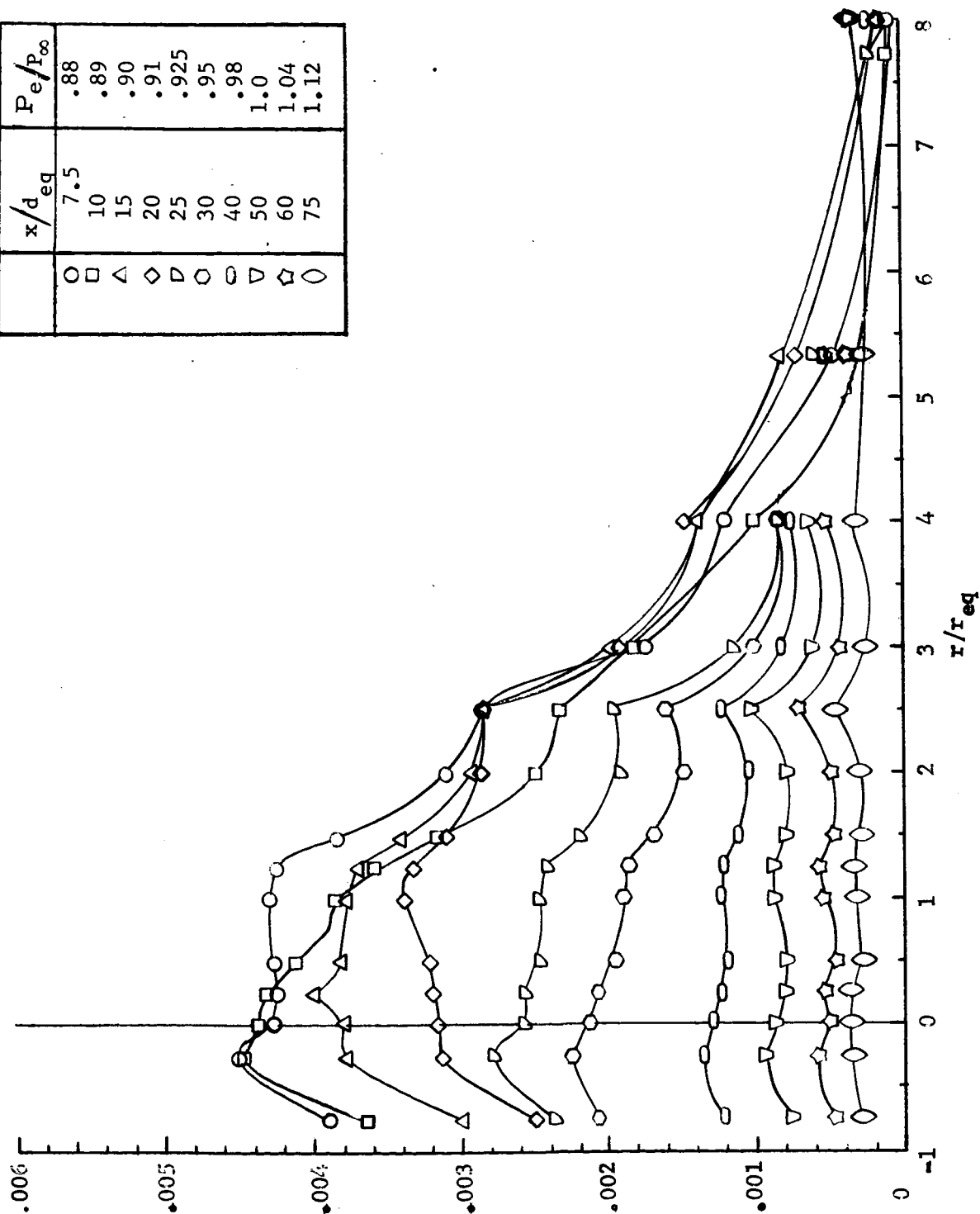


Figure 62.-Radial variation of 18 (24 - mod 2)-nozzle configuration impingement pressures; WSTF Phase II, test 11E.

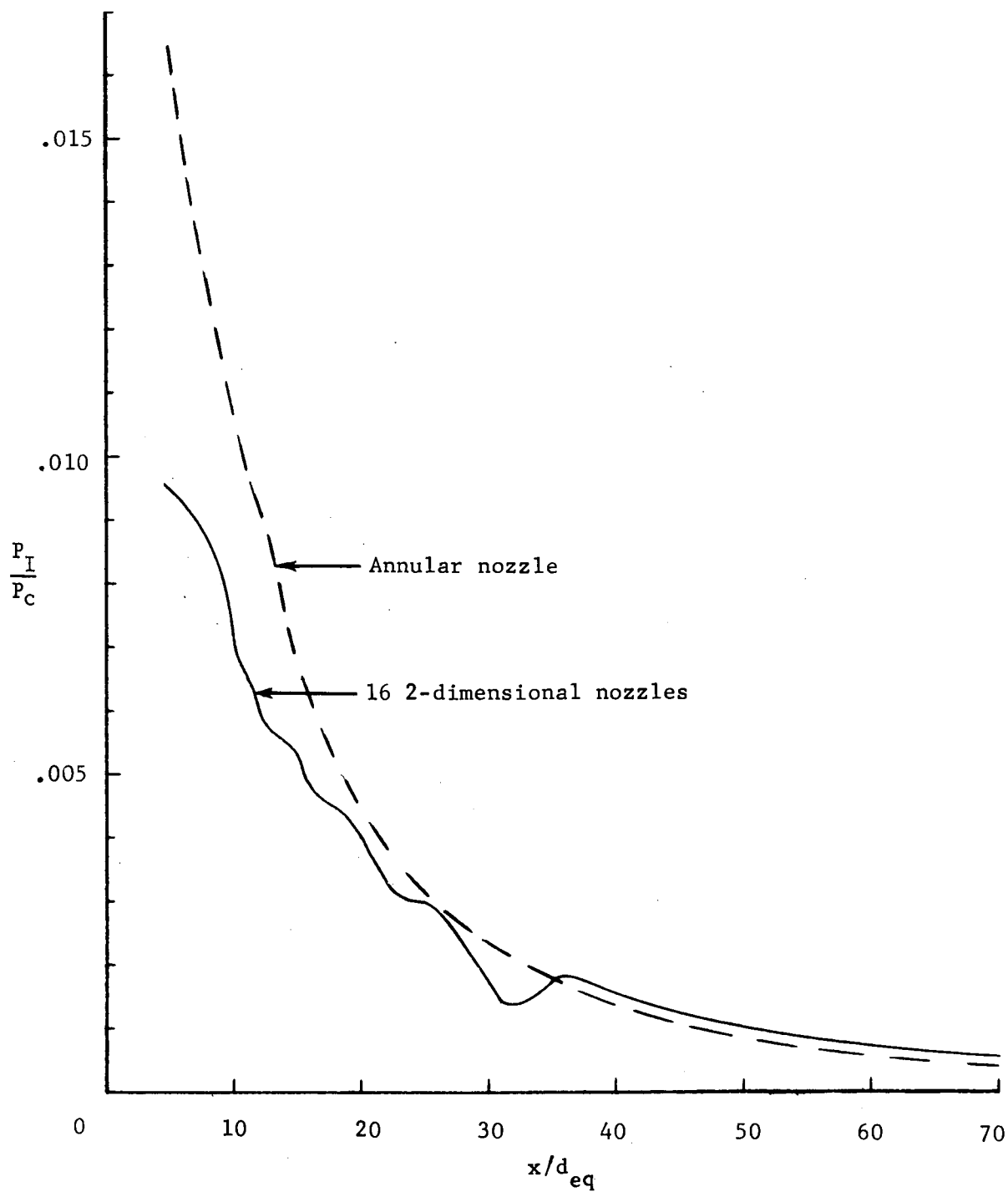


Figure 63.-Axial variation of multiple 2-dimensional nozzles and annular nozzle impingement pressures; WSTF Phase II, tests 11G, 11H.

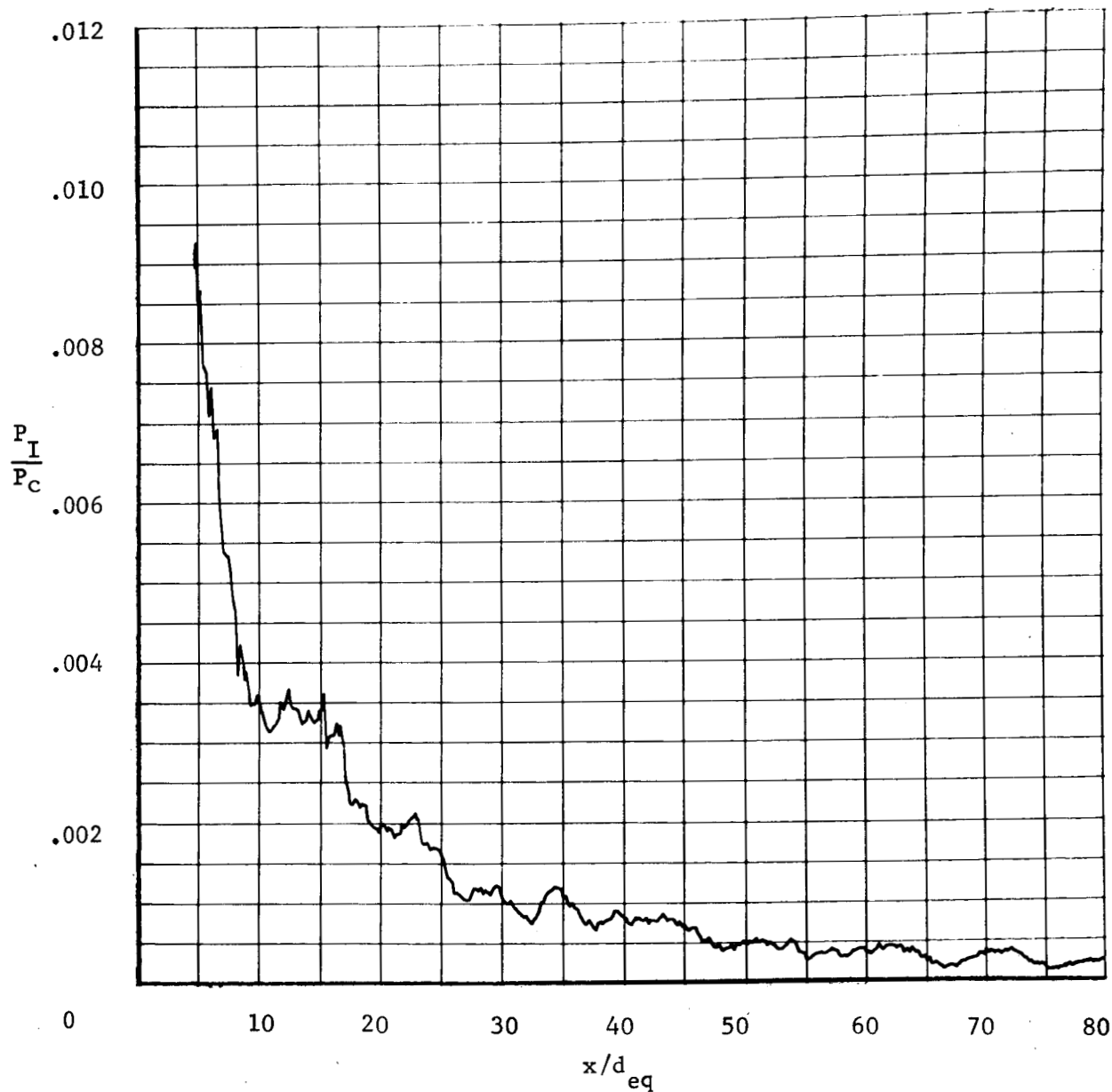


Figure 64.-Axial variation of fluted nozzle configuration impingement pressures;
WSTF Phase II, test 111.

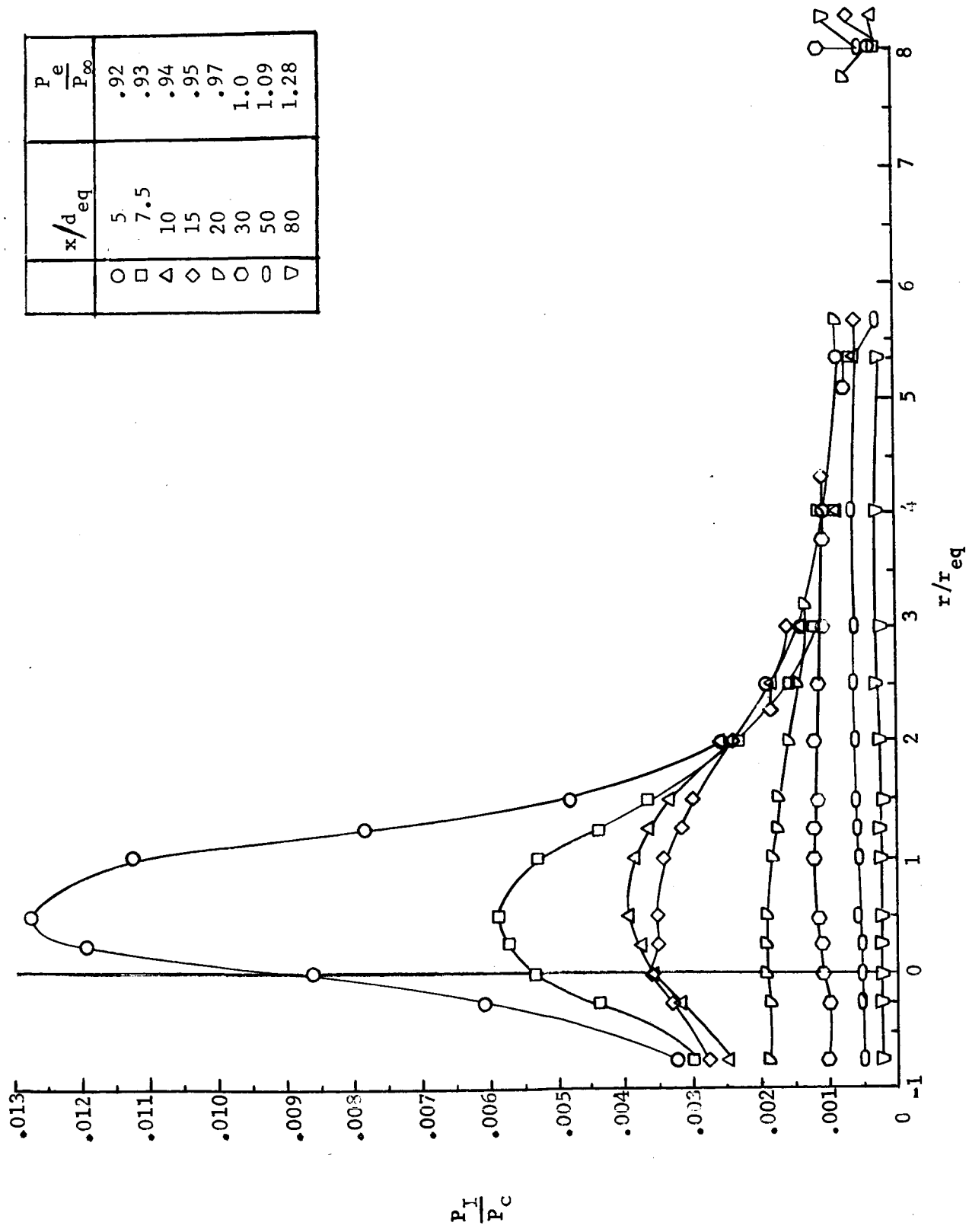


Figure 65.-Radial variation of fluted nozzle configuration impingement pressures;
WSTF Phase II, test 111.

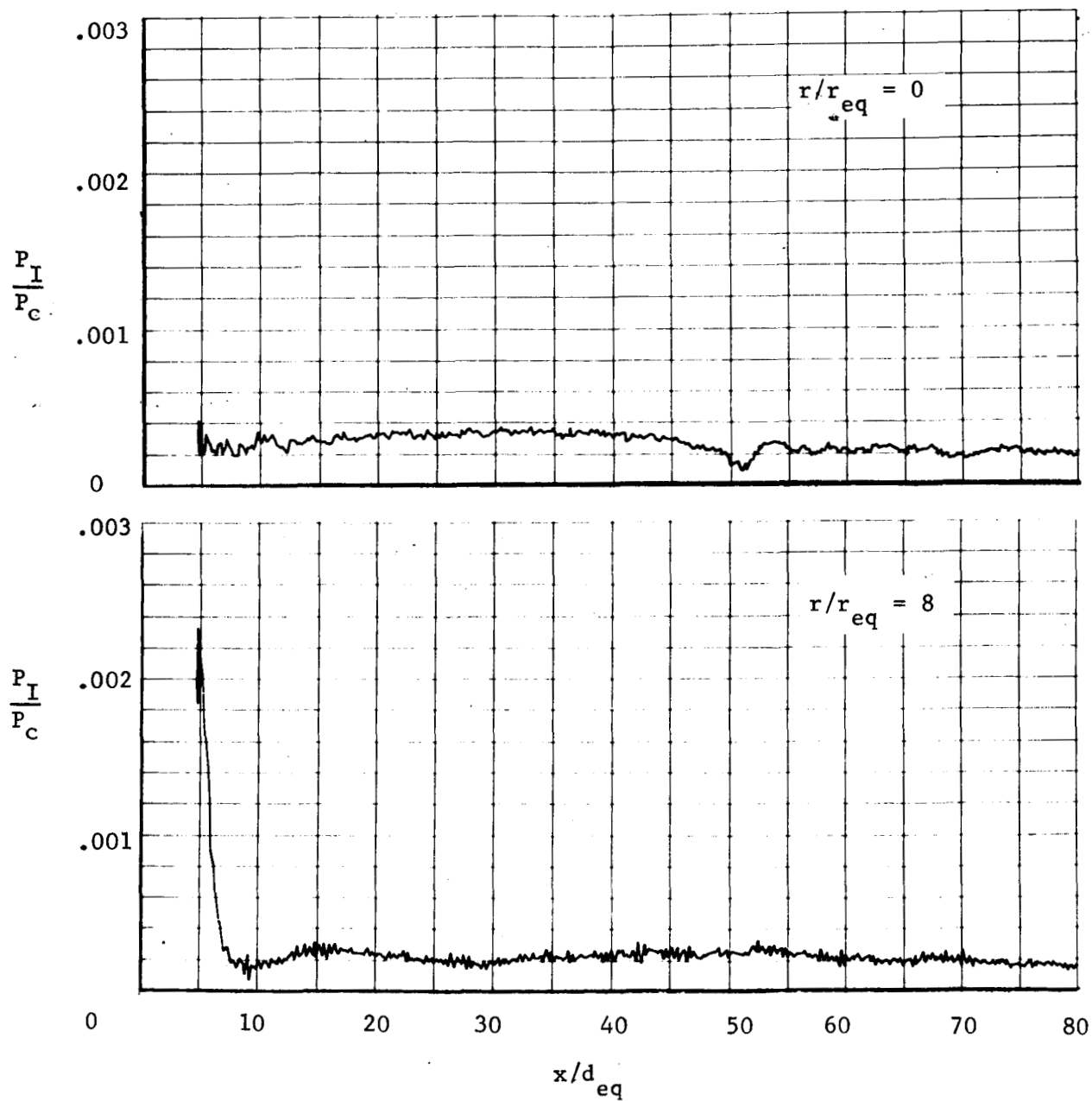


Figure 66.-Axial variation of fluted (mod 1) nozzle configuration impingement pressures; WSTF Phase II, test 11J.

	$\frac{x}{d_{eq}}$	$\frac{P_e}{P_\infty}$
○	5	.97
□	15	1.0
△	80	1.35

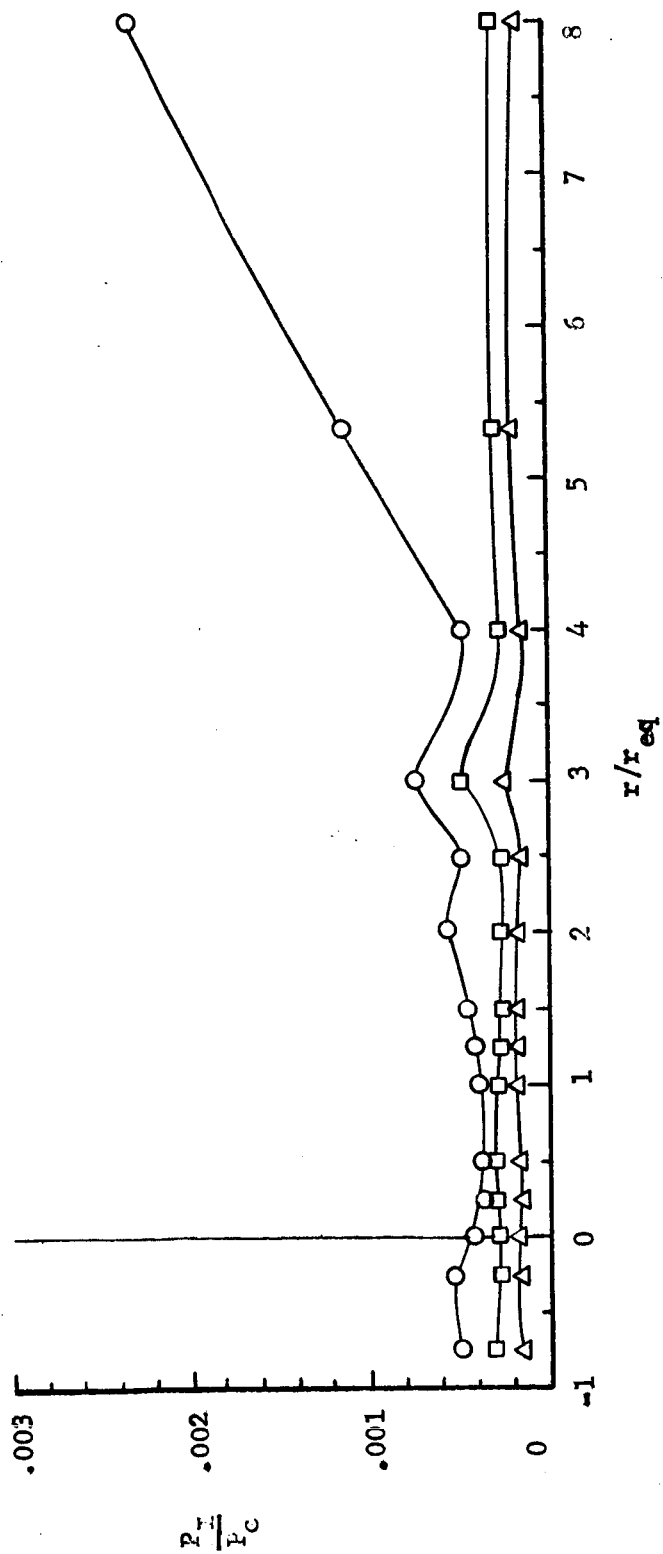


Figure 67. -Radial variation of fluted (mod 1) nozzle configuration impingement pressures; WSTF Phase II, test 11J.

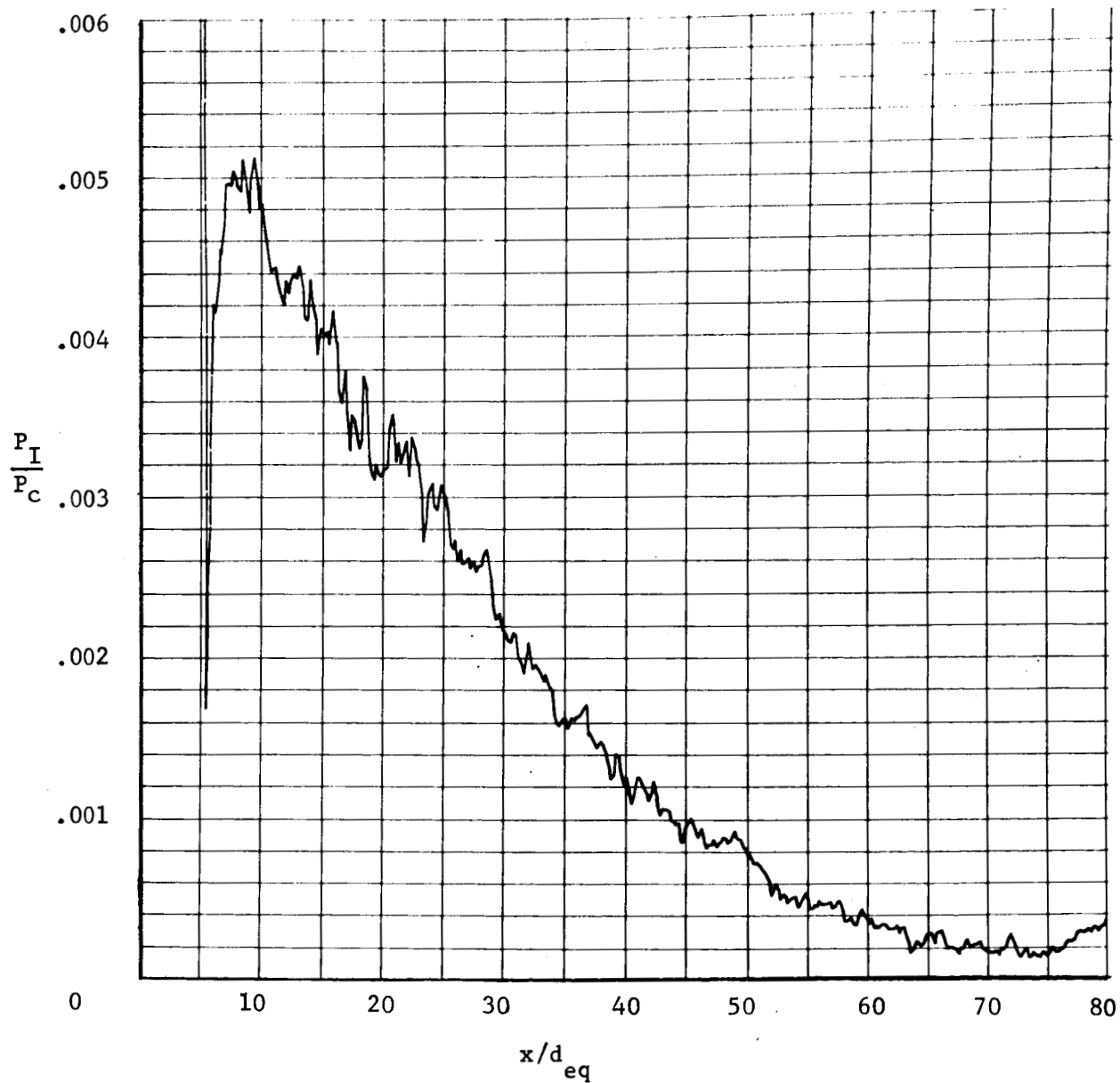


Figure 68.-Axial variation of 18-nozzle configuration impingement pressures;
WSTF Phase II, test 11K.

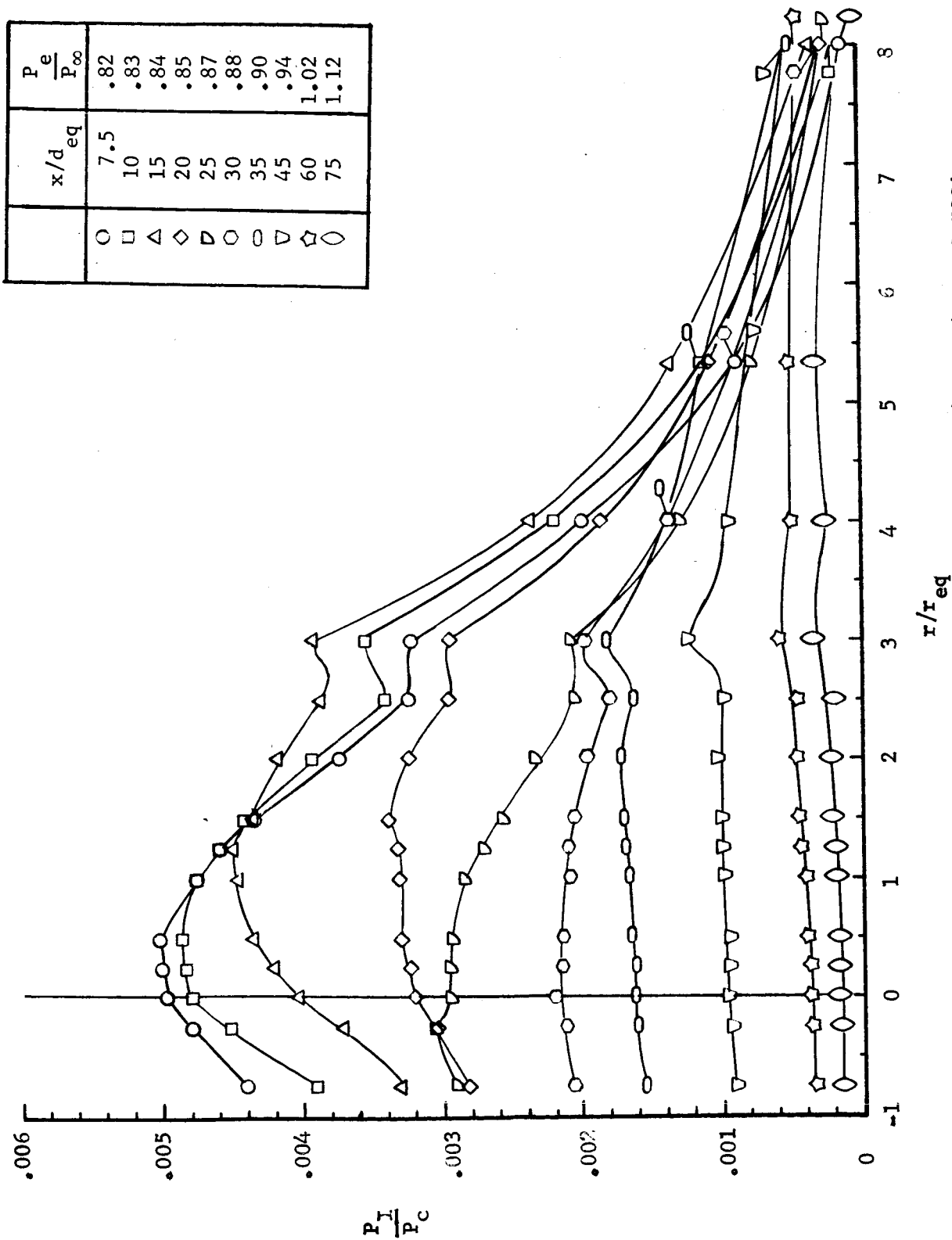


Figure 69.-Radial variation of 18-nozzle configuration impingement pressures;
WSTF Phase II, test 11K.

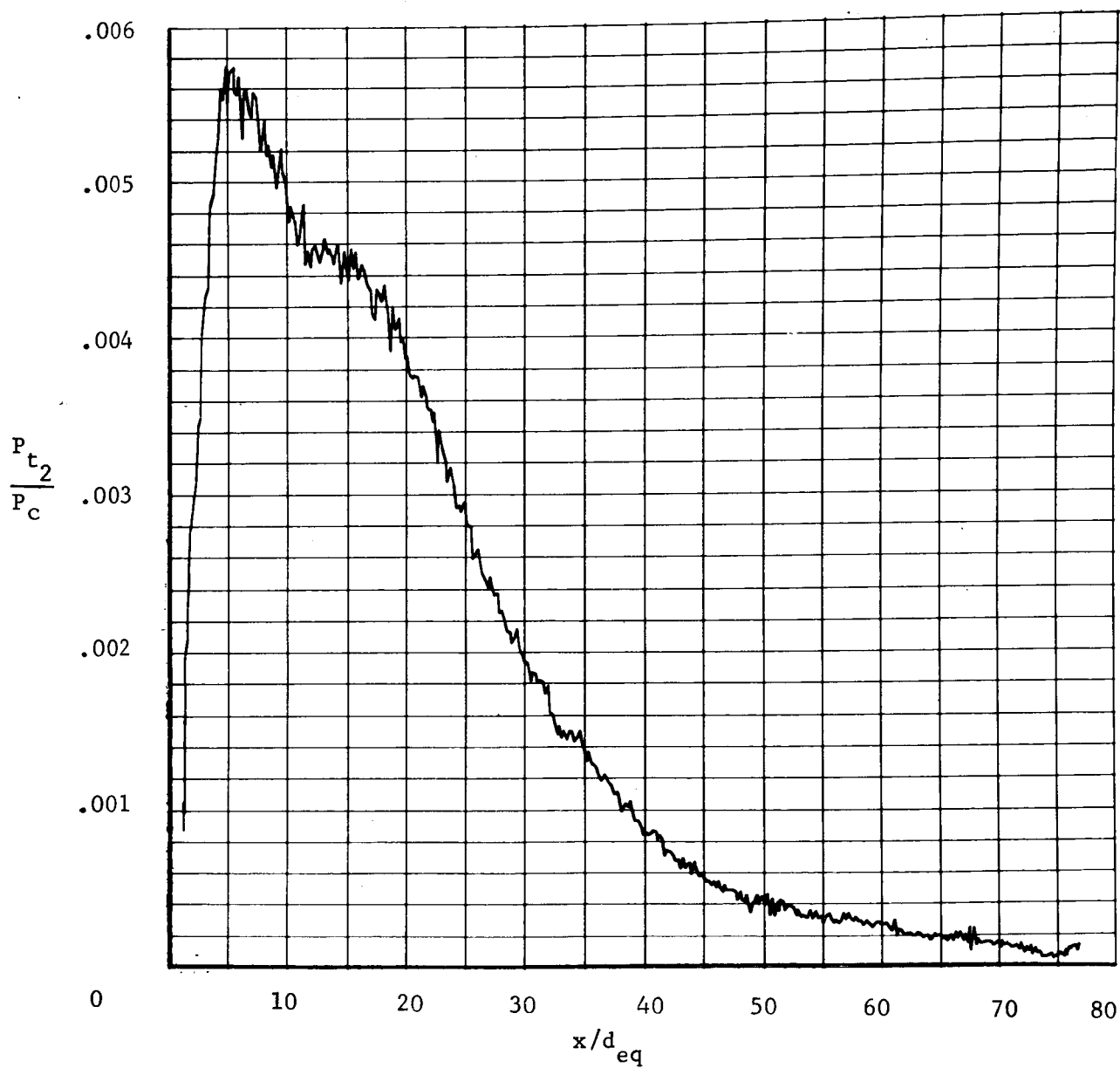


Figure 70.-Axial variation of 18-nozzle configuration pitot pressure;
WSTF Phase II, test 29.

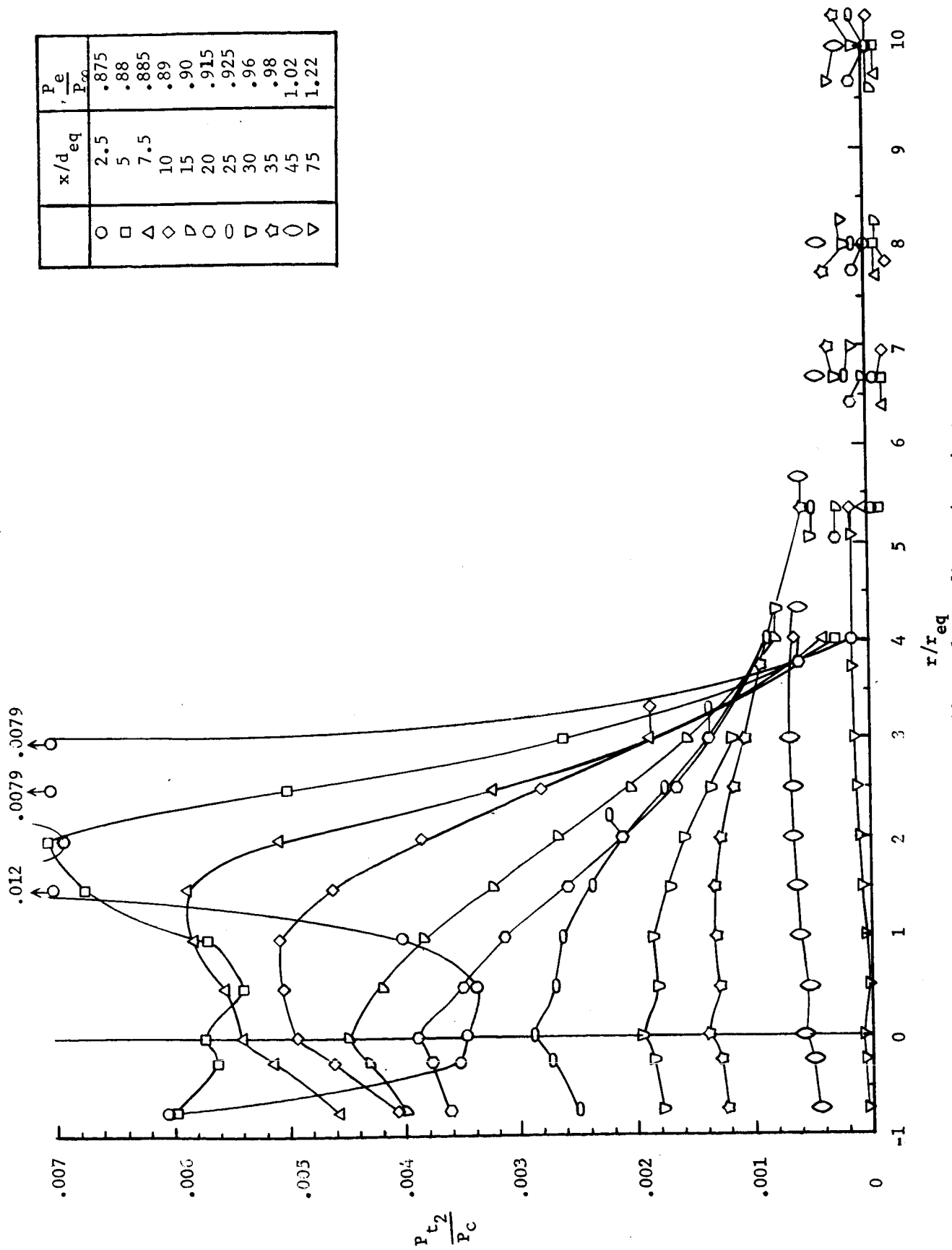


Figure 71-Radial variation of 18 nozzle configuration pitot pressure;
WSTF Phase II, test 29.

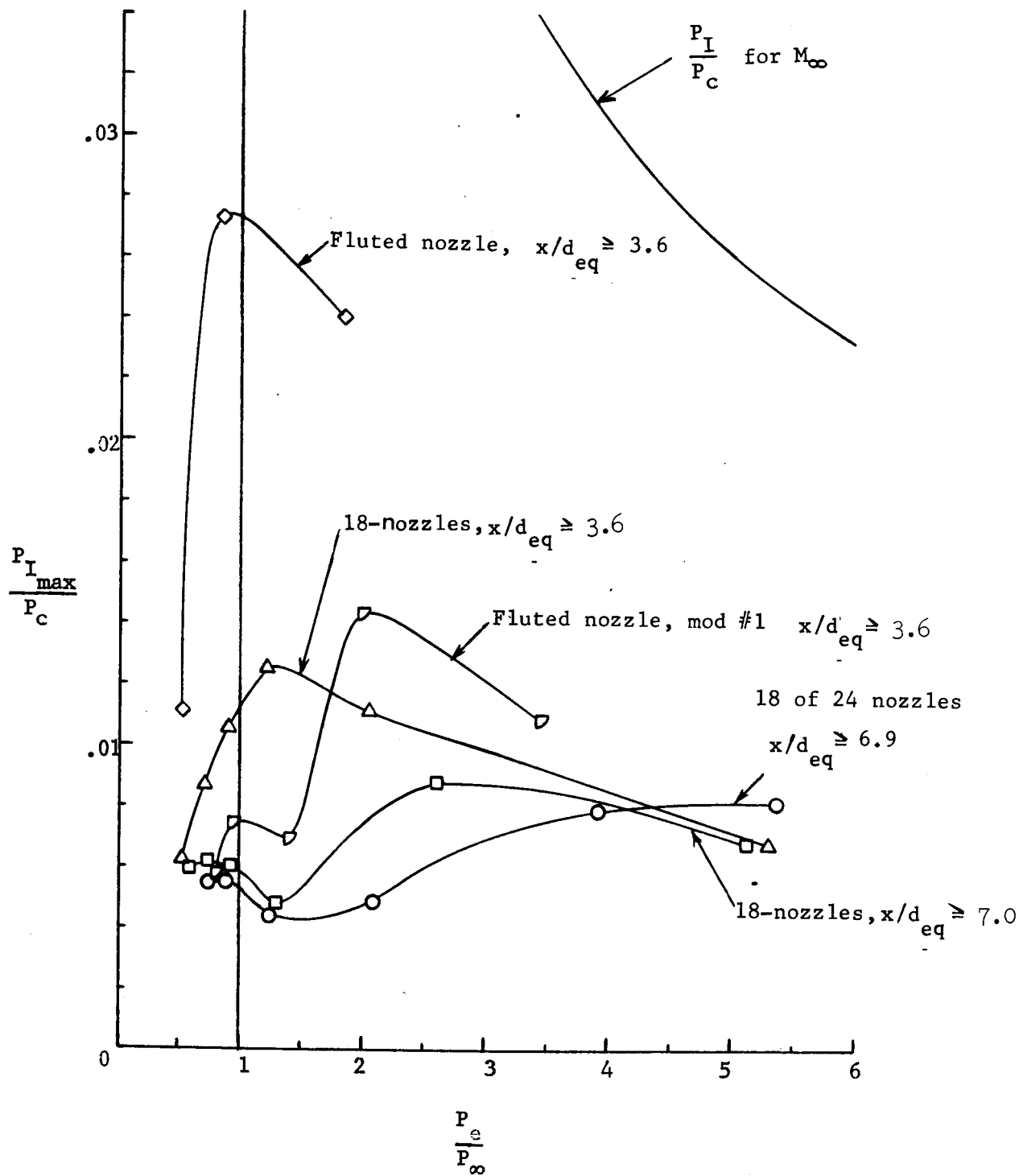


Figure 72.-Effect of pressure ratio on maximum impingement pressure; LRC cold-gas.

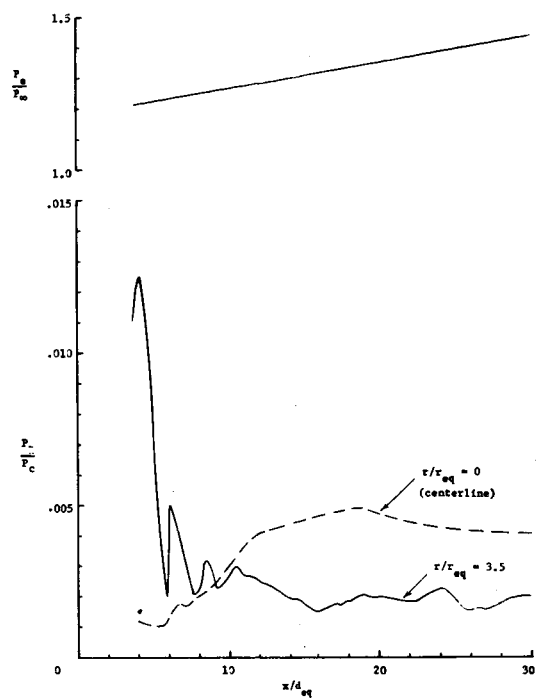


Figure 73.- Axial variation of 18-nozzle impingement pressure; LRC cold-gas.

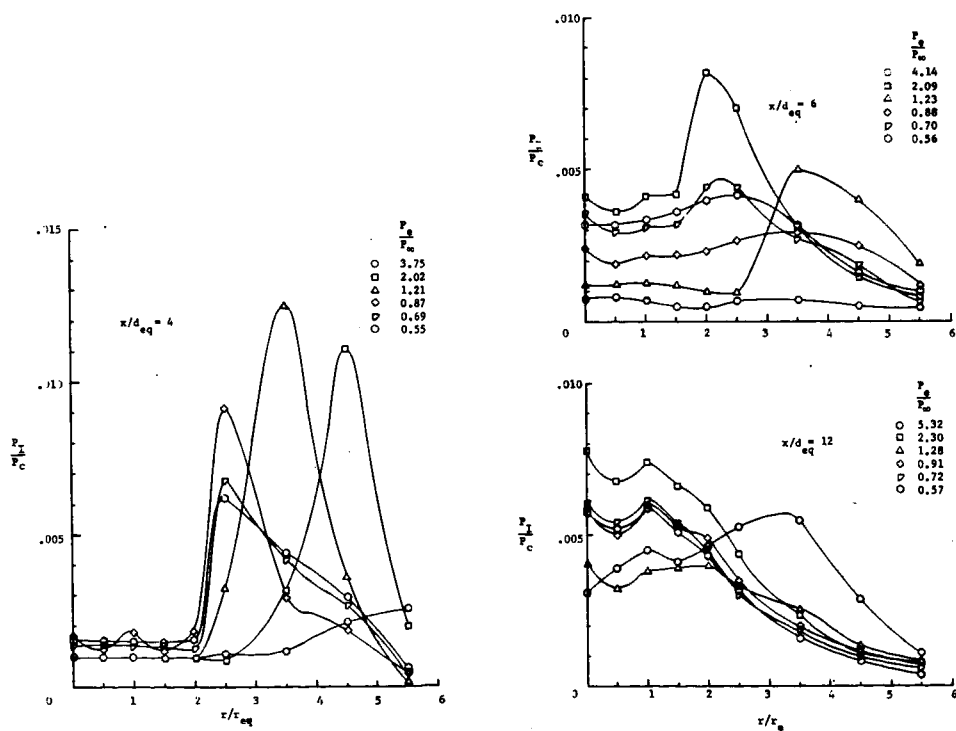


Figure 74.- Radial variation of 18-nozzle impingement pressure; LRC cold-gas.

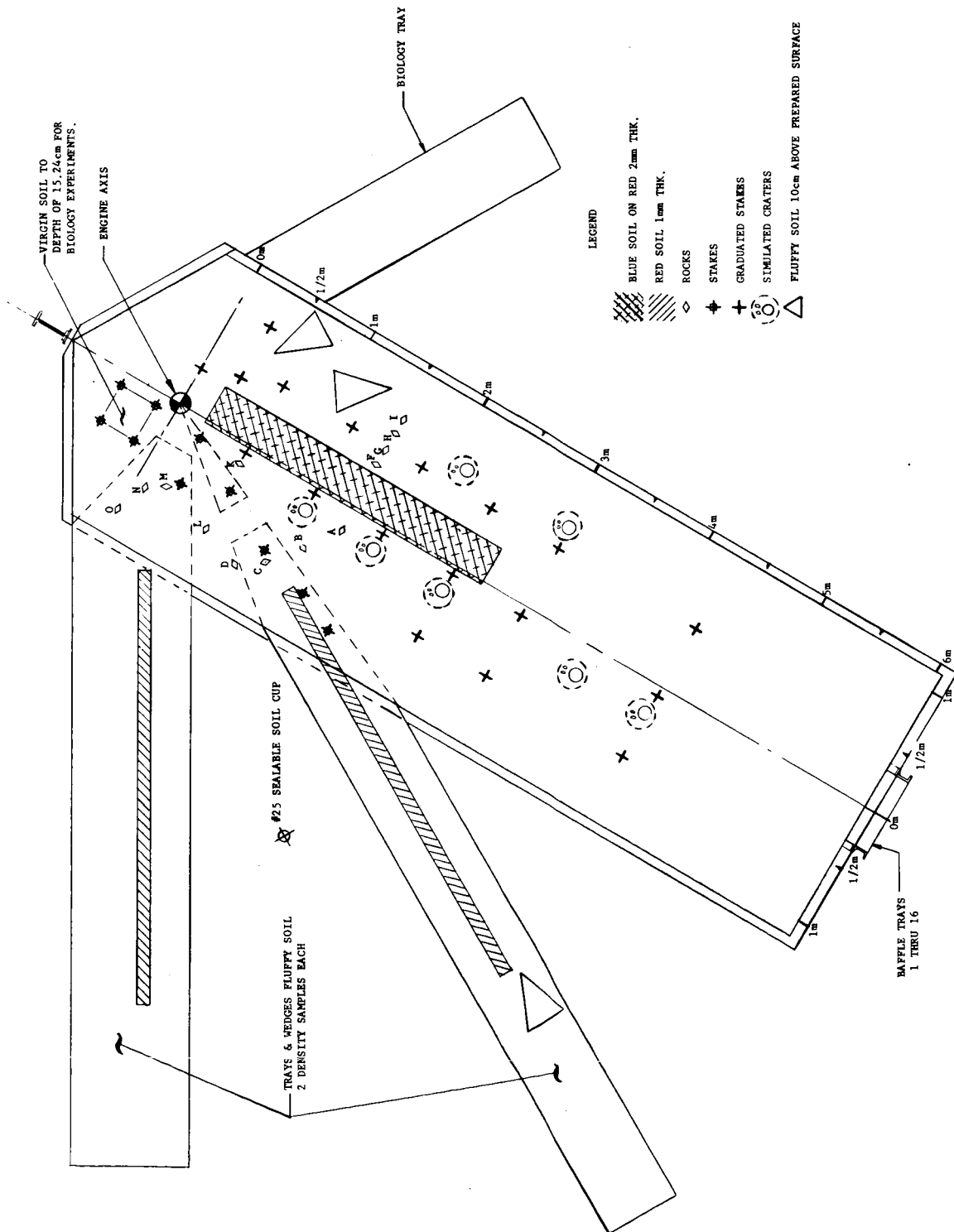


Figure 75a.- Pretest 12E surface elements.

Legend



Location and soil density in kilograms per cubic meter

*

Post test measurements when different from initial values

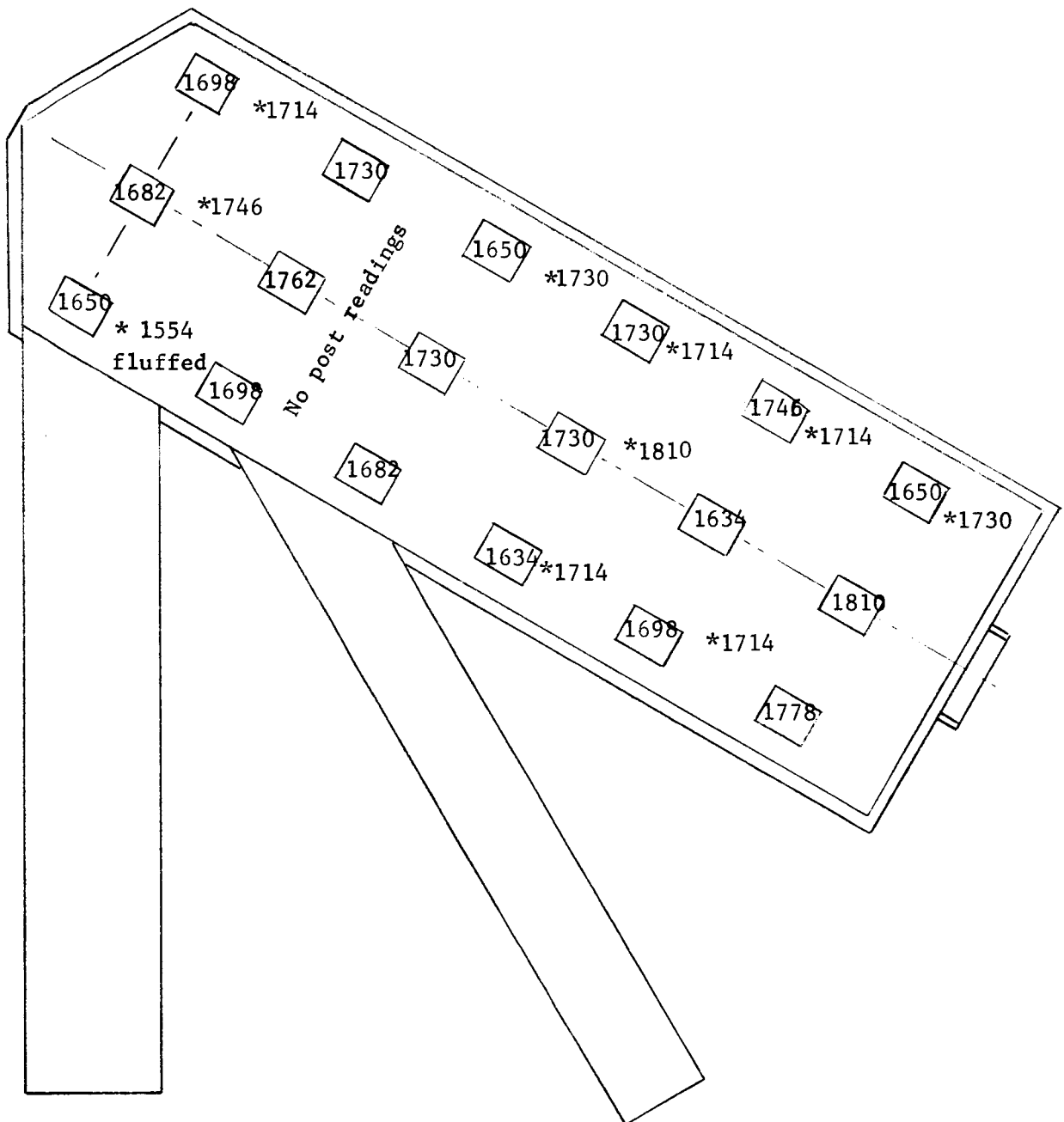


Figure 76.- Soil bed density for WSTF Phase II, test 12E.

NASA-4517
0771-1758

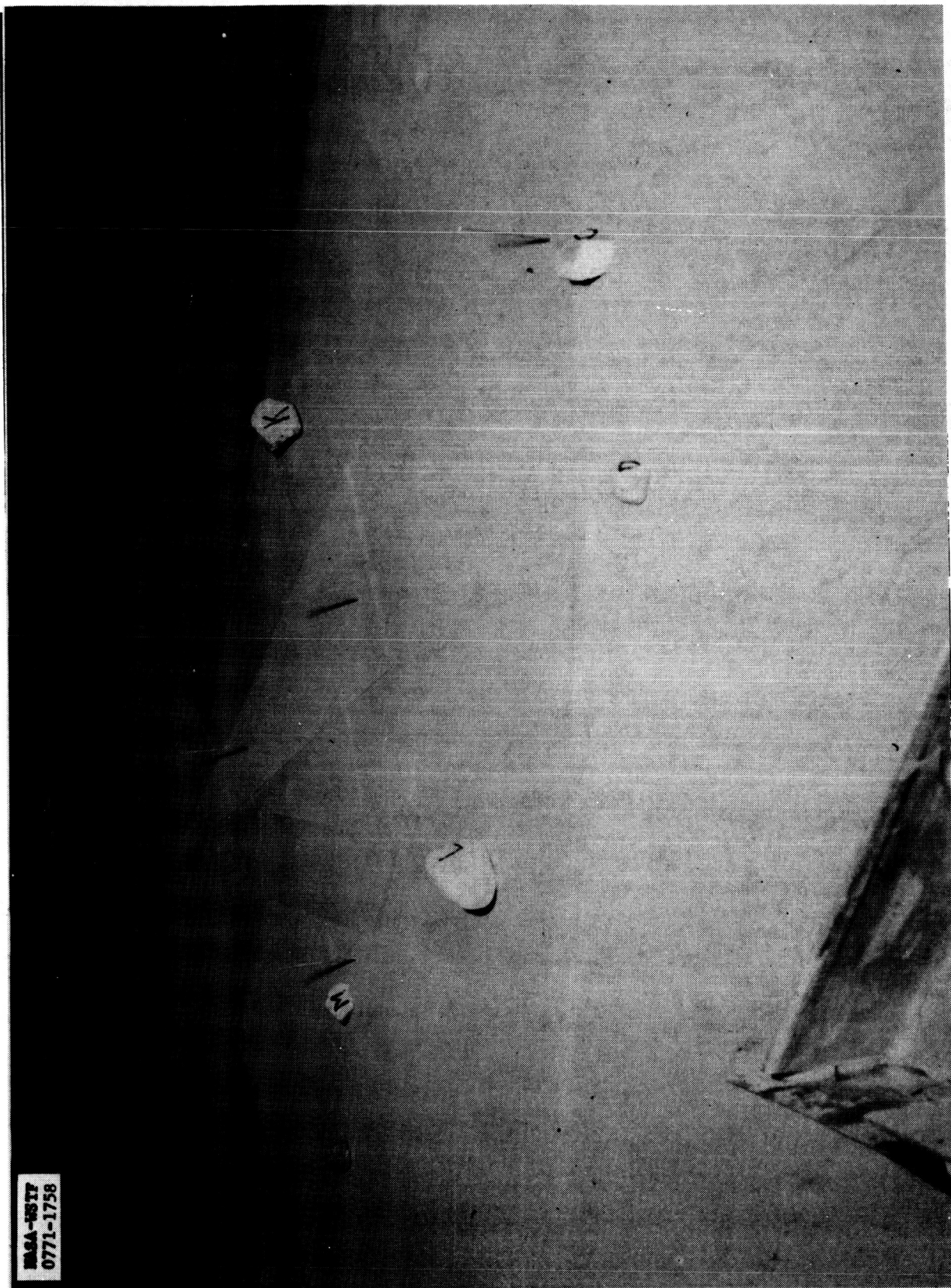


Figure 77.- General view of the pretest surface elements for test of 18-nozzle configuration conducted in lunar nominal soil model.



NASA-WSTP
0771-1760

Figure 78.- View of the side soil trays where they join the main soil bed showing one millimeter colored soil strip, pretest 12E.

NASA-WSTF
0771-1765



Figure 79.- General view of the distribution of surface elements after test of 18-nozzle configuration conducted in lunar nominal soil model.

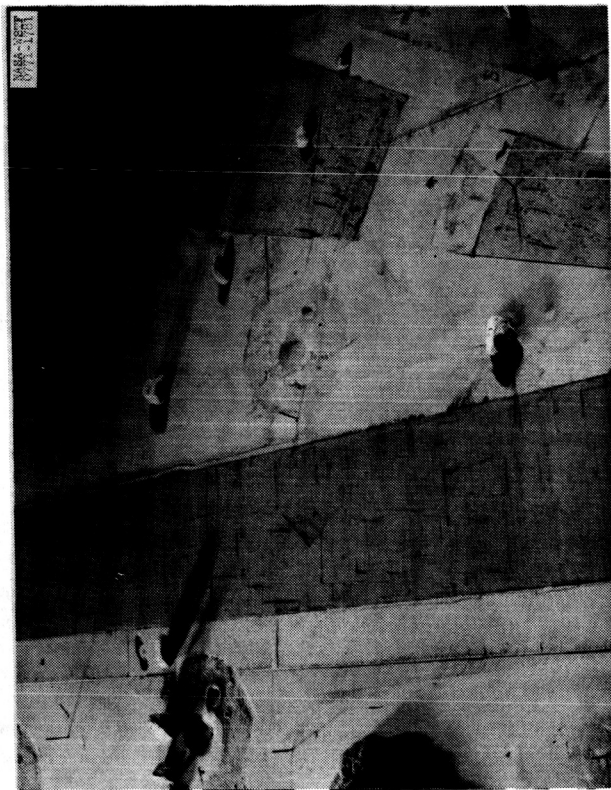


Figure 80.- Stereo-photography of Pretest 12 E soil test.



Figure 81.- Stereo-photography of post-test 12E soil test.

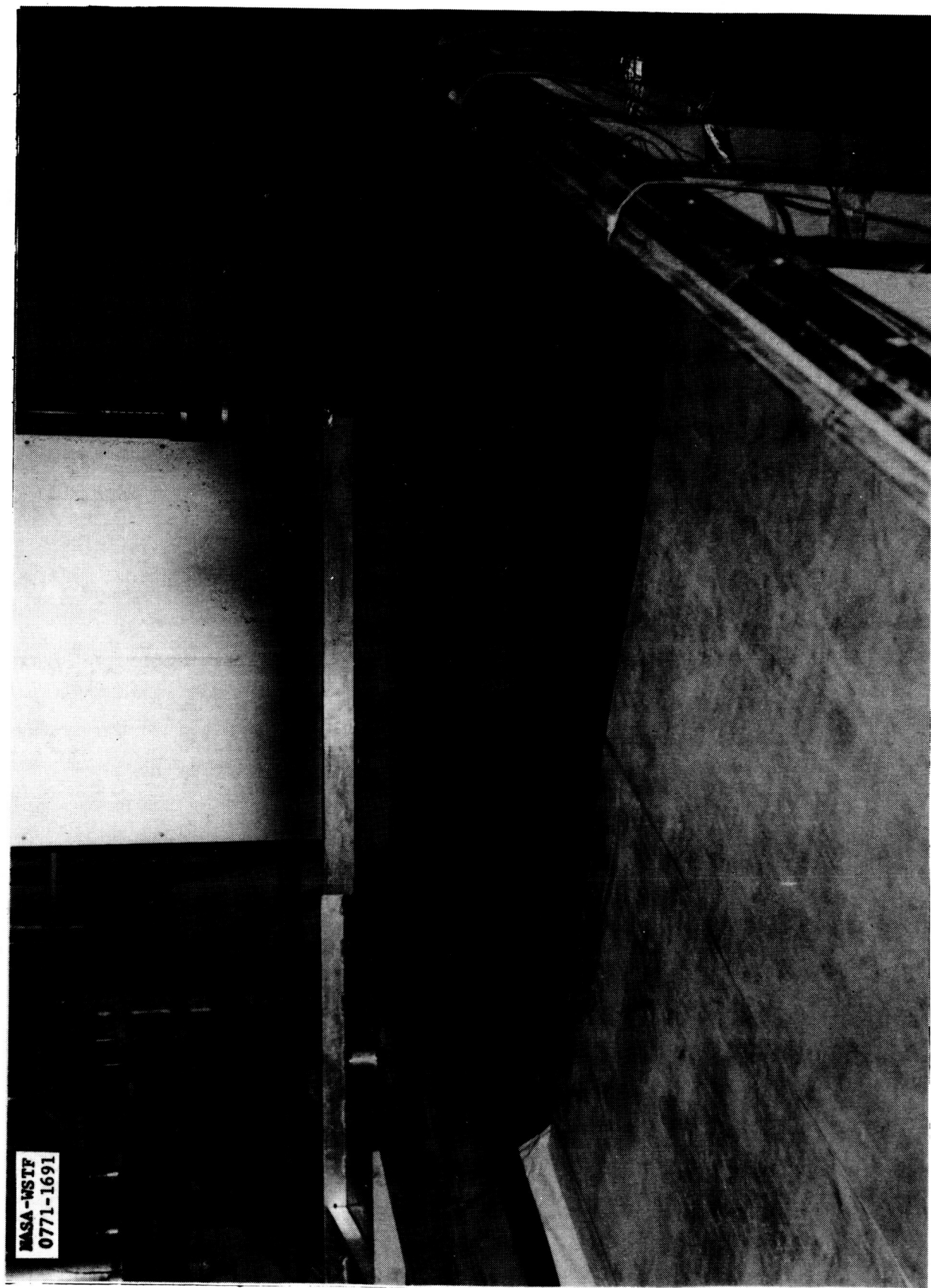


Figure 82.- View of the soil container modified for the volcanic dune sand model employed in tests 12F, G and H.

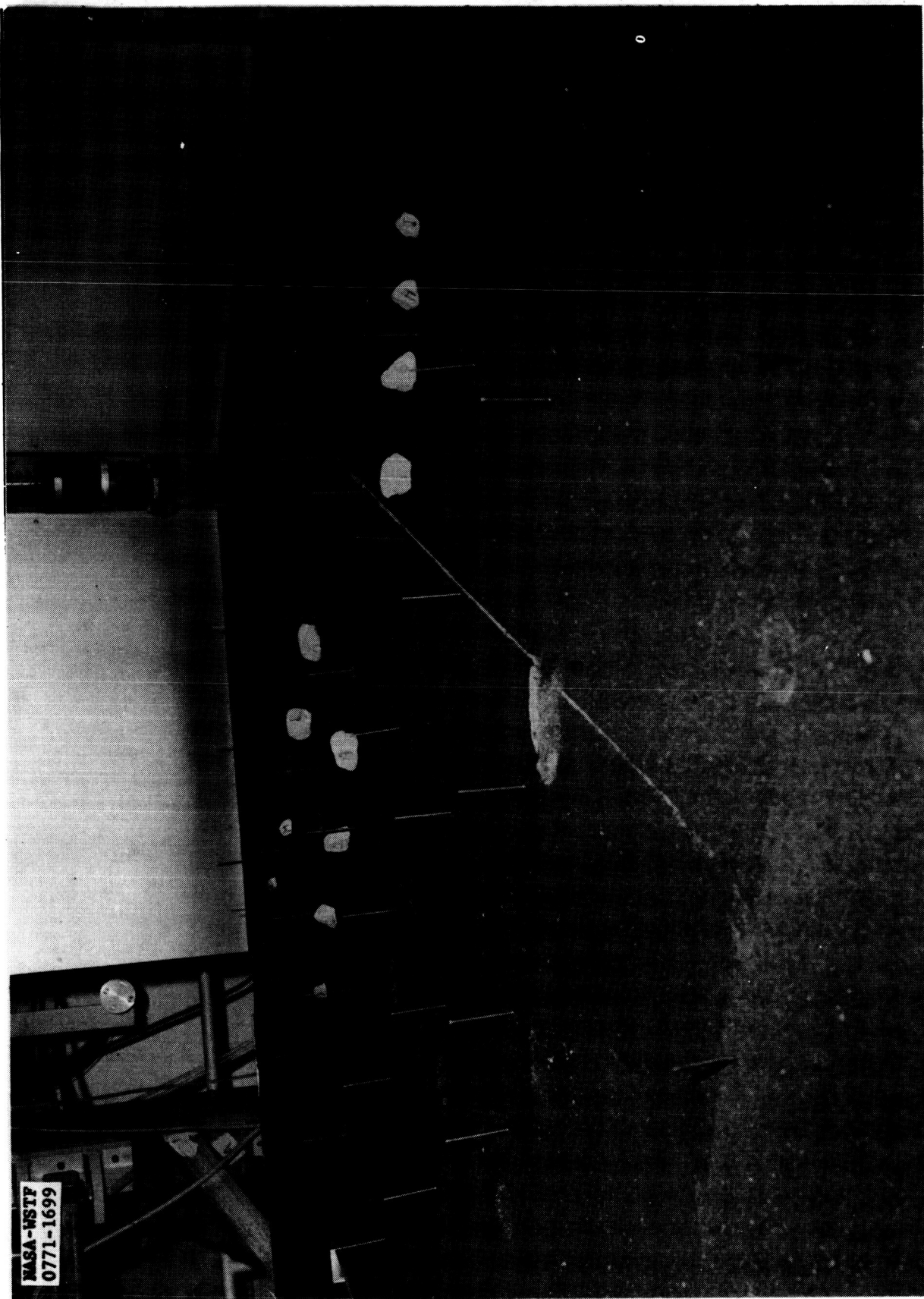


Figure 83.- View of the pretest surface elements for test 12F.

Legend



Location and soil density in kilograms per cubic meter

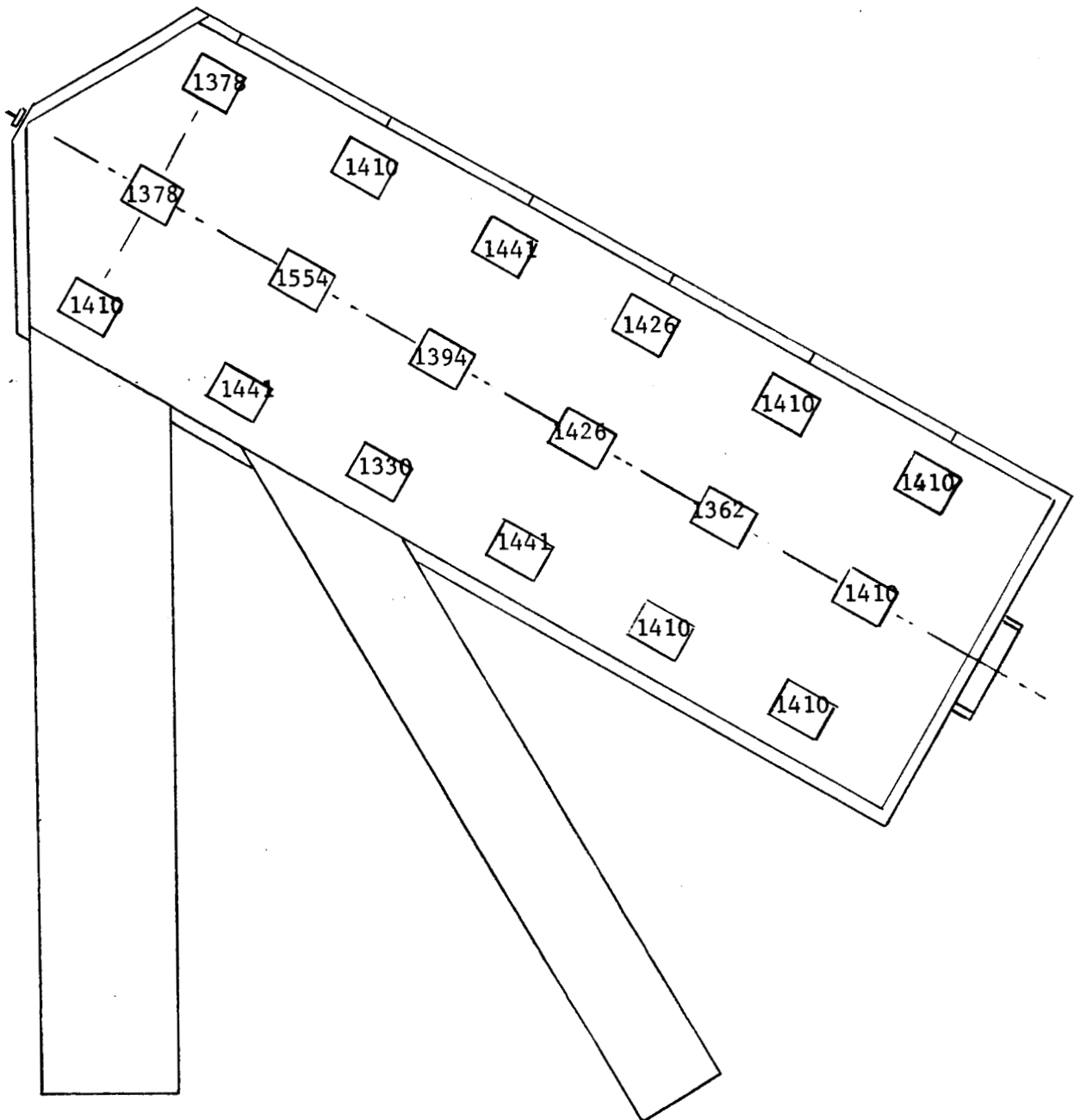
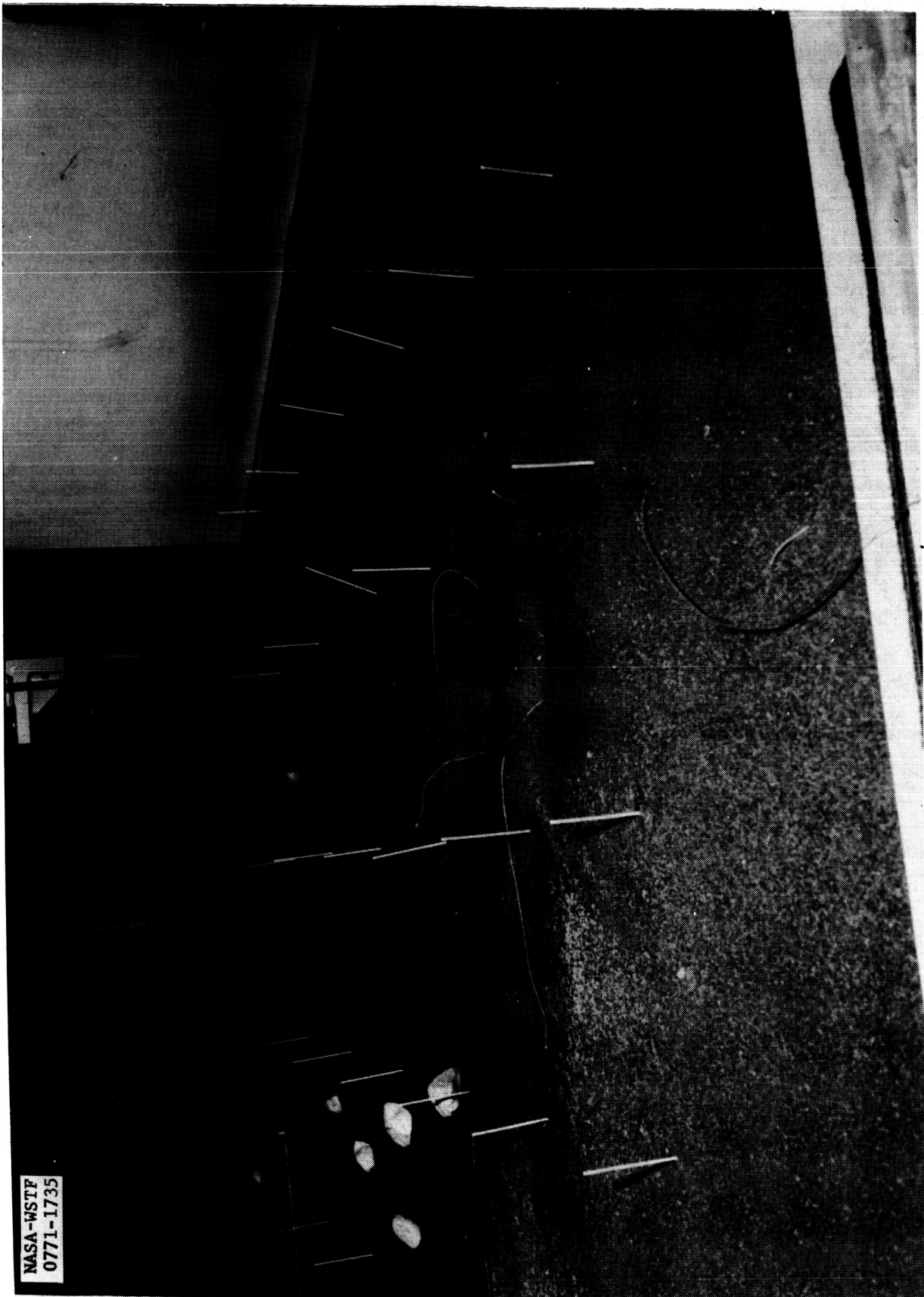


Figure 85.- Soil bed density for WSTF Phase II, test 12F.



NASA-WSTF
0771-1735

Figure 86.- View of the central crater made up of 18 discrete depressions formed during test 12F.

NASA-WSTF
0771-1688



Figure 87.- View of multilayer colored soil strip in test 12F after sectioning.

NASA-WSTF
0771-1736

Figure 88.- Soil bed of dune sand after test 12F showing 18 craters made by nozzles.

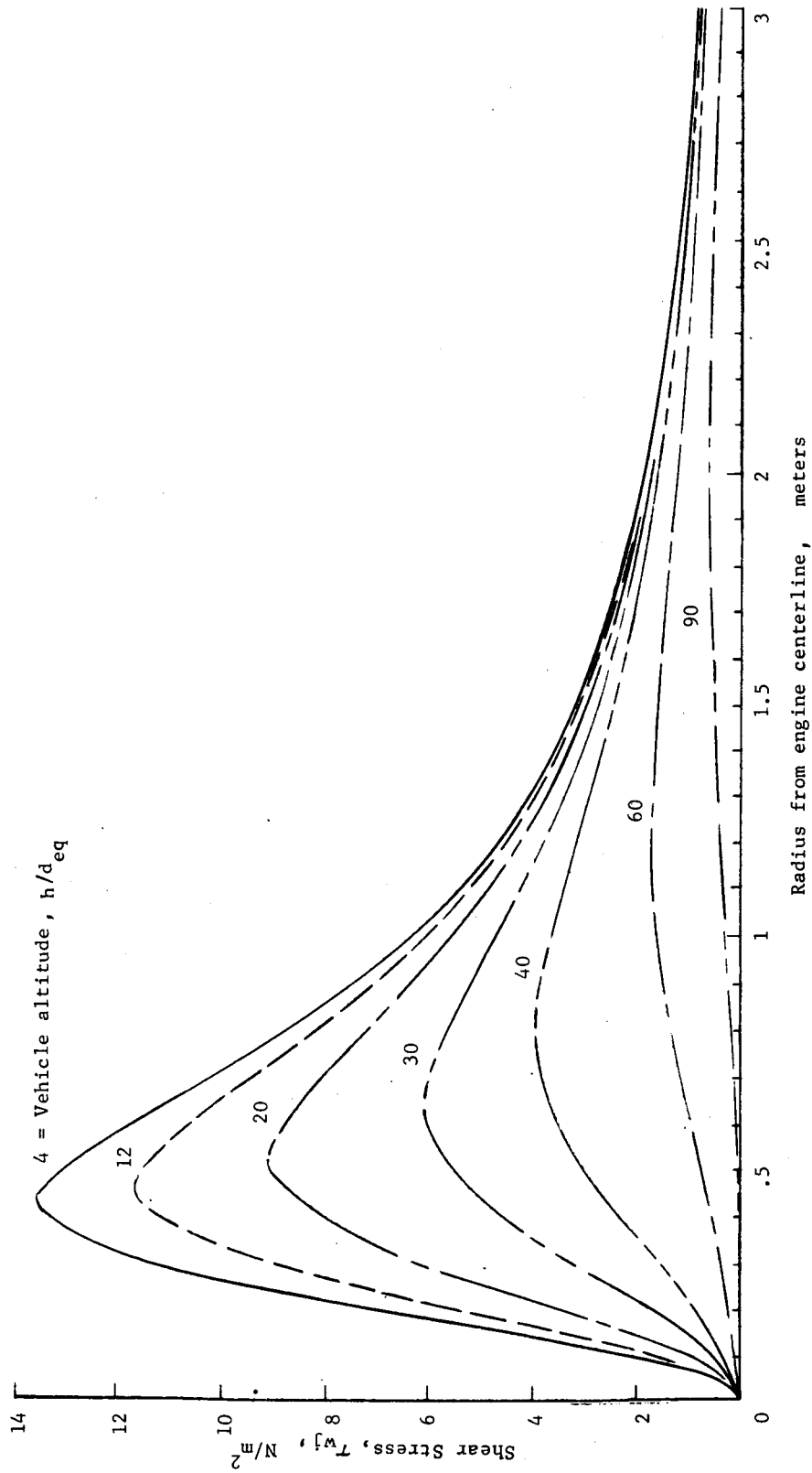


Figure 89.- Estimated Viking surface shear stress distribution.

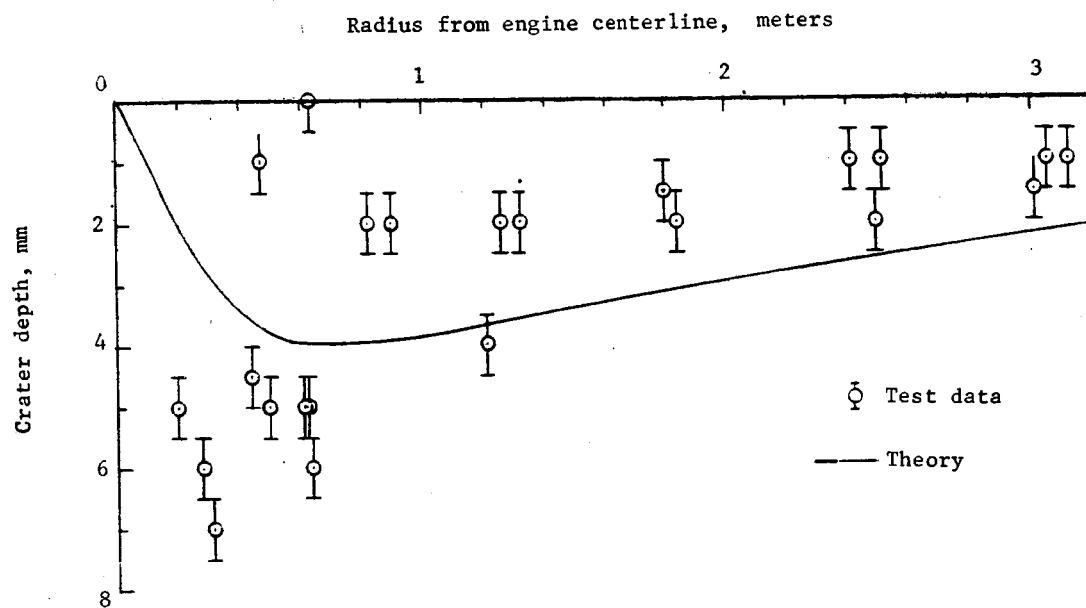


Figure 90.- Comparison of viscous erosion theory and test results on lunar nominal soil model (WSTF Phase II - test 12E).

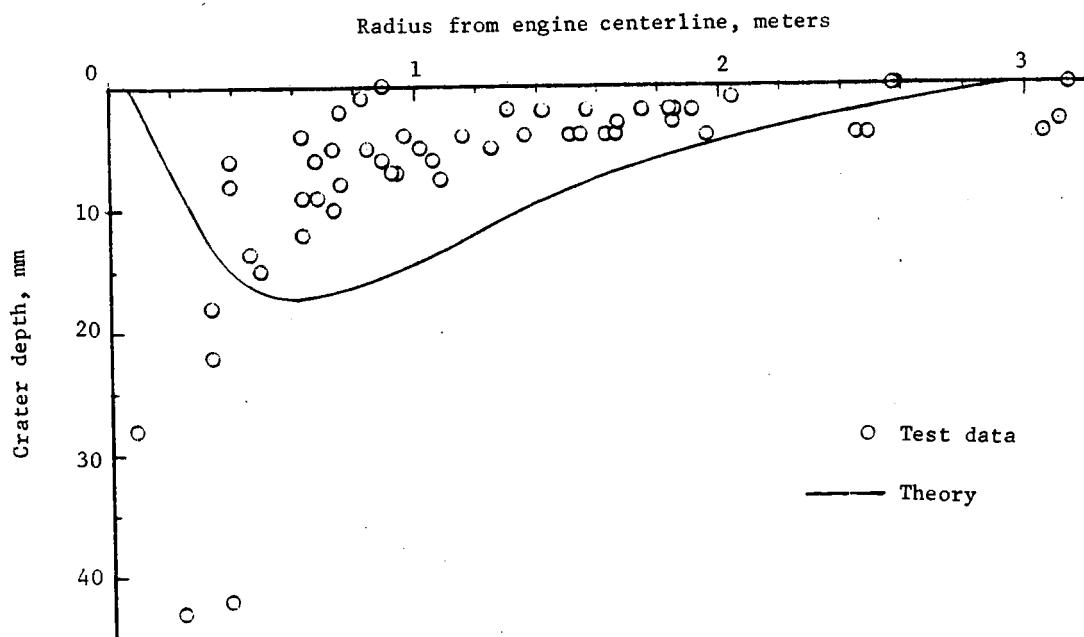


Figure 91.- Comparison of viscous erosion theory and test results on dune sand soil model (WSTF phase II - test 12F).

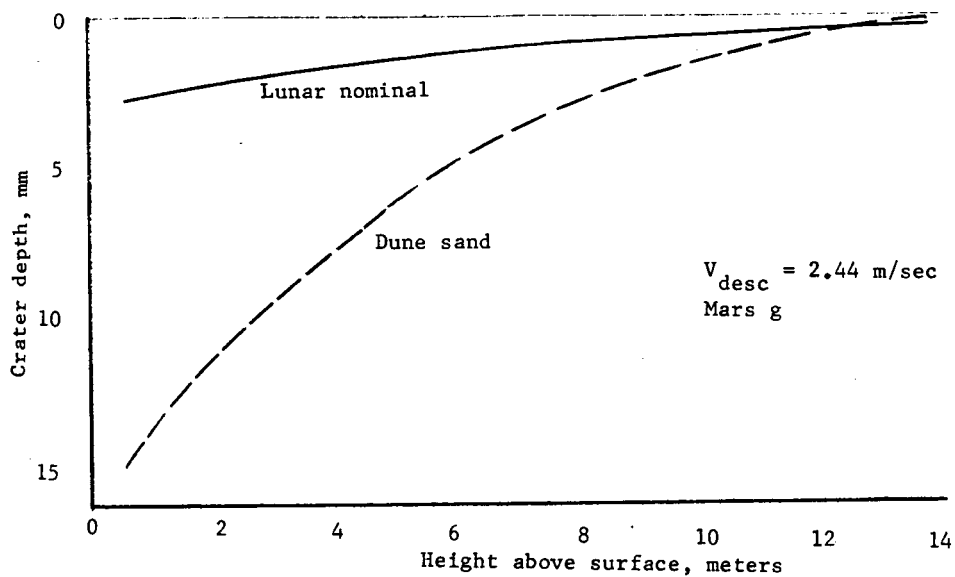


Figure 92.-Variation of viscous erosion crater depth with altitude.

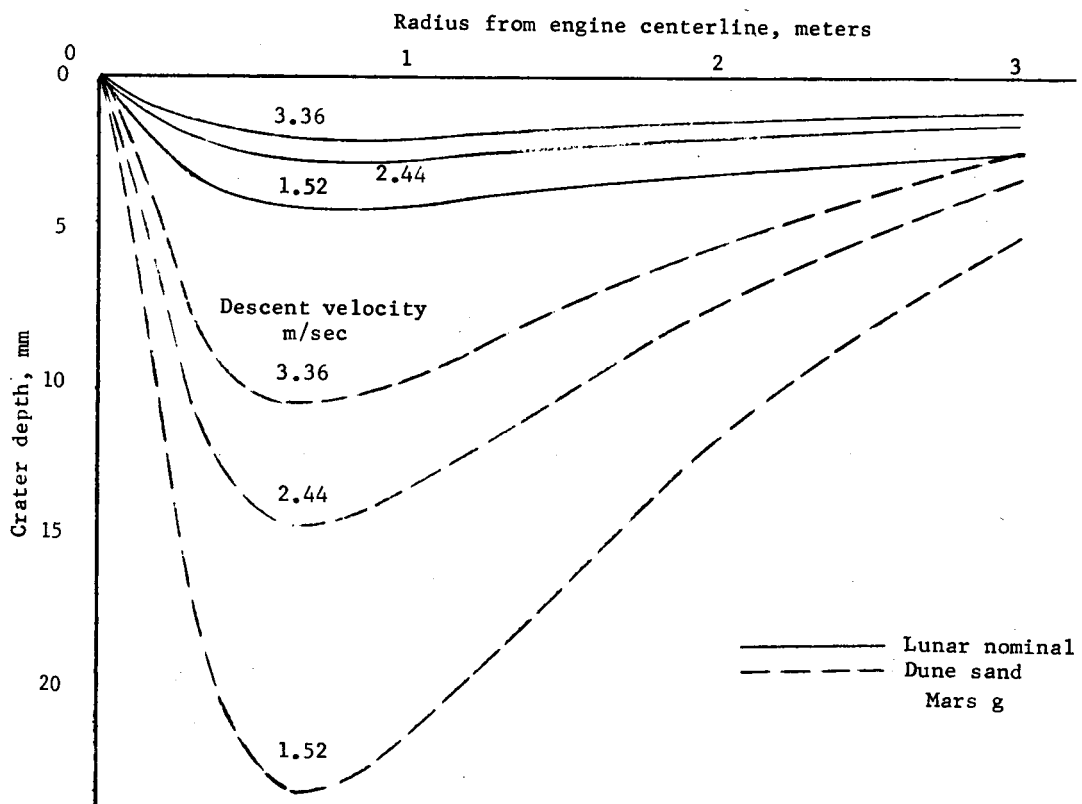


Figure 93.- Effect of descent velocity on viscous erosion under Martian gravity.

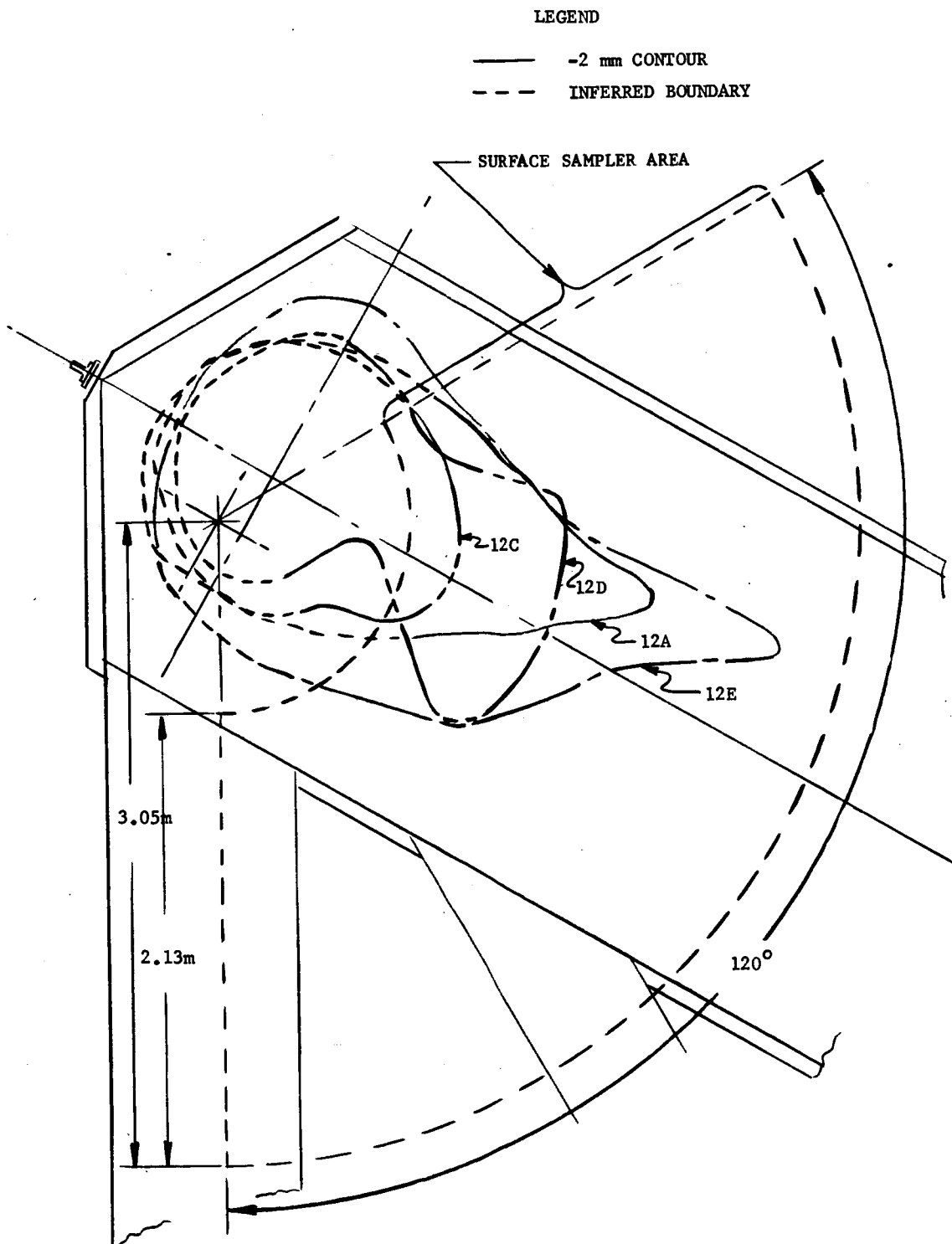


Figure 94.- Contour map of -2 mm erosion area for tests 12A, 12C, 12D, 12E, conducted in lunar nominal (hazen) model.

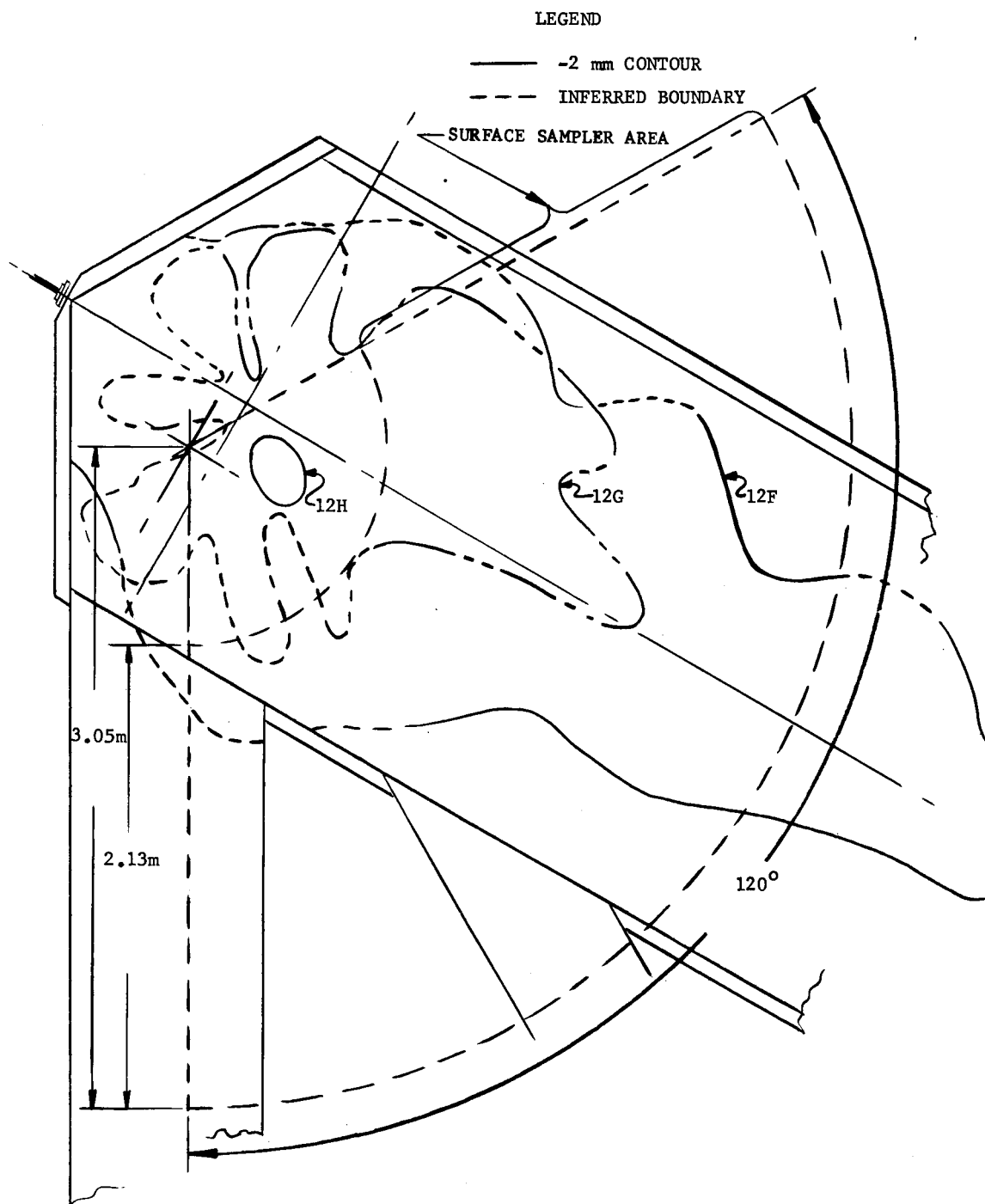


Figure 95.- Contour map of -2 mm erosion area for tests 12F, 12G, and 12H conducted in volcanic dune sand model.

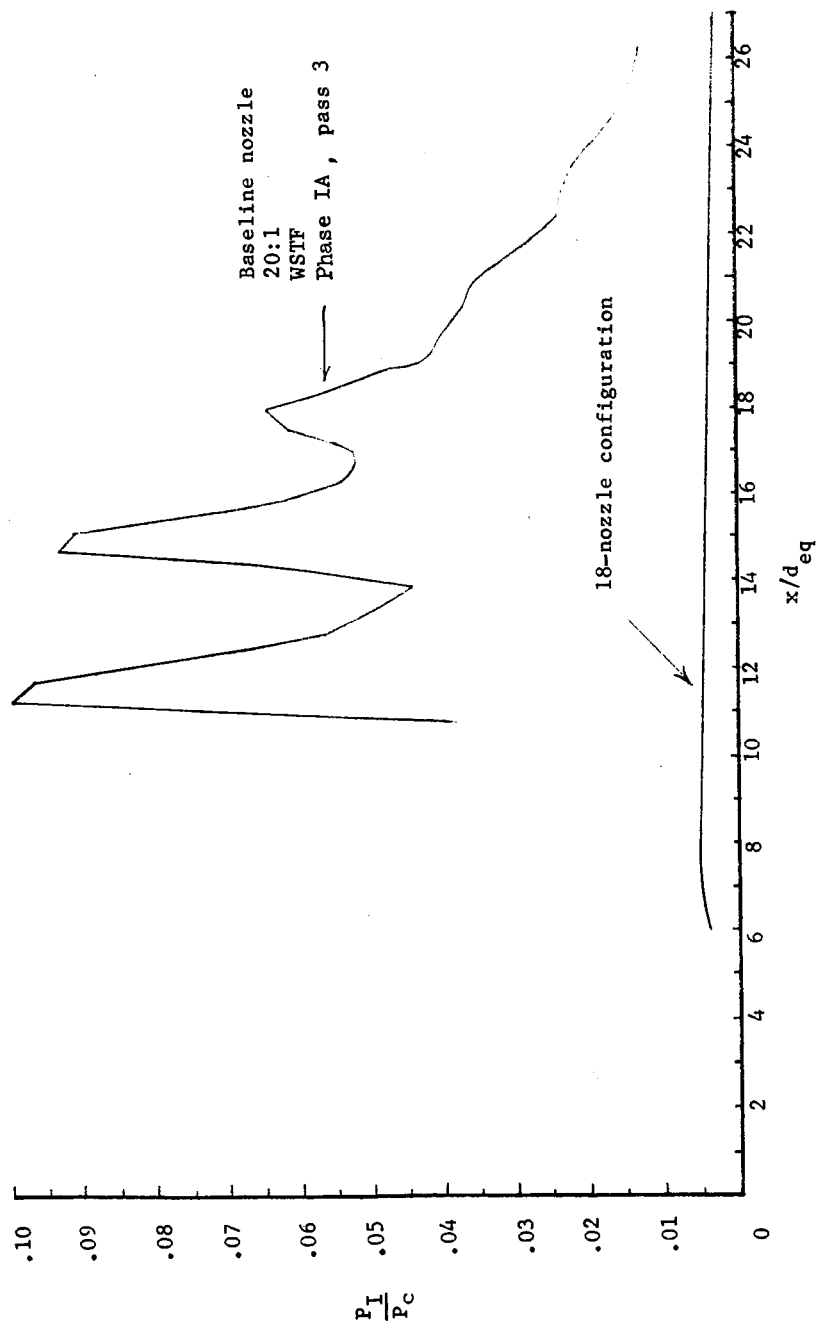


Figure 96.- Comparison of original baseline nozzle and new Viking 18-nozzle configuration centerline impingement pressures.

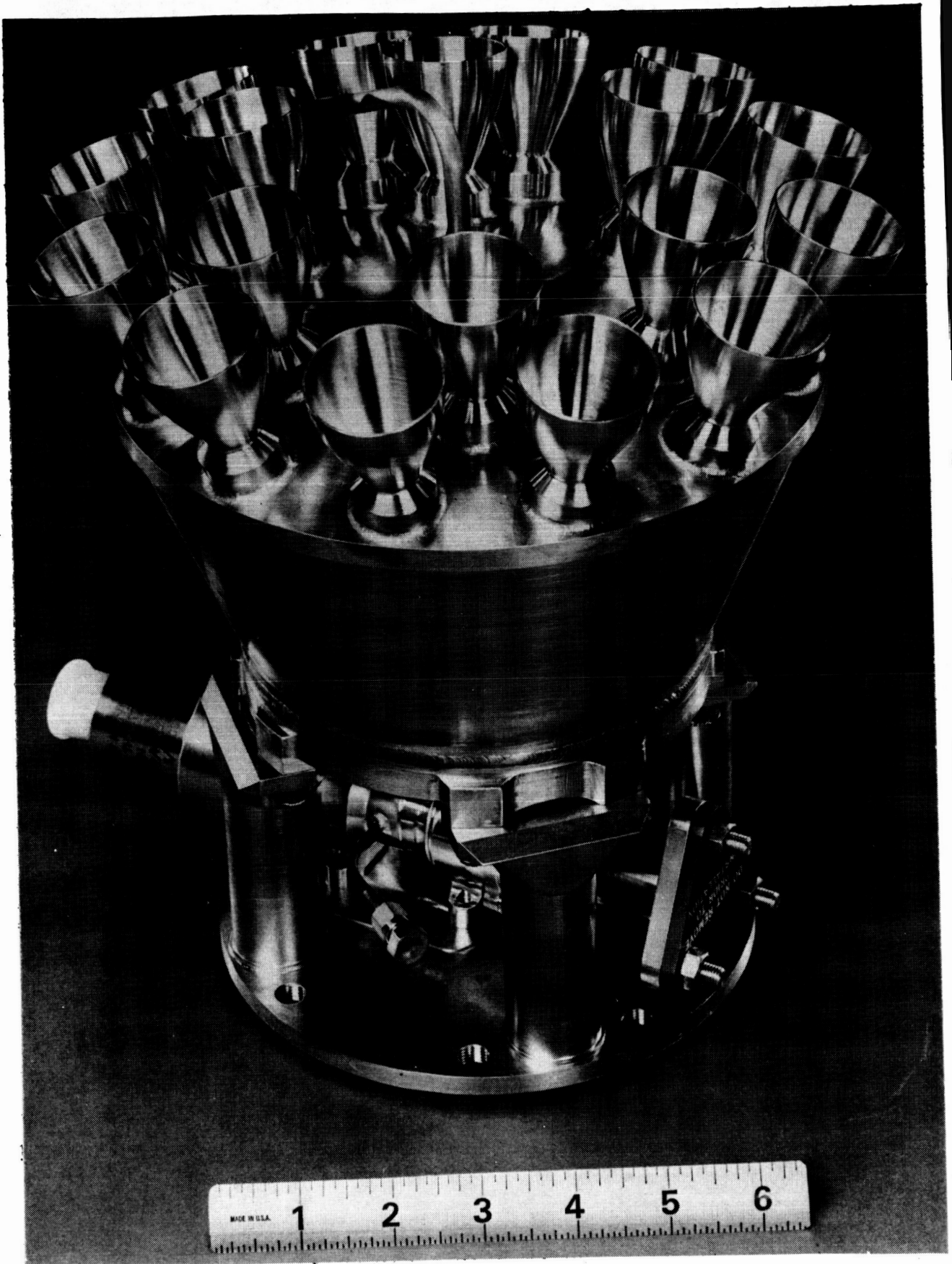


Figure 97.- Flight weight terminal descent engine with 18 nozzles.

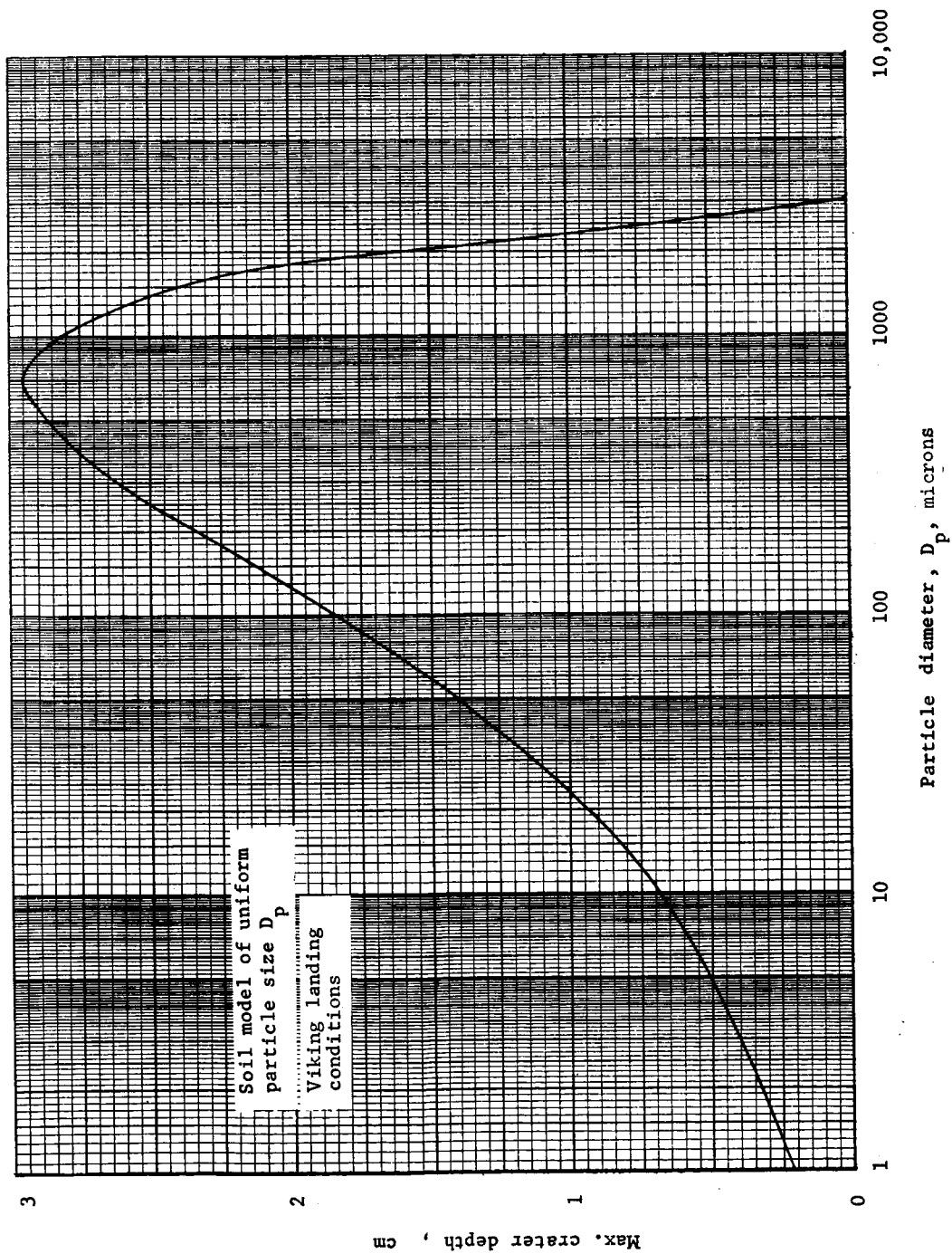


Figure 98.-Effect of particle size on soil erosion.